Investigating Diacylglycerol Kinase Function and Regulation Using Chemical Proteomics and Mass Spectrometry Lipidomics

Roberto Carlos Mendez
Rochester, New York

B.A. Chemistry and English, with a cluster in Advance Macroeconomics, University of Rochester, 2001

A Dissertation presented to the Graduate Faculty of the University of Virginia in Candidacy for the Degree of Doctor of Philosophy

Department of Chemistry

University of Virginia
July 2022

Abstract

Diacylglycerol kinases (DGKs) regulate cell metabolism and signaling through poorly defined mechanisms with regards to lipid specificity. My thesis work aims to bridge gaps in our knowledge by investigating isoform-specific functions of DGKs using chemoproteomic and lipidomic methods. We aim to apply novel technologies to explore DGKs to unravel how individual members of this enzyme family can regulate distinct cell biology. We have made progress in determining DGKθ-mediated alterations in the lipidome. These studies have provided key insights into molecular lipid composition at the level of fatty acyl chain length and unsaturation, using tandem LC-MS/MS techniques. We discovered a putative role for this DGK isoform in the Lands cycle.

We applied modern technologies for perturbing protein function, such as CRISPR/Cas9, PROTAC, and autoSTOMP, along with mass spectrometry techniques, to probe DGK metabolic function. We have demonstrated that targeted protein degradation (using dTAG method) can be used to probe lipid substrate specificity of DGK isoforms. This allowed us to then focus our chemoproteomic efforts to identify important/critical sites on all ten DGK enzymes with importance for metabolic function. Collectively, the ligandable sites identified represent the first step towards developing potent and selective inhibitors for individual DGK isoforms. Based on my collective work, we provide evidence for distinct ligand binding pockets for individual DGK isoforms, which is reflected in specific lipid substrates regulated in cells.

Acknowledgment

I would like to thank my PI and mentor, Prof. Ku-Lung (Ken) Hsu, for the support and guidance he provided while under his instruction. I will always be grateful for all the lessons and insight he bestowed on me throughout my stay at UVA, academically and professionally. I would also like to express my deepest gratitude to every member in our lab for their support and guidance, their editing help, and their sound advice in believing that anything is possible.

I would like to thank Profs. Thurl Harris, John Lazo, Dave Cafiso, and Michael Hilinski for being part of my dissertation committee. I can still remember my initial conversations I had with them as a first-year graduate student, especially when I went to their weekly group meetings. It allowed me to appreciate the depth and scope of the different research happening at UVA. Throughout my stay at UVA, they always listened to me, and they provided guidance and sound advice when I needed the most. I would like to also say many thanks to Dr. Jasmine Crenshaw for all the positive support and guidance. I can assuredly say that without her insight and mentoring I would have not been as successful as I am today.

I would also like to pay my special regards to all the members of the custodial staff, especially Andrew Dillard, Raymond Jackson, Vicky Briggs, Sandy Morris, Sona Chitadze, and Sonam Dolkar who not only kept our spaces clean but also provided encouraging words in the early hours of the morning. Andrew was the first person to provide encouraging words at the beginning of every morning. Also, many thanks to Michael Birckhead and Danny Via, along with all the

Stockroom staff for always acquiring the orders I desperately needed for my experiments.

In addition, I would like to thank all my family and friends for their support, especially my two sisters. Without their support, I am certain I would not have achieved my goals and dreams. I would also like to thank my parents who always encourage curiosity and engagement in higher learning. And finally, I would like to recognize the invaluable assistance of my fellow military members, Dave Hooten and Chris Sacra. I am certain that without their support I would not be here earning my degree. There are many, many more individual I would like to give thanks to for their support and encouragement, which made this dissertation possible today.

(Blank page)

Table of Contents

Chapter 1. Introduction

In this dissertation, we will focus on application of lipidomics and chemoproteomics to understand diacylglycerol kinase (DGK)-regulated metabolism. There is still a lot that we do not know about DGK metabolomic functions and my work seeks to bridge gaps in knowledge by investigating isoform-specific functions of DGKs. In addition, we will apply novel technologies to investigate deeper into DGKs function. Chapter 1 will provide an overview of the current understanding, from our group and wider scientific community, of DGKs and the growing complexity of their lipid substrates and the opportunities for discovery. Additionally, Chapter 1 will provide a general overview of my thesis work. In Chapter 2, we will focus on substrate specificity for DGKθ and its putative role in the Lands cycle. We selected DGKθ for initial investigations with goal of applying our findings to the rest of the DGK superfamily (10 mammalian enzymes in total). Chapters 3 and 5 will discuss novel technologies for perturbing protein function, such as CRISPR/Cas9, PROTAC, and autoSTOMP, that were used in my thesis work including perturbing cellular activity to better understand DGK metabolic functions. In addition, we will use and apply mass spectrometry techniques to understand DGK function in Chapters 2 and 4. In chapter 4, our focus will be performing chemoproteomics studies to identify sites on all ten DGK enzymes that are important for function and covalent small molecule binding. Chapter 5 will focus on automated spatially targeted optical microproteomics through a collaboration with Ewald Lab here at UVA to determine protein complexity of subcellular structure as a tool for future investigation of DGKs.

1.1 *Diacylglycerol Structure and Function*

1.1.1 *Lipid Complexity and Challenges for Biochemical Analyses*

Our understanding of lipid biology has been expanding at a phenomenal rate over the last few decades, touching every aspect of research science. Lipids have a critical function in cells and are widely distributed in the plasma membrane and subcellular organelles.[1] Their structure and function vary widely within and between plants and animals. These differences affect their production, transportation, and recognition by receptors.[2-5] In addition to being an energy source and providing structural composition to biological membranes, lipids serve as signaling molecules and function as secondary messengers.[6] Furthermore, the global analysis of lipid molecules, "lipidomics," in the context of genomics and proteomics studies has expanded our understanding of cellular pathophysiology.[2, 5] Lipids can be divided into eight categories (fatty acyls, glycerolipids, glycerophospholipids, sphingolipids, sterol lipids, prenol lipids, saccharolipids, and polyketides) as shown in **(Figure 1.1.1)**.[2, 4, 7]

We will focus our attention on diacylglycerols kinases,[2, 8] and how they recognize lipid substrates based on structure of constituent fatty acids, which represents their most basic building block. And, we will focus on the metabolic pathways of glycerolipids and glycerophospholipids by these kinases, which is a fundamental process in complex biological systems.[9] Production of diacylglycerols (DAGs) upon cellular activation is a critical regulatory event for signal transduction that occurs in the plasma membrane (PM) and downstream of key receptors.[10, 11]

1.1.2 *The Diacylglycerol Kinase (DGK) Superfamily*

Currently, ten mammalian DGK isozymes (DGKα, β, γ, δ, ε, ζ, η, θ, ι and κ) have been identified, as shown in **(Figure 1.1.2)**.[12, 13] In addition, the ten DGK isozymes are organized into five subtypes (I-V) that vary with respect to domain organization and cellular distribution.[14, 15] The ten isozymes share conserved lipid kinase domains (split into the DAGKc and DAGKa regions) and a minimum of two C1 domains (cysteine-rich domains).[16-18] DGKβ, γ, δ, η, ζ, and ι have one to three alternative splice variants, which can alter the protein-coding sequence.[19] DGK isozymes are involved in many pathophysiological events; for example, cancer, cardiac hypertrophy, and hypertension.[20, 21] DGKs are differentiated principally by regulatory domains that are implicated in regulation of DGK activation (EF hand motifs), membrane localization (PH domain), and protein-protein interactions (PDZ domain)[22]

Diacylglycerol kinases (DGKs) have been implicated in the catalytic phosphorylation of DAG to produce phosphatidic acid (PA) and thus serve as a critical regulatory point in cell signaling.[23-25] DGKs are a group of enzymes that catalyze ATP-dependent phosphorylation of diacylglycerol (consumed) to produce phosphatidic acid (generated).[13, 22] DGKs modulate the levels of these two important signaling lipids, which are well-known secondary messengers.[26] Depending on the needs of the cell, DGK can regulate DAG and PA either in the forward direction (produce more PA) or in the reverse direction (produce more DAG).[27] Whether DGKs can metabolize alternative substrates other than DAG and PA is currently unknown.[28-30]

There are several target proteins that respond to cellular changes in DAG and PA. For example, DAG consumption has been reported with DGKα, β and γ when inhibiting RasGRP1, PKCβI, and PKCγ, respectively.[31-33] DGKδ interacts with PKCα, PKCδ, PKCε, and PKCη.[34] In addition, *sn*-1,2 DAG serves as an intracellular signaling molecule that is used to activate protein kinase C (PKC),.[35-38] DGKζ reduces the activities of PKCα and RasGRP1, when DAG is consumed.[39, 40] Finally, when DAG levels are increased, DGK isozymes regulates subcellular localization of PKCε.[41] Examples of PA production include DGKζ was that demonstrated to enhance the activities of mTOR and PIP5Kiα;[42, 43] DGKα and DGKγ activated PKCζ and β2-chimaerin, respectively.[44, 45] Finally, DGKδ activates Praja-1 when PA levels of production are increased.

The molecular structures of DAG and PA each contain two acyl chains of various compositions either at the s*n*-1,2 positions, *sn*-1,3 position, or *sn*-2,3 positions.[46] The chains range from 14 to 22 carbon atoms and contain zero to six double bonds, at the *sn*-1 and *sn*-2 positions.[47] In mammalian cells, a minimum of 50 structurally distinct DAG and PA species have been recorded.[14, 47, 48] *In vitro* studies have provided clues and preliminary evidence that DGKs can exhibit fatty acyl specificity in substrates (e.g. DGKε's preference for arachidonoyl-DAGs, which exclusively produce 1-stearoyl-2-arachidonoyl-DG (C18:0/C20:4-DG)).[49] As DAG and PA play critical roles in cell function, it is not surprising that there is an interest in understanding the mechanisms underlying the catalysis and regulation of DAG and PA modulating lipids.[15] Recent efforts using LC-MS support

mechanisms for substrate selectivity other than the 1-stearoyl-2-arachidonoyl-DG (C18:0/C20:4-DG)).[17, 50]

- DGKα:

Palmitic acid (C16:0)- and/or palmitoleic acid (C16:1)-containing phosphatidic acids such as C14:1/C16:1-, C14:0/C16:1-, C14:0/C16:0-, C16:1/C16:2-, C16:1/C16:1-, C16:0/C16:1-, C16:0/C16:0-, C16:0/C18:1- and C16:0/C18:0-PA are generated by DGKα in starved Jurkat T cells.[13, 51]

- DGKξ:

Recently, C16:0/C16:0-PA and, to a lesser extent, C14:0/C16:0-PA and C16:0/C18:0-PA, were found to be exclusively generated during differentiation of Neuro 2A neuronal cells in a DGKζ-dependent manner.[13, 52]

- DGKδ:

It was recently found that, in response to high glucose-stimulation, C16:0- and/or C16:1-containing PA species such as C14:0/C16:1-PA, C14:0/C16:0-PA, C16:0/C16:1-PA, C16:0/C16:0-PA, C16:0/C18:1-PA, and C16:0/C18:0-PA were generated by DGKδ in C2C12 myoblast cells.[13, 53] It is noteworthy that only the level of 1-stearoyl-2-docosahexaenoyl (C18:0/C22:6)-PA was decreased in the DGKδ-KO mouse brain, suggesting that DGKδ generates C18:0/C22:6-PA in the brain.[54] Intriguingly, C18:0/C22:6-PA selectively bound to Praja-1 and enhanced its activity.[54] These results indicate that DGKδ generates distinct PA species in different tissue/cells and/or in response to different stimuli.[13]

- DGKη:

The levels of polyunsaturated fatty acid (PUFA)-containing PA species such as C18:1/C18:2-, C18:0/C20:3-, C18:0/C22:5-, C18:0/C22:4-, and C18:0/C22:3-PA

are decreased in the DGKη-KO brain, suggesting that DGKη generates these PUFA-containing PA species in the brain.[13, 55]

- DGKκ:

In DGKκ-deficient cortical neurons, L-quisqualic acid (a group 1 metabotropic glutamate receptor agonist)-dependent increases in C36:1 (C18:0/C18:1)-, C38:1 (C18:0/C20:1)-, and C38:2 (C18:1/C20:1)-PA levels were attenuated.[13]

- DGKθ:

Overexpression of DGKθ mainly increases the amount of C18:1/C18:1-PA in mouse primary hepatocytes.[13]

1.2 *Lipid Metabolic Pathways of Importance for DGK Function*

1.2.1 *Membrane Contact Sites, Acyl Editing, and Acyl Fluxes*

Phospholipids can be synthesized by distinct enzymatic pathways.[56] We focus our attention on three pathways with the most impact on our results; the Lands cycle, *de novo* pathway (Kennedy pathway), and Phosphatidylinositol (PI) Cycle.[57, 58] In addition, these three pathways incorporate membrane contact sites (MCS) and lipid transfer proteins (LTP), which shuttle lipids form one organelle to another.[59] Finally, acyl editing of phosphatidylcholine, which provides a novel route of re-synthesizing of PC via lysophosphatidylcholine (LPC) after its deacylation, and diacylglycerols (DAG) control major acyl fluxes through PC to provide polyunsaturated fatty acids (PUFA) for triacylglycerol (TAG) synthesis.[60-62]

These pathways maintain the diverse composition of proteins and lipids, contained in cell membranes.[63-65] Eukaryotic cells generate thousands of different lipids with profound effects on metabolic activities throughout cells.[9, 65, 66] For example, lipids synthesized in the endoplasmic reticulum (ER) travel throughout the cytosol, targeting other organelles in the cell at specific contact sites.[10, 67-70] The exchange of signals and metabolites in these regions of close proximity between two distinct organelles has been defined as “membrane contact site” (MCS).[69, 71, 72] These MCS perform diverse functional roles resulting in unique proteome and local lipid composition.[72] Lipid species at MCSs are transported on specialized lipid transfer proteins (LTPs) that produce or modify lipids, establishing lipid gradients that ultimately contribute to the lipid transport process.[73, 74] The

complex interactions between MCS and LTPs are also likely to add selectivity to the lipid transfer process.[63, 74, 75]

1.2.2 *Remodeling Pathway (Lands Cycle)*

The Lands cycle (i.e. remodeling pathway), a fundamental biochemical process that takes place between the cytosol and plasma membrane.[57] It is a major pathway of phosphatidylcholine (PC) acyl remodeling or acyl exchange, accomplished by both lipid acyltransferases and phospholipases during recycling of glycerophospholipids (GPL) or phospholipids (PL).[76, 77] Lands showed that radioisotope labelling using ^{14}C-acetate and ^{14}C-glycerol did not produce equal ratios of each other.[78] The ratio of labeled fatty acyl (FA) versus glycerol in PC was much higher than that of triacylglycerols (TAGs). Lands surmised that an exchange of the *sn*-2 acyl moiety of phospholipids through the deacylation step of PC to produce lysophosphatidylcholine (LPC) followed by reacylation step of LPC to regenerate PC was occuring.[79]

This remodeling pathway has been shown to be mediated by lysophospholipid acyltransferases (LPLAT), which transfer a fatty acyl chain onto lysophospholipids to produce phospholipids, which is a reacylation step.[9, 80, 81] In the reverse reaction, the phospholipid is converted back to a lysophospholipid and a free fatty acid chain via phospholipase A_2 action (PLA_2), which is a de-acylation step.[81, 82] Thus, the coordinated action of LPLAT and PLA_2 can efficiently remodel the fatty acyl composition of phospholipids and thus the cell membrane.[57, 77]

The Lands cycle involves remodeling of phospholipids, which does not lead to net gains of glycerolipids molecules.[83] These phospholipids can be synthesized by the Kennedy pathway, which can generate saturated and monounsaturated fatty acyl groups on the *sn*-1, *sn*-2, *sn*-3 positions of the phospholipid.[57] The acyl exchange can generate new PC molecules with a different fatty acyl chain length at the *sn*-2 position. The de novo glycerolipids pathway includes the incorporation of glycerol backbone.[83, 84] Finally, the acyl editing pathway can operates through the coenzyme A and PC exchange along with lysophosphatidylcholine acyltransferase (LPCAT), which has been shown in plants to have significant reversibility in LPCAT[77] and suggests that the forward and reverse exchange of LPCAT can achieve acyl exchange.[61, 77, 85] Thus, DAG controls major acyl fluxes through PCs to provide PUFAs in exchange for TAG synthesis .[60, 61, 85, 86] These PUFAs are synthesized on the PC located on the lipid membrane; however, how fatty acids enter or leave the PC, especially after being modified to participate in the TAG assembly is not well understood and requires further investigation.[60]

1.2.3 *De Novo TAG Biosynthesis (Kennedy Pathway)*

De novo TAG biosynthesis, also known as the Kennedy pathway, was first reported in 1961, using rat liver as an enzyme source.[87, 88] . There are numerous studies that describe *de novo* TAG biosynthesis, and all can be grouped into three steps: 1) FA synthesis in plastids, 2) acyl-CoA pool formation in the cytosol, and 3) TAG formation in the ER then forming as lipid droplets (LDs) in the cytosol.[60] The Kennedy pathway begins with the acylation of a stereospecific (*sn*)-glycerol-

3-phosphate (G3P) catalyzed by acyl-CoA:*sn*-glycerol-3-phosphate acyltransferase (GPAT) and acyl-CoA lysophosphatidic acid acyltransferase (LPAAT), forming phosphatidic acid (PA).[88] Dephosphorylation of PA through phosphatidic acid phosphatase (PAP) forms diacylglycerol (DAG).[77, 88]

The synthesis of PC is accomplished by the transfer of phosphocholine from cytidine-5′-diphosphate (CDP)-choline to DAG. TAGs are also formed through the formation of DAG from PC; TAG biosynthesis through the acyl-CoA–dependent acylation of the *sn*-3 position by diacylglycerol acyltransferase. In addition, TAG can be formed independent of acyl-CoA donors by phospholipid:diacylglycerol acyltransferase (PDAT), which transfers an acyl group from the *sn*-2 position of PC to the *sn*-3 position of DAG to create TAGs.[89]

Substrate specificity of the acyltransferases of the Kennedy pathway is one of the determining factors of the composition of glycerolipid molecules.[77, 90-92] Glycerolipid biosynthesis has an asymmetric distribution of FA between the *sn-1* and *sn-2* positions: Saturated and monounsaturated FAs are normally found at the *sn*-1 position, whereas PUFAs are enriched at the *sn*-2 position.[92] GPAT and LPAAT are not only stereo-specific with regard to acylation of the glycerol backbone but also selective in terms of acyl-CoA donors.[77, 90, 92, 93]

1.2.4 *Phosphatidylinositol (PI) Cycle*

The phosphatidylinositol cycle (PI cycle) plays an important role in cell signaling on the plasma membrane and endoplasmic reticulum.[94] It is an important pathway for the synthesis of PIs.[68] PIs are glycerophospholipids with an inositol

headgroup **(Figure 1.2.1)**.[63, 95] They represent roughly 15% of membrane phospholipids, but make a remarkable contribution to practically all aspects of a cell's function.[94] When phosphorylated to form phosphoinositides (PIPs), these PIPs play a greater role in subcellular processes, such as membrane trafficking, cytoskeletal function, cell growth and proliferation.[68, 95] PIs are synthesized in a manner similar to other complex phospholipids; the activated DAG and cytidine diphosphate-diacylglycerol (CDP-DAG) coupled to an inositol molecule, catalyzed by the enzyme PI synthase as shown in **(Figure 1.2.2)**.[63, 96, 97] PIs are thought to be synthesized largely within membranes of the ER.[97, 98] Consequently, how newly synthesized PIs are transported out from the ER to maintain PPI availability within the PM is not well understood.

Fatty acyl moieties of membrane lipids exhibit diversity in their acyl chain lengths, degrees of unsaturation, and stereochemistry.[99, 100] Lipids involved in signaling pathways, such as those in the PI cycle, contain discreet acyl chain compositions that reflect subcellular locale and metabolic/signaling function. As a result, defining the chemical composition of lipid substrates is key to understanding how lipid biology is regulated.[57, 101-103] As mentioned above, it has been shown that DGKs display fatty acyl specificity as evidenced by DGKε's preference for DAG lipids containing stearic acid and arachidonic acid (18:0/20:4) in the *sn*-1 and *sn*-2 positions, respectively.[22, 103-105] In agreement with its fatty acyl specificity, DGKε has been linked to regulation of the PI cycle where arachidonoyl-DAGs are primarily metabolized.[9, 80, 106] Although changes in fatty acyl composition have advanced our understanding of how phospholipid remodeling contributes to

physiology, we still do not fully understand how these acyl chain compositions may participate in the membrane remodeling pathway. New technologies, such as CRISPR/Cas9 and targeted protein degradation (e.g., proteolysis targeting chimera or PROTAC), are providing unique approaches in deciphering lipid pathways.[100, 105, 107, 108]

1.3 *Modern Methods for Perturbing Protein Function*

1.3.1 *Genetic Disruption: CRISPR/Cas9*

A key step in drug development is to better understand the link between a specific gene and a physiopathological event.[109, 110] Gain (recombinant overexpression) or loss of function (knockout) are used to study the function of a protein, providing unique insight into the gene's function with some limitations. Currently, protein function can be probed by investigating and perturbing expression at multiple scales including DNA, mRNA, and protein. For example, gene editing using CRISPR-Cas9 (short for clustered regularly interspaced short palindromic repeats and CRISPR-associated protein 9) is a powerful technology for modifying genomic information.[111] RNA interference is an example of perturbing protein function at the RNA level. Finally, pharmacological inhibition of a target protein is an example of perturbing protein at the protein level. When these technologies perturb any of these three levels (DNA, mRNA, and protein), they do not provide insight into activity changes that are dynamic and rapidly changing in cells in response to stimuli, stress, and other perturbations.[112] Several targeted chemical biology approaches including protein degradation technologies have overcome many of this limitation. For example, auxin-inducible degron (AID),[113] HaloTAG via Halo-PROTAC,[114] hydrophobic tagging,[115] and small molecule-assisted shutoff (SMASh)[116] are targeted protein degradation technologies that use small molecule degraders.[111, 112]

Gene editing is a method that changes an organism's genomic information. These technologies allow genetic material to be added, removed, or altered at

chosen locations in the genome. Applications for CRISPR/Cas9 technologies are numerous and are versatile platforms for many biochemical applications.[115, 117, 118] By exploiting endogenous cellular DNA repair pathways, we can create specific edits at a desired location in the genome, such as a double-strand break (DSB). DSBs are deleterious to the cell, and cells have evolved mechanisms to repair them. Generation of a DSB can be used to probe the function of a gene and observe the resulting phenotype produced (i.e., knocking out, KO, of a gene). Thus, researchers can exploit CRISPR/Cas9 for genome editing purposes. By target selection, generating and delivery of CRISPR/Cas9 components, and finally identifying the desired mutation, one can in principle edit any gene of interest. In addition, one can also insert a vector of interest next to the DSB.

A recent application of CRISPR technology is use of the degradation tag (dTAG) system, which consists of a hybrid chemical biology system combining the benefits of small molecule perturbations with precision genetic editing (CRISPR-Cas9).[111, 119, 120] Based on initial studies, there is enormous potential for applying the dTAG system for investigating protein function in biological systems are affected. Other application technologies include PROTAC, HaloTAG, and dTAG are explained in further detail next.

1.3.2 *Targeted Protein Degradation: PROTAC*

In recent years, advancements in emerging technologies based on Proteolysis Targeting Chimeras (PROTACs) have shown great promise as a novel strategy for chemical knockdown of a protein of interest (POI).[121, 122] Their

advantages include the potential to reduce systemic drug exposure and target proteins that are not currently therapeutically tractable, e.g. transcription factors; removal of proteins which exert scaffolding functions independent of their catalytic/kinase activity.[121, 123, 124] Another advantage of PROTAC over genetic depletion of target proteins through RNA interference or CRISPR in terms of rapid onset and minimization of the opportunity for cellular adaptation to loss of the protein.[125]

The hallmark of PROTAC is that it uses the endogenous cells' ubiquitin-proteasome system (UPS) to degrade the selected POI.[126] The UPS plays a critical role in maintaining intracellular protein homeostasis by eliminating misfolded proteins, in a stepwise manner.[127] Ubiquitin is a small, 76-amino acid, present in all eukaryotic cells, which directs the movement of important proteins in the cell and participates defective protein degradation **(Figure 1.3.1)**.[128] It begins with ubiquitin activation by enzyme E1. This is followed by ubiquitin-conjugating enzyme (E2) resulting in trans-thioesterfication of ubiquitin.[129] Finally, E3 ubiquitin ligase promotes the transfer of ubiquitin onto the POI, resulting in a polyubiquitin tags, which serve as a signal for protein degradation via the 26S proteasome.[129, 130]

The special bifunctional small molecule used in PROTAC is a powerful chemical tool that binds the POI to the E3 ligase by forming a stable ternary complex promoting the polyubiquitination of POI and causing proteasome-mediated degradation of POI **(Figure 1.3.1)**. There are three components for PROTAC ligand: 1) an E3 ubiquitin ligase ligand (which will bind to the E3 ligase,

2) a POI ligand (which will bind to the POI), and 3) a linker (binding 1 and 2 together).[122] The E3 ubiquitin ligase ligand is responsible for specifically recruiting E3 ubiquitin ligase; the POI ligand is employed to target and hijack POI; and the linker moiety is used for conjugating these two ligands.

PROTAC has found promising applications for drug discovery with several candidates in clinical trials, for example ARV-110 and ARV-471.[131] These applications are used to investigate intractable drug targets.[126] PROTAC provides novel modalities when investigating kinase-independent functions.[132] Kinase inhibitors provide effective strategies for developing conventional small-molecule drugs. For example, phosphatidylinositol 3-kinases (PI3Ks) play an important role in cell proliferation and differentiation.[133] PI3Ks have been used for PI3K degradation using pomalidomide and piperazine linker derivatives.[127]

1.3.2a *dTAG*

The degradation tag (dTAG) system is a versatile protein degradation technology, which combines genome engineering editing to real time experimental changes.[111, 134, 135] dTAG provides a strategy to chemically control protein levels by manipulating the cell's degradation machinery.[136, 137] dTAG ligands can target proteins, which is expressed as a chimera with mutant $FKBP12^{F36V}$ (either by CRISPR/Cas9-mediated locus-specific knock-in or lentiviral transgene expression).[111, 138] The dTAG ligand is composed of an E3 ligase ligand linked to a highly selective $FKBP12^{F36V}$ ligand, which form a ternary complex between the fusion protein and E3 ligase causing polyubiquitination and degradation of the

target protein. **(Figure 1.3.1)**.[138] dTAG can be inserted next to the locus of interest using microhomology-mediated end-joining (MMEJ) methodologies and CRISPR/Cas9 technology, with the PITCh (Precise Integration into Target Chromosome) system.[111, 134, 139]

Genome engineering technologies provide novel advances in functional genomic studies, such as knock-outs and gene knock-ins, along with various genomic rearrangements such as chromosomal deletions, inversions, and translocations.[120, 139, 140]

Gene editing technologies have been possible with advancements in Cas9 nuclease generating DNA double-strand break (DSB) by using guide RNA (gRNA).[120, 141] The DSB is repaired by either nonhomologous end joining (NHEJ) or homologous recombination (HR) mediated repair.[120, 142] Both NHEJ and HR have advantages such as exchange of generic material between and within species, but there are limitations.[143-145] In contrast, a third mediated repair approach, microhomology-mediated end joining (MMEJ), provides a high-fidelity alternative to both NHEJ and HR.[139, 146] For example, their efficiencies differ between cell type and organisms, with MMEJ-based mechanism being effective in tagging endogenous proteins in human cells.[147-149] MMEJ mediated repair requires a shorter number (about 20) base pairs (bp) of microhomology flanking the upstream and downstream of the DSB site. In addition, MMEJ repair occurs during the mitosis and synthesis phase of the cell cycle; while HR does not.[146, 150]

1.3.2b *HaloTag*

HaloTAG technology can perform comprehensive protein analysis using a single genetic construct **(Figure 1.3.1)**. HaloTAG can be used to isolated, purify, and degrade proteins of interest, which makes HaloTag more advantageous than the dTAG.[117] dTAG can only be used for degradation; while, HaloTAG can have multiple functions. In addition HaloTAG has been used in cellular imaging.[117, 151] HaloTAG technology consists of a genetically edited bacterial haloalkane dehalogenase enzyme (*Rhodococcus rhodochrous*) fused to a POI.[152] The HaloTAG ligand is a bifunctional ligand, which can have its functional moiety exchanged to meet the needs of the experiment, such as fluorescent or a reactive molecule. The warhead moiety on the HaloTAG ligand will bind irreversibly to the HaloTAG fused POI. For example when the functional moiety is a reactive degradation moiety and it binds to the HaloTAG fused POI, it will expose hydrophobic regions of the POI causing the HaloTag fusion protein to degrade in a proteasome-dependent manner.[117, 153] Thus, the HaloTag system will allow us to block the HaloTag fusion protein and act as an alternative for an inhibitor.

1.4 *Overview of LC-MS Methods for Functional Profiling of Lipid Pathways*

1.4.1 *LC-MS Lipidomics*

Recent advances in tandem liquid chromatography mass spectrometry (LC-MS/MS) techniques have enabled development of sensitive profiling of lipid on a global scale.[99, 154] Lipidomics is a global profiling methodology to detect, identify, and quantify lipids extracted from biological sources using tandem LC-MS/MS **(Figure 1.4.1)**. This technique provides the necessary resolution, sensitivity, selectivity, and throughput for technically demanding global analyses.[154, 155] However, the downside is the misidentification and inaccurate quantification of lipid molecules.[156] Overall, liquid chromatography combined with mass spectrometry (LC-MS) has become a mainstay in biomolecule analysis.[157]

Analysis of lipids using LC-MS/MS is a daunting task. There are many aspects that need to be considered before samples can be run on a mass spectrometer instrument.[156] Current lipid extraction methods are unable to extract all lipids species from a single lysate sample or for an all-encompassing single LC-MS experimental run. Due to structural diversity, lipids tend to have a wide range of physiochemical properties, making it all but certain that the extraction process will not capture all lipid species.[158] Thus, it is important to choose the appropriate extraction protocol appropriate to address a specific research question. Biphasic extraction methods are often used. These incorporate non-polar organic solvents for extracting lipids and polar solvents for solubilizing of polar contaminants.[159] The Folch method using a 2:1 (*v*/*v*) solvent mixture of chloroform/methanol, followed

by purification of the extracts with a salt solution (0.003 N $CaCl_2$ or $MgCl_2$, or 0.05 N NaCl or KCl) provides an efficient extraction for specific lipidomic analysis.

1.4.2 *Activity Based Protein Profiling (ABPP)*

Although tremendous strides have been made, the identification of druggable targets remains a challenge.[160] One major challenge is the lack of knowledge about the underlying cellular target that are responsible for the phenotypic effects.[161] Chemical proteomic (chemoproteomic) methods address many of these issues in identifying targets for drug development.[162] Activity-based protein profiling (ABPP) has emerged as one of a growing number chemical proteomic approaches that uses small-molecule probes to exploit the interaction mechanisms between compounds and targets within complex biological systems.[162-164] ABPP helps us assess activity of molecular targets and whether small molecules can engage particular binding sites on proteins **(Figure 1.4.1)**.[163, 165] The workflow of ABPP consists of 1) designing and synthesizing small-molecule compounds, 2) validating the target proteins (antibody by Western, recombinant proteins, isothermal titration calorimetry, fluorescence polarization immunoassay), 3) verifying the modes of action of small molecules (generic methods and imaging technologies).[166]

ATP acyl phosphate activity-based probes can assess functional binding to ATP pockets in native lysates[50]. ATP acyl phosphates are used for global, activity-based profiling of ATP-binding pockets of kinases and ATPases. This activity-based probe is directed to kinase active sites by ATP recognition followed by

covalent binding of lysines proximal to the acyl phosphate electrophile[167, 168] The chemical proteomic studies to date have been performed largely in cell lysates[50]. While informative, the binding profiles obtained in vitro may not reflect protein states that are subject to dynamic regulation in cellular environments.

To address the inability of ATP acyl phosphates to probe kinases in cells, orthogonal chemical proteomics have been developed. For example, recent work from the Taunton group used sulfonyl-fluoride probes containing a kinase active-site binding element for profiling inhibitor binding to kinases in live cells.[169] The Hsu lab developed sulfonyl-triazoles that covalently modify tyrosines and lysines on kinases and other proteins through sulfur-triazole exchange (SuTEx) chemistry.[170] SuTEx probes, such as TH211, are capable of functional profiling of kinases (e.g., DGKα) in live T cells[171]. The TH211 probe contains a sulfonyl-triazole electrophile (SuTEx[170]) that reacts with tyrosine and lysines when directed to DGK active sites with the kinase binding element RF001 derived from the DGK inhibitor ritanserin[172-176].

1.5 *Conclusion*

In this dissertation, we aim to better understand DGK function and specificity through novel cellular technologies that can perturb DGKs metabolic function. Our intent is to address many of problems associated with the difficulty in understanding DGKs and to apply novel technologies to explore deeper into DGKs function in the hope that we can unravel the many mysteries shrouding DGK's metabolic pathways. It is our aim to see if established metabolic pathways can be elucidated by using mass spectrometry analysis. We aim to make a connection between Lands cycle to DGKθ as its metabolic pathways. In addition, we aim to use novel technologies as tools to better understand DGKs. As shown in Chapter 1, it provides an overview of what I will cover in Chapters 2 through 5. More detail will be provided in the following Chapters.

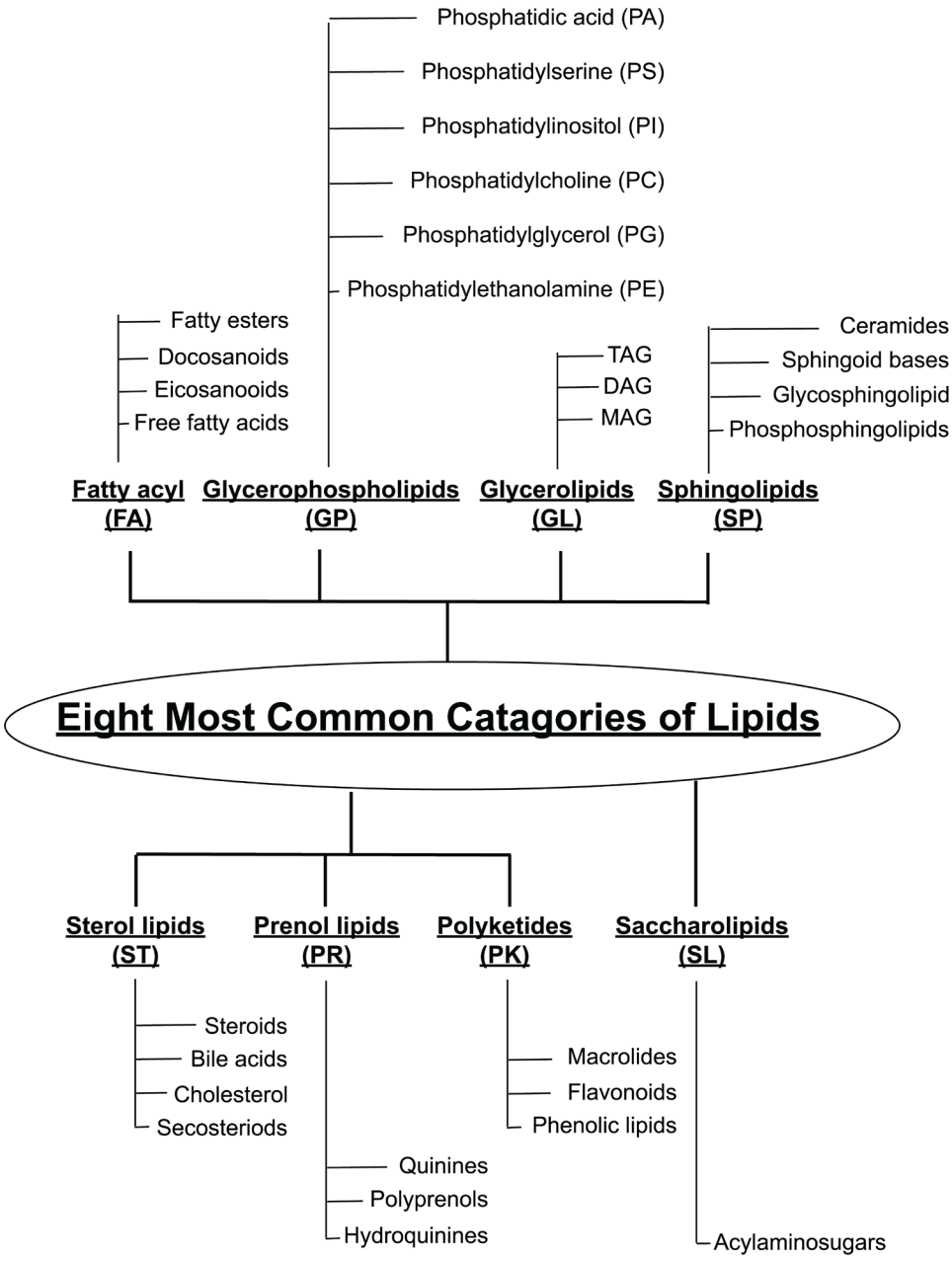

Figure 1.1.1 shows most commonly known lipids.[7] For a more complete set on lipid molecules and their structures visit: Lipid Maps (http://www.lipidmaps.org), Lipid Library (http://lipidlibrary.co.uk), Lipid Bank (http://lipidbank.jp), LIPIDAT http://www.lipidat.chemistry.ohiostate.edu), and Cyberlipids (http://www.cyberlipid.org).[2]

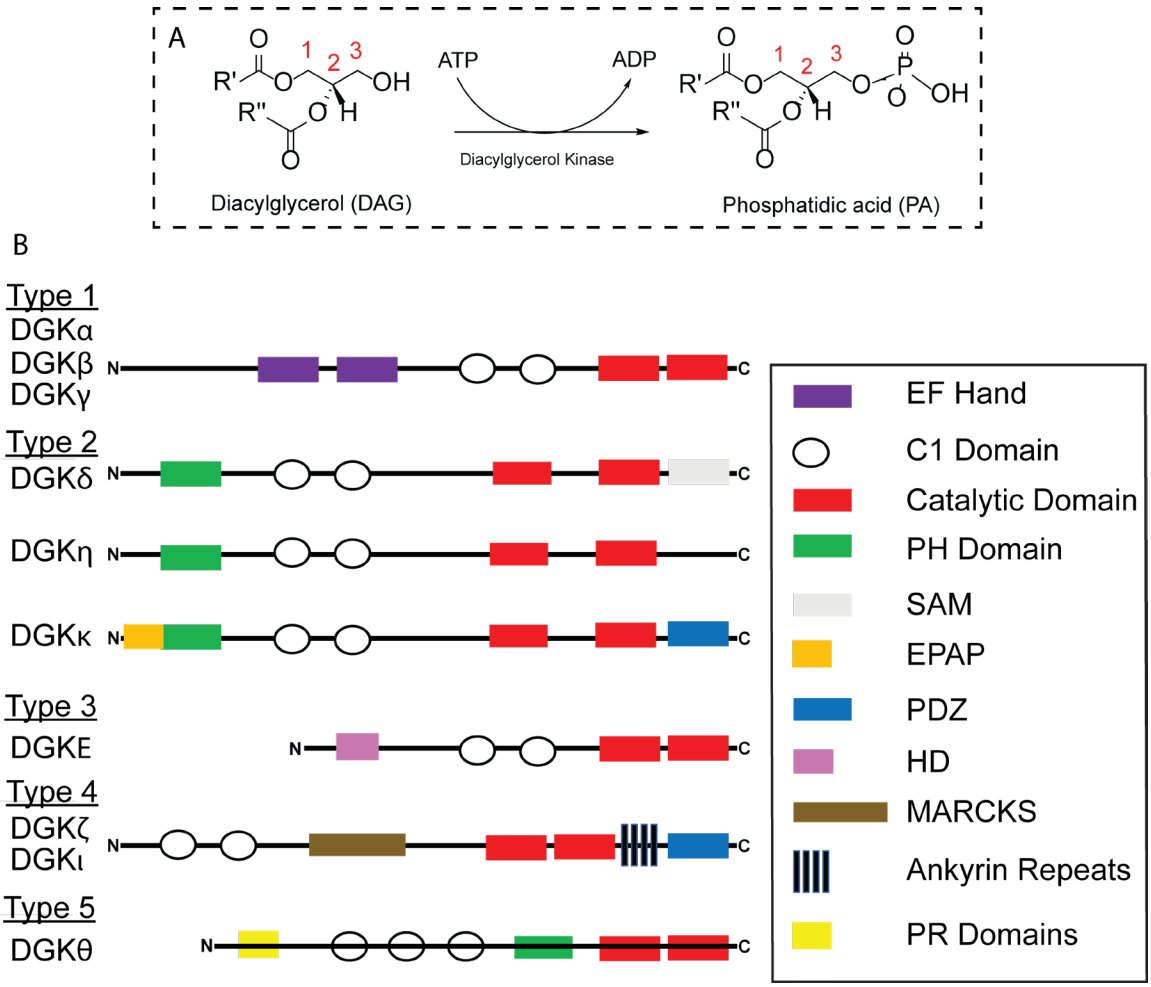

Figure 1.1.2 Ten mammalian DGK isozymes. (A) DGKs catalyze ATP-dependent phosphorylation of diacylglycerols to biosynthesize phosphatidic acid. DGK-regulated lipid substrates and products regulate downstream protein receptors through changes in localization, activation, and protein-protein interactions. (B) DGKs are multidomain lipid kinases that differ principally in composition of regulatory domains outside of the conserved catalytic domain. Alternative splice variants of each isozyme are not shown.

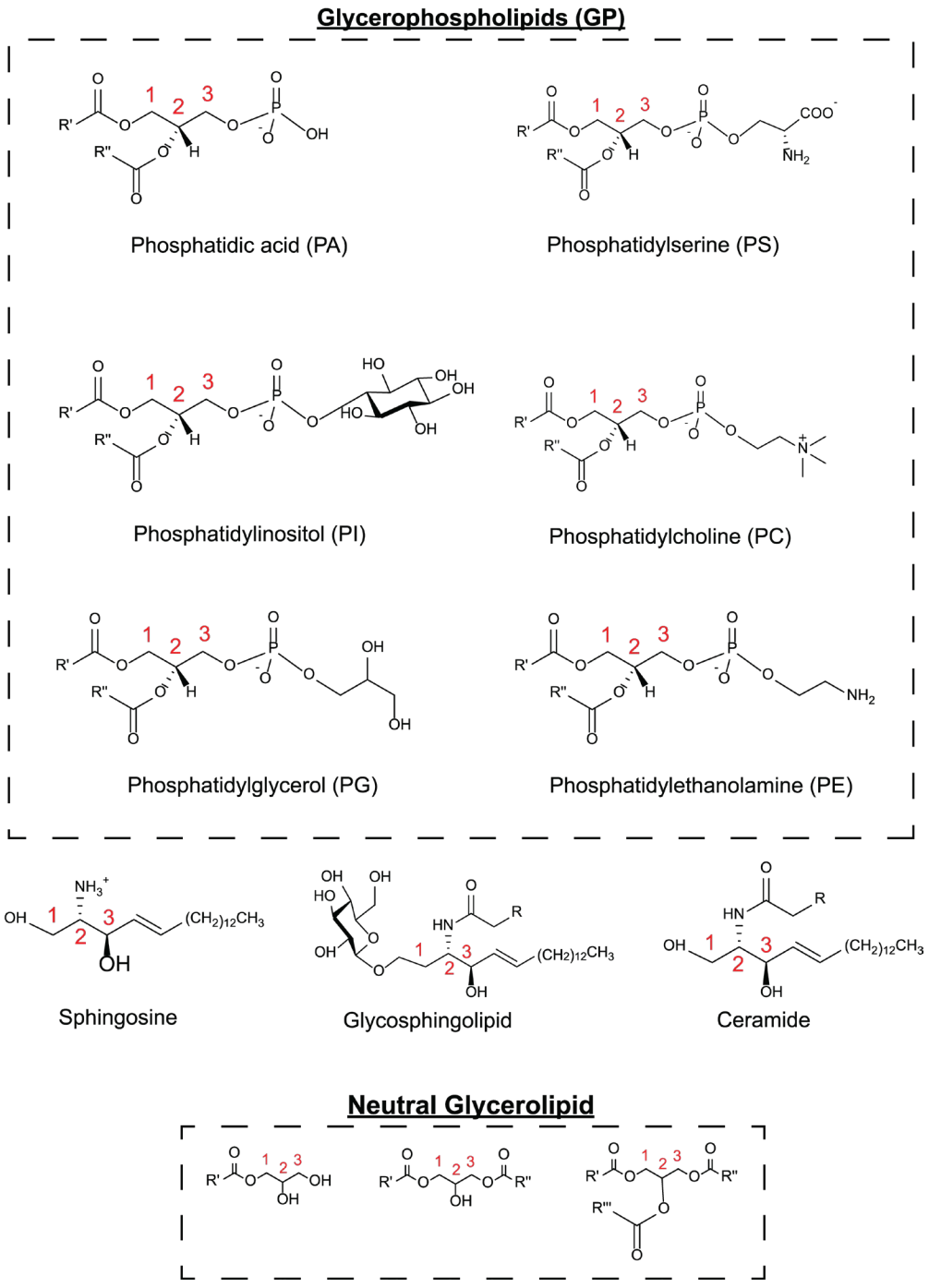

Figure 1.2.1 The molecular structure. Lipid categories according to Lipid MAPS classification with representative structures for individual categories. [7] For a more complete set on lipid molecules and their structures visit: Lipid Maps (http://www.lipidmaps.org), Lipid Library (http://lipidlibrary.co.uk), Lipid Bank

(http://lipidbank.jp), LIPIDAT http://www.lipidat.chemistry.ohiostate.edu), and Cyberlipids (http://www.cyberlipid.org).[2]

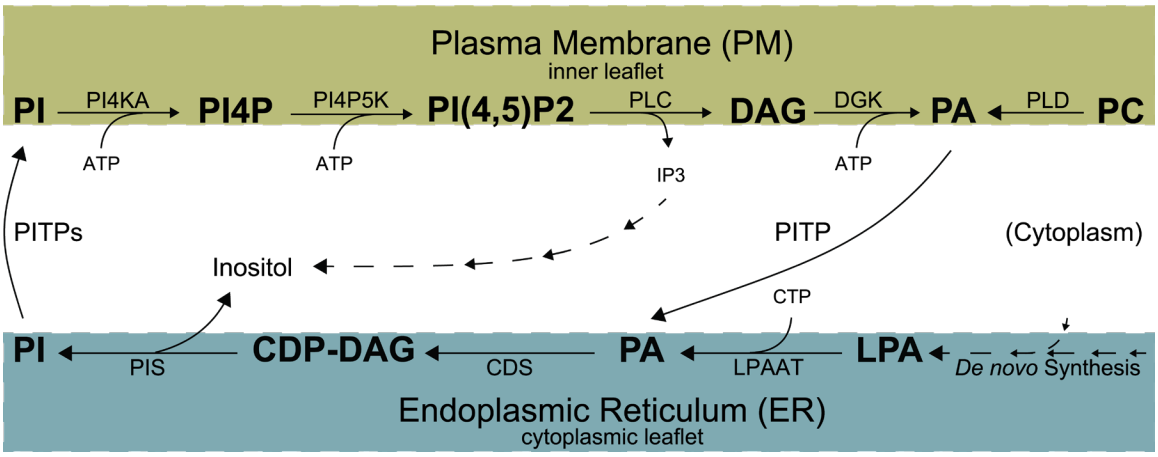

Figure 1.2.2 The phosphatidylinositol cycle.[63, 96] Phosphatidylinositol (PI) is synthesized from phosphatidic acid (PA) within the endoplasmic reticulum (ER) through the sequential activity of the integral membrane proteins CDP-DAG synthase (CDS), which produces cytidine diphosphate (CDP)-activated diacylglycerol (DAG) as an intermediate, and PI synthase (PIS or CDIPT).[63] plasma membrane (PM), PI-4-phosphate (PI4P), PI-4,5-bisphosphate PI(4,5)P_2, phospholipase C (PLC), diacylglycerol (DAG), phospholipase D (PLD), phosphatidylcholine (PC), and PI transfer proteins (PITPs).

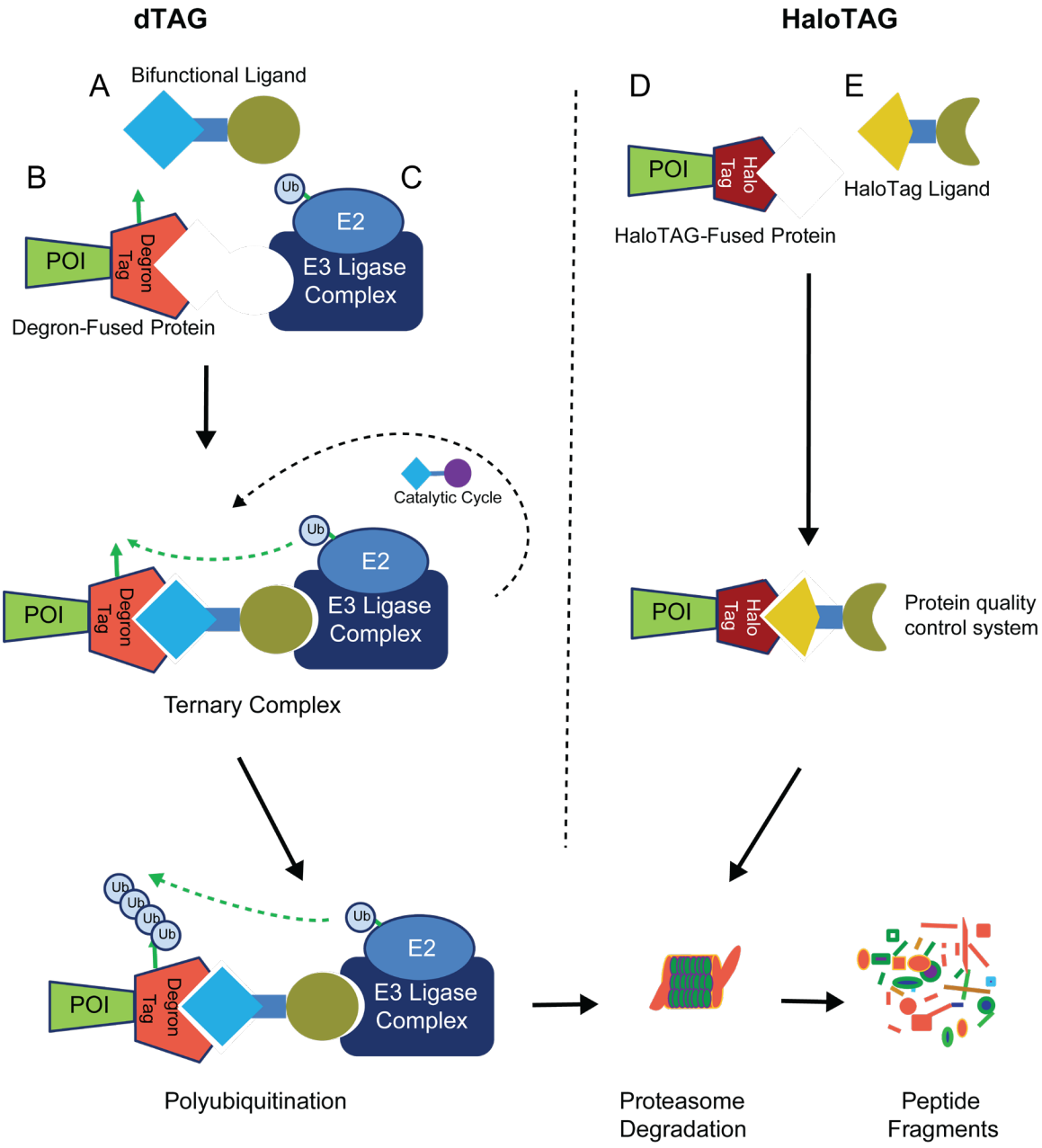

Figure 1.3.1 Ligand targets fused-protein for degradation. (A) bifunctional Ligand, dTAG-13; (B) Degron-fused protein of interest; and (C) E3 ligase complex with E2 and ubiquitin. When (A) binds (B) and (C), ternary complex is formed. HaloTag consists of two molecules, (D) HaloTag -fused protein and (E) HaloTAG ligand. Using PROTAC mode of action (MOA) as an example – protein function is

modulated by induced degradation. The PROTACs initiates a degradation cascade with POI ubiquitination followed by subsequent 26S proteasomal degradation of the POI.[177]

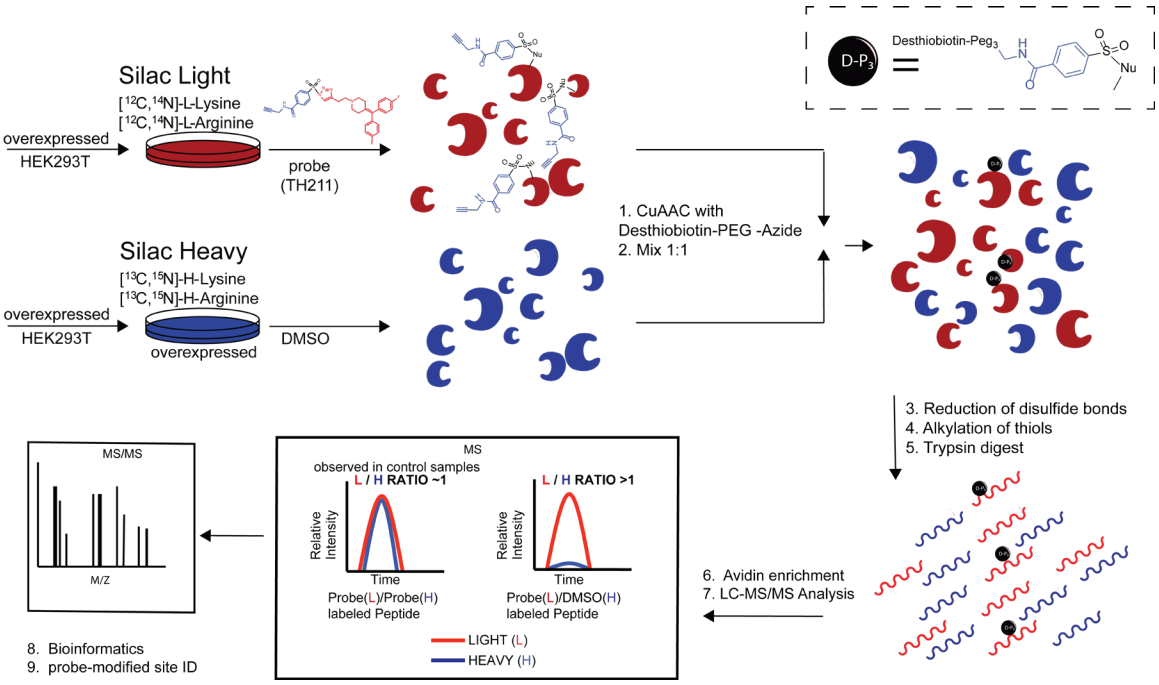

Figure 1.4.1 Activity Based Protein Profiling (ABPP). Proteins modified with SuTEx probes such as TH211 contain an alkyne reporter tag that facilitates copper-catalyzed azide-alkyne cycloaddition (CuAAC) conjugation of a desthiobiotin-azide enrichment handle. Desthiobiotinylated proteins are digested with trypsin protease to produce probe-modified peptides that are enriched by avidin chromatography followed by LC-MS/MS analysis. Bioinformatics can identify probe-modified peptide sequences and site of probe modification that can be used to infer covalent binding of SuTEx probes to intact proteins from lysate and live cell studies.

1.6 *References*

(1) Nakano, T.; Goto, K. Diacylglycerol Kinase epsilon in Adipose Tissues: A Crosstalk Between Signal Transduction and Energy Metabolism. *Front Physiol* **2022**, *13*, 815085. DOI: 10.3389/fphys.2022.815085 From NLM PubMed-not-MEDLINE.

(2) Fahy, E.; Subramaniam, S.; Brown, H. A.; Glass, C. K.; Merrill, A. H.; Murphy, R. C.; Raetz, C. R. H.; Russell, D. W.; Seyama, Y.; Shaw, W.; et al. A comprehensive classification system for lipids. *Journal of Lipid Research* **2005**, *46* (5), 839-861. DOI: 10.1194/jlr.E400004-JLR200.

(3) Fahy, E.; Subramaniam, S.; Brown, H. A.; Glass, C. K.; Merrill, A. H.; Murphy, R. C.; Raetz, C. R. H.; Russell, D. W.; Seyama, Y.; Shaw, W.; et al. A Comprehensive Classification System for Lipids. *Handbook of Biochemistry and Molecular Biology, 5th Edition* **2018**, 298-321. DOI: BOOK_DOI 10.1201/b21846.

(4) Fahy, E. A comprehensive classification system for lipids (vol 46, pg 839, 2005). *Journal of Lipid Research* **2010**, *51* (6), 1618-1618. DOI: 10.1194/jlr.E400004ERR.

(5) Fahy, E.; Subramaniam, S.; Murphy, R. C.; Nishijima, M.; Raetz, C. R. H.; Shimizu, T.; Spener, F.; van Meer, G.; Wakelam, M. J. O.; Dennis, E. A. Update of the LIPID MAPS comprehensive classification system for lipids. *Journal of Lipid Research* **2009**, *50*, S9-S14. DOI: 10.1194/jlr.R800095-JLR200.

(6) Matsushita, Y.; Nakagawa, H.; Koike, K. Lipid Metabolism in Oncology: Why It Matters, How to Research, and How to Treat. *Cancers* **2021**, *13* (3), 474. DOI: ARTN 474.10.3390/cancers13030474.

(7) Hsu, F. F. Mass spectrometry-based shotgun lipidomics - a critical review from the technical point of view. *Analytical and Bioanalytical Chemistry* **2018**, *410* (25), 6387-6409. DOI: 10.1007/s00216-018-1252-y.

(8) Castane, H.; Baiges-Gaya, G.; Hernandez-Aguilera, A.; Rodriguez-Tomas, E.; Fernandez-Arroyo, S.; Herrero, P.; Delpino-Rius, A.; Canela, N.; Menendez, J. A.; Camps, J.; et al. Coupling Machine Learning and Lipidomics as a Tool to Investigate Metabolic Dysfunction-Associated Fatty Liver Disease. A General Overview. *Biomolecules* **2021**, *11* (3), 473. DOI: ARTN 473.10.3390/biom11030473.

(9) Harayama, T.; Riezman, H. Understanding the diversity of membrane lipid composition. *Nat Rev Mol Cell Biol* **2018**, *19* (5), 281-296. DOI: 10.1038/nrm.2017.138.

(10) Jacquemyn, J.; Cascalho, A.; Goodchild, R. E. The ins and outs of endoplasmic reticulum-controlled lipid biosynthesis. *EMBO Rep* **2017**, *18* (11), 1905-1921. DOI: 10.15252/embr.201643426.

(11) Hilgemann, D. W.; Dai, G.; Collins, A.; Larricia, V.; Magi, S.; Deisl, C.; Fine, M. Lipid signaling to membrane proteins: From second messengers to membrane domains and adapter-free endocytosis. *J Gen Physiol* **2018**, *150* (2), 211-224. DOI: 10.1085/jgp.201711875.

(12) Goto, K.; Hozumi, Y.; Kondo, H. Diacylglycerol, phosphatidic acid, and the converting enzyme, diacylglycerol kinase, in the nucleus. *Bba-Mol Cell Biol L* **2006**, *1761* (5-6), 535-541. DOI: 10.1016/j.bbalip.2006.04.001.

(13) Sakane, F.; Hoshino, F.; Murakami, C. New Era of Diacylglycerol Kinase, Phosphatidic Acid and Phosphatidic Acid-Binding Protein. *International Journal of Molecular Sciences* **2020**, *21* (18), 6794. DOI: ARTN 6794.10.3390/ijms21186794.

(14) Ma, Q.; Gabelli, S. B.; Raben, D. M. Diacylglycerol kinases: Relationship to other lipid kinases. *Adv Biol Regul* **2019**, *71*, 104-110. DOI: 10.1016/j.jbior.2018.09.014 From NLM Medline.

(15) Ma, Q.; Srinivasan, L.; Gabelli, S. B.; Raben, D. M. Elusive structure of mammalian DGKs. *Adv Biol Regul* **2022**, *83*, 100847. DOI: 10.1016/j.jbior.2021.100847 From NLM Medline.

(16) Merida, I.; Avila-Flores, A.; Merino, E. Diacylglycerol kinases: at the hub of cell signalling. *Biochem J* **2008**, *409* (1), 1-18. DOI: 10.1042/BJ20071040.

(17) Ware, T. B.; Franks, C. E.; Granade, M. E.; Zhang, M.; Kim, K. B.; Park, K. S.; Gahlmann, A.; Harris, T. E.; Hsu, K. L. Reprogramming fatty acyl specificity of lipid kinases via C1 domain engineering. *Nat Chem Biol* **2020**, *16* (2), 170-178. DOI: 10.1038/s41589-019-0445-9 From NLM Medline.

(18) Colon-Gonzalez, F.; Kazanietz, M. G. C1 domains exposed: from diacylglycerol binding to protein-protein interactions. *Biochim Biophys Acta* **2006**, *1761* (8), 827-837. DOI: 10.1016/j.bbalip.2006.05.001.

(19) Sakane, F.; Imai, S.; Yamada, K.; Murakami, T.; Tsushima, S.; Kanoh, H. Alternative splicing of the human diacylglycerol kinase delta gene generates two isoforms differing in their expression patterns and in regulatory functions. *J Biol Chem* **2002**, *277* (45), 43519-43526. DOI: 10.1074/jbc.M206895200.

(20) Sato, M.; Liu, K.; Sasaki, S.; Kunii, N.; Sakai, H.; Mizuno, H.; Saga, H.; Sakane, F. Evaluations of the Selectivities of the Diacylglycerol Kinase Inhibitors R59022 and R59949 Among Diacylglycerol Kinase Isozymes Using a New Non-Radioactive Assay Method. *Pharmacology* **2013**, *92* (1-2), 99-107. DOI: 10.1159/000351849.

(21) Sakane, F.; Mizuno, S.; Komenoi, S. Diacylglycerol Kinases as Emerging Potential Drug Targets for a Variety of Diseases: An Update. *Front Cell Dev Biol* **2016**, *4*, 82. DOI: 10.3389/fcell.2016.00082.

(22) Shulga, Y. V.; Topham, M. K.; Epand, R. M. Regulation and Functions of Diacylglycerol Kinases. *Chemical Reviews* **2011**, *111* (10), 6186-6208. DOI: 10.1021/cr1004106 (acccessed 2012/08/27).

(23) Tu-Sekine, B.; Goldschmidt, H.; Raben, D. M. Diacylglycerol, phosphatidic acid, and their metabolic enzymes in synaptic vesicle recycling. *Adv Biol Regul* **2015**, *57*, 147-152. DOI: 10.1016/j.jbior.2014.09.010.

(24) Raben, D. M.; Barber, C. N. Phosphatidic acid and neurotransmission. *Adv Biol Regul* **2017**, *63*, 15-21. DOI: 10.1016/j.jbior.2016.09.004.

(25) Barber, C. N.; Huganir, R. L.; Raben, D. M. Phosphatidic acid-producing enzymes regulating the synaptic vesicle cycle: Role for PLD? *Adv Biol Regul* **2018**, *67*, 141-147. DOI: 10.1016/j.jbior.2017.09.009.

(26) Carrasco, S.; Merida, I. Diacylglycerol, when simplicity becomes complex. *Trends Biochem Sci* **2007**, *32* (1), 27-36. DOI: S0968-0004(06)00321-5 [pii].10.1016/j.tibs.2006.11.004.

(27) Hurley, J. H.; Newton, A. C.; Parker, P. J.; Blumberg, P. M.; Nishizuka, Y. Taxonomy and function of C1 protein kinase C homology domains. *Protein Sci* **1997**, *6* (2), 477-480. DOI: 10.1002/pro.5560060228 From NLM Medline.

(28) Tu-Sekine, B.; Ostroski, M.; Raben, D. M. Modulation of diacylglycerol kinase theta activity by alpha-thrombin and phospholipids. *Biochemistry* **2007**, *46* (3), 924-932. DOI: 10.1021/bi061170c.

(29) Cai, J.; Abramovici, H.; Gee, S. H.; Topham, M. K. Diacylglycerol kinases as sources of phosphatidic acid. *Biochim Biophys Acta* **2009**, *1791* (9), 942-948. DOI: 10.1016/j.bbalip.2009.02.010.

(30) Sakane, F.; Mizuno, S.; Takahashi, D.; Sakai, H. Where do substrates of diacylglycerol kinases come from? Diacylglycerol kinases utilize diacylglycerol species supplied from phosphatidylinositol turnover-independent pathways. *Adv Biol Regul* **2018**, *67*, 101-108. DOI: 10.1016/j.jbior.2017.09.003.

(31) Jones, D. R.; Sanjuan, M. A.; Stone, J. C.; Merida, I. Expression of a catalytically inactive form of diacylglycerol kinase induces sustained signaling through RasGRP. *Faseb Journal* **2002**, *16* (2), 595-+. DOI: 10.1096/fj.01-0762fje.

(32) Ueyama, T.; Lennartz, M. R.; Noda, Y.; Kobayashi, T.; Shirai, Y.; Kikitake, K.; Yamasaki, T.; Hayashi, S.; Sakai, N.; Seguchi, H.; et al. Superoxide production at phagosomal cup/phagosome through beta I protein kinase C during

Fc gamma R-mediated phagocytosis in microglia. *Journal of Immunology* **2004**, *173* (7), 4582-4589. DOI: DOI 10.4049/jimmunol.173.7.4582.

(33) Yamaguchi, Y.; Shirai, Y.; Matsubara, T.; Sanse, K.; Kuriyama, M.; Oshiro, N.; Yoshino, K. I.; Yonezawa, K.; Ono, Y.; Saito, N. Phosphorylation and up-regulation of diacylglycerol kinase gamma via its interaction with protein kinase C gamma. *Journal of Biological Chemistry* **2006**, *281* (42), 31627-31637. DOI: 10.1074/jbc.M606992200.

(34) Chibalin, A. V.; Leng, Y.; Vieira, E.; Krook, A.; Bjornholm, M.; Long, Y. C.; Kotova, O.; Zhong, Z.; Sakane, F.; Steiler, T.; et al. Downregulation of diacylglycerol kinase delta contributes to hyperglycemia-induced insulin resistance. *Cell* **2008**, *132* (3), 375-386. DOI: 10.1016/j.cell.2007.12.035.

(35) Kanoh, H.; Yamada, K.; Sakane, F. Diacylglycerol Kinase - a Key Modulator of Signal Transduction. *Trends in Biochemical Sciences* **1990**, *15* (2), 47-50. DOI: Doi 10.1016/0968-0004(90)90172-8.

(36) Nishizuka, Y. Intracellular Signaling by Hydrolysis of Phospholipids and Activation of Protein-Kinase-C. *Science* **1992**, *258* (5082), 607-614. DOI: DOI 10.1126/science.1411571.

(37) Sakane, F.; Imai, S.; Kai, M.; Yasuda, S.; Kanoh, H. Diacylglycerol kinases: why so many of them? *Biochim Biophys Acta* **2007**, *1771* (7), 793-806. DOI: 10.1016/j.bbalip.2007.04.006.

(38) Goto, K.; Tanaka, T.; Nakano, T.; Okada, M.; Hozumi, Y.; Topham, M. K.; Martelli, A. M. DGKζ under stress conditions: “to be nuclear or cytoplasmic, that is the question”. *Adv Biol Regul* **2014**, *54*, 242-253. DOI: 10.1016/j.jbior.2013.08.007 From NLM.

(39) Luo, B.; Prescott, S. M.; Topham, M. K. Association of diacylglycerol kinase zeta with protein kinase C alpha: spatial regulation of diacylglycerol signaling. *J Cell Biol* **2003**, *160* (6), 929-937. DOI: 10.1083/jcb.200208120.

(40) Luo, B.; Prescott, S. M.; Topham, M. K. Protein kinase C alpha phosphorylates and negatively regulates diacylglycerol kinase zeta. *J Biol Chem* **2003**, *278* (41), 39542-39547. DOI: 10.1074/jbc.M307153200.

(41) O'Seaghdha, C. M.; Wu, H.; Yang, Q.; Kapur, K.; Guessous, I.; Zuber, A. M.; Kottgen, A.; Stoudmann, C.; Teumer, A.; Kutalik, Z.; et al. Meta-analysis of genome-wide association studies identifies six new Loci for serum calcium concentrations. *PLoS Genet* **2013**, *9* (9), e1003796. DOI: 10.1371/journal.pgen.1003796.

(42) Avila-Flores, A.; Santos, T.; Rincon, E.; Merida, I. Modulation of the mammalian target of rapamycin pathway by diacylglycerol kinase-produced

phosphatidic acid. *Journal of Biological Chemistry* **2005**, *280* (11), 10091-10099. DOI: 10.1074/jbc.M412296200.

(43) Luo, B.; Prescott, S. M.; Topham, M. K. Diacylglycerol kinase zeta regulates phosphatidylinositol 4-phosphate 5-kinase Ialpha by a novel mechanism. *Cell Signal* **2004**, *16* (8), 891-897. DOI: 10.1016/j.cellsig.2004.01.010.

(44) Kai, M.; Yasuda, S.; Imai, S. I.; Toyota, M.; Kanoh, H.; Sakane, F. Diacylglycerol kinase alpha enhances protein kinase C zeta-dependent phosphorylation at Ser311 of p65/RelA subunit of nuclear factor-kappa B. *Febs Letters* **2009**, *583* (19), 3265-3268. DOI: 10.1016/j.febslet.2009.09.017.

(45) Yasuda, S.; Kai, M.; Imai, S.; Kanoh, H.; Sakane, F. Diacylglycerol kinase gamma interacts with and activates beta 2-chimaerin, a Rac-specific GAP, in response to epidermal growth factor. *Febs Letters* **2007**, *581* (3), 551-557. DOI: 10.1016/j.febslet.2007.01.022.

(46) Zechner, R.; Zimmermann, R.; Eichmann, T. O.; Kohlwein, S. D.; Haemmerle, G.; Lass, A.; Madeo, F. FAT SIGNALS - Lipases and Lipolysis in Lipid Metabolism and Signaling. *Cell Metab* **2012**, *15* (3), 279-291. DOI: 10.1016/j.cmet.2011.12.018.

(47) Tu-Sekine, B.; Goldschmidt, H. L.; Raben, D. M. DGK-theta: Structure, enzymology, and physiological roles. *Front Cell Dev Biol* **2016**, *4*, 101. DOI: 10.3389/fcell.2016.00101.

(48) Tu-Sekine, B.; Raben, D. M. Dual regulation of diacylglycerol kinase (DGK)-theta: polybasic proteins promote activation by phospholipids and increase substrate affinity. *J Biol Chem* **2012**, *287* (50), 41619-41627. DOI: 10.1074/jbc.M112.404855.

(49) D'Souza, K.; Epand, R. M. Enrichment of phosphatidylinositols with specific acyl chains. *Biochim Biophys Acta* **2014**, *1838* (6), 1501-1508. DOI: 10.1016/j.bbamem.2013.10.003.

(50) Ware, T. B.; Hsu, K. L. Advances in chemical proteomic evaluation of lipid kinases-DAG kinases as a case study. *Curr Opin Chem Biol* **2021**, *65*, 101-108. DOI: 10.1016/j.cbpa.2021.06.007.

(51) Murakami, Y.; Murakami, C.; Hoshino, F.; Lu, Q.; Akiyama, R.; Yamaki, A.; Takahashi, D.; Sakane, F. Palmitic acid- and/or palmitoleic acid-containing phosphatidic acids are generated by diacylglycerol kinase alpha in starved Jurkat T cells. *Biochem Bioph Res Co* **2020**, *525* (4), 1054-1060. DOI: 10.1016/j.bbrc.2020.02.162.

(52) Mizuno, S.; Kado, S.; Goto, K.; Takahashi, D.; Sakane, F. Diacylglycerol kinase zeta generates dipalmitoyl-phosphatidic acid species during

neuroblastoma cell differentiation. *Biochem Biophys Rep* **2016**, *8*, 352-359. DOI: 10.1016/j.bbrep.2016.10.004.

(53) Sakai, H.; Kado, S.; Taketomi, A.; Sakane, F. Diacylglycerol kinase delta phosphorylates phosphatidylcholine-specific phospholipase C-dependent, palmitic acid-containing diacylglycerol species in response to high glucose levels. *J Biol Chem* **2014**, *289* (38), 26607-26617. DOI: 10.1074/jbc.M114.590950.

(54) Lu, Q.; Murakami, C.; Murakami, Y.; Hoshino, F.; Asami, M.; Usuki, T.; Sakai, H.; Sakane, F. 1-Stearoyl-2-docosahexaenoyl-phosphatidic acid interacts with and activates Praja-1, the E3 ubiquitin ligase acting on the serotonin transporter in the brain. *Febs Letters* **2020**, *594* (11), 1787-1796. DOI: 10.1002/1873-3468.13765.

(55) Komenoi, S.; Suzuki, Y.; Asami, M.; Murakami, C.; Hoshino, F.; Chiba, S.; Takahashi, D.; Kado, S.; Sakane, F. Microarray analysis of gene expression in the diacylglycerol kinase eta knockout mouse brain. *Biochemistry and Biophysics Reports* **2019**, *19*, 100660. DOI: ARTN 100660.10.1016/j.bbrep.2019.100660 From NLM PubMed-not-MEDLINE.

(56) Henneberry, A. L.; Wright, M. M.; McMaster, C. R. The major sites of cellular phospholipid synthesis and molecular determinants of fatty acid and lipid head group specificity. *Molecular Biology of the Cell* **2002**, *13* (9), 3148-3161. DOI: 10.1091/mbc.01-11-0540.

(57) Murphy, R. C.; Folco, G. Lysophospholipid acyltransferases and leukotriene biosynthesis: intersection of the Lands cycle and the arachidonate PI cycle. *J Lipid Res* **2019**, *60* (2), 219-226. DOI: 10.1194/jlr.S091371.

(58) Moessinger, C.; Klizaite, K.; Steinhagen, A.; Philippou-Massier, J.; Shevchenko, A.; Hoch, M.; Ejsing, C. S.; Thiele, C. Two different pathways of phosphatidylcholine synthesis, the Kennedy Pathway and the Lands Cycle, differentially regulate cellular triacylglycerol storage. *BMC Cell Biol* **2014**, *15*, 43. DOI: 10.1186/s12860-014-0043-3.

(59) Reinisch, K. M.; Prinz, W. A. Mechanisms of nonvesicular lipid transport. *Journal of Cell Biology* **2021**, *220* (3), e202012058. DOI: ARTN e202012058.10.1083/jcb.202012058.

(60) Bates, P. D.; Fatihi, A.; Snapp, A. R.; Carlsson, A. S.; Browse, J.; Lu, C. F. Acyl Editing and Headgroup Exchange Are the Major Mechanisms That Direct Polyunsaturated Fatty Acid Flux into Triacylglycerols. *Plant Physiol* **2012**, *160* (3), 1530-1539. DOI: 10.1104/pp.112.204438.

(61) Stymne, S.; Stobart, A. K. The Biosynthesis of Triacylglycerols in Microsomal Preparations of Developing Cotyledons of Sunflower (Helianthus-Annuus L). *Biochemical Journal* **1984**, *220* (2), 481-488. DOI: DOI 10.1042/bj2200481.

(62) Yurchenko, O. P.; Nykiforuk, C. L.; Moloney, M. M.; Stahl, U.; Banas, A.; Stymne, S.; Weselake, R. J. A 10-kDa acyl-CoA-binding protein (ACBP) from Brassica napus enhances acyl exchange between acyl-CoA and phosphatidylcholine. *Plant Biotechnol J* **2009**, *7* (7), 602-610. DOI: 10.1111/j.1467-7652.2009.00427.x.

(63) Pemberton, J. G.; Kim, Y. J.; Balla, T. Integrated regulation of the phosphatidylinositol cycle and phosphoinositide-driven lipid transport at ER-PM contact sites. *Traffic* **2020**, *21* (2), 200-219. DOI: 10.1111/tra.12709.

(64) van Meer, G.; Voelker, D. R.; Feigenson, G. W. Membrane lipids: where they are and how they behave. *Nat Rev Mol Cell Bio* **2008**, *9* (2), 112-124. DOI: 10.1038/nrm2330.

(65) van Meer, G.; de Kroon, A. I. P. M. Lipid map of the mammalian cell. *Journal of Cell Science* **2011**, *124* (1), 5-8. DOI: 10.1242/jcs.071233.

(66) Yang, Y. B.; Lee, M.; Fairn, G. D. Phospholipid subcellular localization and dynamics. *Journal of Biological Chemistry* **2018**, *293* (17), 6230-6240. DOI: 10.1074/jbc.R117.000582.

(67) Jackson, C. L.; Walch, L.; Verbavatz, J. M. Lipids and Their Trafficking: An Integral Part of Cellular Organization. *Dev Cell* **2016**, *39* (2), 139-153. DOI: 10.1016/j.devcel.2016.09.030.

(68) Balla, T. Phosphoinositides: Tiny Lipids with Giant Impact on Cell Regulation. *Physiol Rev* **2013**, *93* (3), 1019-1137. DOI: 10.1152/physrev.00028.2012.

(69) Nixon-Abell, J.; Obara, C. J.; Weigel, A. V.; Li, D.; Legant, W. R.; Xu, C. S.; Pasolli, H. A.; Harvey, K.; Hess, H. F.; Betzig, E.; et al. Increased spatiotemporal resolution reveals highly dynamic dense tubular matrices in the peripheral ER. *Science* **2016**, *354* (6311), 433. DOI: ARTN aaf3928.10.1126/science.aaf3928.

(70) Guo, Y. T.; Li, D.; Zhang, S. W.; Yang, Y. R.; Liu, J. J.; Wang, X. Y.; Liu, C.; Milkie, D. E.; Moore, R. P.; Tulu, U. S.; et al. Visualizing Intracellular Organelle and Cytoskeletal Interactions at Nanoscale Resolution on Millisecond Timescales. *Cell* **2018**, *175* (5), 1430-+. DOI: 10.1016/j.cell.2018.09.057.

(71) Prinz, W. A.; Toulmay, A.; Balla, T. The functional universe of membrane contact sites. *Nat Rev Mol Cell Bio* **2020**, *21* (1), 7-24. DOI: 10.1038/s41580-019-0180-9.

(72) Scorrano, L.; De Matteis, M. A.; Emr, S.; Giordano, F.; Hajnoczky, G.; Kornmann, B.; Lackner, L. L.; Levine, T. P.; Pellegrini, L.; Reinisch, K.; et al. Coming together to define membrane contact sites. *Nature Communications* **2019**, *10*. DOI: ARTN 1287.10.1038/s41467-019-09253-3.

(73) Chiapparino, A.; Maeda, K.; Turei, D.; Saez-Rodriguez, J.; Gavin, A. C. The orchestra of lipid-transfer proteins at the crossroads between metabolism and signaling. *Progress in Lipid Research* **2016**, *61*, 30-39. DOI: 10.1016/j.plipres.2015.10.004.

(74) Wong, L. H.; Gatta, A. T.; Levine, T. P. Lipid transfer proteins: the lipid commute via shuttles, bridges and tubes. *Nat Rev Mol Cell Bio* **2019**, *20* (2), 85-101. DOI: 10.1038/s41580-018-0071-5.

(75) Wong, L. H.; Copic, A.; Levine, T. P. Advances on the Transfer of Lots by Lot Transfer Proteins. *Trends in Biochemical Sciences* **2017**, *42* (7), 516-530. DOI: 10.1016/j.tibs.2017.05.001.

(76) O'Donnell, V. B. New appreciation for an old pathway: the Lands Cycle moves into new arenas in health and disease. *Biochem Soc T* **2022**, *50* (1), 1-11. DOI: 10.1042/Bst20210579.

(77) Wang, L.; Shen, W.; Kazachkov, M.; Chen, G.; Chen, Q.; Carlsson, A. S.; Stymne, S.; Weselake, R. J.; Zou, J. Metabolic interactions between the Lands cycle and the Kennedy pathway of glycerolipid synthesis in Arabidopsis developing seeds. *Plant Cell* **2012**, *24* (11), 4652-4669. DOI: 10.1105/tpc.112.104604.

(78) Lands, W. E. M. Metabolism of Glycerolipides - Comparison of Lecithin and Triglyceride Synthesis. *Journal of Biological Chemistry* **1958**, *231* (2), 883-888.

(79) Lands, W. E. Metabolism of glycerolipids. 2. The enzymatic acylation of lysolecithin. *J Biol Chem* **1960**, *235*, 2233-2237.

(80) Wang, B.; Tontonoz, P. Phospholipid remodeling in physiology and disease. *Annu Rev Physiol* **2019**, *81*, 165-188. DOI: 10.1146/annurev-physiol-020518-114444.

(81) Kita, Y.; Shindou, H.; Shimizu, T. Cytosolic phospholipase A2 and lysophospholipid acyltransferases. *Biochim Biophys Acta Mol Cell Biol Lipids* **2019**, *1864* (6), 838-845. DOI: 10.1016/j.bbalip.2018.08.006 From NLM Medline.

(82) Shindou, H.; Hishikawa, D.; Harayama, T.; Yuki, K.; Shimizu, T. Recent progress on acyl CoA: lysophospholipid acyltransferase research. *J Lipid Res* **2009**, *50 Suppl*, S46-51. DOI: 10.1194/jlr.R800035-JLR200.

(83) Bates, P. D.; Durrett, T. P.; Ohlrogge, J. B.; Pollard, M. Analysis of Acyl Fluxes through Multiple Pathways of Triacylglycerol Synthesis in Developing Soybean Embryos. *Plant Physiol* **2009**, *150* (1), 55-72. DOI: 10.1104/pp.109.137737.

(84) Shindou, H.; Shimizu, T. Acyl-CoA:lysophospholipid acyltransferases. *J Biol Chem* **2009**, *284* (1), 1-5. DOI: 10.1074/jbc.R800046200.

(85) Bates, P. D. Understanding the control of acyl flux through the lipid metabolic network of plant oil biosynthesis. *Bba-Mol Cell Biol L* **2016**, *1861* (9), 1214-1225. DOI: 10.1016/j.bbalip.2016.03.021.

(86) Bae, S. H.; Zoclanclounon, Y. A. B.; Kumar, T. S.; Oh, J. H.; Lee, J.; Kim, T. H.; Park, K. Y. Advances in Understanding the Genetic Basis of Fatty Acids Biosynthesis in Perilla: An Update. *Plants-Basel* **2022**, *11* (9), e1207. DOI: ARTN 1207/10.3390/plants11091207.

(87) Kennedy, E. P. Biosynthesis of Complex Lipids. *Fed Proc* **1961**, *20* (4), 934-940.

(88) Rangan, P.; Maurya, R.; Singh, S. Can omic tools help generate alternative newer sources of edible seed oil? *Plant Direct* **2022**, *6* (6), e399. DOI: ARTN e399.10.1002/pld3.399 From NLM PubMed-not-MEDLINE.

(89) Banas, A.; Dahlqvist, A.; Stahl, U.; Lenman, M.; Stymne, S. The involvement of phospholipid : diacylglycerol acyltransferases in triacylglycerol production. *Biochem Soc T* **2000**, *28*, 703-705. DOI: Doi 10.1042/0300-5127:0280703.

(90) Griffiths, G.; Stobart, A. K.; Stymne, S. The Acylation of Sn-Glycerol 3-Phosphate and the Metabolism of Phosphatidate in Microsomal Preparations from the Developing Cotyledons of Safflower (Carthamus-Tinctorius L) Seed. *Biochemical Journal* **1985**, *230* (2), 379-388. DOI: DOI 10.1042/bj2300379.

(91) Oo, K. C.; Huang, A. H. C. Lysophosphatidate Acyltransferase Activities in the Microsomes from Palm Endosperm, Maize Scutellum, and Rapeseed Cotyledon of Maturing Seeds. *Plant Physiol* **1989**, *91* (4), 1288-1295. DOI: DOI 10.1104/pp.91.4.1288.

(92) Kim, H. U.; Li, Y. B.; Huang, A. H. C. Ubiquitous and endoplasmic reticulum-located lysophosphatidyl acyltransferase, LPAT2, is essential for female but not male gametophyte development in Arabidopsis. *Plant Cell* **2005**, *17* (4), 1073-1089. DOI: 10.1105/tpc.104.030403.

(93) Ohlrogge, J.; Browse, J. Lipid Biosynthesis. *Plant Cell* **1995**, *7* (7), 957-970. DOI: DOI 10.1105/tpc.7.7.957.

(94) Dickson, E. J.; Hille, B. Understanding phosphoinositides: rare, dynamic, and essential membrane phospholipids. *Biochemical Journal* **2019**, *476*, 1-23. DOI: 10.1042/Bcj20180022.

(95) Sasaki, T.; Takasuga, S.; Sasaki, J.; Kofuji, S.; Eguchi, S.; Yamazaki, M.; Suzuki, A. Mammalian phosphoinositide kinases and phosphatases. *Progress in Lipid Research* **2009**, *48* (6), 307-343. DOI: 10.1016/j.plipres.2009.06.001.

(96) Raghu, P.; Joseph, A.; Krishnan, H.; Singh, P.; Saha, S. Phosphoinositides: Regulators of Nervous System Function in Health and Disease. *Front Mol*

Neurosci **2019**, *12*, 208. DOI: 10.3389/fnmol.2019.00208 From NLM PubMed-not-MEDLINE.

(97) Blunsom, N. J.; Cockcroft, S. Phosphatidylinositol synthesis at the endoplasmic reticulum. *Biochim Biophys Acta Mol Cell Biol Lipids* **2020**, *1865* (1), 158471. DOI: 10.1016/j.bbalip.2019.05.015 From NLM Medline.

(98) Antonsson, B. Phosphatidylinositol synthase from mammalian tissues. *Bba-Lipid Lipid Met* **1997**, *1348* (1-2), 179-186. DOI: Doi 10.1016/S0005-2760(97)00105-7.

(99) Breitkopf, S. B.; Ricoult, S. J. H.; Yuan, M.; Xu, Y.; Peake, D. A.; Manning, B. D.; Asara, J. M. A relative quantitative positive/negative ion switching method for untargeted lipidomics via high resolution LC-MS/MS from any biological source. *Metabolomics* **2017**, *13* (3). DOI: 10.1007/s11306-016-1157-8.

(100) Traynor-Kaplan, A.; Kruse, M.; Dickson, E. J.; Dai, G.; Vivas, O.; Yu, H.; Whittington, D.; Hille, B. Fatty-acyl chain profiles of cellular phosphoinositides. *Biochim Biophys Acta* **2017**, *1862* (5), 513-522. DOI: 10.1016/j.bbalip.2017.02.002.

(101) Wepy, J. A.; Galligan, J. J.; Kingsley, P. J.; Xu, S.; Goodman, M. C.; Tallman, K. A.; Rouzer, C. A.; Marnett, L. J. Lysophospholipases cooperate to mediate lipid homeostasis and lysophospholipid signaling. *J Lipid Res* **2019**, *60* (2), 360-374. DOI: 10.1194/jlr.M087890.

(102) Shulga, Y. V.; Myers, D. S.; Ivanova, P. T.; Milne, S. B.; Brown, H. A.; Topham, M. K.; Epand, R. M. Molecular species of phosphatidylinositol-cycle intermediates in the endoplasmic reticulum and plasma membrane. *Biochemistry* **2010**, *49* (2), 312-317. DOI: 10.1021/bi901551e.

(103) Nadler, A.; Reither, G.; Feng, S.; Stein, F.; Reither, S.; Muller, R.; Schultz, C. The fatty acid composition of diacylglycerols determines local signaling patterns. *Angew Chem Int Ed Engl* **2013**, *52* (24), 6330-6334. DOI: 10.1002/anie.201301716.

(104) Shulga, Y. V.; Topham, M. K.; Epand, R. M. Substrate specificity of diacylglycerol kinase-epsilon and the phosphatidylinositol cycle. *FEBS Lett* **2011**, *585* (24), 4025-4028. DOI: 10.1016/j.febslet.2011.11.016.

(105) Epand, R. M. Features of the phosphatidylinositol cycle and its role in signal transduction. *J Membr Biol* **2017**, *250* (4), 353-366. DOI: 10.1007/s00232-016-9909-y.

(106) Lung, M.; Shulga, Y. V.; Ivanova, P. T.; Myers, D. S.; Milne, S. B.; Brown, H. A.; Topham, M. K.; Epand, R. M. Diacylglycerol kinase epsilon is selective for both acyl chains of phosphatidic acid or diacylglycerol. *J Biol Chem* **2009**, *284* (45), 31062-31073. DOI: 10.1074/jbc.M109.050617.

(107) Bozelli, J. C., Jr.; Epand, R. M. Role of membrane shape in regulating the phosphatidylinositol cycle at contact sites. *Chem Phys Lipids* **2019**, *221*, 24-29. DOI: 10.1016/j.chemphyslip.2019.03.002.

(108) Bozelli, J. C., Jr.; Jennings, W.; Black, S.; Hou, Y. H.; Lameire, D.; Chatha, P.; Kimura, T.; Berno, B.; Khondker, A.; Rheinstadter, M. C.; et al. Membrane curvature allosterically regulates the phosphatidylinositol cycle, controlling its rate and acyl-chain composition of its lipid intermediates. *J Biol Chem* **2018**, *293* (46), 17780-17791. DOI: 10.1074/jbc.RA118.005293.

(109) Lee, J.; Bayarsaikhan, D.; Bayarsaikhan, G.; Kim, J. S.; Schwarzbach, E.; Lee, B. Recent advances in genome editing of stem cells for drug discovery and therapeutic application. *Pharmacol Ther* **2020**, *209*, 107501. DOI: 10.1016/j.pharmthera.2020.107501 From NLM Medline.

(110) Li, H.; Yang, Y.; Hong, W.; Huang, M.; Wu, M.; Zhao, X. Applications of genome editing technology in the targeted therapy of human diseases: mechanisms, advances and prospects. *Signal Transduct Target Ther* **2020**, *5* (1), 1. DOI: 10.1038/s41392-019-0089-y From NLM Medline.

(111) Nabet, B.; Roberts, J. M.; Buckley, D. L.; Paulk, J.; Dastjerdi, S.; Yang, A.; Leggett, A. L.; Erb, M. A.; Lawlor, M. A.; Souza, A.; et al. The dTAG system for immediate and target-specific protein degradation. *Nature Chemical Biology* **2018**, *14* (5), 431-+. DOI: 10.1038/s41589-018-0021-8.

(112) Moll, J. r.; Colombo, R. *Target identification and validation in drug discovery : methods and protocols*; Humana Press, 2013.

(113) Nishimura, K.; Fukagawa, T.; Takisawa, H.; Kakimoto, T.; Kanemaki, M. An auxin-based degron system for the rapid depletion of proteins in nonplant cells. *Nature Methods* **2009**, *6* (12), 917-U978. DOI: 10.1038/nmeth.1401.

(114) Buckley, D. L.; Raina, K.; Darricarrere, N.; Hines, J.; Gustafson, J. L.; Smith, I. E.; Miah, A. H.; Harling, J. D.; Crews, C. M. HaloPROTACS: Use of small molecule PROTACs to induce degradation of HaloTag fusion proteins. *ACS Chem Biol* **2015**, *10* (8), 1831-1837. DOI: 10.1021/acschembio.5b00442.

(115) Neklesa, T. K.; Tae, H. S.; Schneekloth, A. R.; Stulberg, M. J.; Corson, T. W.; Sundberg, T. B.; Raina, K.; Holley, S. A.; Crews, C. M. Small-molecule hydrophobic tagging-induced degradation of HaloTag fusion proteins. *Nat Chem Biol* **2011**, *7* (8), 538-543. DOI: 10.1038/nchembio.597.

(116) Chung, H. K.; Jacobs, C. L.; Huo, Y. W.; Yang, J.; Krumm, S. A.; Plemper, R. K.; Tsien, R. Y.; Lin, M. Z. Tunable and reversible drug control of protein production via a self-excising degron. *Nature Chemical Biology* **2015**, *11* (9), 713-+. DOI: 10.1038/Nchembio.1869.

(117) England, C. G.; Luo, H.; Cai, W. HaloTag technology: a versatile platform for biomedical applications. *Bioconjug Chem* **2015**, *26* (6), 975-986. DOI: 10.1021/acs.bioconjchem.5b00191.

(118) Goldschmidt, H. L.; Tu-Sekine, B.; Volk, L.; Anggono, V.; Huganir, R. L.; Raben, D. M. DGKtheta Catalytic activity is required for efficient recycling of presynaptic vesicles at excitatory synapses. *Cell Rep* **2016**, *14* (2), 200-207. DOI: 10.1016/j.celrep.2015.12.022.

(119) Zhong, Y.; Chi, F.; Wu, H.; Liu, Y.; Xie, Z.; Huang, W.; Shi, W.; Qian, H. Emerging targeted protein degradation tools for innovative drug discovery: From classical PROTACs to the novel and beyond. *Eur J Med Chem* **2022**, *231*, 114142. DOI: 10.1016/j.ejmech.2022.114142 From NLM Medline.

(120) Lin, D. W.; Chung, B. P.; Huang, J. W.; Wang, X. R.; Huang, L.; Kaiser, P. Microhomology-based CRISPR tagging tools for protein tracking, purification, and depletion. *Journal of Biological Chemistry* **2019**, *294* (28), 10877-10885. DOI: 10.1074/jbc.RA119.008422.

(121) Lai, A. C.; Crews, C. M. Induced protein degradation: an emerging drug discovery paradigm. *Nature Reviews Drug Discovery* **2017**, *16* (2), 101-114. DOI: 10.1038/nrd.2016.211.

(122) Coleman, K. G.; Crews, C. M. Proteolysis-Targeting Chimeras: Harnessing the Ubiquitin-Proteasome System to Induce Degradation of Specific Target Proteins. *Annu Rev Canc Biol* **2018**, *2*, 41-58. DOI: 10.1146/annurev-cancerbio-030617-050430.

(123) Campbell, J.; Ryan, C. J.; Brough, R.; Bajrami, I.; Pemberton, H. N.; Chong, I. Y.; Costa-Cabral, S.; Frankum, J.; Gulati, A.; Holme, H.; et al. Large-Scale Profiling of Kinase Dependencies in Cancer Cell Lines. *Cell Reports* **2016**, *14* (10), 2490-2501. DOI: 10.1016/j.celrep.2016.02.023.

(124) Vivanco, I.; Chen, Z. C.; Tanos, B.; Oldrini, B.; Hsieh, W. Y.; Yannuzzi, N.; Campos, C.; Mellinghoff, I. K. A kinase-independent function of AKT promotes cancer cell survival. *Elife* **2014**, *3*. DOI: ARTN e03751.10.7554/eLife.03751.

(125) Chopra, R.; Sadok, A.; Collins, I. A critical evaluation of the approaches to targeted protein degradation for drug discovery. *Drug Discovery Today: Technologies* **2019**, *31*, 5-13. DOI: doi.org/10.1016/j.ddtec.2019.02.002.

(126) Zeng, S. X.; Huang, W. H.; Zheng, X. L.; Cheng, L. Y.; Zhang, Z. M.; Wang, J.; Shen, Z. R. Proteolysis targeting chimera (PROTAC) in drug discovery paradigm: Recent progress and future challenges. *Eur J Med Chem* **2021**, *210*. DOI: ARTN 112981.10.1016/j.ejmech.2020.112981.

(127) Bricelj, A.; Steinebach, C.; Kuchta, R.; Gutschow, M.; Sosic, I. E3 Ligase Ligands in Successful PROTACs: An Overview of Syntheses and Linker

Attachment Points. *Front Chem* **2021**, *9*, 707317. DOI: ARTN 707317.10.3389/fchem.2021.707317 From NLM PubMed-not-MEDLINE.

(128) Colberg, L.; Cammann, C.; Greinacher, A.; Seifert, U. Structure and function of the ubiquitin-proteasome system in platelets. *J Thromb Haemost* **2020**, *18* (4), 771-780. DOI: 10.1111/jth.14730.

(129) Bakos, G.; Yu, L.; Gak, I. A.; Roumeliotis, T. I.; Liakopoulos, D.; Choudhary, J. S.; Mansfeld, J. An E2-ubiquitin thioester-driven approach to identify substrates modified with ubiquitin and ubiquitin-like molecules. *Nature Communications* **2018**, *9* (1), 4776. DOI: ARTN 4776.10.1038/s41467-018-07251-5 From NLM Medline.

(130) Kleiger, G.; Mayor, T. Perilous journey: a tour of the ubiquitin-proteasome system. *Trends Cell Biol* **2014**, *24* (6), 352-359. DOI: 10.1016/j.tcb.2013.12.003.

(131) Qi, S. M.; Dong, J.; Xu, Z. Y.; Cheng, X. D.; Zhang, W. D.; Qin, J. J. PROTAC: An Effective Targeted Protein Degradation Strategy for Cancer Therapy. *Front Pharmacol* **2021**, *12*, 692574. DOI: 10.3389/fphar.2021.692574 From NLM PubMed-not-MEDLINE.

(132) Rauch, J.; Volinsky, N.; Romano, D.; Kolch, W. The secret life of kinases: functions beyond catalysis. *Cell Commun Signal* **2011**, *9* (1), 23. DOI: 10.1186/1478-811X-9-23 From NLM PubMed-not-MEDLINE.

(133) Thorpe, L. M.; Yuzugullu, H.; Zhao, J. J. PI3K in cancer: divergent roles of isoforms, modes of activation and therapeutic targeting. *Nature Reviews Cancer* **2015**, *15* (1), 7-24. DOI: 10.1038/nrc3860.

(134) Winter, G. E.; Buckley, D. L.; Paulk, J.; Roberts, J. M.; Souza, A.; Dhe-Paganon, S.; Bradner, J. E. Phthalimide conjugation as a strategy for in vivo target protein degradation. *Science* **2015**, *348* (6241), 1376-1381. DOI: 10.1126/science.aab1433.

(135) An, S.; Fu, L. Small-molecule PROTACs: An emerging and promising approach for the development of targeted therapy drugs. *EBioMedicine* **2018**, *36*, 553-562. DOI: 10.1016/j.ebiom.2018.09.005.

(136) Nabet, B. Charting a New Path Towards Degrading Every Protein. *Chembiochem* **2021**, *22* (3), 483-484. DOI: 10.1002/cbic.202000531.

(137) Sakamoto, K. M.; Kim, K. B.; Kumagai, A.; Mercurio, F.; Crews, C. M.; Deshaies, R. J. Protacs: Chimeric molecules that target proteins to the Skp1-Cullin-F box complex for ubiquitination and degradation. *P Natl Acad Sci USA* **2001**, *98* (15), 8554-8559. DOI: DOI 10.1073/pnas.141230798.

(138) Collins, I.; Wang, H.; Caldwell, J. J.; Chopra, R. Chemical approaches to targeted protein degradation through modulation of the ubiquitin-proteasome pathway. *Biochem J* **2017**, *474* (7), 1127-1147. DOI: 10.1042/BCJ20160762.

(139) Sakuma, T.; Nakade, S.; Sakane, Y.; Suzuki, K. T.; Yamamoto, T. MMEJ-assisted gene knock-in using TALENs and CRISPR-Cas9 with the PITCh systems. *Nat Protoc* **2016**, *11* (1), 118-133. DOI: 10.1038/nprot.2015.140.

(140) Sakuma, T.; Woltjen, K. Nuclease-mediated genome editing: At the front-line of functional genomics technology. *Dev Growth Differ* **2014**, *56* (1), 2-13. DOI: 10.1111/dgd.12111 From NLM Medline.

(141) Esvelt, K. M.; Mali, P.; Braff, J. L.; Moosburner, M.; Yaung, S. J.; Church, G. M. Orthogonal Cas9 proteins for RNA-guided gene regulation and editing. *Nature Methods* **2013**, *10* (11), 1116-1121. DOI: 10.1038/Nmeth.2681.

(142) Cong, L.; Ran, F. A.; Cox, D.; Lin, S. L.; Barretto, R.; Habib, N.; Hsu, P. D.; Wu, X. B.; Jiang, W. Y.; Marraffini, L. A.; et al. Multiplex Genome Engineering Using CRISPR/Cas Systems. *Science* **2013**, *339* (6121), 819-823. DOI: 10.1126/science.1231143.

(143) Gonzalez-Torres, P.; Rodriguez-Mateos, F.; Anton, J.; Gabaldon, T. Impact of Homologous Recombination on the Evolution of Prokaryotic Core Genomes. *Mbio* **2019**, *10* (1). DOI: 10.1128/mBio.02494-18 From NLM Medline.

(144) Brandsma, I.; Gent, D. C. Pathway choice in DNA double strand break repair: observations of a balancing act. *Genome Integr* **2012**, *3* (1), 9. DOI: 10.1186/2041-9414-3-9 From NLM PubMed-not-MEDLINE.

(145) Mao, Z. Y.; Bozzella, M.; Seluanov, A.; Gorbunova, V. Comparison of nonhomologous end joining and homologous recombination in human cells. *DNA Repair* **2008**, *7* (10), 1765-1771. DOI: 10.1016/j.dnarep.2008.06.018.

(146) Nakade, S.; Tsubota, T.; Sakane, Y.; Kume, S.; Sakamoto, N.; Obara, M.; Daimon, T.; Sezutsu, H.; Yamamoto, T.; Sakuma, T.; et al. Microhomology-mediated end-joining-dependent integration of donor DNA in cells and animals using TALENs and CRISPR/Cas9. *Nature Communications* **2014**, *5*. DOI: ARTN 5560.10.1038/ncomms6560.

(147) Gratz, S. J.; Cummings, A. M.; Nguyen, J. N.; Hamm, D. C.; Donohue, L. K.; Harrison, M. M.; Wildonger, J.; O'Connor-Giles, K. M. Genome engineering of Drosophila with the CRISPR RNA-guided Cas9 nuclease. *Genetics* **2013**, *194* (4), 1029-1035. DOI: 10.1534/genetics.113.152710 From NLM Medline.

(148) Wang, H. Y.; Yang, H.; Shivalila, C. S.; Dawlaty, M. M.; Cheng, A. W.; Zhang, F.; Jaenisch, R. One-Step Generation of Mice Carrying Mutations in Multiple Genes by CRISPR/Cas-Mediated Genome Engineering. *Cell* **2013**, *153* (4), 910-918. DOI: 10.1016/j.cell.2013.04.025.

(149) Yasue, A.; Mitsui, S. N.; Watanabe, T.; Sakuma, T.; Oyadomari, S.; Yamamoto, T.; Noji, S.; Mito, T.; Tanaka, E. Highly efficient targeted mutagenesis in one-cell mouse embryos mediated by the TALEN and CRISPR/Cas systems. *Sci Rep* **2014**, *4*, 5705. DOI: 10.1038/srep05705 From NLM Medline.

(150) Taleei, R.; Nikjoo, H. Biochemical DSB-repair model for mammalian cells in G1 and early S phases of the cell cycle. *Mutat Res-Gen Tox En* **2013**, *756* (1-2), 206-212. DOI: 10.1016/j.mrgentox.2013.06.004.

(151) Shan, L.; Wang, D.; Mao, Q.; Xia, H. Establishment of a DGKtheta Endogenous Promoter Luciferase Reporter HepG2 Cell Line for Studying the Transcriptional Regulation of DGKtheta Gene. *Appl Biochem Biotechnol* **2019**, *187* (4), 1344-1355. DOI: 10.1007/s12010-018-2890-4 From NLM Medline.

(152) Los, G. V.; Encell, L. P.; McDougall, M. G.; Hartzell, D. D.; Karassina, N.; Zimprich, C.; Wood, M. G.; Learish, R.; Ohana, R. F.; Urh, M.; et al. HaloTag: a novel protein labeling technology for cell imaging and protein analysis. *ACS Chem Biol* **2008**, *3* (6), 373-382. DOI: 10.1021/cb800025k.

(153) Popa, I.; Berkovich, R.; Alegre-Cebollada, J.; Badilla, C. L.; Rivas-Pardo, J. A.; Taniguchi, Y.; Kawakami, M.; Fernandez, J. M. Nanomechanics of HaloTag tethers. *J Am Chem Soc* **2013**, *135* (34), 12762-12771. DOI: 10.1021/ja4056382.

(154) Contrepois, K.; Mahmoudi, S.; Ubhi, B. K.; Papsdorf, K.; Hornburg, D.; Brunet, A.; Snyder, M. Cross-platform comparison of untargeted and targeted lipidomics approaches on aging mouse plasma. *Sci Rep* **2018**, *8* (1), 17747. DOI: 10.1038/s41598-018-35807-4.

(155) Aretz, I.; Meierhofer, D. Advantages and Pitfalls of Mass Spectrometry Based Metabolome Profiling in Systems Biology. *Int J Mol Sci* **2016**, *17* (5), 632. DOI: 10.3390/ijms17050632 From NLM Medline.

(156) Liebisch, G.; Ekroos, K.; Hermansson, M.; Ejsing, C. S. Reporting of lipidomics data should be standardized. *Biochim Biophys Acta Mol Cell Biol Lipids* **2017**, *1862* (8), 747-751. DOI: 10.1016/j.bbalip.2017.02.013.

(157) Bian, Y.; Zheng, R.; Bayer, F. P.; Wong, C.; Chang, Y. C.; Meng, C.; Zolg, D. P.; Reinecke, M.; Zecha, J.; Wiechmann, S.; et al. Robust, reproducible and quantitative analysis of thousands of proteomes by micro-flow LC-MS/MS. *Nat Commun* **2020**, *11* (1), 157. DOI: 10.1038/s41467-019-13973-x From NLM Medline.

(158) Aldana, J.; Romero-Otero, A.; Cala, M. P. Exploring the Lipidome: Current Lipid Extraction Techniques for Mass Spectrometry Analysis. *Metabolites* **2020**, *10* (6). DOI: 10.3390/metabo10060231 From NLM PubMed-not-MEDLINE.

(159) Saini, R. K.; Prasad, P.; Shang, X. M.; Keum, Y. S. Advances in Lipid Extraction Methods-A Review. *International Journal of Molecular Sciences* **2021**, *22* (24). DOI: ARTN 13643.10.3390/ijms222413643.

(160) Meissner, F.; Geddes-McAlister, J.; Mann, M.; Bantscheff, M. The emerging role of mass spectrometry-based proteomics in drug discovery. *Nature Reviews Drug Discovery* **2022**. DOI: 10.1038/s41573-022-00409-3.

(161) Xu, J. Q.; Li, X. Q.; Ding, K.; Li, Z. Q. Applications of Activity-Based Protein Profiling (ABPP) and Bioimaging in Drug Discovery. *Chem-Asian J* **2020**, *15* (1), 34-41. DOI: 10.1002/asia.201901500.

(162) Speers, A. E.; Cravatt, B. F. Activity-Based Protein Profiling (ABPP) and Click Chemistry (CC)-ABPP by MudPIT Mass Spectrometry. *Curr Protoc Chem Biol* **2009**, *1*, 29-41. DOI: 10.1002/9780470559277.ch090138 From NLM PubMed-not-MEDLINE.

(163) Cravatt, B. F.; Wright, A. T.; Kozarich, J. W. Activity-based protein profiling: from enzyme chemistry to proteomic chemistry. *Annu Rev Biochem* **2008**, *77*, 383-414. DOI: 10.1146/annurev.biochem.75.101304.124125.

(164) Jessani, N.; Cravatt, B. F. The development and application of methods for activity-based protein profiling. *Current Opinion in Chemical Biology* **2004**, *8* (1), 54-59. DOI: 10.1016/j.cbpa.2003.11.004.

(165) Kozarich, J. W. Activity-based proteomics: enzyme chemistry redux. *Current Opinion in Chemical Biology* **2003**, *7* (1), 78-83. DOI: 10.1016/S1367-5931(02)00013-3.

(166) Wang, S.; Tian, Y.; Wang, M.; Wang, M.; Sun, G. B.; Sun, X. B. Advanced activity-based protein profiling application strategies for drug development. *Front Pharmacol* **2018**, *9*, 353. DOI: 10.3389/fphar.2018.00353.

(167) Patricelli, Matthew P.; Nomanbhoy, Tyzoon K.; Wu, J.; Brown, H.; Zhou, D.; Zhang, J.; Jagannathan, S.; Aban, A.; Okerberg, E.; Herring, C.; et al. In Situ Kinase Profiling Reveals Functionally Relevant Properties of Native Kinases. *Chemistry & Biology* **2011**, *18* (6), 699-710. DOI: dx.doi.org/10.1016/j.chembiol.2011.04.011.

(168) Patricelli, M. P.; Szardenings, A. K.; Liyanage, M.; Nomanbhoy, T. K.; Wu, M.; Weissig, H.; Aban, A.; Chun, D.; Tanner, S.; Kozarich, J. W. Functional interrogation of the kinome using nucleotide acyl phosphates. *Biochemistry* **2007**, *46* (2), 350-358. DOI: 10.1021/bi062142x.

(169) Zhao, Q.; Ouyang, X. H.; Wan, X. B.; Gajiwala, K. S.; Kath, J. C.; Jones, L. H.; Burlingame, A. L.; Taunton, J. Broad-Spectrum Kinase Profiling in Live Cells with Lysine-Targeted Sulfonyl Fluoride Probes. *Journal of the American Chemical Society* **2017**, *139* (2), 680-685. DOI: 10.1021/jacs.6b08536.

(170) Borne, A. L.; Brulet, J. W.; Yuan, K.; Hsu, K. L. Development and biological applications of sulfur-triazole exchange (SuTEx) chemistry. *Rsc Chem Biol* **2021**, *2* (2), 322-337, 10.1039/D0CB00180E. DOI: 10.1039/d0cb00180e.

(171) Huang, T.; Hosseinibarkooie, S.; Borne, A. L.; Granade, M. E.; Brulet, J. W.; Harris, T. E.; Ferris, H. A.; Hsu, K.-L. Chemoproteomic profiling of kinases in live cells using electrophilic sulfonyl triazole probes. *Chemical Science* **2021**, *12* (9), 3295-3307, 10.1039/D0SC06623K. DOI: 10.1039/d0sc06623k.

(172) Boroda, S.; Niccum, M.; Raje, V.; Purow, B. W.; Harris, T. E. Dual activities of ritanserin and R59022 as DGKalpha inhibitors and serotonin receptor antagonists. *Biochem Pharmacol* **2017**, *123*, 29-39. DOI: 10.1016/j.bcp.2016.10.011.

(173) Olmez, I.; Love, S.; Xiao, A.; Manigat, L.; Randolph, P.; McKenna, B. D.; Neal, B. P.; Boroda, S.; Li, M.; Brenneman, B.; et al. Targeting the mesenchymal subtype in glioblastoma and other cancers via inhibition of diacylglycerol kinase alpha. *Neuro Oncol* **2018**, *20* (2), 192-202. DOI: 10.1093/neuonc/nox119.

(174) Franks, C. E.; Campbell, S. T.; Purow, B. W.; Harris, T. E.; Hsu, K. L. The Ligand binding landscape of diacylglycerol kinases. *Cell Chem Biol* **2017**, *24* (7), 870-880 e875. DOI: 10.1016/j.chembiol.2017.06.007.

(175) McCloud, R. L.; Franks, C. E.; Campbell, S. T.; Purow, B. W.; Harris, T. E.; Hsu, K. L. Deconstructing Lipid Kinase Inhibitors by Chemical Proteomics. *Biochemistry* **2018**, *57* (2), 231-236. DOI: 10.1021/acs.biochem.7b00962.

(176) Granade, M. E.; Manigat, L. C.; Lemke, M. C.; Purow, B. W.; Harris, T. E. Identification of ritanserin analogs that display DGK isoform specificity. *Biochem Pharmacol* **2022**, *197*, 114908. DOI: 10.1016/j.bcp.2022.114908.

(177) Pettersson, M.; Crews, C. M. PROteolysis TArgeting Chimeras (PROTACs) - past, present and future. *Drug Discov Today Technol* **2019**, *31*, 15-27. DOI: 10.1016/j.ddtec.2019.01.002.

Chapter 2. Substrate Specificity for Diacylglycerol Kinase-θ

2.1 *Abstract*

Diacylglycerol kinases comprise a family of enzymes that catalyze the ATP-dependent phosphorylation of diacylglycerol (DAG) to phosphatidic acid (PA).[1] It has been established that DGKε exhibits specificity for arachidonoyl containing forms of DAG.[2]

We set out to quantitatively determine the global molecular lipid composition when overexpressed DGKθ in HEK293T cells using tandem LC-MS/MS techniques, use two technologies, overexpression of recombinant DGKθ and of HaloTAG fusion DGKθ, as novel approaches expanding our lipidomic understanding of DGKθ substrate specificity. We have provided some answers as to how DGKθ metabolism may be involved in fatty acyl remodeling via the Lands cycle. We have shown great progress in determining global alterations in lipidome upon DGKθ, which have provided interesting insight into molecular lipid composition at the level of fatty acyl chain length and unsaturation, using tandem LC-MS/MS techniques. This has allowed us to explore into substrate specificity and its putative role in the Lands cycle.

Future work is needed to fully define lipid substrate specificity of DGKθ but our current work establishes the foundation for methodology and preliminary data.

2.2 *Introduction*

Metabolism of glycerolipids and glycerophospholipids by kinases is a fundamental process in cell metabolism and signaling.[3] For example, production of diacylglycerols (DAGs) upon cellular activation is a critical regulatory event for signal transduction that occurs in the plasma membrane (PM).[4, 5] Diacylglycerol kinases (DGKs) have been implicated in the ATP-dependent phosphorylation of DAG to produce phosphatidic acid (PA) and thus serve as a critical regulatory point in cell signaling **(Scheme 2.2.1)**.[6, 7, 8] Whether DGKs can metabolize substrates in addition to DAG and PA is currently unknown.[9, 10, 11]

Our current understanding of mammalian DGKs structure and function is limited due in part to a lack of a three-dimensional X-ray structures of full length protein.[12] While analysis of primary amino acid sequences of DGKs has helped organize the DGK superfamily into 5 principal subtypes, the functional ramifications of expressing 10 mammalian isoforms in cell and tissues remain poorly defined. [12-15] *In vitro* studies have provided clues and preliminary evidence that DGKs can exhibit fatty acyl specificity in substrates (e.g. DGKε's preference for arachidonoyl-DAGs and metabolic specificity of lipid kinases to assign a role for atypical C1 domains in cell metabolism).[16, 17] Global and systematic evaluations of DGK substrate specificity in living systems are needed. The focus of this study is to elucidate novel substrate specificity for DGKθ.[3, 18]

Fatty acyl moieties of membrane lipids exhibit diversity in their acyl chain lengths, degrees of unsaturation, and stereochemistry.[19, 20] Lipids involved in signaling pathways, such as those in the PI cycle, contain discreet acyl chain

compositions that reflect subcellular location and metabolic/signaling function. As a result, defining the chemical composition of lipid substrates is key to understanding how lipid biology is regulated.[21-25] As mentioned above, it has been shown that DGKs display fatty acyl specificity as evidenced by DGKε's preference for DAG lipids containing stearic acid and arachidonic acid (C18:0/C20:4) in the *sn*-1 and *sn*-2 positions, respectively.[24, 26-28] In agreement with its fatty acyl specificity, DGKε has been linked to regulation of the PI cycle where arachidonoyl-DAGs are primarily metabolized.[3, 18, 29] Although advances in our understanding of fatty acyl composition has helped us understand phospholipid remodeling, we still do not fully understand how these acyl chain compositions may participate in membrane remodeling pathways. New methodologies are providing unique approaches in deciphering lipid pathways.[20, 28, 30, 31]

Recent advances in liquid chromatography mass spectrometry (LC-MS/MS) techniques have enabled interesting development of sensitive profiling of molecular structures on a global scale, which we would like to deploy.[19, 32, 33] Although gas chromatography, nuclear magnetic resonance spectroscopy can provide interesting insights, nowadays the gold standard is MS.[34] Lipidomics is a global profiling methodology to detect, identify, and quantify lipids extracted from biological sources using LC-MS/MS; which provides the necessary resolution, sensitivity, selectivity, and throughput for these demanding global analyses.[32, 33] The prime advantage is their broad lipid recovery combined with the removal of unwanted polar metabolites, proteins, and salts during the lipid extraction.[34, 35]

Using LC-MS/MS we identified changes in the acyl chain lengths and degrees of unsaturation of lipids in response to recombinant overexpression of DGKθ. Specifically, we detected changes in the following lipid species ceramides (Cer), triglycerides (TG), lysophosphatidylcholines (LPC), phosphatidylcholines (PC), lysophosphatidylethanolamines (LPE), phosphatidylethanolamines (PE), and phosphatidylinositols (PI). We quantified these changes by global analysis of lipids in HEK293T cells overexpressing recombinant DGKθ using a data-dependent "top ten" LC-MS acquisition method (i.e., ddMS2). This untargeted LC-MS method consists of first separating lipid species by C-18 reverse-phase liquid chromatography (RPLC) followed by mass analysis using a Q-Exactive Plus mass spectrometer. A top ten ddMS2 cycle consisted of one MS1 scan followed by ten MS2 scans.[36, 37] These changes were reproduced across three biological replicates and each biological replicate was reproduced across three technical replicates. To determine specificity, we compared cellular changes in lipids mediated by DGKθ with another isoform, DGKX, and confirmed that these lipid substrates were not altered.

Based on our lipidomics findings above, we propose that DGKθ may be involved in fatty acyl chain remodeling through the Lands cycle, which takes place between the cytosol and plasma membrane, **(Figure 2.2.1)**.[21] In the Lands cycle, lysophospholipid acyltransferases (LPLAT) transfer fatty acyl chains onto lysophospholipids to produce phospholipids.[3, 18, 38] In the reverse reaction, a phospholipid is converted back to a lysophospholipid and a free fatty acid chain via phospholipase A_2 action (PLA_2).[38, 39] Thus, the coordinated action of LPLAT

and PLA_2 can efficiently remodel the fatty acyl composition of phospholipids and thereby the cell membrane.[21, 40]

In addition, we propose a novel approach using CRISPR/Cas9 technology to knock out a gene and HaloTAG technology to knockdown a gene, DGKθ. Applications for CASPR/Cas9 and HaloTAG technologies are numerous and well documented; both are versatile platforms for many biochemical applications.[41-43] For example, it has been reported that HaloTAG can be used to isolate and purify proteins, and it has been used in cellular imaging.[42, 44] For this work, HaloTAG was used to "tag" the protein of interest, DGKθ. We aimed to transfect the HaloTAG DGKθ protein of interest (POI) into HEK293T cells. After establishing a DGKθ-HaloTAG cell line by CRISPR/Cas9, we synthesized a HaloTAG ligand of interest that binds irreversibly to the HaloTAG DGKθ fusion protein with high specificity.[45] When the ligand binds to the POI (DGKθ), it exposes hydrophobic regions of the POI causing the HaloTAG-DGKθ fusion protein to degrade in a proteasome-dependent manner **(Figure 2.2.2)**.[42, 46] Thus, the HaloTAG system will allow us to block the HaloTAG DGKθ fusion protein and act as an alternative for an inhibitor. Currently, there are no selective inhibitors available for DGKθ. We aimed to measure DGKθ degradation by identifying decreasing lipid substrate levels using tandem mass spectrometry.[42, 47]

We hypothesized DGKθ metabolism directly supplies DAG and PA lipids involved in fatty acyl remodeling of membranes via the Lands cycle. Our goal is to use LC-MS metabolomics to identify and track changes in the lipidome in response

to transient overexpression of DGKθ and to endogenous knock-out of the DGKθ locus in live HEK293T cells.

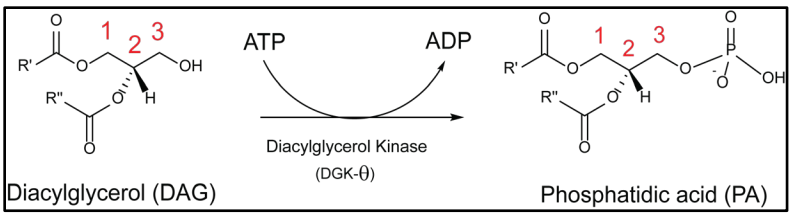

Scheme 2.2.1 Catalytic DGKθ. Catalytic reaction of DAG to generate PA by Diacylglycerol Kinase θ.

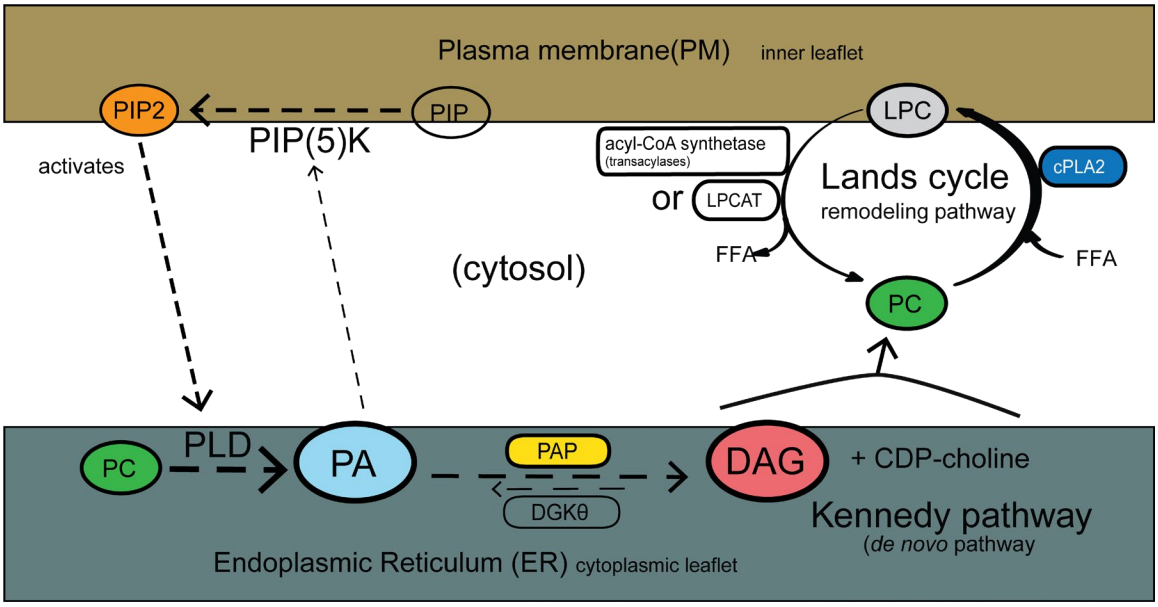

Figure 2.2.1 A proposed mechanism for DGKθ regulated metabolism. Phosphatidic acid phosphohydrolase (PAP), which converts PA to DAG. Cytosolic phospholipase A (cPLA) enzyme catalyzes the hydrolysis of ester bonds at *sn*-2 ($cPLA_2$) position of membrane phospholipids (PL), producing free fatty acids and lysophospholipids (lyso-PLs). The combination of lyso-PLs and free fatty acids (FFA) into PLs through a reacylation process is mediated by lysophospholipid acyltransferases (LPLAT).

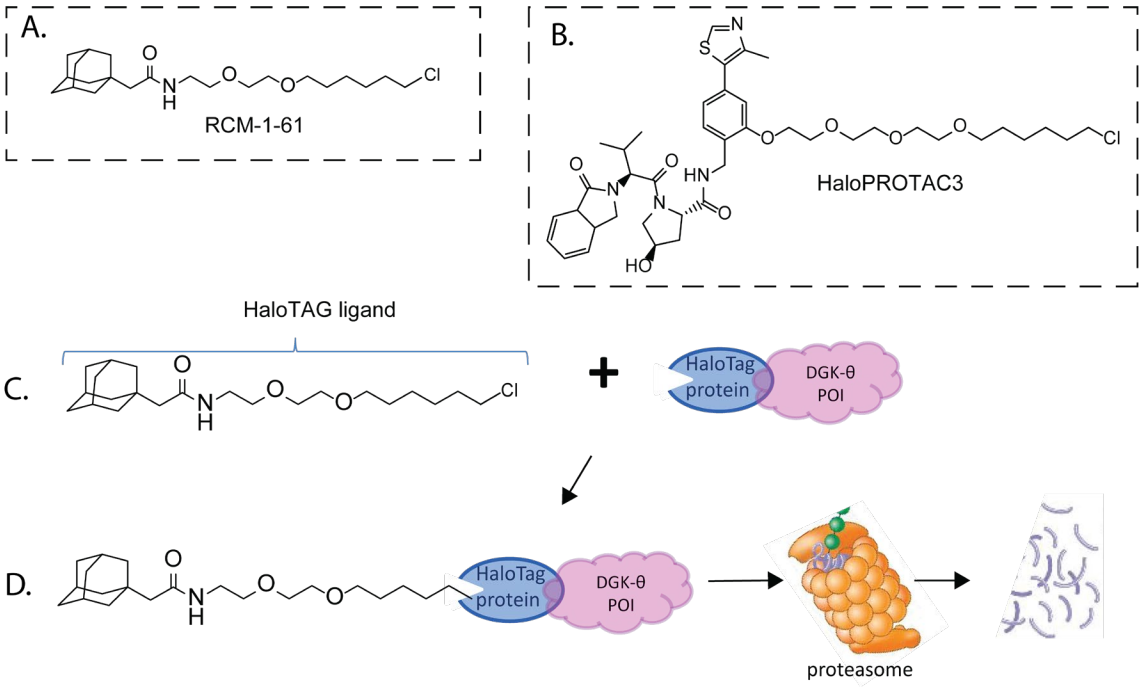

Figure 2.2.2 HaloTAG protein was obtained from Promega vector. (A) and (B) HaloTAG ligands RCM-1-61 and HaloPROTAC3. (C) The HaloTAG ligand will bind to the HaloTAG Protein which is genetically attached to the protein of interest (POI). (D) Once ligand and HaloTAG protein are attached, a knockdown of the protein will occur via the degradation mechanism of a nearby proteasome.

2.3 *Materials and Methods*

Reagents. Unless otherwise specified, all reagents were purchased from Fisher Scientific. Polyethyleneimine (Polysciences Inc., Cat# 24765), 1-stearoyl-2-arachidonoyl-d8-*sn*-glycerol (SAG-d8; Cayman Chemical Company, Cat# 10009872), and arachidonic acid-d8 (AA-d8; Cayman Chemical Company, Cat# 390010).

Reagents for DGKθ knockout. Unless otherwise specified, all reagents were donated from Synthego. 24-well cell culture plates (Corning, Catalog #3526), Lipofectamine™ CRISPRMAX™ Cas9 Transfection Reagent (includes Cas9 Plus Reagent and CRISPRMAX™ Transfection Reagent) (Thermo Fisher Scientific, Catalog #CMAX00001), Opti-MEM™ - Reduced Serum Medium (Thermo Fisher Scientific, Catalog #31985062), 24-well cell culture plates (Corning, Catalog #3526).

Cell culture. HEK293T cells were purchased from ATCC. HEK293T cells were cultured in DMEM with 10% FBS (U.S. Source, Omega Scientific) and 1% L-glutamine (Thermo Fisher Scientific) in 10 cm^2 plates. Media in cell cultures were switched to serum-free DMEM 4 h prior to harvesting for all lipid analyses. All cells were grown to ~80% confluency in a 37 °C incubator with 5% CO_2. Cells were switched to serum-free DMEM media prior to compound treatments.

Transient transfection. Recombinant DGK proteins were produced by transient transfection of HEK293T cells with recombinant DNA. Vectors were either developed by Dr. Thurl Harris (University of Virginia, School of Medicine) or gifted to Dr. Kevin Lynch (University of Virginia, School of Medicine) by Dr. Kaoru Goto

(Yamagata University, School of Medicine) and Dr. Fumio Sakane (Chiba University) and were kindly shared for these studies: pcDNA3.1-FLAG-DGKH (human) and pCMV-Tag2B-FLAG-DGKQ (human). Vector pFN21AB1326 HaloTAG-DGKθ was purchased from Promega (Promega plasmid # FHC01210). HEK293T cells were plated at a concentration of $4.40x10^4$ cells in complete DMEM and grown to 70-75% confluency. A polyethyleneimine (PEI) stock solution was prepared (1 mg/mL, pH 7.4) and filter sterilized. Serum-free DMEM (600 µL) was mixed gently with 20 µL of sterile PEI (1 mg/mL, and pH 7.4), and 2.6 µg DNA in a sterile microfuge tube. Mixtures were incubated for 30 min at 25 °C. The mixture was then added dropwise to each 10 cm^2 plate, rocked back and forth to mix, and placed back in the 37 °C incubator. Cell pellets were harvested after two full days of growth, snap frozen in liquid N_2, and stored at -80 °C until use.

Reverse lipofection for DGKθ knockout. Multi-guide sg(RNA) vectors were donated by Synthego (Gene Knockout Kit v2-human-DGKθ-1.5nmol and Transfection Optimization Kit (Multi-guide) Add-On). Assembled ribonucleoprotein RNP complexes (1.3:1 sgRNA to Cas9 ratio); Opti-MEM (25 µL) was mixed gently with multi-guide sgRNA and Cas9 to 3 µM working stock concentration (1.3 µL and 1.0 µL, respectively), and Lipofectamine Cas9 Plus Reagent (1.0 µL) in a sterile microfuge tube. Allowed to incubate for 5-10 min at 25 °C. Prepared transfection solution; Opti-MEM (25 µL) was mixed with Lipofectamine CRISPRMAX reagent (1.5 µL) and allowed to incubate for 5 min at 25 °C in a sterile microfuge tube. Prepared RNP complexes-transfection solution mixture; RNP complex mixture (28.3 µL) mixed with the transfection solution (26.5 µL) directly and mixed well by

pipetting up and down for 5-10 min at 25 °C. RNP-Transfection Mixture and Cell Suspension; mixed gently in 1.2x10^5 HEK293T cells in serum-free DMEM (500 µL) with RNP-Transfection mixture (50 µL) in a microfuge tube. Transferred 255 µL into a well of a 24-well culture plate (total two wells) in a 37 °C incubator with 5% CO^2 for 2-3 days. One well was split and placed in a 10 cm^2 plate. The other well's cell pellet was harvested after two full days of growth, snap frozen in liquid N_2, and stored at -80 °C until use.

Western blot analysis of recombinant protein expression. The following antibodies were purchased for western blot studies: Anti-FLAG antibody produced in rabbit (Sigma-Aldrich) Cat# F7425; Anti-HaloTAG pAb is a rabbit polyclonal antibody raised against the HaloTAG protein (Promega, part # G928A); GFP transfection plasmid; Goat anti-mouse DyLight 650 (Thermo Fisher Scientific Cat# 84545); and Goat anti-rabbit DyLight 550 (Thermo Fisher Scientific Cat# 84541). Cell lysates were separated via ultracentrifugation at 100,000 x *g* for 45 min at 4 °C. Proteins were separated by SDS-PAGE (7.5% polyacrylamide, TGX Stain-Free Mini Gel) at 150 V for 55 min. Gel transfers were performed using the Bio-Rad Trans-Blot Turbo RTA Midi NitrocelluloseTransfer Kit with a Bio-Rad Trans-Blot Turbo Transfer System (25V, 10 min). The nitrocellulose blot was then incubated in blocking solution (30 mL, 3% BSA in TBS-T (1.5 M NaCl, 0.25 M Tris pH 7.4 in ddH_2O)) for 1 h at 25 °C with gentle shaking. The blot was then transferred immediately to primary antibody solution (1:1,000 anti-FLAG) and incubated overnight at 4 °C with gentle shaking. The blot was then rinsed 5 times for 5 min in TBS-T, transferred immediately into secondary antibody solution

(1:10,000 anti-species DyLight 550 or DyLight 650 in TBS-T), and incubated for 1 h at 25 °C with gentle shaking. The blot was then rinsed 5 times for 5 min in TBS-T, transferred into ddH_2O, and imaged by in-blot fluorescence scanning on a ChemiDoc MP Imaging System. Each lane displayed in western blots represents an individual biological replicate of that overexpression/treatment condition.

Agarose gels electrophoresis of DGKθ knockout.[48] The following sequencing primers were generated:

Sequencing Primers	Sequence
FWD	CTGGGAGGTGGAGGAGTT
REV	AATGAGGCGGGCACTTAC
FWD	GGATACACTCATTGTCCTCCAG
REV	AGCTTCCTTGAGATGCTTGT

DNA was extracted from culture and mixed with QuickExtract DNA Extraction Solution (Lucigen) for a final 200 µL volume, according to the manufacturer's instructions. Amplification reactions contained 25 µL of Q5 Hot Start High Fidelity 2x MM (NEB), 1 µL (10 pmol/µL) of each primer, 18 µL water, and 5 µL DNA. Samples were amplified in a commercial PCR thermocycler running a 30 sec 98 initial step for enzyme activation followed by 35 cycles of 5 sec at 98 for denaturation, 10 sec at 66 for annealing and 20 sec at 72 for elongation, plus a 2 min 72 final elongation step. The amplified products were separated electrophoretically on 1.0% (1g/100mL) agarose gels for 1 hr at 100Volts. A 1 kbp

ladder (NEB Plus DNA Ladder, N0550S) was used as a size standard on the first lane. Imaged on a ChemiDoc MP Imaging System. Each lane displayed in western blots represents an individual biological replicate of that mock/knockout condition.

Western blot analysis of DGKθ knockout. The following antibodies were purchased for western blot studies: Human/Mouse/Rat DGKθ Antibody, monoclonal mouse IgG_1 Clone (R&D Systems) Cat# 652308 and Goat anti-mouse DyLight 650 (Thermo Fisher Scientific) Cat# 84545. Cell lysates were separated via ultracentrifugation at 100,000 x *g* for 45 min at 4 °C. Proteins were separated by SDS-PAGE (7.5% polyacrylamide, TGX Stain-Free Mini Gel) at 150 V for 55 min. Gel transfers were performed using the Bio-Rad Trans-Blot Turbo RTA Midi NitrocelluloseTransfer Kit with a Bio-Rad Trans-Blot Turbo Transfer System (25V, 10 min). The nitrocellulose blot was then incubated in blocking solution (30 mL, 3% BSA in TBS-T (1.5 M NaCl, 0.25 M Tris pH 7.4 in ddH_2O)) for 1 h at 25 °C with gentle shaking. The blot was then transferred immediately to the primary antibody solution (1:1,000 anti- DGKθ) and incubated overnight at 4 °C with gentle shaking. The blot was then rinsed 5 times for 5 min in TBS-T, transferred immediately into the secondary antibody solution (1:10,000 anti-species DyLight 550 or DyLight 650 in TBS-T), and incubated for 1 h at 25 °C with gentle shaking. The blot was then rinsed 5 times for 5 min in TBS-T, transferred into ddH_2O, and imaged by in-blot fluorescence scanning on a ChemiDoc MP Imaging System. Each lane displayed in western blots represents an individual biological replicate of that overexpression/treatment condition.

Lipid extraction. A modified Bligh Dyer method ($CHCl_3$:MeOH:H_2O/1:2:2; 0.1N HCl) was used to extract lipids from HEK293T cell pellets (~6.0 million cells). Antioxidant BHT (butylated hydroxy toluene) was added at 50 µg/mL during extraction. $CHCl_3$ (1 mL), and MeOH (2 mL) were added with 1.5 mL of ddH_2O containing resuspended HEK293T cells in a two-dram vial. 1N HCl (500 µL) was added last to bring the final concentration of acid to 0.1 N. Samples were vortexed, incubated on ice for 20 min, and centrifuged at 2,000 x *g* for 5 min at 4 °C. Lipid standards (10 pmol each of AA-d8 and SAG-d8) were added to organic solvents prior to mixing and lipid extraction of cells. The organic layer was transferred, and aqueous layer extracted with addition of 1.5 mL of 1:2 $CHCl_3$:MeOH solution. The extracted organic layers were combined and dried under nitrogen stream. Samples were resuspended in 240 µL of 1:1 MeOH:IPA and stored at −80 °C until further analysis.

LC-MS/MS analysis of lipid extracts. The lipid samples were analyzed by LC-MS/MS. A Dionex Ultimate 3000 RS UHPLC system was used with an analytical column (Kinetex® 1.7 µm C18 100 Å, Phenomenex, LC column 100 x 2.1 mm) and reverse phase LC solvents (C: ACN:H_2O/50:50, 10 mM NH_4HCO2, 1% formic acid; D: ACN:IPA:H_2O/10:88:2, 10 mM NH_4HCO2, 1% formic acid) with the following gradient: Flowrate 0.25 mL/min, 0 min 65% C, 4 min 40% C, 12 min 15% C, 21 min 0% C, 24 min, 0% C, 24.1 min 100% C, 27 min 0% C, 30 min 100% C, 33 min 0% C, 35 min 65% C. The eluted lipids were ionized by electrospray using a HESI-II ion source coupled to a Q-Exactive Plus Orbitrap mass spectrometer (Thermo Scientific). Data acquisition was performed using both parallel reaction monitoring

(PRM) targeted and top10 data-dependent (ddMS2) global analysis methods. Lipid identifications and peak alignments were performed using LipidSearchTM (Version 4) software while quantitative analysis of the aligned intensities was exported and analyzed using Prism GraphPad (Version 7.03). Positive and negative ion annotations of each sample were combined and aligned within a chromatographic time window to allow greater confidence in lipid identifications using appropriate MS2 product ions and neutral losses from the compiled dataset in LipidSearchTM (Version 4) analysis software. Aligned results were further filtered by retention time constraints, signal to noise ratio of diagnostic fragment ions, liquid identification confidence by ID quality, and peak quality specifications.

Sequence alignments. Lipid kinase sequences were obtained from Uniprot (https://www.uniprot.org) and the HaloTAG fusion DGKθ protein sequence was obtained from Kazusa (Kazusa, www.kazusa.or.jp). All sequences were aligned using Benchling (www.benchling.com).

General information of chemical synthesis. All chemicals used were all reagent grade and used as supplied, except where noted. ^{1}H and ^{13}C spectra were recorded on a Varian Inova 600 (600 MHz) spectrometer in $CDCl_3$ with chemical shifts referenced to internal standards ($CDCl_3$: 7.26 ppm ^{1}H, 77.16 ppm ^{13}C) unless stated otherwise. Splitting patterns are indicated as follows: s, singlet; d, doublet; t, triplet; q, quartet; m, multiplet; br, broad singlet for ^{1}H-NMR data. NMR chemical shifts (δ) are reported in ppm and coupling constants (J) are reported in Hz. All reactions were monitored by Thin-Layer Chromatography carried out on precoated Merck silica gel 60 F254 plates (0.25 mm thickness); compounds were visualized

by UV light and different stains of a TLC plate. All reactions were carried out under nitrogen or argon atmosphere with dried solvents under anhydrous conditions and yields refer to chromatographically homogenous materials unless otherwise stated. All evaporations were carried out under reduced pressure on Büchi and Heildoph rotary evaporator below 40 °C unless otherwise specified. Silica gel (200-400) mesh were used for column chromatography.

2.4 *Results*

2.4.1 *Establishing Methodology*

We first established the detection and quantification parameters of global analysis of lipids in HEK293T cells overexpressing recombinant DGKθ using a data-dependent "top ten" LC-MS acquisition method (i.e., ddMS2). This untargeted LC-MS method consists of first separating lipid species by C-18 reverse-phase liquid chromatography (RPLC) followed by mass analysis using a Q-Exactive Plus mass spectrometer. A top ten ddMS2 cycle consisted of one MS1 scan followed by ten MS2 scans.[36, 37] The 10 most abundant MS1 ions are selected for fragmentation to generate MS2 fragment ions for lipid identification.[19, 32] This approach allowed us to perform an exploratory detection of a broad range of the lipidome in HEK293T cells overexpressing recombinant DGKθ compared with that in non-overexpressing cells.[36, 37]

The MS data were processed and analyzed using LipidSearch (Version 4.0) software, which uses the fragment ions for lipid identification and the extracted ion chromatograms peak areas for quantification.[19] The chromatograms of identified and quantified lipids were used for alignment of sample sets for comparative analyses, **(Figure 2.4.2)**.[19] LipidSearch was used to search the experimental MS2 spectra against an *in silico* reference library of known theoretical compound fragmentation patterns for lipids sorted based on lipid class and the MS ionization and fragmentation modes. In this way, we identified fatty acid chains and head groups from more than 22 main lipid classes and 66 sub classes.[19]

The ddMS2 method was used to identify the structure and composition of more than 500 unique lipid species corresponding to 22 lipid classes, including: neutral glycerolipids, glycosphingolipids, ceramides, phospholipids, lysophospholipids, sterols, sphingosines, and sphingolipids. These lipids could be classified by their polarity, i.e., polar (phospholipids, sphingolipids, glycolipids, etc.) and nonpolar (triacylglycerol, cholesterol, cholesteryl ester, etc.) classes.[49] We focused our attention on lipids that serve as intermediates in metabolism.[49, 50] Examples of lipid metabolite precursors include phospholipids, sphingolipids, glycolipids, glycerophospholipids, cholesterols, steroid, triacylglycerols, fatty acids, bile acids, eicosanoids, and ketone bodies.[50] Although LipidSearch performed the bulk of the work in detecting and quantifying all lipids, we verified that the software was correctly associating the MS2 spectra with the correct corresponding MS1 peak and therefore the precursor *m/z*. Many lipids with similar *m/z* values co-eluted, which complicates the spectra and results in incorrect assignments by the software algorithm and requires manual verification.[51] To increase efficiency of verification, we applied new software approaches, such as using RStudio, to reduce the time required to verify the chemical structures.[52]

2.4.2 *Assessment of Lipid Coverage for DGKθ and DGKη*

We next assessed lipids detected in HEK293T cell line that overexpressed each of the two DGKs, DGKθ and DGKη. We included DGKη in our studies to determine isoform specificity in our findings. DGKθ's major distinguishing feature from DGKη is that it has three C1 domains, unlike DGKη that contains two C1

domains.[53] In addition, they are classified into different subtypes, DGKθ - Type V and DGKη - Type II.[26, 54] If overexpression of each DGK yields a unique lipidomic profile, we can hypothesize that DGKθ displays isoform-specific metabolic functions compared with DGKη. By comparing these two DGKs, we should be able to determine whether lipidomics results are isoform specific for each of the DGK isozyme.

We analyzed the samples in positive and negative ion MS modes with three biological replicates and two analytical technical replicates for each of the mock and DGK overexpressed samples. All statistical comparisons were performed using Graphpad Prism's statistical software with one unpaired t-test. For DGKθ samples, we analyzed 13 mock and 15 DGKθ overexpressed samples in the positive ion mode and 14 mock and 18 DGKθ overexpressed samples in the negative ion mode. For DGKη, we analyzed 13 mock and 18 DGKη overexpressed in positive ion mode and 14 mock and 14 DGKη overexpressed samples in negative ion mode. All rows were sampled from populations with the same standard deviation scatter. Lipids were retain to have an abundance fold change < 2 (mock/overexpressed) and a p-value of < 0.05 **(Figure 2.4.3)**.[55] We observed that fold change does not correlate with the magnitude of the lipid chromatographic peak areas. We identified a total of 428 and 380 unique lipids form DGKθ- and DGKη- overexpressed samples, respectively, and 450 lipids from the control (mock) samples.

Next, we categorized the identified lipids into respective classes **(Figure 2.4.1)**. For example, lipids that contain a ceramide moiety were grouped under the

ceramide column, and ceramide lipid abundances from DGKθ and DGKη samples were significant in that they stood out on **(Figure 2.4.1)**. For instance, **(Figure 2.4.1)** in shows that DGKθ samples had 15 additional ceramide lipids compared with DGKη samples. This may suggest that DGKθ metabolic pathways are affecting mechanism of action related to ceramide, which may suggest that it is influencing the levels of ceramides (Cer), triglycerides (TG), lysophosphatidylcholines (LPC), phosphatidylcholines (PC), lysophosphatidylethanolamines (LPE), phosphatidylethanolamines (PE), and phosphatidylinositols (PI); while the levels for DGKη's lipid classes were overall lower. The results indicate that the DGKθ and DGKη isozymes are regulating different metabolic pathways. We have not yet compared lipid profiles of the other eight isozymes using these LC-MS/MS parameters to determine if any of the other eight isozymes have lipid profiles similar to that of DGKθ.

2.4.3 *Manual Spectral Signal Identification*

We then performed a manual spectral signal identification that corresponded to a lipid class for the raw files associated with DGKθ activity. Spectral signals identified correspond to PC and LPC. The same approach was conducted for PE, PA, PS, PI, etc. Lipids were detected as $[M+H]^+$, $[M+NH_4]^+$, and $[M+HCOO]^+$ molecular ions in positive ion mode and $[M+H]^-$ and $[M+NH_4]^-$ in negative ion mode. $[M+Na]^+$, $[M+K]^+$, and $[M+Cl]^-$ ions were not detected because sodium, potassium and chloride salts were not used in the HPLC solvents. In the positive ion mode, LPCs were observed as adducts of H^+ and NH_4^+. We did not observe PCs in the positive

mode. In the negative ion mode, most PCs and LPCs were observed, only as the formate ($HCOO^-$) adduct ion.

2.4.4 *Analysis of Phosphatidylcholine (PC) by CID MS/MS*

Phosphate-related ions were not observed in the mass spectra of PCs, for example, *m/z* 152.9958 (glycerol-3-phosphate ion with loss of H_2O), *m/z* 96.9696 (H_2PO_4-ion from phosphate), *m/z* 78.9591 (PO_3-ion from phosphate) were not observed. A possible reason for this lack of observance is due to the mobile phase solvents used and the scan parameters. In addition, $[M-H]^-$ ions were not observed due to 'fixed positive charge' quaternary alkyl ammonium group within the phosphocholine head group.[56, 57] In addition, *m/z* 168.0431 (phosphocholine with a loss of CH_3) and *m/z* 224.0693 (glycerophosphocholine with a loss of CH_3 and H_2O) were not observed, **(Figure 2.4.5)** and **(Figure 2.4.6)**.

In the positive ion mode, PC fragment ions were inconsistently detected. A probable cause for no detection may be due to mobile phase conditions, such as pH. It has been reported that protonated molecular species are readily formed if the conditions are acidic and modifiers (like ammonium salt) have been added in the mobile phase.[58] We did add ammonium salts as a modifier in our lipid solution; however, we did not see a noticeable increased and/or improved separation of lipid species.[59]

2.4.5 *Analysis of LPC by CID MS/MS*

There was one LPC species that was identified in the negative mode here: LPC(C16:0). Some fragment ions were not observed in the spectral scans for LPC(C16:0); for instance, *m/z* 78.9591 (PO_3- ion from phosphate), *m/z* 96.9696 ($H2PO_4$- ion from phosphate), *m/z* 168.0431 (phosphocholine with loss of CH_3), *m/z* 409.2361 (loss of choline from precursor ion), and *m/z* 495.3330 (precursor ion $[M+]^-$). LPC(C16:0) had three fragment ions; *m/z* 480.3091 ($[M\text{-}CH_3]^-$ ion), *m/z* 255.2329 (sn-1 $RCOO^-$ ion), and *m/z* 224.0689 (neutral loss of sn-1 RCOOH group, loss of CH_3 from the precursor ion) were identified by LipidSearch data-base. On MS/MS spectra inspection, two fragment ions were identified, *m/z* 480.3091 ($[M\text{-}CH_3]^-$ ion) and *m/z* 255.2329 (sn-1 $RCOO^-$ ion). There were two fragment ions identified in the positive mode, *m/z* 496.3400 and *m/z* 184.0734.

2.4.6 *Identifying and Validating all Lipid Substrates*

We set out to determine whether overexpressing DGKθ in HEK293T cells would increase the levels of select lipid substrates. When organizing these lipid substrates, a pattern emerged that implicated the involvement of DGKθ in the Kennedy pathway and the Lands cycle.[3, 18, 21-23]

We organized all the lipid substrates by acyl chain lengths along with their degree of unsaturation composition and compiled 148 unique compositions. We selected the top 12 acyl chains and sorted them based on their degree of unsaturation and then counted how many lipid substrates had a similar composition **(Table 2.4.1)**. We identified 1-palmitoyl, 2-oleoyl (designated

C16:0/C18:1) in six lipid substrates; PI, DAG, PA, PE, PC, and MePC, for which increased levels were measured in DGKθ overexpressing cells. At first glance, PI, DAG, and PA are lipid substrates associated with the PI cycle. However, further investigation suggests that these five lipids are not participating in the PI cycle fully but rather they are participating in the Kennedy pathway (*de novo* pathway) and in the Lands cycle (remodeling pathway) **(Figure 2.2.1)**. DGKθ may be acting as a repressor, causing the PA to be converted into DAG; however, we have not been able to conclusively show this with the current results. To complicate matters, increased PA levels activate PIP5K, which in turn causes PIP_2 to activate PLD, converting PC to PA, which creates a positive-feedback loop.[60] It is possible that DGKθ may have a unique binding site, which may directly or indirectly be used to convert PA to DAG. Further studies are required to support a unique binding site. It has been reported that the C1 domains of DGKs are known to bind phorbol esters and DAG.[14, 61, 62] However, the C1 domain of DGKθ does not bind DAG, and the catalytic domain of DGKθ.[14, 63] Our proposed mechanism from the Kennedy pathway into the Lands cycle still requires elucidation to make the connection with DGKθ's metabolic pathway.

The Lands cycle provides a route for acyl remodeling to modify fatty acid composition of phospholipids derived from the Kennedy pathway.[40] We observed elevated levels of many different lysophospholipids, which suggests that the Lands cycle is converting lysophospholipids to phospholipids. How exactly the enzymatic activity occurs with the overexpression of DGKθ is still unknown. We investigated

many different acyl chains along with their degrees of unsaturation associated with lysophospholipids; LPC, LPE, LPI, LPS, LPG, and LPA, respectively **(Table 2.4.2)**.

LPC and LPE had the greatest number of acyl chains lengths and degrees of unsaturation, 13 for LPC and 12 for LPE. It has been reported that PC is the major phospholipid component in a cell. Both the quantity of PC and the fatty acyl chain composition of PC are important regulators of lipid metabolism.[18, 64] Thus, LPC and LPE levels may be ubiquitous to all metabolic pathways in cells. The production of these phospholipids and lysophospholipids is by Phospholipase A_2 (PLA_2) and Lysophosphatidylcholine acyltransferases (LPCAT). PLA_2 is a family of enzymes that produce free fatty acids and lysophospholipids. PLA_2 belongs to a superfamily that has more than 30 known enzymes in mammals, each with their own biological function that is unique.[38] Of interest to us is ACSVL3, which has an acyl-CoA selectivity of C16:0/C18:1. ACSVL3 may play a role in our proposed mechanism with DGKθ.[65, 66] The PLA_2 activity leads to subsequent re-acylation processes mediated by Lysophosphatidylcholine acyltransferases (LPCAT).[40] Among the phospholipid remodeling enzymes, LPCAT3 (also known as MBOA5) fits into our proposed mechanism. It has been shown that LPCAT3 is associated with very low density lipoprotein (VLDL) particles as they bud from the ER and move to the Golgi.[18] It is possible that LPCAT3 modifies the palmitoyl and oleoyl-PC composition.

2.4.7 *Identifying and Validating DGKθ Knockout (KO) Cells*

We attempted to establish a DGKθ knockout HEK293T cell line using CRISPR/Cas9. As a genetic disruption control, a DGKθ KO cell line would assist in identifying lipids associated with DGKθ metabolomics. Goldschmidt et al. identified important cellular functions for DGKθ using knockout DGKθ mice.[43] By knocking out the DGKθ gene, we could identify endogenous lipid species level changes associated with DGKθ. We incorporated CRISPR/Cas9 technology because it allows us the flexibility to modify locus sites in our DGKθ gene.[44, 67]

In our preliminary attempts to KO DGKθ, we were able to disrupt the function of DGKθ **(Figure 2.4.8B).** However, subsequent cell line iterations showed the function of DGKθ returning. We have not achieved a full knockout of the endogenous DGKθ gene in live HEK293T cells using CRISPR/Cas9 technology. A technical problem may deal with a rich DC content near the specific site that we want to KO. The gene of interest that we wanted to KO is surrounded by cytosine (C) and guanine (G) rich regions, which results in lower cleavage efficiency when using CRISPR/Cas9 technology.[68-70] We considered other possible KO genes for DGKθ, which might allow us to identify novel lipid substrates/products for this lipid kinase using LC-MS/MS; however, these sites were also difficult due to the cytosine and guanine levels.

2.4.8 *Identifying and Validating Recombinant HaloTAG-DGKθ*

We have shown progress in our novel approach using CRISPR/Cas9 technology in tandem with HaloTAG technology. Our initial data show that we

successfully transfected the HaloTAG DGKθ protein of interest (POI) in HEK293T cells; however, our subsequent data did not yield similar results. We synthesized a HaloTAG ligand (adamantanyl), which was shown to have bonded irreversibly to the HaloTAG DGKθ fusion protein with specificity. We observed that the half-maximum inhibitory concentration of our ligand (RCM-1-61), was 20 μM.[42] And, our time trials achieved full inhibition by 48 hrs, **(Figure 2.4.9)**. However, we were not able to repeat knockdown of the HaloTAG DGKθ POI. The DGKθ-HaloTAG plasmid was sequenced to verify that there was no degradation of the plasmid vector **(Figure 2.4.7)**. In addition, we verified the synthesis of the HaloTAG ligand of interest, 2-((3r,5r,7r)-Adamantan-1-yl)-N-(2-(2-((6-chlorohexyl)oxy)ethoxy)ethyl)acetamide (**6**). ^{1}H-NMR and ^{13}C-NMR were performed to verify the compound identities Our preliminary time-course experiments, although promising, will need to be replicated. We performed additional concentration and time trials **(Figure 2.4.10)**; however, they were unsuccessful. The length of time required to degrade the HaloTAG protein (DGKθ) may not be due to the knockdown of the HaloTAG ligand, but instead maybe due to cell viability. A future goal is to measure cell viability and the efficacy of our HaloTAG ligand in HEK293T. We would aim to use a WST-1 assay, which is an efficient test to investigate cellular viability.[71] It is a fundamental technique for the assessment of biological reaction of cells when exposing them to stimulus like the HaloTAG ligand.[71] In addition, we would assess cell viability on U-87MG cell line and compare these results with HEK293T and see if there are differences in viability. [72, 73]

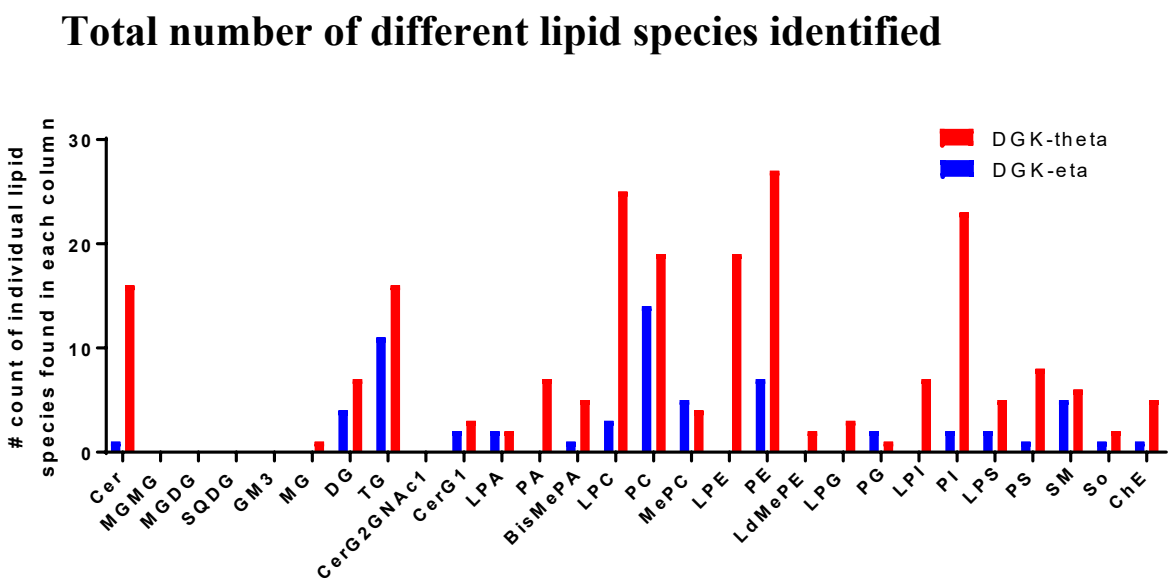

Figure 2.4.1 Total number of lipid species found in all samples. Total number of lipid classes identified in each sample is annotated in the y-axis. LipidSearch platform generated chromatographic peak areas to produce bar graph. nomenclature list 1: This list shows the abbreviations of key lipid class nomenclature used in this report.

Cer = Ceramides
MGMG = monoglactosylmonacylglycerol
MGDG = monoglactosyldiacylglycerol
SQDG = sulfoquinovosyldiaacylcerol
GM3 = Glycosphingolipids
MG = monoglyceride
DG = diglyceride
TG = triglyceride
CerG2GNAc1 = simple Glc serines
CerG1 =
LPA = lysophosphatidic acid
PA = phosphatidic acid
BisMePA = bis-methyl phosphatidic acid
LPC = lysophosphatidylcholine
PC = phosphatidylcholine
MePC = methyl phosphatidylcholine
LPE = lysophosphatidylethanolamine
PE = phosphatidylethanolamine
LdMePE = lysodimethylphosphatidylethanolamine
LPG = lysophosphatidylglycerol
PG = phosphatidylglycerol
LPI = lysophosphatidylinositol
PI = phosphatidylinositol
LPS = lysophosphatidylserine
PS = phosphatidylserine
SM = sphingomyelin
So = sphingosine
ChE = cholesterol ester

(Levels that Increased) acyl chain length and degrees of unsaturation	# of different lipid substrates
(16:0)	9
(18:1)	7
(16:0/18:1)	6
(18:0)	6
(16:1)	5
(20:3)	5
(20:4)	5
(22:6)	5
(18:0/16:0)	4
(18:0/18:1)	3
(18:0/18:2)	3
(18:0/20:4)	3

Table 2.4.1 DGKθ acyl chain length. A list of lipids (acyl chain length:degree of unsaturation) were measured to increase in abundance with DGKθ overexpression and the corresponding number of different substrates. Minor FAs were omitted. The levels on the table represent levels that increased. Levels that decreased were not included.

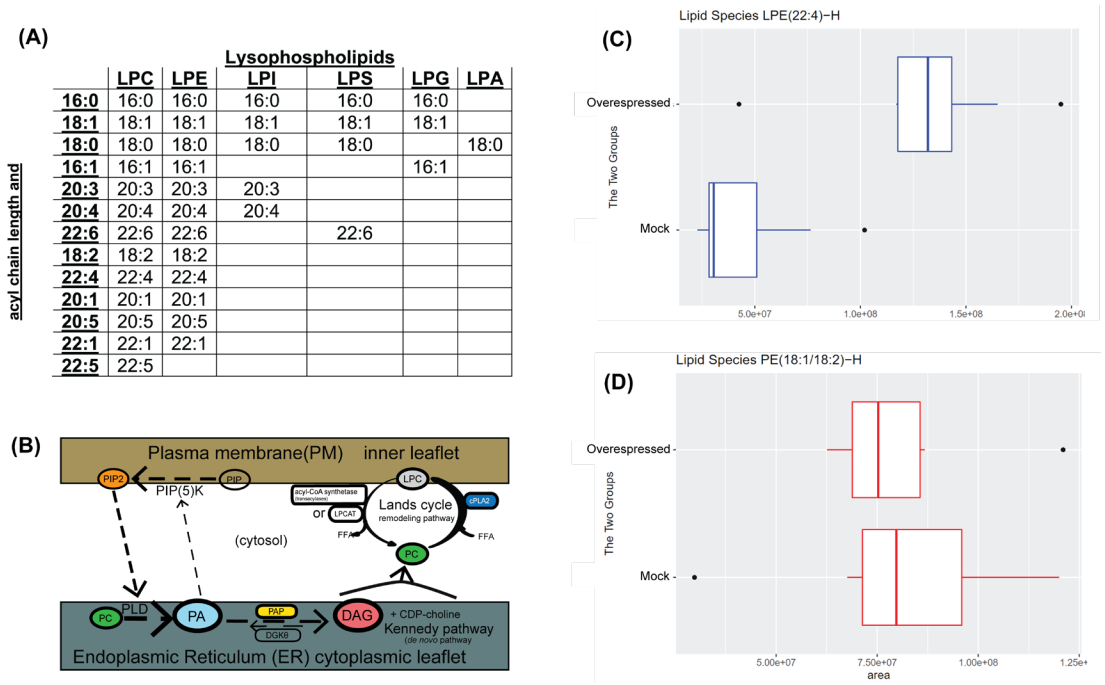

Table 2.4.2 Lysophospholipids species. (A) identification of upregulated (LPC, LPE, LPS, LPI, LPG, and LPA). (B) The data suggest that palmitoyl, stearoyl, oleoyl, arachidonoyl, and docosahexanoyl were observed. LPC and LPE had a total of 13 and 12 unique fatty acyl chains designated to these two LysoPLs. These studies provided key insights into molecular lipid composition at the level of fatty acyl chain length and unsaturation, using tandem LC-MS/MS techniques. We discover a putative role for this DGK isoform in the Lands cycle. (C) is a representation of LPE(22:4)-H as shown in (A). LPE(22:4)-H were retain to have an abundance fold change < 2 (mock/overexpressed) and a p-value of < 0.05. (D) is a representtion of a lipid species that does not retain to have an abundance fold change < 2 (mock/overexpressed) and a p-value of < 0.05; hence it failed to be included in the table in (A). Plots were created using RStudio software with R package “ggplot2 and ”ggrepel.”

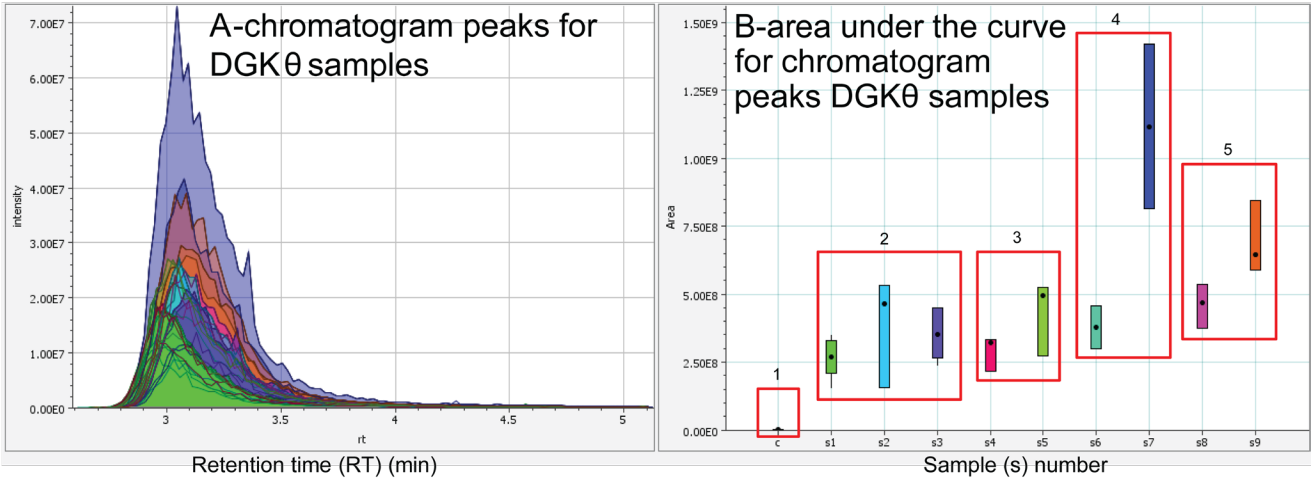

Figure 2.4.2 chromatogram peaks. Positive ion LC-MS data for PC(17:0/17:0) and PE(17:0/17:0), (negative mode was not included). (A) extracted ion chromatograms for DGKθ samples, intensity (no units) vs. retention time (min). (B) shows area under the curve for chromatogram peaks in part (A), Area vs. samples. Samples are marked (1), internal standard (c, control); (2), three mock samples for each of the duplicate DGKθ samples (s1, s2, and s3); (3), DGKθ samples for trial 1 (s4 and s5); (4), DGKθ samples for trial 2 (s6 and s7); and (5) DGKθ samples for trial 3 (s8 and s9). LipidSearch software was used to generate both figures.

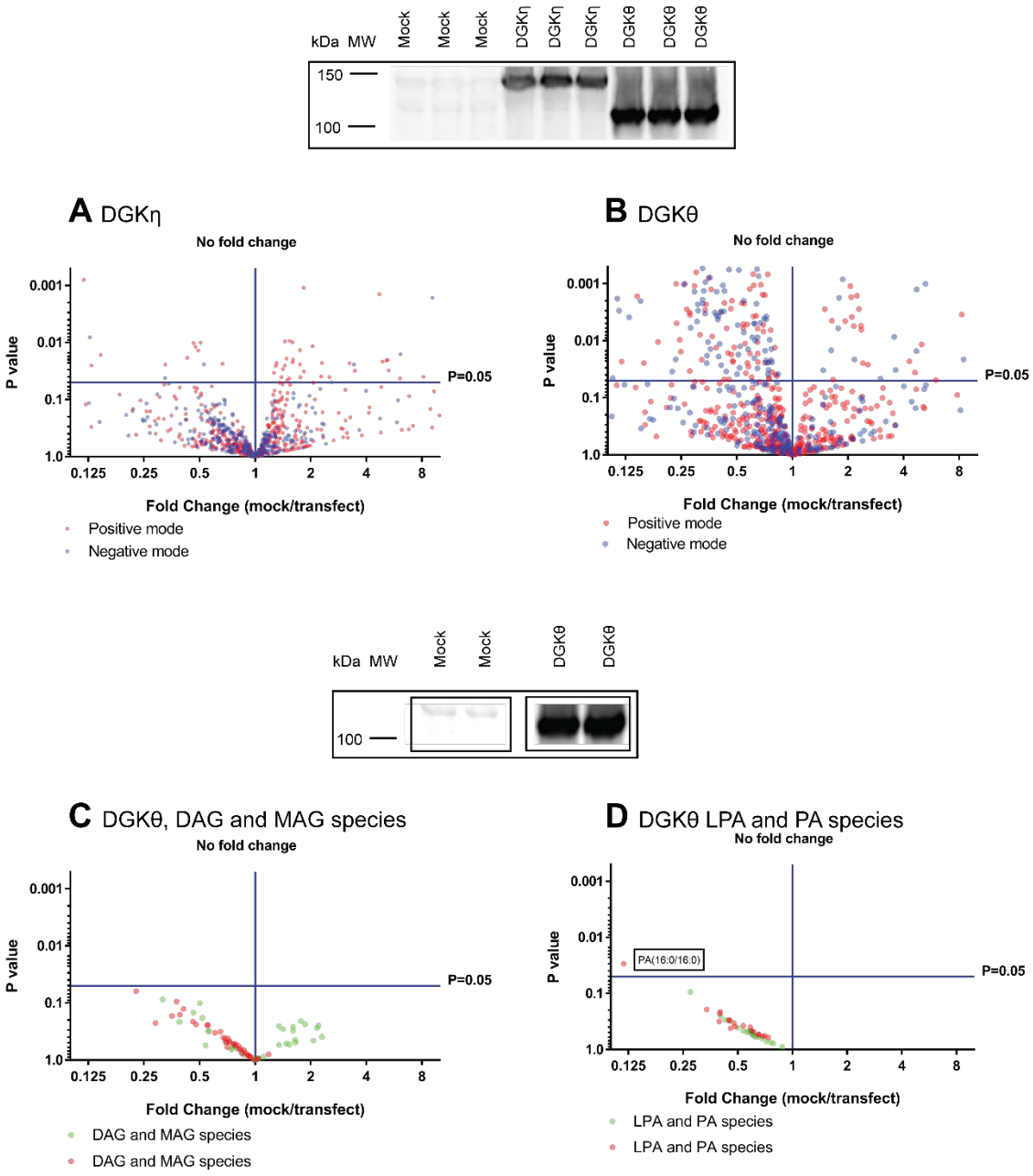

Figure 2.4.3 Volcano plots for DGKη and DGKθ. Two DGKη and DGKθ expression on Western Blot membrane. (A) and (B) Volcano Plots for DGKη and DGKθ. (C) Volcano Plot for DGKθ's DAG and MAG species. (D) Volcano Plot for DGKθ's LPA and PA species. Red dots are positive ion mode and blue/green dots

are negative ion mode. Volcano plot show lipid species that are significant with a fold change of less than 2 (mock/transfect) and a p-value of <0.05.

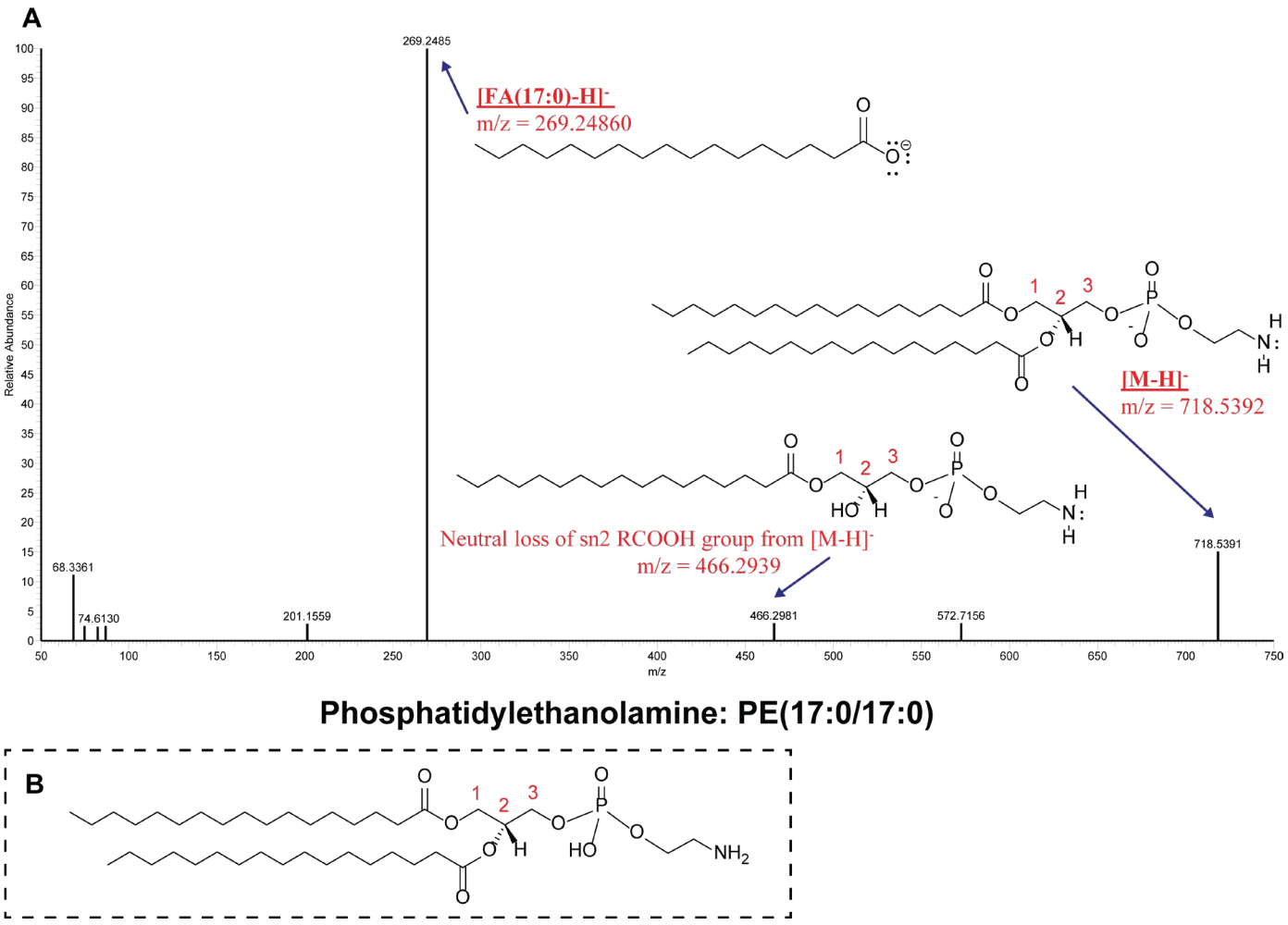

Figure 2.4.5 Negative ion ESI mass spectra for phosphatidylethanolamine PC(17:0/17:0). (A) MS/MS spectra, precursor and fragment ions labeled respectively with their (B) chemical formula.

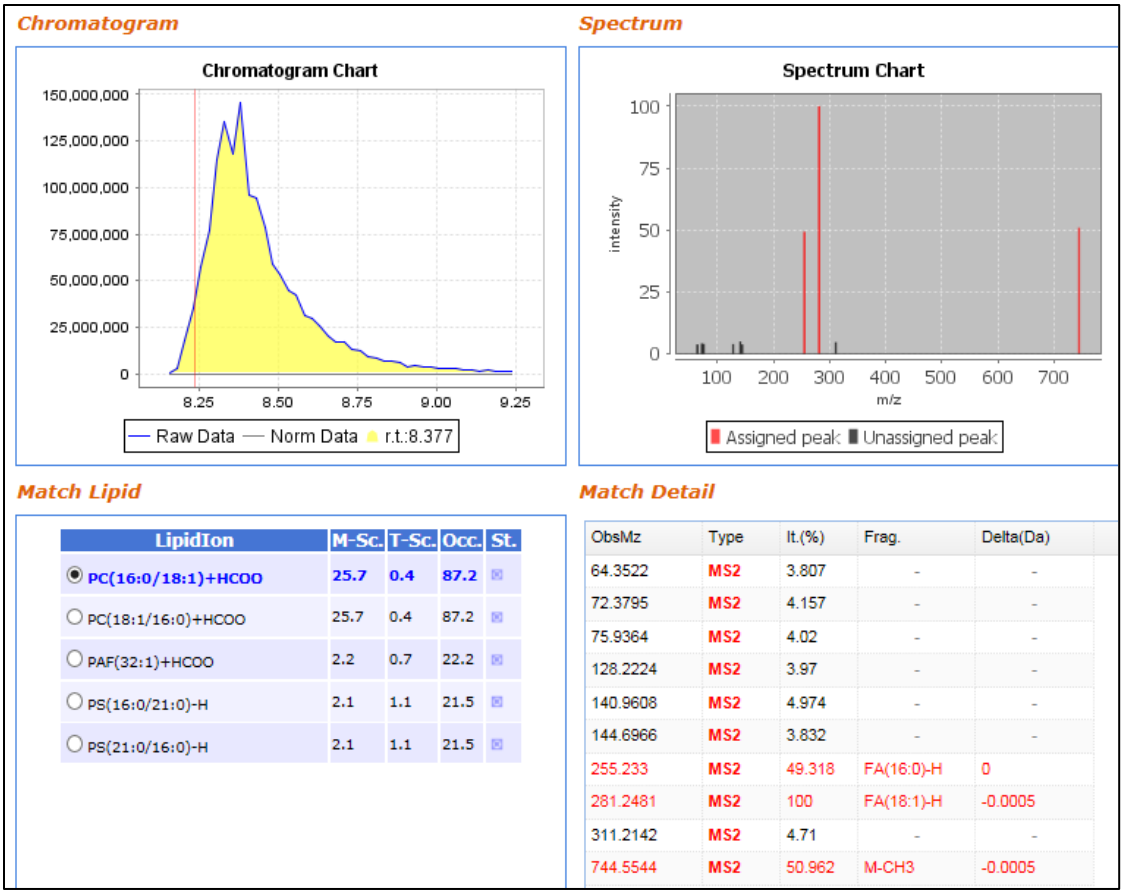

Figure 2.4.6 Negative ion ESI mass spectra for phosphatidylcholine PC(16:0/18:1). Figure provides a chromatogram, spectrum chart, lipid fragmentation ion details; Top left, chromatogram chart of PC(16:0/18:1) with a retention time 8.377 min. Top right, shows spectrum chart with highest intensity peaks at *m/z* 255 and *m/z* 281. Bottom left and right show details on lipid ion identification matches. LipidSearch software was used to generate figures, which integrates MS1 peak areas and proceeds to interpret the MS2 fragment ions for lipid ion identification based on an internal database.[19]

```
########################################
#
# Aligned_sequences: 2
# 1: GENEwiz
# 2: Promega
# Matrix: EBLOSUM62
# Gap_penalty: 10.0
# Extend_penalty: 0.5
#
# Length: 277
# Identity:     277/277 (100.0%)
# Similarity:   277/277 (100.0%)
# Gaps:           0/277 ( 0.0%)
# Score: 1507.0
#
#
########################################

GENEwiz             1 MHYVDVGPRDGTPVLFLHGNPTSSYVWRNIIPHVAPTHRCIAPDLIGMGK     50
                      ||||||||||||||||||||||||||||||||||||||||||||||||||
Promega            22 MHYVDVGPRDGTPVLFLHGNPTSSYVWRNIIPHVAPTHRCIAPDLIGMGK |   71

GENEwiz            51 SDKPDLGYFFDDHVRFMDAFIEALGLEEVVLVIHDWGSALGFHWAKRNPE    100
                      ||||||||||||||||||||||||||||||||||||||||||||||||||||
Promega            72 SDKPDLGYFFDDHVRFMDAFIEALGLEEVVLVIHDWGSALGFHWAKRNPE    121

GENEwiz           101 RVKGIAFMEFIRPIPTWDEWPEFARETFQAFRTTDVGRKLIIDQNVFIEG    150
                      ||||||||||||||||||||||||||||||||||||||||||||||||||||
Promega           122 RVKGIAFMEFIRPIPTWDEWPEFARETFQAFRTTDVGRKLIIDQNVFIEG    171

GENEwiz           151 TLPMGVVRPLTEVEMDHYREPFLNPVDREPLWRFPNELPIAGEPANIVAL    200
                      ||||||||||||||||||||||||||||||||||||||||||||||||||||
Promega           172 TLPMGVVRPLTEVEMDHYREPFLNPVDREPLWRFPNELPIAGEPANIVAL    221

GENEwiz           201 VEEYMDWLHQSPVPKLLFWGTPGVLIPPAEAARLAKSLPNCKAVDIGPGL    250
                      ||||||||||||||||||||||||||||||||||||||||||||||||||||
Promega           222 VEEYMDWLHQSPVPKLLFWGTPGVLIPPAEAARLAKSLPNCKAVDIGPGL    271

GENEwiz           251 NLLQEDNPDLIGSEIARWLSTLEISGE    277
                      ||||||||||||||||||||||||||||
Promega           272 NLLQEDNPDLIGSEIARWLSTLEISGE    298
```

Figure 2.4.7 Sequence Alignment. DGKθ plasmid sequence to verify transfection of plasmid.. – EMBOSS Water (https://www.ebi.ac.uk/Tools/psa/emboss_water/).

Inclusion list for precursor ion species, with their acyl chain length along with their degrees of unsaturation.	
TAG, DAG, MAG, PC, PE, PI, PS, PG, PA	**LPC, LPE, LPI, LPS, LPG, LPA**
(16:0/18:1)	16:0
(18:0/16:0)	16:1 16:2
(18:0/18:1)	18:0
(18:0/18:2)	18:1
(18:0/20:4)	18:2
	20:1
	20:3
	20:4
	20:5
	22:1
	22:4
	22:5
	22:6

Table 2.4.3 Inclusion list for precursor ion species. The inclusion list has four ion species of interest: DAG, PA, PC, and PE. In addition, there are six lysophopholipids (lysoPL) of interest; LPC, LPE, LPS, LPI, LPG, and LPA. The data suggests that palmitoyl, stearoyl, oleoyl, arachidonoyl, and docosahexanoyl were seen more than three times in the different LysoPLs species.

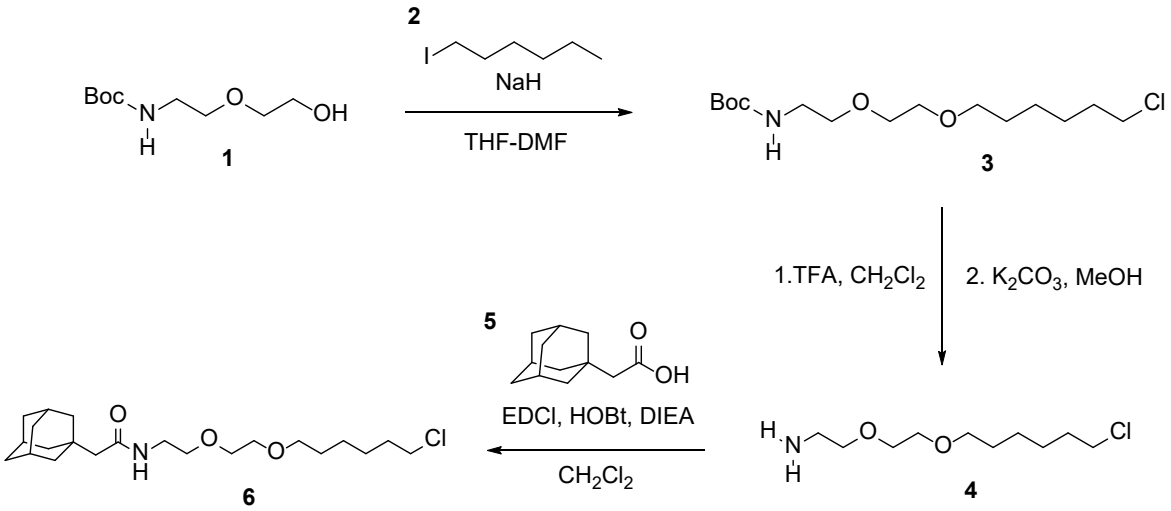

Scheme 2.4.1 Synthesis of 2-((3r,5r,7r)-Adamantan-1-yl)-N-(2-(2-((6-chlorohexyl)oxy)ethoxy)ethyl)acetamide (6)

Synthesis of 2-((3r,5r,7r)-Adamantan-1-yl)-N-(2-(2-((6-chlorohexyl)oxy)ethoxy)ethyl)acetamide (6):

tert-Butyl (2-(2-((6-chlorohexyl)oxy)ethoxy)ethyl)carbamate (**3**):

To a solution of *tert*-butyl (2-(2-hydroxyethoxy)ethyl)carbamate **1** (Combi-Blocks 3.0 g, 14.62 mmol) in THF (60 mL) and DMF (30 mL) at 0 °C added portion wise NaH (60% dispersion in mineral oil, 943.9 mg, 19.45 mmol). After stirring at 0 °C for 0.5 h, 6-chloro-1-iodohexane **2** (Oakwood Chemicals 3.2 mL, 20.47 mmol) was added to the mixture at 0 °C. The reaction mixture was stirred at 0 °C for 20 min, at rt for 24 h, and quenched at 0 °C with saturated NH_4Cl solution in H_2O. The solvent was removed under reduced pressure, then extracted four times with ethyl acetate and the combined extracts were washed with brine, dried over $MgSO_4$, filtered, and concentrated. The residue was flashed chromatographed on silica gel to afford *tert*-butyl (2-(2-((6-chlorohexyl)oxy)ethoxy)ethyl) carbamate **3** (1.9 g,

40%). TLC (33% EtOAc in hexanes), R_f 0.34 (Ninhydrin). ^{1}H NMR (600 MHz, $CDCl_3$) δ 4.98 (brs, 1H), 3.61-3.51 (m, 8H), 3.46 (t, 2H), 3.31 (t, 2H), 1.81 1.74 (m, 2H), 1.61- 1.57 (m, 2H), 1.49-1.33 (m, 4H), 1.43 (s, 9H) ppm. ^{13}C NMR (600 MHz, $CDCl_3$) δ155.9, 79.2, 71.2, 70.3, 70.2, 70.0, 45.0, 32.5, 29.4, 28.4, 26.7, 25.4 ppm.

2-(2-((6-Chlorohexyl)oxy)ethoxy)ethanamine (**4**):

To a solution of *tert*-butyl (2-(2-((6-chlorohexyl) oxy)ethoxy)ethyl)carbamate **3** (1.54 g, 4.76 mmol) in CH_2Cl_2 (35 mL) at 0 °C were added TFA (5.8 mL). After stirring at 0 °C for 2.5 h, TFA and solvent were removed in vacuo and the residue was diluted with MeOH (30 mL). The solution was cooled to 0 °C and K_2CO_3 (1.92 g, 13.67 mmol) was added to the mixture. The mixture was stirred at the same temperature for 10 min, filtered, and evaporated. The residue was diluted with H_2O (35 mL) and the mixture was extracted five times with ethyl acetate. The combined extracts were dried over $MgSO_4$, filtered, and concentrated to give 2-(2-((6-chlorohexyl)oxy)ethoxy)ethanamine **4** (1.259g, 93%). TLC (5% CH_3OH in EtOAc), Rf 0.08 (CAM). ^{1}H NMR (600 MHz, $CDCl_3$) δ 6.47 (brs, 1H), 3.69 (t, 2H), 3.63-3.60 (m, 2H), 3.56-3.53 (m, 2H), 3.52 (t, 2H), 3.44 (t, 2H), 3.12 (t, 2H), 1.79-1.71 (m, 2H), 1.60-1.53 (m, 2H), 1.46-1.39 (m, 2H), 1.36-1.28 (m, 2H) ppm. ^{13}C NMR (600 MHz, $CDCl_3$) δ71.1, 70.1, 69.7, 45.0, 39.4, 32.4, 29.1, 26.5, 25.1 ppm.

2-((3*r*,5*r*,7*r*)-Adamantan-1-yl)-*N*-(2-(2-((6-chlorohexyl)oxy)ethoxy)ethyl)acetamide (**6**):

To a solution of 1-adamantaneacetic acid **5** (Combi-Blocks, 1.421 g, 7.315 mmol, 1.3 equiv.) and 2- (2-((6-chlorohexyl)oxy)ethoxy)ethanamine **4** (1.259 g, 5.627 mmol, 1.0 equiv.) in CH_2Cl_2 (57 mL) at rt were added HOBt (1.495 g, 7.12 mmol, 1.2 equiv.) and DIEA (3.0 µL, 3.0 equiv.). The reaction mixture was cooled to 0 °C and EDCI (1.34 g, 16.88 mmol, 3.0 equiv.) was added to the mixture. The resulting mixture was stirred at rt for 26 h and quenched at 0 °C with H_2O (20 mL). The mixture was extracted twice with ethyl acetate and the combined extracts were washed with brine, dried over $MgSO_4$, filtered, and concentrated. TLC (5% CH_3OH in CH2Cl2), Rf 0.40 (CAM). ^{1}H NMR (600 MHz, $CDCl_3$) δ 5.87 (brs, 1H), 3.61-3.60 (m, 2H), 3.57-3.54 (m, 4H), 3.53-3.52 (m, 2H), 3.47-3.43 (m, 4H), 1.96 (s, 2H), 1.92 (s, 2H), 1.80-1.75 (m, 2H), 1.70-1.58 (m, 13H), 1.48-1.43 (m, 2H), 1.40-1.35 (m, 2H) ppm. ^{13}C NMR (600 MHz, $CDCl_3$) δ171.1, 70.4, 70.4, 70.1, 51.9, 45.1, 42.8, 39.1, 36.9, 32.9, 32.7, 29.6, 28.8, 26.8, 25.6 ppm.

^{1}H-NMR ($CDCl_3$, 600 MHz) for compound 3:

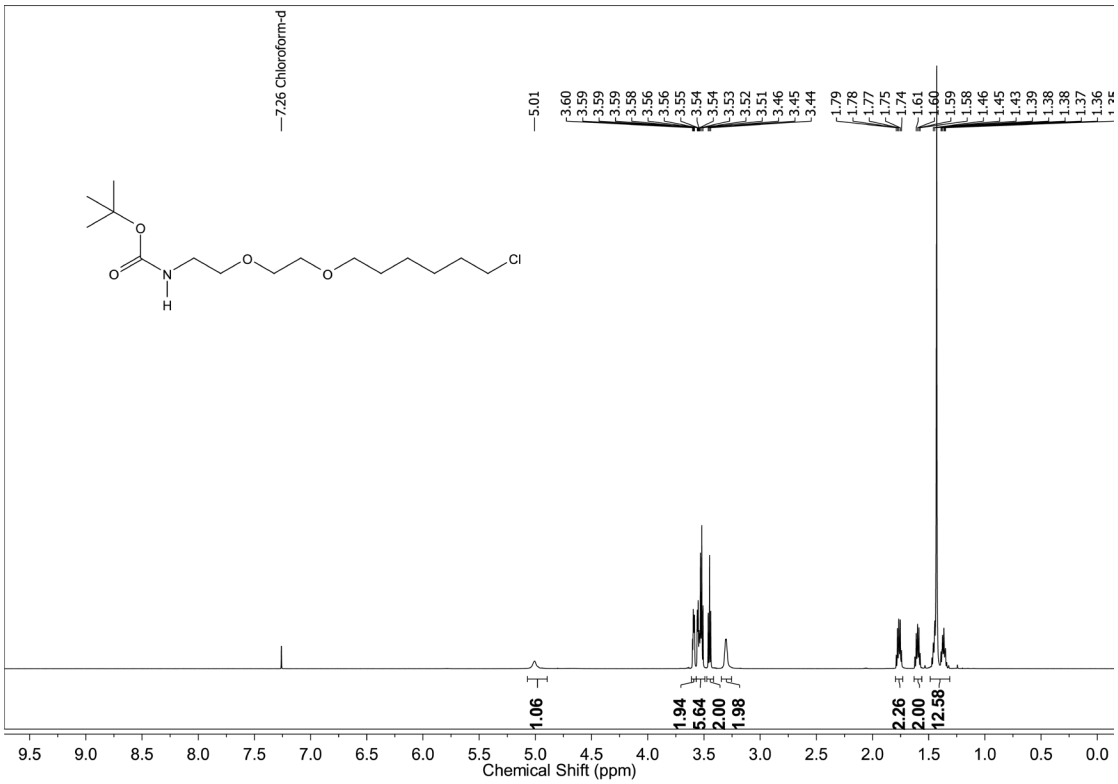

^{13}C-NMR ($CDCl_3$, 600 MHz) for compound 3:

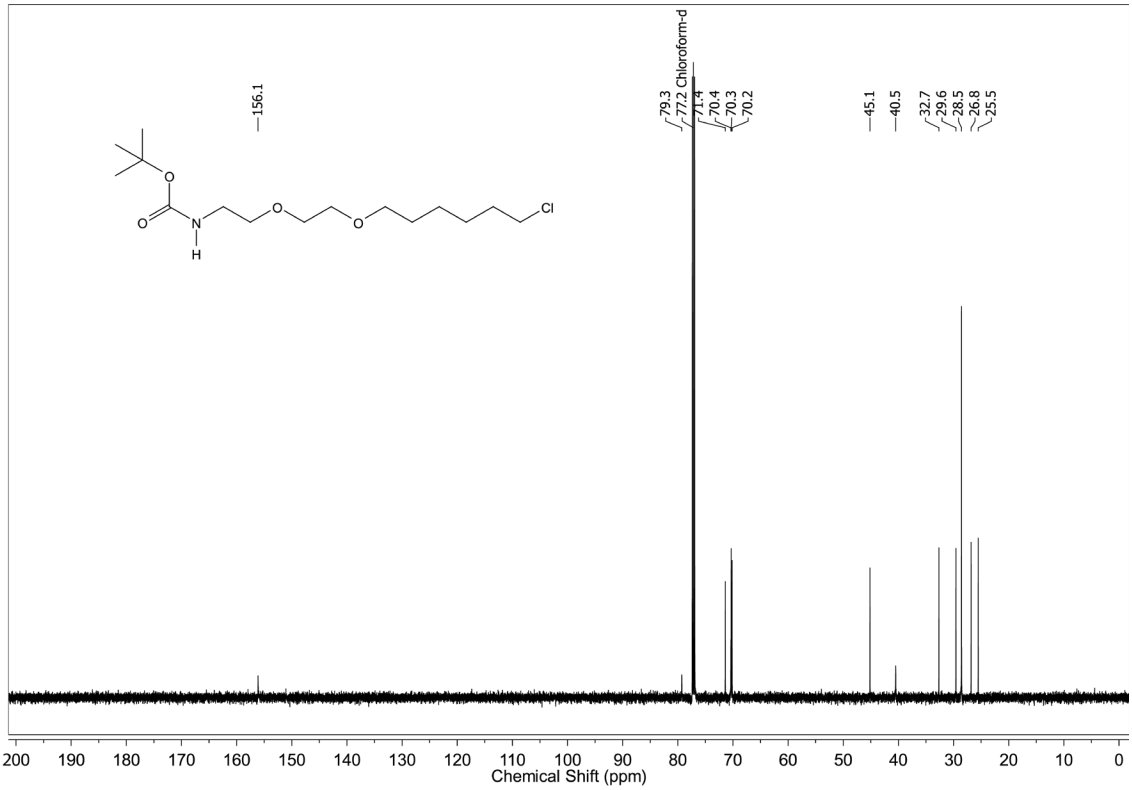

^{1}H-NMR ($CDCl_3$, 600 MHz) for compound 4:

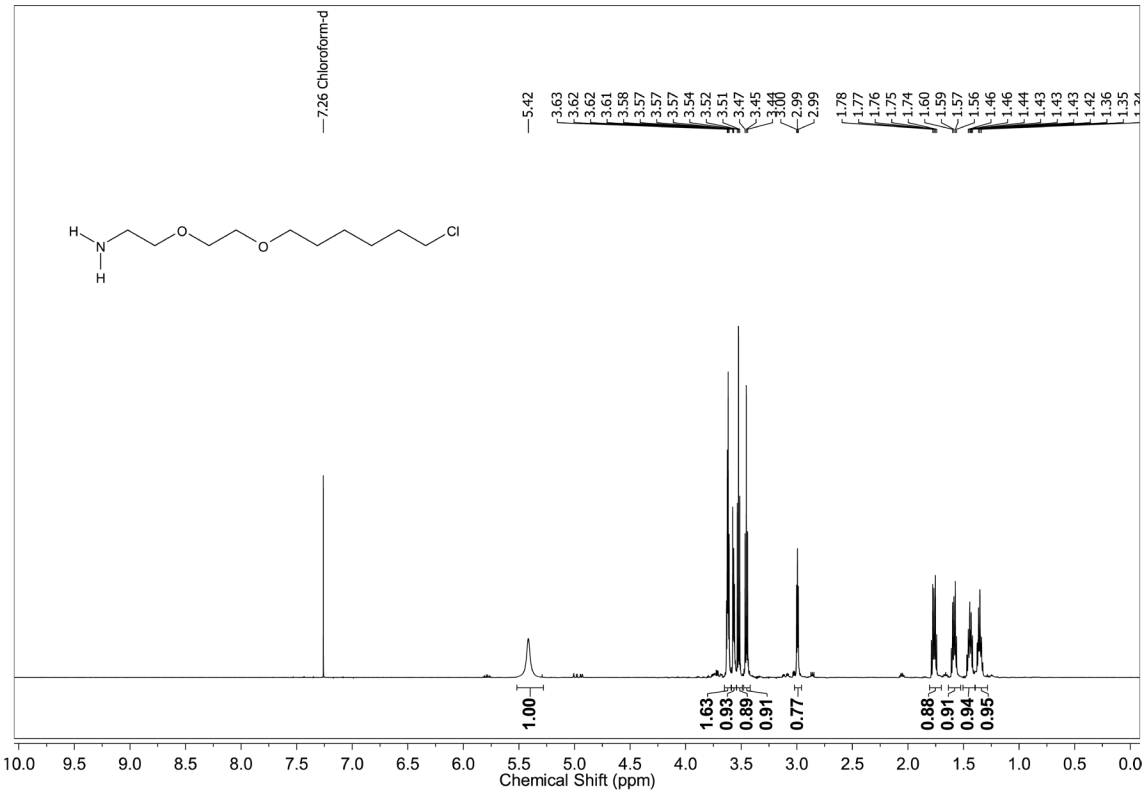

^{13}C-NMR ($CDCl_3$, 600 MHz) for compound 4:

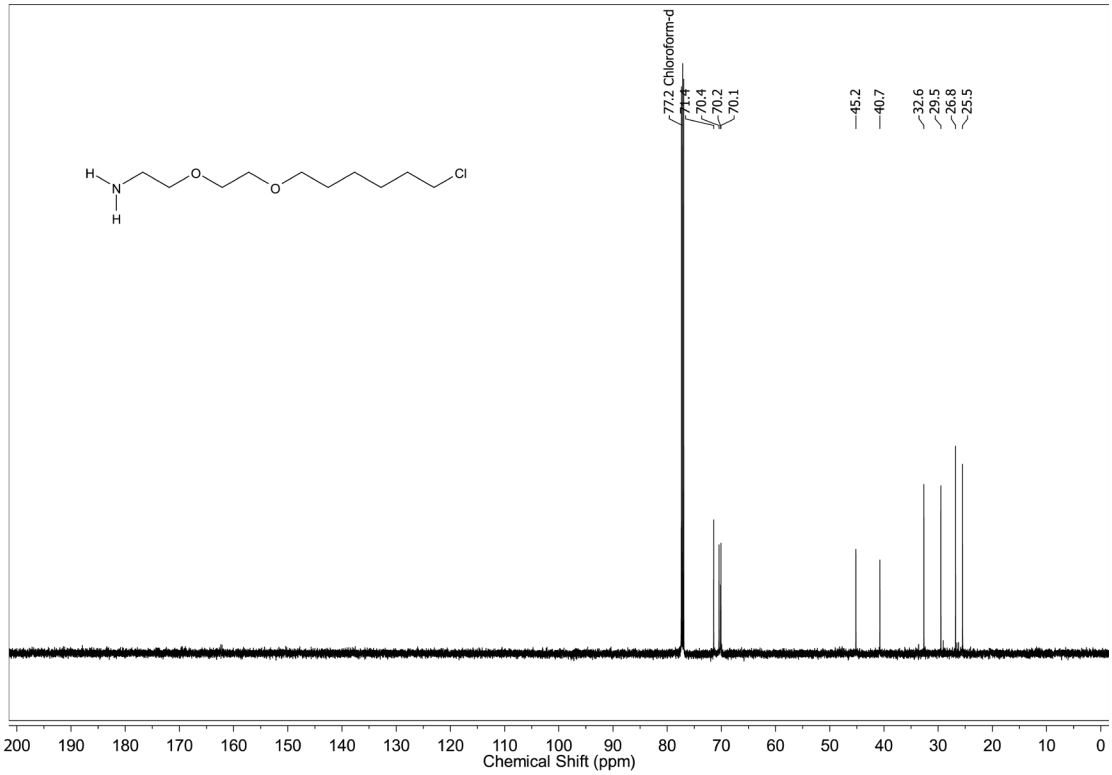

^{1}H-NMR ($CDCl_3$, 600 MHz) for compound 6:

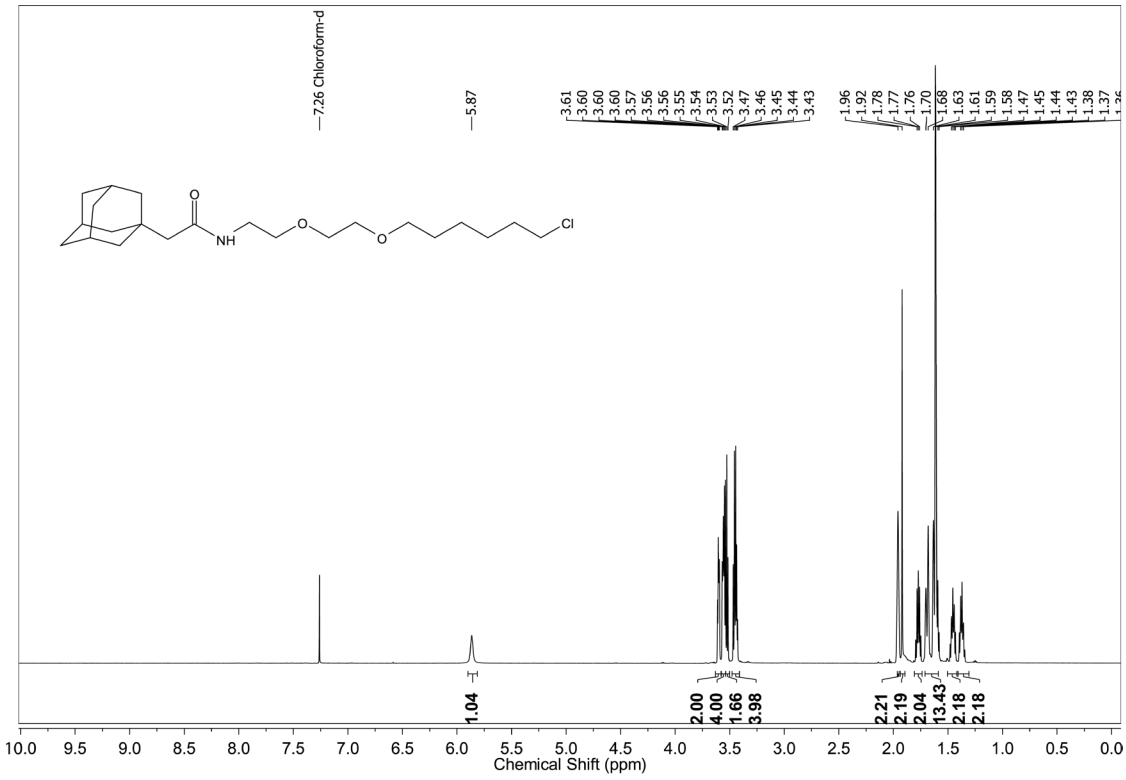

^{13}C-NMR ($CDCl_3$, 600 MHz) for compound 6:

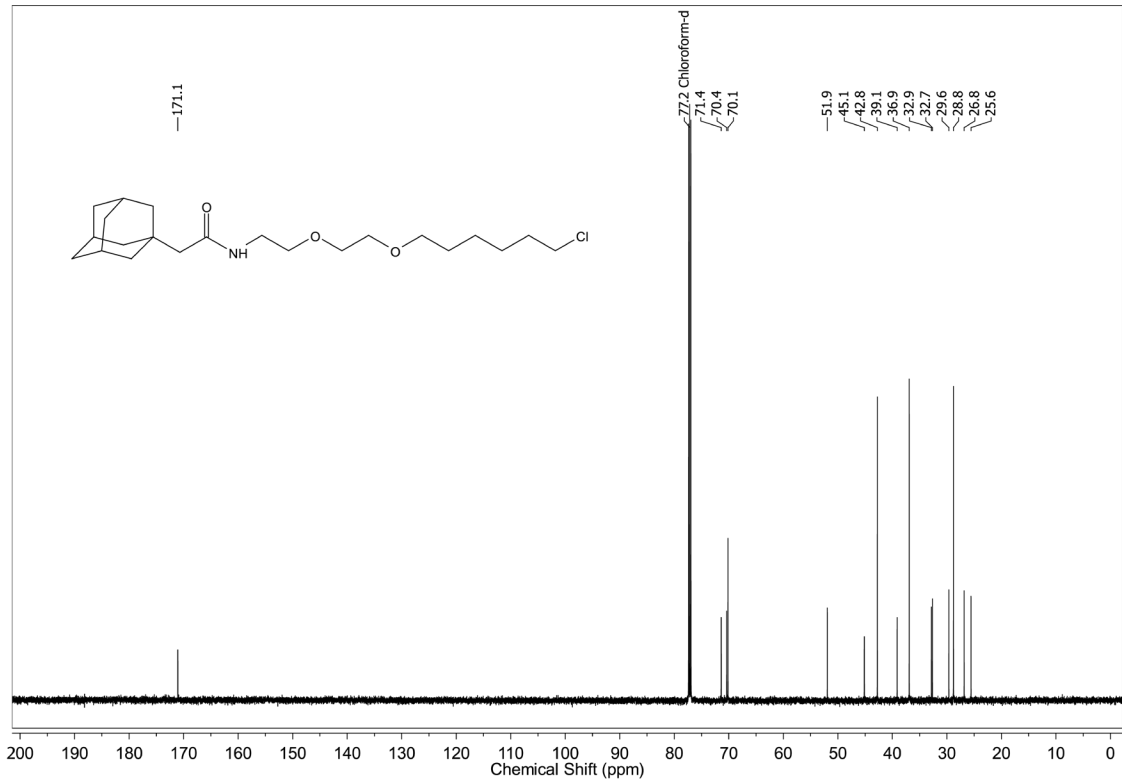

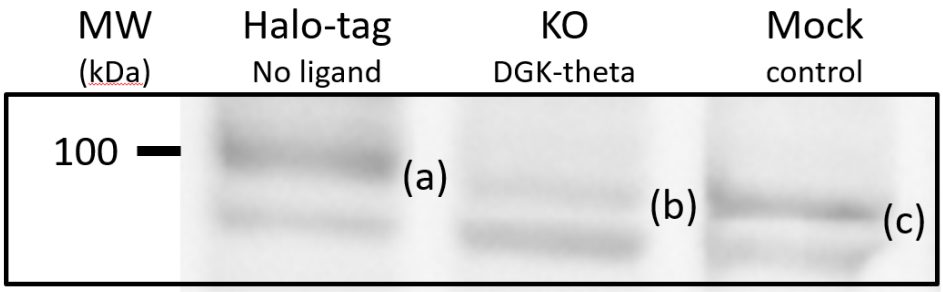

Figure 2.4.8 Western blot, soluble membrane, HEK293T cells. HaloTAG, knock out of DGKθ, and mock are displayed. (a) HaloTAG DGKθ fusion protein band, 143kDa (not shown). No adamantanyl ligand was introduced. Endogenous DGKθ band shown, 101kDa. (b) shows partial knock out of DGKθ cell line using CRISPR/Cas9, 101kDa. (c) shows mock sample with a DGKθ band, 101kDa.

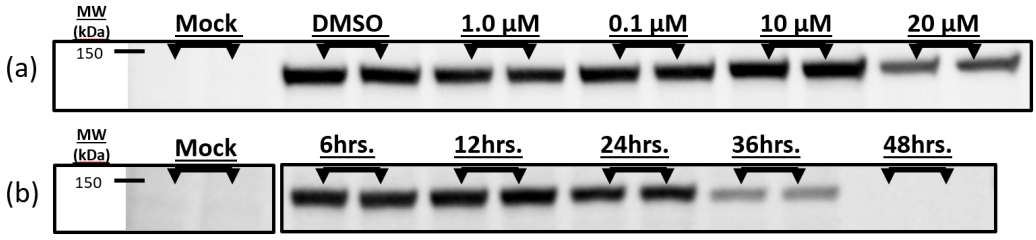

Figure 2.4.9 HaloTAG DGKθ expression on Western blot, HEK293T cells, soluble fractions. HaloTAG DGKθ expression on Western blot, HEK293T cells. (a) Overexpreession HaloTAG DGKθ concentration trails, a concentration of 20µM caused the adamantanyl ligand to degrade HaloTAG DGKθ. (b) time-course trail, exposure of the adamantanyl ligand with 48 hrs providing complete knockdown of the HaloTAG DGKθ fusion protein.

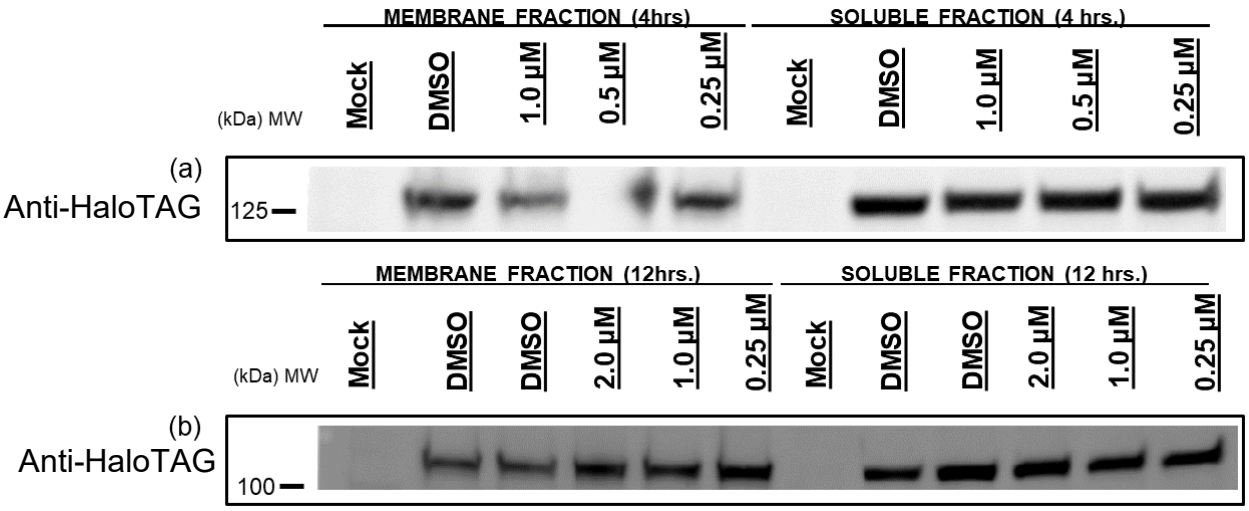

Figure 2.4.10 HaloTAG DGKθ expression on Western blot, HEK293T cells, soluble and membrane fractions. (a) Overexpression HaloTAG DGKθ fusion protein concentration trials, rcm-1-61 ligand was unsuccessful to degrade HaloTAG DGKθ fusion protein, exposure concentration of 1.0, 0.5, 0.25 µM respectively in a time exposure of 4 hrs for membrane and soluble fractions. (b) Overexpression HaloTAG DGKθ fusion protein concentration trials, rcm-1-61 ligand was unsuccessful to degrade HaloTAG DGKθ fusion protein, exposure concentration of 2.0, 0.5, 0.25 µM respectively in a time exposure of 12 hrs, both membrane and soluble fractions.

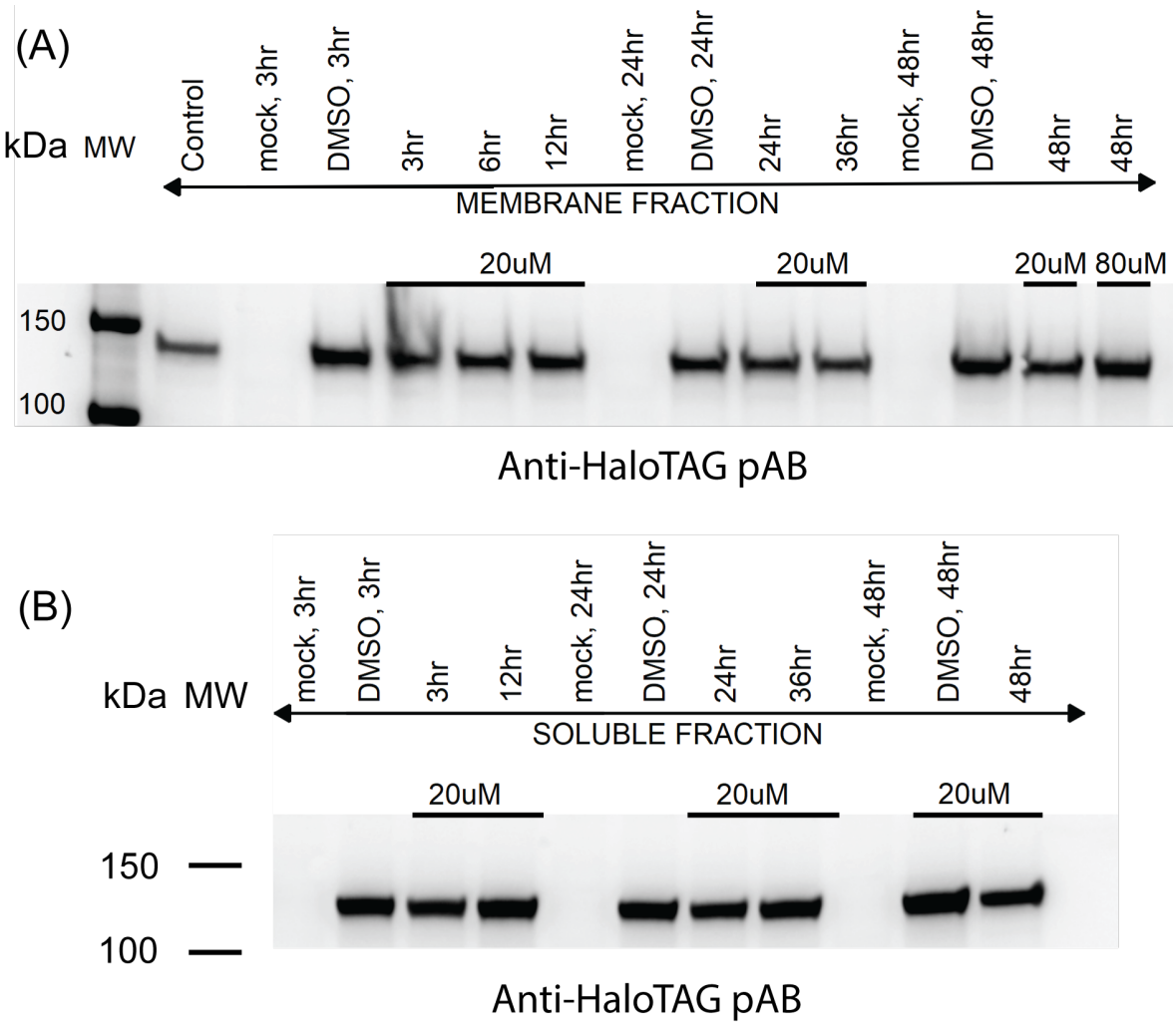

Figure 2.4.11 HaloTAG DGKθ expression on Western blot, HEK293T cells, soluble and membrane fractions. (a) Overexpression HaloTAG DGKθ fusion protein time and concentration trials, using rcm-1-61 ligand was unsuccessful to degrade HaloTAG DGKθ fusion protein, exposure concentration of 20 μM and one 80 μM respectively in a time trials 3, 6, 12, 24, 36, 48 hrs. (b) Overexpression HaloTAG DGKθ fusion protein time trials, rcm-1-61ligand was unsuccessful to degrade HaloTAG DGKθ fusion protein, exposure concentration of 20 μM respectively in a time exposure of 3, 12, 24, 36, 48 hrs.

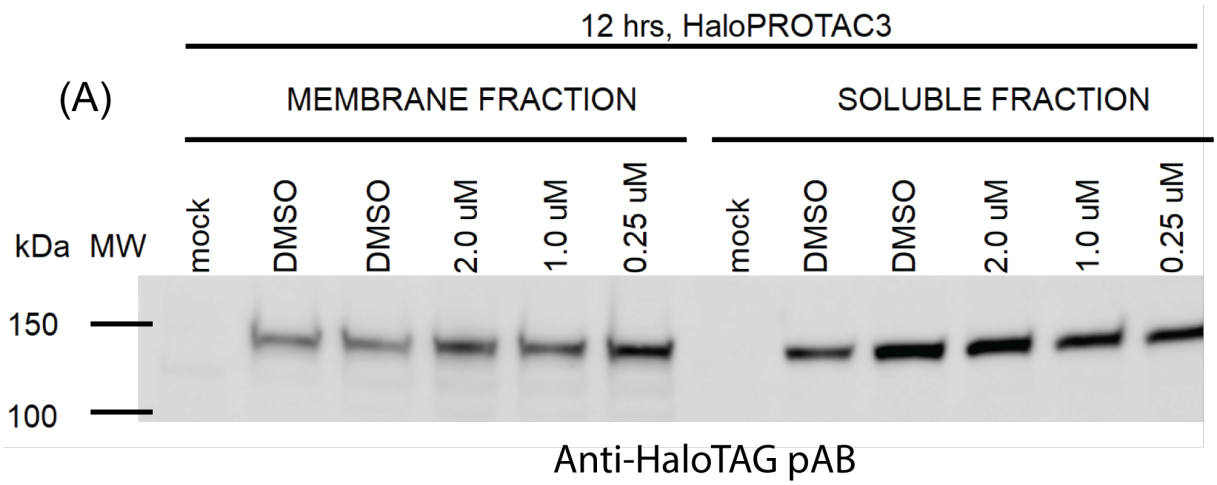

Figure 2.4.12 HaloTAG DGKθ expression on Western blot, HEK293T cells, soluble and membrane fractions. (a) Overexpression HaloTAG DGKθ fusion protein concentration trials, HaloPROTAC3 ligand was unsuccessful to degrade HaloTAG DGKθ fusion protein, exposure concentration of 0.25, 1.0, 2.0 μM respectively in a time exposure of 12 hrs, membrane and soluble membranes.

2.5 *Discussion*

We were able to show that DGKθ metabolism has an impact on the fatty acyl remodeling of membranes via the Lands cycle. Specifically, we identified changes in ceramides (Cer), triglycerides (TG), lysophosphatidylcholines (LPC), phosphatidylcholines (PC), lysophosphatidylethanolamines (LPE), phosphatidylethanolamines (PE), and phosphatidylinositols (PI) lipids. Our preliminary results using LC-MS metabolomics to identify and track changes in the lipidome in response to transient overexpression of DGKθ are promising and establish the foundation for future studies. Our knockout of endogenous DGKθ gene in HEK293T cells, along with our overexpressed HaloTAG-DGKθ fusion protein, establish the needed cell models for future investigations.

We were able to quantitatively determine the lipid changes in cells with molecular specificity (at the level of fatty acyl chain length and unsaturation) in live HEK293T cells using LC-MS/MS techniques. These advancements in LC-MS/MS techniques have enabled development of sensitive, selective profiling of molecular structures on a global scale.[74, 75] LC-MS/MS has enabled the identification of acyl chains lengths and degrees of unsaturation of lipids in response to overexpressed DGKθ disruption.[17, 74]

Future studies may target ACSVL3 and LPCAT3, which may reveal how the lipids and their interactions with proteins can validate our proposed mechanism for DGKθ. One course of action that we propose is to inhibit ACSVL3 and LPCAT3 and identify changes in lipids of defined acyl chains lengths and degrees of unsaturation in response to recombinant overexpression of DGKθ, with the aid of

LC-MS/MS and LipidSearch software analysis. These results will help verify that the Lands cycle is involved when overexpressing DGKθ. To validate our current results for overexpressed DGKθ in HEK293T cells, we could use degradation tag (dTAG) technology. This technology would allow us to perform chemical knockdown DGKθ.

Our initial data supports DGKθ KO; however, we were not able to KO DGKθ gene to the point to mutate the DNA sequence in a way that stops all the DGKθ gene expression permanently. One reason for this might be that we might not have deleted all the DGKθ from all of the alleles. Since we were not able to have a DGKθ KO HEK293T, we attempted to perform on other cell lines Colo205 and Jurkat, but those experiments were unsuccessful.

Although we were successful in transient transfection of HaloTAG-DGKθ, we were not able to knockdown HaloTAG-DGKθ, using the HaloTAG ligand. One reason for this difficulty is how the HaloTAG protein is fused together with the DGKθ protein at the N-terminus of the DGKθ protein. Both DGKθ protein and HaloTag protein may be fused in such a way to conformationally block the ligand active site from forming the covalent bond to the ligand to begin the degradation pathway.[76, 77] The ligand has to access this active site pocket precisely to form the specific and irreversible bond.[76] A second reason for this difficulty might be the ligand we used. We performed the experiments using HaloPROTAC3 ligand, with no visible knockdown on our membranes. A future goal is to measure cell viability and the efficacy of our approach using a WST-1 assay. The overall goal was to

perform tandem mass spectrometry analysis for both the HaloTAG and CRISPR/Cas9 KO samples.[32, 50]

The targeted results should validate and support our untargeted results for overexpressed DGKθ. The number of lipid substrates searched (targets) is often limited and specific.[32] Targeted approaches are high-throughput because data generation provides quick quantitative results.[32] A targeted method would detect and quantify specific lipids species placed on an inclusion list would provide better insight into DGKθ's metabolic pathways. We have identified a list of precursor ions **(Table 2.4.3)**. These precursor ions will be able to verify our untargeted results.

This work provided elucidation as to how DGKθ metabolism may be involved in fatty acyl remodeling via the Lands cycle. We set out to quantitatively determine the molecular lipid composition of gain of DGKθ function (recombinant overexpression) in HEK293T cells using tandem LC-MS/MS techniques. What sets this project apart is that we used two technologies, HaloTAG and CRISPR/Cas9, in ways that have not been used before to expand our lipidomic understanding of DGKθ.

2.6 *Acknowledgments*

We thank all members of the Hsu Lab for helpful discussions and review of the manuscript, specifically Mark Ross, Dina Bai, and Adam Libby. In addition, Xiaolong Wei from the Adli Lab, Department of Biochemistry and Molecular Genetics, Charlottesville, VA, USA, for helping us with CRISPR biology techniques. In addition, I would like to thank Harris Lab, Department of Pharmacology, Charlottesville, VA, USA, for their support. This work was supported by the Pharmacology Science Training Grant, Department of Pharmacology, Charlottesville, VA, USA.

2.7 *References*

(1) Bozelli, J. C., Jr.; Yune, J.; Takahashi, D.; Sakane, F.; Epand, R. M. Membrane morphology determines diacylglycerol kinase alpha substrate acyl chain specificity. *FASEB J* **2021**, *35* (6), e21602. DOI: 10.1096/fj.202100264R From NLM Medline.

(2) Bozelli, J. C., Jr.; Aulakh, S. S.; Epand, R. M. Membrane shape as determinant of protein properties. *Biophys Chem* **2021**, *273*, 106587. DOI: 10.1016/j.bpc.2021.106587 From NLM Medline.

(3) Harayama, T.; Riezman, H. Understanding the diversity of membrane lipid composition. *Nat Rev Mol Cell Biol* **2018**, *19* (5), 281-296. DOI: 10.1038/nrm.2017.138.

(4) Jacquemyn, J.; Cascalho, A.; Goodchild, R. E. The ins and outs of endoplasmic reticulum-controlled lipid biosynthesis. *EMBO Rep* **2017**, *18* (11), 1905-1921. DOI: 10.15252/embr.201643426.

(5) Hilgemann, D. W.; Dai, G.; Collins, A.; Larricia, V.; Magi, S.; Deisl, C.; Fine, M. Lipid signaling to membrane proteins: From second messengers to membrane domains and adapter-free endocytosis. *J Gen Physiol* **2018**, *150* (2), 211-224. DOI: 10.1085/jgp.201711875.

(6) Tu-Sekine, B.; Goldschmidt, H.; Raben, D. M. Diacylglycerol, phosphatidic acid, and their metabolic enzymes in synaptic vesicle recycling. *Adv Biol Regul* **2015**, *57*, 147-152. DOI: 10.1016/j.jbior.2014.09.010.

(7) Raben, D. M.; Barber, C. N. Phosphatidic acid and neurotransmission. *Adv Biol Regul* **2017**, *63*, 15-21. DOI: 10.1016/j.jbior.2016.09.004.

(8) Barber, C. N.; Huganir, R. L.; Raben, D. M. Phosphatidic acid-producing enzymes regulating the synaptic vesicle cycle: Role for PLD? *Adv Biol Regul* **2018**, *67*, 141-147. DOI: 10.1016/j.jbior.2017.09.009.

(9) Tu-Sekine, B.; Ostroski, M.; Raben, D. M. Modulation of diacylglycerol kinase theta activity by alpha-thrombin and phospholipids. *Biochemistry* **2007**, *46* (3), 924-932. DOI: 10.1021/bi061170c.

(10) Cai, J.; Abramovici, H.; Gee, S. H.; Topham, M. K. Diacylglycerol kinases as sources of phosphatidic acid. *Biochim Biophys Acta* **2009**, *1791* (9), 942-948. DOI: 10.1016/j.bbalip.2009.02.010.

(11) Sakane, F.; Mizuno, S.; Takahashi, D.; Sakai, H. Where do substrates of diacylglycerol kinases come from? Diacylglycerol kinases utilize diacylglycerol

species supplied from phosphatidylinositol turnover-independent pathways. *Adv Biol Regul* **2018**, *67*, 101-108. DOI: 10.1016/j.jbior.2017.09.003.

(12) Tu-Sekine, B.; Goldschmidt, H. L.; Raben, D. M. DGK-theta: Structure, enzymology, and physiological roles. *Front Cell Dev Biol* **2016**, *4*, 101. DOI: 10.3389/fcell.2016.00101.

(13) Tu-Sekine, B.; Raben, D. M. Dual regulation of diacylglycerol kinase (DGK)-theta: polybasic proteins promote activation by phospholipids and increase substrate affinity. *J Biol Chem* **2012**, *287* (50), 41619-41627. DOI: 10.1074/jbc.M112.404855.

(14) Ma, Q.; Gabelli, S. B.; Raben, D. M. Diacylglycerol kinases: Relationship to other lipid kinases. *Adv Biol Regul* **2019**, *71*, 104-110. DOI: 10.1016/j.jbior.2018.09.014 From NLM Medline.

(15) Ueda, S.; Tu-Sekine, B.; Yamanoue, M.; Raben, D. M.; Shirai, Y. The expression of diacylglycerol kinase theta during the organogenesis of mouse embryos. *BMC Dev Biol* **2013**, *13*, 35. DOI: 10.1186/1471-213X-13-35.

(16) D'Souza, K.; Epand, R. M. Enrichment of phosphatidylinositols with specific acyl chains. *Biochim Biophys Acta* **2014**, *1838* (6), 1501-1508. DOI: 10.1016/j.bbamem.2013.10.003.

(17) Ware, T. B.; Franks, C. E.; Granade, M. E.; Zhang, M.; Kim, K. B.; Park, K. S.; Gahlmann, A.; Harris, T. E.; Hsu, K. L. Reprogramming fatty acyl specificity of lipid kinases via C1 domain engineering. *Nat Chem Biol* **2020**, *16* (2), 170-178. DOI: 10.1038/s41589-019-0445-9 From NLM Medline.

(18) Wang, B.; Tontonoz, P. Phospholipid remodeling in physiology and disease. *Annu Rev Physiol* **2019**, *81*, 165-188. DOI: 10.1146/annurev-physiol-020518-114444.

(19) Breitkopf, S. B.; Ricoult, S. J. H.; Yuan, M.; Xu, Y.; Peake, D. A.; Manning, B. D.; Asara, J. M. A relative quantitative positive/negative ion switching method for untargeted lipidomics via high resolution LC-MS/MS from any biological source. *Metabolomics* **2017**, *13* (3). DOI: 10.1007/s11306-016-1157-8.

(20) Traynor-Kaplan, A.; Kruse, M.; Dickson, E. J.; Dai, G.; Vivas, O.; Yu, H.; Whittington, D.; Hille, B. Fatty-acyl chain profiles of cellular phosphoinositides. *Biochim Biophys Acta* **2017**, *1862* (5), 513-522. DOI: 10.1016/j.bbalip.2017.02.002.

(21) Murphy, R. C.; Folco, G. Lysophospholipid acyltransferases and leukotriene biosynthesis: intersection of the Lands cycle and the arachidonate PI cycle. *J Lipid Res* **2019**, *60* (2), 219-226. DOI: 10.1194/jlr.S091371.

(22) Wepy, J. A.; Galligan, J. J.; Kingsley, P. J.; Xu, S.; Goodman, M. C.; Tallman, K. A.; Rouzer, C. A.; Marnett, L. J. Lysophospholipases cooperate to mediate lipid homeostasis and lysophospholipid signaling. *J Lipid Res* **2019**, *60* (2), 360-374. DOI: 10.1194/jlr.M087890.

(23) Shulga, Y. V.; Myers, D. S.; Ivanova, P. T.; Milne, S. B.; Brown, H. A.; Topham, M. K.; Epand, R. M. Molecular species of phosphatidylinositol-cycle intermediates in the endoplasmic reticulum and plasma membrane. *Biochemistry* **2010**, *49* (2), 312-317. DOI: 10.1021/bi901551e.

(24) Nadler, A.; Reither, G.; Feng, S.; Stein, F.; Reither, S.; Muller, R.; Schultz, C. The fatty acid composition of diacylglycerols determines local signaling patterns. *Angew Chem Int Ed Engl* **2013**, *52* (24), 6330-6334. DOI: 10.1002/anie.201301716.

(25) Shulga, Y. V.; Loukov, D.; Ivanova, P. T.; Milne, S. B.; Myers, D. S.; Hatch, G. M.; Umeh, G.; Jalan, D.; Fullerton, M. D.; Steinberg, G. R.; et al. Diacylglycerol kinase delta promotes lipogenesis. *Biochemistry* **2013**, *52* (44), 7766-7776. DOI: 10.1021/bi401178y.

(26) Shulga, Y. V.; Topham, M. K.; Epand, R. M. Regulation and Functions of Diacylglycerol Kinases. *Chemical Reviews* **2011**, *111* (10), 6186-6208. DOI: 10.1021/cr1004106 (acccessed 2012/08/27).

(27) Shulga, Y. V.; Topham, M. K.; Epand, R. M. Substrate specificity of diacylglycerol kinase-epsilon and the phosphatidylinositol cycle. *FEBS Lett* **2011**, *585* (24), 4025-4028. DOI: 10.1016/j.febslet.2011.11.016.

(28) Epand, R. M. Features of the phosphatidylinositol cycle and its role in signal transduction. *J Membr Biol* **2017**, *250* (4), 353-366. DOI: 10.1007/s00232-016-9909-y.

(29) Lung, M.; Shulga, Y. V.; Ivanova, P. T.; Myers, D. S.; Milne, S. B.; Brown, H. A.; Topham, M. K.; Epand, R. M. Diacylglycerol kinase epsilon is selective for both acyl chains of phosphatidic acid or diacylglycerol. *J Biol Chem* **2009**, *284* (45), 31062-31073. DOI: 10.1074/jbc.M109.050617.

(30) Bozelli, J. C., Jr.; Epand, R. M. Role of membrane shape in regulating the phosphatidylinositol cycle at contact sites. *Chem Phys Lipids* **2019**, *221*, 24-29. DOI: 10.1016/j.chemphyslip.2019.03.002.

(31) Bozelli, J. C., Jr.; Jennings, W.; Black, S.; Hou, Y. H.; Lameire, D.; Chatha, P.; Kimura, T.; Berno, B.; Khondker, A.; Rheinstadter, M. C.; et al. Membrane curvature allosterically regulates the phosphatidylinositol cycle, controlling its rate and acyl-chain composition of its lipid intermediates. *J Biol Chem* **2018**, *293* (46), 17780-17791. DOI: 10.1074/jbc.RA118.005293.

(32) Contrepois, K.; Mahmoudi, S.; Ubhi, B. K.; Papsdorf, K.; Hornburg, D.; Brunet, A.; Snyder, M. Cross-platform comparison of untargeted and targeted lipidomics approaches on aging mouse plasma. *Sci Rep* **2018**, *8* (1), 17747. DOI: 10.1038/s41598-018-35807-4.

(33) Aretz, I.; Meierhofer, D. Advantages and Pitfalls of Mass Spectrometry Based Metabolome Profiling in Systems Biology. *Int J Mol Sci* **2016**, *17* (5), 632. DOI: 10.3390/ijms17050632 From NLM Medline.

(34) Holcapek, M.; Liebisch, G.; Ekroos, K. Lipidomic Analysis. *Analytical Chemistry* **2018**, *90* (7), 4249-4257. DOI: 10.1021/acs.analchem.7b05395.

(35) da Costa, E.; Silva, J.; Mendonca, S. H.; Abreu, M. H.; Domingues, M. R. Lipidomic Approaches towards Deciphering Glycolipids from Microalgae as a Reservoir of Bioactive Lipids. *Mar Drugs* **2016**, *14* (5). DOI: 10.3390/md14050101 From NLM Medline.

(36) Doerr, A. DIA mass spectrometry. *Nature Methods* **2014**, *12* (1), 35-35. DOI: 10.1038/nmeth.3234.

(37) Schlotterbeck, J.; Chatterjee, M.; Gawaz, M.; Lammerhofer, M. Comprehensive MS/MS profiling by UHPLC-ESI-QTOF-MS/MS using SWATH data-independent acquisition for the study of platelet lipidomes in coronary artery disease. *Anal Chim Acta* **2019**, *1046*, 1-15. DOI: 10.1016/j.aca.2018.08.060.

(38) Kita, Y.; Shindou, H.; Shimizu, T. Cytosolic phospholipase A2 and lysophospholipid acyltransferases. *Biochim Biophys Acta Mol Cell Biol Lipids* **2019**, *1864* (6), 838-845. DOI: 10.1016/j.bbalip.2018.08.006 From NLM Medline.

(39) Shindou, H.; Hishikawa, D.; Harayama, T.; Yuki, K.; Shimizu, T. Recent progress on acyl CoA: lysophospholipid acyltransferase research. *J Lipid Res* **2009**, *50 Suppl*, S46-51. DOI: 10.1194/jlr.R800035-JLR200.

(40) Wang, L.; Shen, W.; Kazachkov, M.; Chen, G.; Chen, Q.; Carlsson, A. S.; Stymne, S.; Weselake, R. J.; Zou, J. Metabolic interactions between the Lands cycle and the Kennedy pathway of glycerolipid synthesis in Arabidopsis developing seeds. *Plant Cell* **2012**, *24* (11), 4652-4669. DOI: 10.1105/tpc.112.104604.

(41) Neklesa, T. K.; Tae, H. S.; Schneekloth, A. R.; Stulberg, M. J.; Corson, T. W.; Sundberg, T. B.; Raina, K.; Holley, S. A.; Crews, C. M. Small-molecule hydrophobic tagging-induced degradation of HaloTag fusion proteins. *Nat Chem Biol* **2011**, *7* (8), 538-543. DOI: 10.1038/nchembio.597.

(42) England, C. G.; Luo, H.; Cai, W. HaloTag technology: a versatile platform for biomedical applications. *Bioconjug Chem* **2015**, *26* (6), 975-986. DOI: 10.1021/acs.bioconjchem.5b00191.

(43) Goldschmidt, H. L.; Tu-Sekine, B.; Volk, L.; Anggono, V.; Huganir, R. L.; Raben, D. M. DGKtheta Catalytic activity is required for efficient recycling of presynaptic vesicles at excitatory synapses. *Cell Rep* **2016**, *14* (2), 200-207. DOI: 10.1016/j.celrep.2015.12.022.

(44) Shan, L.; Wang, D.; Mao, Q.; Xia, H. Establishment of a DGKtheta Endogenous Promoter Luciferase Reporter HepG2 Cell Line for Studying the Transcriptional Regulation of DGKtheta Gene. *Appl Biochem Biotechnol* **2019**, *187* (4), 1344-1355. DOI: 10.1007/s12010-018-2890-4 From NLM Medline.

(45) Los, G. V.; Encell, L. P.; McDougall, M. G.; Hartzell, D. D.; Karassina, N.; Zimprich, C.; Wood, M. G.; Learish, R.; Ohana, R. F.; Urh, M.; et al. HaloTag: a novel protein labeling technology for cell imaging and protein analysis. *ACS Chem Biol* **2008**, *3* (6), 373-382. DOI: 10.1021/cb800025k.

(46) Popa, I.; Berkovich, R.; Alegre-Cebollada, J.; Badilla, C. L.; Rivas-Pardo, J. A.; Taniguchi, Y.; Kawakami, M.; Fernandez, J. M. Nanomechanics of HaloTag tethers. *J Am Chem Soc* **2013**, *135* (34), 12762-12771. DOI: 10.1021/ja4056382.

(47) Urh, M.; Rosenberg, M. HaloTag, a platform technology for protein analysis. *Curr Chem Genomics* **2012**, *6*, 72-78. DOI: 10.2174/1875397301206010072.

(48) Lee, P. Y.; Costumbrado, J.; Hsu, C. Y.; Kim, Y. H. Agarose gel electrophoresis for the separation of DNA fragments. *J Vis Exp* **2012**, (62). DOI: 10.3791/3923 From NLM Medline.

(49) Gugiu, G. B. Lipid identification by untargeted tandem mass spectrometry coupled with ultra-high-pressure liquid chromatography. *Methods Mol Biol* **2017**, *1609*, 65-82. DOI: 10.1007/978-1-4939-6996-8_8.

(50) Han, X.; Gross, R. W. Shotgun lipidomics: electrospray ionization mass spectrometric analysis and quantitation of cellular lipidomes directly from crude extracts of biological samples. *Mass Spectrom Rev* **2005**, *24* (3), 367-412. DOI: 10.1002/mas.20023.

(51) Gathungu, R. M.; Larrea, P.; Sniatynski, M. J.; Marur, V. R.; Bowden, J. A.; Koelmel, J. P.; Starke-Reed, P.; Hubbard, V. S.; Kristal, B. S. Optimization of electrospray ionization source parameters for lipidomics to reduce misannotation of in-source fragments as precursor ions. *Anal Chem* **2018**, *90* (22), 13523-13532. DOI: 10.1021/acs.analchem.8b03436.

(52) Loraine, A. E.; Blakley, I. C.; Jagadeesan, S.; Harper, J.; Miller, G.; Firon, N. Analysis and visualization of RNA-Seq expression data using RStudio, Bioconductor, and Integrated Genome Browser. *Methods Mol Biol* **2015**, *1284*, 481-501. DOI: 10.1007/978-1-4939-2444-8_24.

(53) Sakai, H.; Sakane, F. Recent progress on type II diacylglycerol kinases: the physiological functions of diacylglycerol kinase delta, eta and kappa and their

involvement in disease. *J Biochem* **2012**, *152* (5), 397-406. DOI: 10.1093/jb/mvs104.

(54) Murakami, T.; Sakane, F.; Imai, S.; Houkin, K.; Kanoh, H. Identification and characterization of two splice variants of human diacylglycerol kinase eta. *J Biol Chem* **2003**, *278* (36), 34364-34372. DOI: 10.1074/jbc.M301542200.

(55) Murphy, R. C. Challenges in mass spectrometry-based lipidomics of neutral lipids. *TrAC Trends in Analytical Chemistry* **2018**, *107*, 91-98. DOI: doi.org/10.1016/j.trac.2018.07.023.

(56) Godzien, J.; Ciborowski, M.; Martinez-Alcazar, M. P.; Samczuk, P.; Kretowski, A.; Barbas, C. Rapid and reliable identification of phospholipids for untargeted metabolomics with LC-ESI-QTOF-MS/MS. *J Proteome Res* **2015**, *14* (8), 3204-3216. DOI: 10.1021/acs.jproteome.5b00169.

(57) Zhang, Y.; Zhang, P.; Cheng, Y. Structural characterization of isoprenylated flavonoids from Kushen by electrospray ionization multistage tandem mass spectrometry. *J Mass Spectrom* **2008**, *43* (10), 1421-1431. DOI: 10.1002/jms.1423.

(58) Tanaka, T.; Tsuchiya, R.; Hozumi, Y.; Nakano, T.; Okada, M.; Goto, K. Reciprocal regulation of p53 and NF-kappaB by diacylglycerol kinase zeta. *Adv Biol Regul* **2016**, *60*, 15-21. DOI: 10.1016/j.jbior.2015.09.009.

(59) Gao, S.; Zhang, Z. P.; Karnes, H. T. Sensitivity enhancement in liquid chromatography/atmospheric pressure ionization mass spectrometry using derivatization and mobile phase additives. *J Chromatogr B Analyt Technol Biomed Life Sci* **2005**, *825* (2), 98-110. DOI: 10.1016/j.jchromb.2005.04.021.

(60) Litvak, V.; Dahan, N.; Ramachandran, S.; Sabanay, H.; Lev, S. Maintenance of the diacylglycerol level in the Golgi apparatus by the Nir2 protein is critical for Golgi secretory function. *Nat Cell Biol* **2005**, *7* (3), 225-234. DOI: 10.1038/ncb1221.

(61) Rahman, G. M.; Das, J. Modeling studies on the structural determinants for the DAG/phorbol ester binding to C1 domain. *J Biomol Struct Dyn* **2015**, *33* (1), 219-232. DOI: 10.1080/07391102.2014.895679.

(62) Das, J.; Rahman, G. M. C1 domains: structure and ligand-binding properties. *Chem Rev* **2014**, *114* (24), 12108-12131. DOI: 10.1021/cr300481j.

(63) Sakane, F.; Kai, M.; Wada, I.; Imai, S.; Kanoh, H. The C-terminal part of diacylglycerol kinase alpha lacking zinc fingers serves as a catalytic domain. *Biochem J* **1996**, *318 (Pt 2)*, 583-590. DOI: 10.1042/bj3180583 From NLM Medline.

(64) Hishikawa, D.; Hashidate, T.; Shimizu, T.; Shindou, H. Diversity and function of membrane glycerophospholipids generated by the remodeling pathway in mammalian cells. *J Lipid Res* **2014**, *55* (5), 799-807. DOI: 10.1194/jlr.R046094.

(65) Perez-Chacon, G.; Astudillo, A. M.; Balgoma, D.; Balboa, M. A.; Balsinde, J. Control of free arachidonic acid levels by phospholipases A2 and lysophospholipid acyltransferases. *Biochim Biophys Acta* **2009**, *1791* (12), 1103-1113. DOI: 10.1016/j.bbalip.2009.08.007.

(66) Vasquez, A. M.; Mouchlis, V. D.; Dennis, E. A. Review of four major distinct types of human phospholipase A2. *Adv Biol Regul* **2018**, *67*, 212-218. DOI: 10.1016/j.jbior.2017.10.009.

(67) Li, Z.; Zhao, J.; Muhammad, N.; Wang, D.; Mao, Q.; Xia, H. Establishment of a HEK293 cell line by CRISPR/Cas9-mediated luciferase knock-in to study transcriptional regulation of the human SREBP1 gene. *Biotechnol Lett* **2018**, *40* (11-12), 1495-1506. DOI: 10.1007/s10529-018-2608-2.

(68) Liu, Y.; Wei, W. P.; Ye, B. C. High GC Content Cas9-Mediated Genome-Editing and Biosynthetic Gene Cluster Activation in Saccharopolyspora erythraea. *Acs Synth Biol* **2018**, *7* (5), 1338-1348. DOI: 10.1021/acssynbio.7b00448.

(69) Liu, X.; Homma, A.; Sayadi, J.; Yang, S.; Ohashi, J.; Takumi, T. Sequence features associated with the cleavage efficiency of CRISPR/Cas9 system. *Sci Rep* **2016**, *6*, 19675. DOI: 10.1038/srep19675 From NLM Medline.

(70) Doench, J. G.; Hartenian, E.; Graham, D. B.; Tothova, Z.; Hegde, M.; Smith, I.; Sullender, M.; Ebert, B. L.; Xavier, R. J.; Root, D. E. Rational design of highly active sgRNAs for CRISPR-Cas9-mediated gene inactivation. *Nature Biotechnology* **2014**, *32* (12), 1262-U1130. DOI: 10.1038/nbt.3026.

(71) Yin, L. M.; Wei, Y.; Wang, Y.; Xu, Y. D.; Yang, Y. Q. Long Term and Standard Incubations of WST-1 Reagent Reflect the Same Inhibitory Trend of Cell Viability in Rat Airway Smooth Muscle Cells. *Int J Med Sci* **2013**, *10* (1), 68-72. DOI: 10.7150/ijms.5256.

(72) Allen, M.; Bjerke, M.; Edlund, H.; Nelander, S.; Westermark, B. Origin of the U87MG glioma cell line: Good news and bad news. *Sci Transl Med* **2016**, *8* (354), 354re353. DOI: 10.1126/scitranslmed.aaf6853.

(73) Jung, I. Y.; Kim, Y. Y.; Yu, H. S.; Lee, M.; Kim, S.; Lee, J. CRISPR/Cas9-Mediated Knockout of DGK Improves Antitumor Activities of Human T Cells. *Cancer Res* **2018**, *78* (16), 4692-4703. DOI: 10.1158/0008-5472.CAN-18-0030.

(74) Blevins, M. S.; James, V. K.; Herrera, C. M.; Purcell, A. B.; Trent, M. S.; Brodbelt, J. S. Unsaturation Elements and Other Modifications of Phospholipids in Bacteria: New Insight from Ultraviolet Photodissociation Mass Spectrometry.

Analytical Chemistry **2020**, *92* (13), 9146-9155. DOI: 10.1021/acs.analchem.0c01449.

(75) Callender, H. L.; Forrester, J. S.; Ivanova, P.; Preininger, A.; Milne, S.; Brown, H. A. Quantification of diacylglycerol species from cellular extracts by electrospray ionization mass Spectrometry using a linear regression algorithm (vol 79, pg 263, 2007). *Analytical Chemistry* **2007**, *79* (20), 7933-7933. DOI: 10.1021/ac701780n.

(76) Marques, S. M.; Slanska, M.; Chmelova, K.; Chaloupkova, R.; Marek, M.; Clark, S.; Damborsky, J.; Kool, E. T.; Bodnar, D.; Prokop, Z. Mechanism-Based Strategy for Optimizing HaloTag Protein Labeling. *Jacs Au* **2022**, *2* (6), 1324-1337. DOI: 10.1021/jacsau.2c00002.

(77) Chen, W. Y.; Younis, M. H.; Zhao, Z. K.; Cai, W. B. Recent biomedical advances enabled by HaloTag technology. *Biocell* **2022**, *46* (8), 1789-1801. DOI: 10.32604/biocell.2022.018197.

Chapter 3. Targeted Protein Degradation of DGKs Using dTAG

3.1 *Abstract*

In Chapter 3 our aim is to develop a degradation tag (dTAG) system protocol to induce rapid and precise degradation of DGKθ, DGKα, and DGKξ proteins. One of our goals was to investigate targeted protein degradation techniques to better understand DGK function through temporally controlled inhibition in cellular systems.

Strategies to directly alter protein levels including targeted protein degradation using small molecules are novel pharmacological approaches, with promising clinical potentials for drug target validation given the selectivity, reversibility, and dose dependency.[1-3] The degradation tag (dTAG) system has the ability to use the endogenous protein degradation machinery in all human cells, which does not require expressing additional exogenous factors.[1-3] The dTAG system pairs uses a small molecule degrader of $FKBP12^{F36V}$ to degrade $FKBP12^{F36V}$ fused in-frame with a target protein, *in vivo*.[2] It is our aim to use this technology in our efforts to understand DGKs metabolic function. In this chapter, we establish that dTAG tag can be knocked-in into the DGKθ locus with promising results. As it will be explained further analysis and verification will be required for DGKθ before we can use this DGKθ-dTAG system on cell lines and evaluate cellular effects.

3.2 *Introduction*

To better understand the metabolic mechanisms of the ten known DGKs, which serve as critical regulatory points in cell signaling, we used novel genetic technologies to chemical knockdown DGK to probe function for enabling future therapeutic discovery efforts.[4-6] It is our goal here in Chapter 3 to apply dTAG for better understanding of the link between a specific gene to specific physiopathological phenotypes.[7,8] As shown in Chapter 2, overexpression (gain of function) is useful in studying the function of a protein and can provide unique insights into a gene's function; however, there are limitations. We can go beyond overexpressing a gene in cell culture and use other technologies such as protein degradation techniques, which can provide insights into a function of endogenous proteins.[9] In this chapter we attempt to address some of the limitations presented in Chapter 2 when overexpressing a protein of interest on a biological system.

Our attempt to use HaloTAG via Halo-PROTAC[10] to knock-down the Halotag-DGKθ protein in HEK293T was unsuccessful. It is interesting to note here that although both HaloTAG and dTAG do not affect gene expression, both do affect the protein expression, as described in Chapter 1 and 2.[11] Both perform a chemical knockdown on their targeted protein, which allows novel knockdown strategies for basic and therapeutic discoveries.[6, 12] In this chapter, we turned our attention to novel degradation technology that uses small molecule degraders on targeted proteins of interest.[2, 3, 13] It has an added advantage that the degradation tag (dTAG) system is a recently introduced hybrid chemical biology system

combining the benefits of small molecule perturbations with precision genetic editing (CRISPR-Cas9) allowing for temporal studies.[2, 14, 15]

The dTAG system is a versatile protein degradation technology which combines genome editing with real time experimental changes.[2, 16, 17] dTAG technology knocks-in a tag next to a gene of interest, assisted by microhomology-mediated end-joining (MMEJ) and CRISPR/Cas9 technology, with the PITCh (Precise Integration into Target Chromosome) system, as shown in **(Figure 3.2.1)** and **(Figure 3.2.2)**.[2, 16, 18] dTAG provides a strategy to chemically control protein levels by manipulating the cell's protein degradation machinery.[1, 19] dTAG ligands can target specific proteins of interest through a proximity-induced interaction between an E3 ubiquitin ligase and the target protein.[5]

Genome engineering technologies have brought novel advances in functional genomic studies. These include knock-outs and gene knock-ins, along with various genomic rearrangements such as chromosomal deletions, inversions, and translocations.[15, 18, 20] Such technologies are possible due to the Cas9 nuclease generating a DNA double-strand break (DSB) by the guide RNA (gRNA).[15, 21] Then, the DSB is repaired by either nonhomologous end joining (NHEJ) or homologous recombination (HR) mediated repair.[15, 22] Both NHEJ and HR have advantages, but there are limitations. In contrast, a third mediated repair approach, microhomology-mediated end joining (MMEJ), provides a high-fidelity alternative to both NHEJ and HR.[18, 23] For example, their efficiencies differ between cell type and organisms, with MMEJ-based mechanism being effective in tagging endogenous proteins in human cells.[24, 25, 26] MMEJ mediated repair requires a

shorter number (about 20) base pairs (bp) of microhomology flanking upstream and downstream sides of the DSB site. In addition, MMEJ repair occurs during the mitosis and synthesis phase of the cell cycle; while HR does not occur.[23, 27]

We chose dTAG technologies as a strategy to understand DGKs for its advantages in perturbing a protein's function. This is especially important because potent and selective inhibitors of individual DGK isoforms are not yet available. As a starting point, we choose DGKθ, DGKα, and DGKξ isozymes before pursuing additional DGK isoforms. We proposed establishing a DGKθ-dTAG cell line using CRISPR/Cas9 technology. This included designing the knock-in strategy and cloning the necessary plasmids, as well as generation, selection, and validation of clones with the degradable alleles. Our system is based on a two-plasmid "Precise Integration into Target Chromosome" (PITCh) system, as shown in **(Figure 3.2.2)**. The PITCh cutting vector has the Cas9-expressing vector, which also expresses two gRNAs (target gRNA and PTICh gRNA).

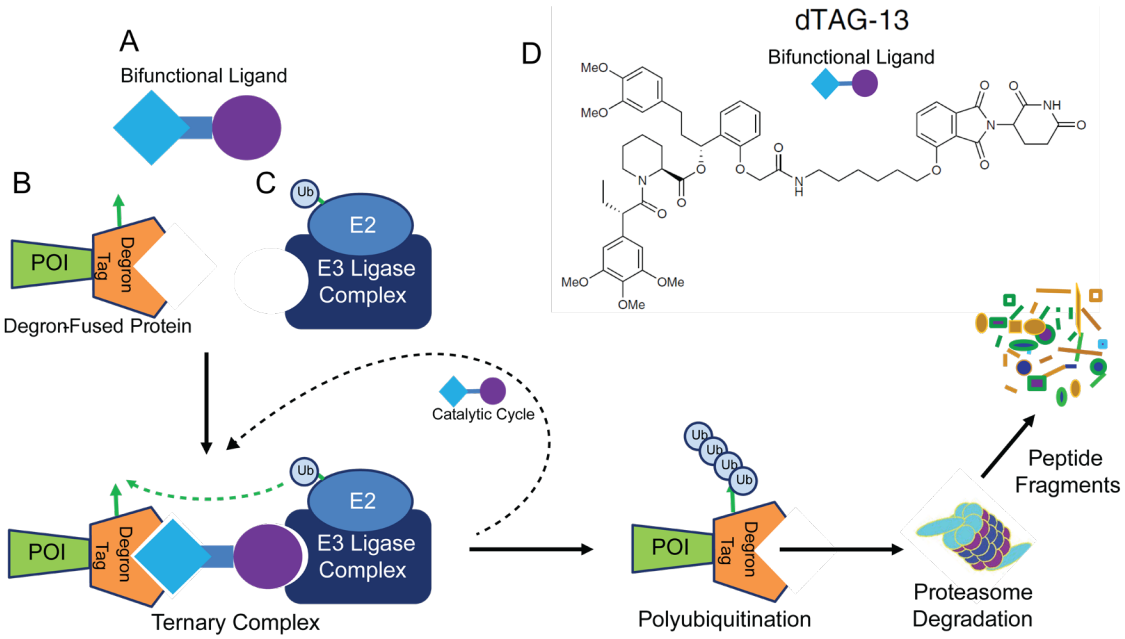

Figure 3.2.1 dTAG ligand targets a fused-protein for degradation. (A) bifunctional Ligand, dTAG-13; (B) Degron-fused protein of interest; and (C) E3 ligase complex with E2 and ubiquitin. When (A) binds (B) and (C), ternary complex is formed. E3 ubiquitin ligase promotes the transfer of ubiquitin onto the POI, resulting in a polyubiquitin tags, which serve as a signal for protein degradation via the 26S proteasome. (D) The chemical structure for dTAG-13, the bifunctional ligand.

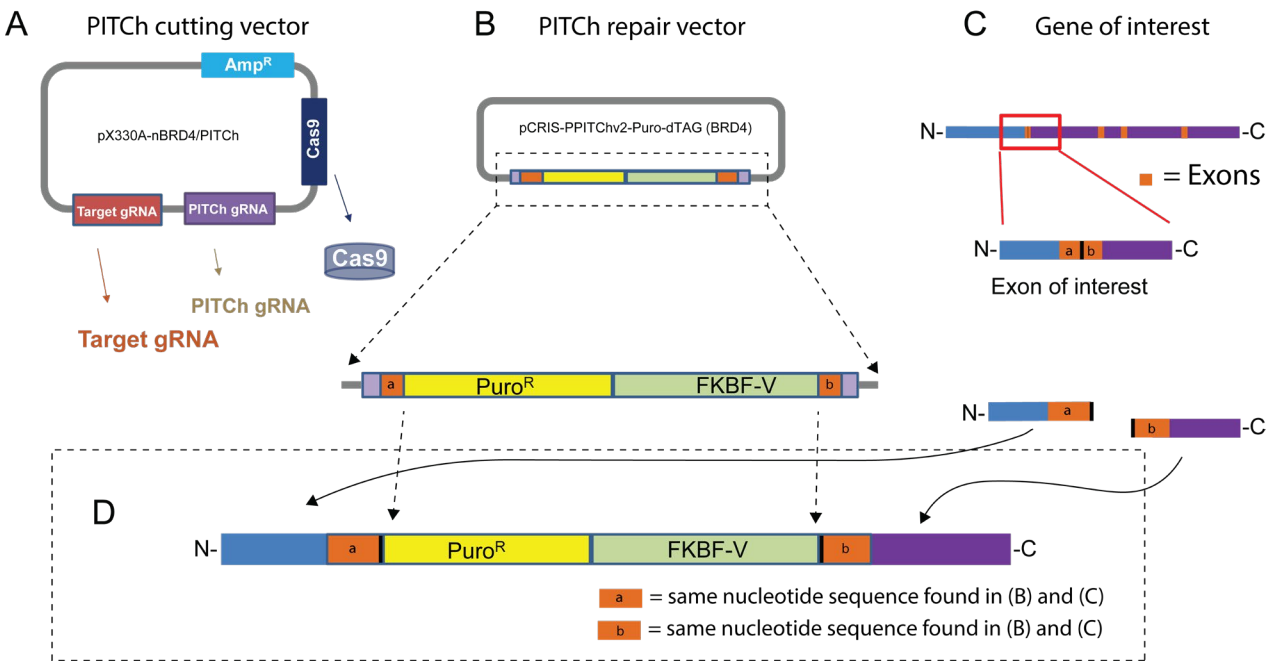

Figure 3.2.2 Identify gene locus of interest. (C) First step is to identify the gene of interest, marked as a black line between the orange region denoting an exon of interest. (B)These orange regions flanking the gene of interest will be flanking the PITCh repair vector. Primers and oligonucleotides are identified by arrows. (A) PITCh cutting vector is the plasmid that contain Target gRNA. (A) and (B) are both PITCh cutting vector and PITCh repair vector that will be inserted into a cell. (D) When the cell expresses these two plasmids, the Target gRNA will target the gene of interest. The PITCh gRNA will cut the PITCh repair vector. Causing the insert of the dTAG vector to be inserted into the exon of interest.

3.3 *Materials and Methods*

The following protocol is for the generation of an N-terminal tagged DGK in HEK293T cells.

Plasmids. Three plasmids were purchased from Addgene. First plasmid, pX330A-1x2 was a gift from Takashi Yamamoto (Addgene plasmid #58766; http//n2t.net/addgene:58766; RRID:Addgene_58766).[28] The vector contains a gRNA scaffold and the Cas9 coding region; it is used to assemble the locus-specific gRNA (by incorporation of gene-specific synthetic oligonucleotide) and to co-express it with Cas9. Second plasmid, pX330S-2-PITCh was a gift from Takashi Yamamoto (Addgene plasmid #63670; http//n2t.net/addgene:63670; RRID:Addgene_63670).[18] This vector contains the PITCh-gRNA and the Cas9 coding region, and it is used to co-express with Cas9. The final plasmid, pCRIS-PITChv2-Puro-dTAG (BRD4) was a gift from James Bradner (Addgene plasmid #91793; http//n2t.net/addgene:91793; RRID:Addgene_91793).[2] This is the donor vector which contains the Puro-P2A-2HA-FKBPV cDNA cassette, which is flanked by microhomologies for the *BRD4* locus and PITCh-gRNA target sites. We generated oligonucleotides for the locus-specific gRNA template, and we designed them using Snapgene (www.snapgene.com) and Benchling (www.benchling.com) software.

Chemical ligand. The heterobifunctional dTAG-ligand (dTAG-13) was purchased and reported previously.[2, 29]

Primers. The following primers were generated for sequencing the gene-specific microhomologies for colony PCR screening, which are shown in the table below.

Primers for colony PCR screening	
FWD	gccttttgctggccttttgctc
REV	cgttacataacttacggtaaatggcccg
Design gene-specific primers, simply replace the 5′ and 3′ microhomologies with the desired sequences	
FWD	tccgcgttacatagcatcgtacgcgtacgtgtttggcgcggacctaaagg ggctcgggccactaggtccaggaatgaccgagtacaagcccacggtggc
REV	agcattctagagcatcgtacgcgtacgtgtttggcccgggctcggccgc cgccgcagatccgccgccacc
Primers for sequencing the gene-specific microhomologies for colony PCR screening	
FWD	gcccttaattgtgagcggataac
REV	caccagggcaagggtctg
PCR primer for genomic PCR and DNA sequencing	
FWD	cgcagtcggaagcagtgtaccg
REV	cgttacataacttacggtaaatggcccg

Construction of the pX330A-1x2 with both annealed DGKθ sgRNAs.

1) Anneal the synthesized oligonucleotides (oligos) designed to target the desired genomic locus and insert them into the pX330A-1x2 vector.

a- Resuspend oligo in nuclease-free H_2O, according to data sheet (100 μM stock solution)

b- Use a PCR tube, add 8 μL of annealing buffer and 1 μL of forward oligo and 1 μL of reverse oligo.

c- Place in thermal cycler and run method starting at 95 °C for 5 minutes and then move down 1 °C every minute until temperature reaches 20 °C.

2) Digest pX330A-1x2 with restriction enzyme *BbsI* (*BpiI*)

a- Add all ingredients to the PCR tube (add restriction enzyme last) and incubate on a thermo-cycler (or heat block) set to 37 °C for 2 hrs.

	Component	**Volume (µL)**
1	Nuclease-free H_2O	34
2	CutSmart	5
3	Plsmid: pX330A-1x2	10
4	*BbsI* (BpiI)	1
	TOTAL	**50**

b- Inactivate at 65 °C for 20 minutes.

c- Run a 1% agarose gel to confirm band isolation. Also include an undigested sample as control.

d- Run a QIAquick gel extraction protocol.

3) Ligation pX330A-1x2 with annealed sgRNA: mix the following components in a PCR tube.

	Component	**Volume (µL)**
1	Nuclease-free H_2O	6
2	DNA vector (8,600 bp)	10
3	DNA Insert (25 bp)	1
4	T4 DNA Ligase buffer (10X)	2
5	T4 DNA Ligase	1
	TOTAL	**20**

a- Vortex and then spin down.

b- Then, place into a thermal cycler to incubate at 16 °C for ~16 hrs or overnight

c- Heat inactivate at 65 °C for 10 min.

d- Transformation: transform the ligation product into new bacteria.

4) Transform the products into XL1-Blue competent cells as follows:

Mix 1 µl of the products and 45 µl of XL1-Blue cells, and electroporate the mixture, using electroporation system. Place mixture into 450 µl of SOC media. Incubate the cells in a shaker incubator at 225 rpm at 37 °C for 60 min. Plate the transformed bacteria onto an LB plate containing 100 µg/mL Carbenicillin, pour all the content onto the LB plate. Culture the bacteria overnight at 37 °C.

5) From the LB plate, identify and mark (using a Sharpie) ~4 colonies. Pick each of the marked colonies twice, using a sterile plastic toothpick.

a-Transfer the contents ion the toothpick into a microtube with 10 µL of water in it. Then, heat at 80 °C for 10 min (use thermocycler).

b-Use the other toothpick to transfer for bacterial growth. Culture in incubator shaker overnight at 37 °C, in 7 mL of Terrific Broth containing 100 µg/mL carbenicillin. Once bacterial growth is complete, Glycerol Stock the selected clones.

--Take 500 µL of overnight culture to 100 µL of 50% glycerol in water. Place in -80 °C.

6) From step 5a, prepare the PCR reaction mix as outlined below: Use colony PCR primers for screening, forward sequence: gccttttgctggccttttgctc and reverse sequence: cgttacataacttacggtaaatggcccg.

	Component	**Volume (µL)**
1	Nuclease-free H_2O	9
2	Orange-F primer (10 µM)	1.25
3	Orange-R primer (10 µM)	1.25
4	picked colony from step 5	1
5	NEB Q5 Hot Start HF 2X Master Mix	12.5
	TOTAL	**25**

7) Run the PCR on a thermocycler with the protocol outlined below.

Cycle Steps	**Temperature**	**Time**	Cycle number
Initial denaturation	98 °C	30 sec	1X
Denature	98 °C	5 sec	
Anneal	71 °C	10 sec	35X
Extend (~300 bp long)	72 °C	10 sec (25 sec/kbp)	
Final extension	72 °C	2 min	1X
Hold	4 °C	HOLD	1X

8) Run a 1% agarose gel to confirm band isolation.

a-Keep the colony that has one band (observe single large band ~300 bp).

Also include a sample as a control.

b-Perform a high-purity plasmid miniprep using QIAprep Spin Miniprep kit.

c-Send the sample for Sanger Sequencing using Genewiz

d- Discard glycerol stock that does not have a single band, ~300 bp.

Construction of the PITCh cutting vector (pX330A-DGKQ-PITCh).

Perform Golden Gate assembly:

9) Once pX330A-1x2 with desired DGKθ oligo is confirmed, mix the following components in a PCR tube:

	Component	**Volume (µL)**
1	Nuclease-free H_2O	14
2	pX330A-1x2 with desired oligo inserted	1
3	pX330S-2-PITCh	1
4	T4 DNA Ligase buffer (10X)	2
5	BsaI-HF	1
6	T4 DNA Ligase	1
	TOTAL	**20**

10) Perform PCR using the thermal cycler under the following conditions:

time	Time (min)
37 °C	5
16 °C	10
	Repeat 25X

a- 4 °C, hold.

11) Transform the products into XL1-Blue competent cells as follows:

Mix 1 µL of the products and 45 µL of XL1-Blue cells, and electroporate the mixture, using electroporation system. Place mixture into 450 µL of SOC media. Incubate the cells in a shaker incubator at 225 rpm at 37 °C for 60 min. Plate the transformed bacteria onto an LB plate containing 100 µg/mL Carbenicillin with X-Gal/IPTG, pour all the content onto the LB plate. Culture the bacteria overnight at 37 °C.

12) White/blue selection: identify and mark white colonies from the blue colonies.[30] From the LB plate, identify and mark (using a Sharpie) ~4 colonies. Pick each of the marked colonies using a sterile plastic toothpick.

13) For bacterial growth: transfer picked colony into 7 mL of Terrific Broth containing 100 µg/mL carbenicillin. Culture in incubator shaker overnight at 37 °C.

14) Once bacterial growth is completed.

--Add 500 µL of overnight culture to 100 µL of 50% glycerol in water. Place in -80 °C for long term storage.

15) Run the remaining bacterial growth on a 1% (wt/vol) agarose gel. Add all ingredients to the PCR tube (add restriction enzyme last) and incubate on a thermo-cycler (or heat block) set to 37° C for 2 hrs.

	Component	Volume (µL)
1	Nuclease-free H_2O	17
2	CutSmart	2.5
3	Plsmid	5
4	BsaI	0.5
	TOTAL	**25**

a- Inactivate at 65° C for 20 min.

b- Confirm correct band isolation. Also include an undigested sample as control (one band at ~10,000 bp). Confirm the presence of the intended bands, one major band. Observe single large band ~8,700 bp. If Assembly did not work, two bands (light band 440 bp and dark band at 8,300 bp) will be observed.

c- Discard the Glycerol Stocks in step 14 that have more than the two bands, especially with a 440 bp band.

d-Perform a high-purity plasmid miniprep using QIAprep Spin Miniprep kit.

e-Send the sample for Sanger Sequencing using Genewiz

Construction of the pPITCh repair vector (pCRIS-PITChv2-Puro-dTAG (DGK)).

Perform Gibson assembly:

16) Prepare plasmid DNA for pCRIS-PITChv2-dTAG (BRD4) using an appropriate miniprep kit. A schematic illustration of CRIS-PITCh (v2) vector construction is shown in **(Figure 3.3.1)**.

17) By using a high-fidelity DNA polymerase, one can perform two separate PCRs: one to amplify the vector (pCRIS-PITChv2-dTAG (BRD4) and one to amplify the insert. Here we linearize the vector and amplify the insert.

18) Linearize pCRIS-PITChv2 vector by digestion with MluI-HF. Set up the reaction mix as described below:

	Component	**Volume (µL)**
1	Nuclease-free H_2O	68
2	pCRIS-PITChv2-FBL (1 0 µg)	20
3	10x CutSmart buffer	10
4	MluI-HF	2
	TOTAL	**100**

19) Split the reaction in 2 x 50 µL and incubate for 2 h at 37 °C. Run on a 0.8% agarose gel, and purify the larger band (ca. 4500 bp) via gel extraction.

20) Amplify the dTAG cassette via PCR to introduce target gene specific microhomology arms. For the insert, use gene-specific primers containing the desired microhomologies. Primers should be carefully designed, because the pCRIS-PITChv2- dTAG (BRD4) contains two identical PITCh-gRNA target sequences, next to the 5′ and 3′ microhomologies. Use Primer insert frw:tccgcgttacatagcatcgtacgcgtacgtgtttggcgcggacctaaaggggctcgggccactaggtccag gaatgaccgagtacaagcccacggtggc and Primer insert rev: agcattctagagcatcgtacgcgtacgtgtttggcccgggctcggccgccgccgcagatccgccgccacc.

21) Prepare the PCR reaction mix as outlined below:

	Component	**Volume (µL)**
1	Nuclease-free H_2O	10.75
2	GC buffer	5
3	Q5 reaction buffer	5
4	Pink-F primer (10 µM)	1.25
5	Pink-R primer (10 µM)	1.25
6	10mM dNTPs	0.5
7	NEB Q5 polymerase	0.25
8	linearized pCRIS-PITChv2-FBL	1
	TOTAL	**25**

22) Run the PCR on a thermocycler with the protocol outlined below.

Cycle Steps	**Temperature**	**Time**	Cycle number
Initial denaturation	98 °C	30 sec	1X
Denature	98 °C	7 sec	
Anneal	70 °C	15 sec	5X
Extend (~1200 bp long)	72 °C	25 sec 20sec/kbp)	
Denature	98 °C	7 sec	
Anneal	72 °C	15 sec	25X
Extend (~1200 bp long)	72 °C	25 sec 20sec/kbp)	
Final extension	72 °C	2 min	1X
Hold	4 °C	HOLD	1X

23) Run the product on a 1% agarose gel, and purify the PCR product (ca. 1200 bp) by gel extraction.

24) Ligate the two purified DNA fragments using the Gibson Assembly. Insert the amplified dTAG cassette into the backbone via Gibson assembly. Mix 30 ng of MluI-digested vector backbone (step 16a) and 20 ng of amplified dTAG cassette (step 16c) and bring to 3 µL total volume. Then add 3 µL 2x NEBuilder HiFi Master Mix, mix thoroughly by pipetting up and down, and incubate for 30 min at 50 °C.

Set up the reaction mix as described below:

	Component	Volume (µL)
1	30 ng of MluI-digested vector backbone	2.0
2	20 ng of amplified dTAG cassette	1.0
3	2x NEBuilder HiFi Master Mix	3
	TOTAL	**6**

25) Add 15 µL nuclease-free H_2O to the mixed product, transform the product, and culture it overnight. The blue/white selection is not needed in this step.

26) Pick 2–4 colonies, and culture them with shaking overnight at 37 °C, in 7 mL of Terrific Broth medium containing 100 µg/mL carbenicillin. In addition, run the PCR product on a 1% (wt/vol) agarose gel.

	Component	Volume (µL)
1	Nuclease-free H_2O	9
2	Primer Forward (green-F) (10 µM)	1.25
3	Primer Reverse (green-R) (10 µM)	1.25
4	Plasmid pCRIS-PITChv2-DGKQ (Gibson)	1
5	NEB Q5 Hot Start HF 2X Master Mix	12.5
	TOTAL	**25**

27) Run the PCR on a thermocycler with the protocol outlined below.

Cycle Steps	**Temperature**	**Time**	Cycle number
Initial denaturation	98 °C	30 sec	1X
Denature	98 °C	5 sec	
Anneal	67 °C	10 sec	35X
Extend (~1361 bp long)	72 °C	27 sec (20-30 sec/kbp)	
Final extension	72 °C	2 min	1X
Hold	4 °C	HOLD	1X

28) Purify the plasmid using an appropriate miniprep kit. and purify the PCR product (ca. 1300 bp) by gel extraction.

29) Confirm the addition of the microhomologies by DNA sequencing using the donor-upstream-seq and donor-downstream-seq primers.

Cell culture and transfection

30) Culture HEK293T cells in 24-well plates. 2 mL of DMEM; containing 10% (vol/vol) FBS and 1x L-glutamine, at 37 °C with 5% CO_2.

31) Reverse transfection. When cells become 80% confluent in a 100 mm dish, remove the medium with an aspirator, add 4 mL of trypsin and incubate it for 5 min at 37 °C. Subsequently, add 10 mL of free-DMEM and transfer the cell solution to a 15 mL Falcon tube. Centrifuge for 5 min at 500*g* at room temperature (18–22 °C). Discard the supernatant, add 10 mL of free-DMEM and mix by pipetting. Repeat, centrifuge for 5 min at 500*g* at room temperature (18–22 °C). Discard the supernatant, add 500 µl of opti-MEM media and mix by pipetting. Seed ~1.0×10^5 cells.

32) *Transfection*. Add 1.06 µg of all-in-one CRISPR-Cas9 vector and 0.99 µg of CRIS-PITCh (v2) vector to a Microtube containing 22 µl of Opti-MEM, then add 4.11 µl of P3000 Reagent. Incubate mixture for 5 min at room temperature. In a second microtube, mix 24 µl with 1.7 µl of Lipofectamine 3000 reagent. Then, mix both microtubes and incubate them for 12 min at room temperature. Add the mixture to the cells in step 31 and pipette into a single well in a 24-well plate. Incubate the cells in a 5% CO_2 incubator at 37 °C for 5 hrs. Replace medium after 5 hrs with 2 mL of fresh DMEM, containing 10% (vol/vol) FBS and 1x L-glutamine.

33) 36 h after transfection, replace the medium with 2 mL of DMEM containing puromycin (2 µg/mL) daily for 7 days.

Single-cell cloning

34) After 5 to 7 days of puromycin exposure, replace media with media containing 10% (vol/vol) FBS and 1x L-glutamine and Penicillin-streptomycin. Collect an aliquot of cells from Steps 31 or 32. Adjust to 1.5–2.0 × 10^3 cells/mL by adding DMEM.

35) Check each well under a microscope to identify wells that contain only a single cell. There will be roughly 10 to 15 clone colonies in the 24-well plate. Transfer each clonal colony to a 96-well plate. Incubate the plate at 37 °C in a CO_2 incubator until confluency is reached.

36) Once confluency is reached in the 96-well plate, genotype clonal cells before transferring them to a 24-well plate.

Genotyping clonal cells

37) Extract genomic DNA from the clonal cells using a QuickExtract from Lucigen. Pipette 2.5 µL of clonal cells and mix with 20 µL of QuickExtract. 68 °C for 6 min, followed by 98 °C for 2 min, and hold at 4 °C

38) Perform genomic PCR as described below. Use Primer insert (purple-F) and Primer insert (purple-R).

Prepare the PCR reaction mix as outlined below:

	Component	**Volume (µL)**
1	Nuclease-free H_2O	10.75
2	GC buffer	5
3	Q5 reaction buffer	5
4	Pink-F primer (10µM)	1.25
5	Pink-R primer (10µM)	1.25
6	10mM dNTPs	0.5
7	NEB Q5 polymerase	0.25
8	linearized pCRIS-PITChv2-FBL	1
	TOTAL	**25**

39) Run the PCR on a thermocycler with the protocol outlined below.

Cycle Steps	**Temperature**	**Time**	Cycle number
Initial denaturation	98 °C	30 sec	1X
Denature	98 °C	10 sec	
Anneal	72 °C	30 sec	35X
Extend (~1388 bp long)	72 °C	27 sec (10-20 sec/kb)	
Final extension	72 °C	2 min	1X
Hold	4 °C	HOLD	1X

40) Run the PCR products on a 1% (wt/vol) agarose gel. Excise the intended band and collect the gel fragments in Microtubes.

41) Purify the DNA from the gel fragments using QIAprep Spin Miniprep kit, clean-up system, according to the manufacturer's instructions.

42) Confirm the genotype by direct sequencing. Send the sample for Sanger Sequencing using Genewiz.

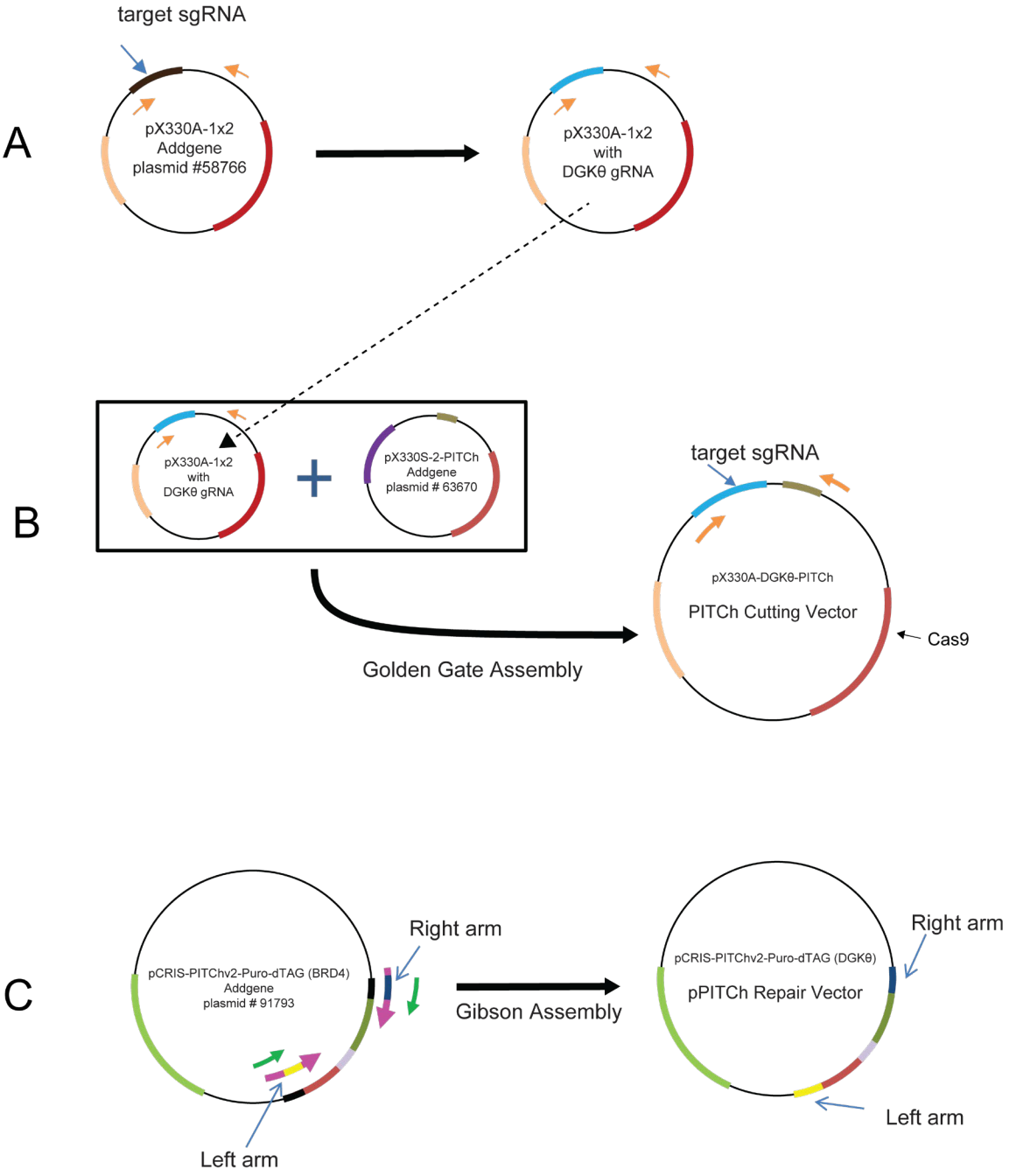

Figure 3.3.1 Assembly of dTAG system. (A) Once primers and oligomers have been purchased, sgRNA oligo can be inserted into designated plasmid. (B) Then perform a Golden Gate Assembly and (C) Gibson Assembly. Primers for colony PCR screening (orange arrows). To design gene-specific primers, simply replace the 5′ and 3′ microhomologies with the desired sequences (pink arrow heads).

Primers for sequencing the gene-specific microhomologies for colony PCR screening (green arrows). PCR primer for genomic PCR and DNA sequencing purple arrows).

3.4 *Results*

3.4.1 *Design of DGKθ sgRNAs into pX330A-1x2 Plasmid*

We were successful in annealing both DGKθ sgRNA oligonucleotides and then inserting them into the pX330A-1x2 plasmid **(Figure 3.3.1A)**. To verify the insertion, we digested the plasmid and ran the plasmids on a 1% agarose gel to confirm their expected band length. For pX330A-1x2 we got a band around 5 kbp **(Figure 3.4.4)**. The restriction enzyme that provided the best results was *BbsI*. In addition, there were several other restriction enzymes that we used to digest other plasmids but these were unsuccessful and they cut within our insert of interest. We also digested other plasmids that we purchased to verify their lengths.

We then verified our ligated pX330A-1x2 with both forward and reversed annealed sgRNA as shown in **(Figure 3.4.5)** on a 1% agarose gel with a single band around ~0.3 kbp, confirming successful annealing and digestion. The final confirmation of nucleic acid sequences of our constructed pX330A-1x2 was determined by Sanger Sequencing sent to Genewiz. The annealing of the two oligos and ligation of the backbone and annealed oligos resulted in the desired expression vector.[31]

3.4.2 *Construction of the PITCh Cutting Vector (pX330A-DGKθ-PITCh)*

Once pX330A-1x2-DGKθ-sgRNA was confirmed, we ligated pX330A-1x2-DGKθ-sgRNA with pX330S-2-PITCh plasmid to produce pX330A-DGKθ-PITCh **(Figure 3.3.1B)**. We attempt to verify the PCR products of pX330A-DGKθ-PITCh plasmid by agarose gel analysis. However, the pX330A-DGKθ-PITCh and

pX330A-1x2 have the same fragments of DNA when pulled through the gel matrix by the electric current, thus making it difficult to visualize the results. This technique did not yield good results **(Figure 3.4.6)**. Both plasmids provided similar bands (light band at 0.44 kbp and dark band at 10.3 kbp).

Instead, we performed a restriction digestion using *BbsI* (*BpiI*), with undigested (as control) along with blue-white screening, which is a rapid and efficient technique for the identification of recombinant bacteria. It relies on the activity of β-galactosidase, an enzyme occurring in E. coli, which cleaves lactose into glucose and galactose. We were confidently able to distinguish and verify both pX330A-DGKθ-PITCh and pX330A-1x2 plasmids. We verified that pX330A-1x2 (blue selection) had a total of three bands at 10 kbp, 8.3 kbp and 0.4 kbp **(Figure 3.4.7)**. pX330A-DGKθ-PITCh had only two bands at 6.0 and 10.0 kbp.

We also performed an additional restriction digestion with *MluI*. which provided similar results as with *BbsI*. Using *MluI* provided single band for pX330A-DGKθ-PITCh at 10.0 kbp **(Figure 3.4.8)**. pX330S-2-PITCh plasmid when digested with *MluI* also provided one band but it was slightly below 10.0 kbp. The pX330A-1x2 had only one band at 60.0 kbp. Final, verification for pX330A-DGKθ-PITCh was determined by Sanger Sequencing at Genewiz.

3.4.3 *Construction of the pPITCh Repair Vector, CRIS-PITCh-Puro-dTAG (DGKθ)*

The construction of CRIS-PITCh-Puro-dTAG(DGKθ) required three steps. The first step, we linearized pCRIS-PITChv2-Puro-dTAG (BRD4) by digestion with *MluI*-HF (High-Fidelity, which have the same specificity as the native enzyme

(*MluI*); but can be performed in a single buffer solution. The digestion was placed on a 1% agarose gel and it produced two bands at 1.5 kbp and 4.5 kbp **(Figure 3.4.9)**. We excised was the 4.5 kbp band for later use. Interestingly, we used vectors other than the pCRIS-PITChv2-Puro-dTAG (BRD4) vector for this step. These included pCRIS-PITChv2 vectors which provided the vector we needed for this step. We also used linearized pCRIS-PITChv2-FBL vector with successful results. When excising the band, we first placed the gel under a UV light and then using a sterilized scalpel blade, we cut out the desired band, including as little of the surrounding gel as possible.

In the second step, we amplified the dTAG cassette via PCR to introduce target gene-specific microhomologies arms specific for DGKθ. We ran our product on a 1% agarose gel and verified the product with a band at 1.2 kbp **(Figure 3.4.10)**. This required similar procedures as above. All other bands were discarded. Once we linearized pCRIS-PITChv2-Puro-dTAG (BRD4) and amplified the dTAG cassette, we combined both and performed a Gibson Assembly as the third step.[32]

3.4.4 *Gibson Assembly*

We ligated the two purified DNA fragments using the Gibson Assembly **(Figure 3.3.1C)**. We inserted the amplified dTAG cassette into the backbone via the Gibson Assembly. We ran the product on a 1% agarose gel and verified the PCR product bands at 1.3 kbp **(Figure 3.4.11)**. We then sent our sample to Genewiz for Sanger Sequencing to verify the nucleic acid sequence.

3.4.5 *Genotyping HEK293T Clones*

We performed a genomic PCR on the *WT* DGKθ exons of interest. We generated several different sequencing primers that attached to different sites on the DGKθ exons. The location of the dTAG also has an effect on how the dTAG will recruit the CRBN E3 ligase complex to targets fused with $FKBP12^{F36V}$. We placed the dTAG either on the N-terminus or C-terminus on an allele to compare dTAG function. The N-terminus provided better preliminary results; however, the C-terminus requires further investigation and may be a viable option.

We then verified the genomic PCR sequences (forward and reverse) on *WT* DGKθ clones **(Figure 3.4.12)**. The gel electrophoresis showed different bands which had different base pair lengths, 1.3 kbp, 0.3 kbp, and 0.6 kbp **(Figure 3.4.12)**. These different base pairs are due to the different location of the sequencing primers targeting different regions of the locus of interest. We chose the PCR sequencing primers that gave a band around 0.4 kbp, to differentiate the knocked-in dTAG DGKθ exons, which will have a PCR sequence around 1.5 kbp.

3.4.6 *Genotyping DGKθ and BRD4 Knock-In (KI) Clones in HEK293T*

Once we determined that the sequencing primers were binding and produce bands on the agarose gel, we proceeded to use these primers on KI dTAG DGKθ colonies produced from HEK293T cells. We achieved preliminary results using dTAG technology in the HEK293T cell line. We successfully showed that we knocked-in dTAG on the endogenous DGKθ protein HEK293T cells. Our preliminary results confirmed that HEK293T cells expressing DGKθ-$FKP12^{F36V}$

produced an expected band on the agarose gel **(Figure 3.4.13)**. A band length of 1.5 kbp on the gel indicates that the knock-in of the dTAG occurred. However, there were two bands indicating that wild type DGKθ was present, 0.4 kbp. This may be due to HEK293T cells being hypotriploid. We also attempted to perform the KI in U87MG cells, which are diploid, unsuccessfully. In addition, we attempted to transfect COLO205 (hypertriploid) and Jurkat (polyploid) live cells unsuccessfully. **(Figure 3.4.14)** presents the results of genotyping several colonies of DGKθ. In addition, we generated, as a positive control, a KI dTAG-BRD4 in HEK293T. Only one sample (#101) generated a KI **(Figure 3.4.14)**. To confirm BRD4 sample #101 can be reproduced, we reran #101, which we confirmed that it produced a band at 2.0 kbp **(Figure 3.4.15)**, indicative of dTAG KI in BRD4. This colony was saved and later tested on a western blot to verify it using HA antibodies. On the other hand, DGKθ knock-in results were promising. Lanes marked #1, #98 were two of six colonies that showed promising results. Not all of these KI have the same base pair length. They are slightly higher or lower around the length of 1.5 kbp. This indicates that the sites where the knock-ins occurred are not the same.

3.4.7 *Genotyping WT and KI DGK(α and ξ) KI Clones HEK293T*

We also performed PCR electrophoresis on WT DGK along with DGKα and DGKξ proteins **(Figure 3.4.18)**. The bands on the gel show different sequencing primers targeting different regions on the locus of interest. In the first two of four sites, the primers target DGK α at site 1. For the third and fourth sequencing primers, the primers of DGK α target site 3 There were three sets of primers that

target two sites for DGKξ. Unfortunately, site 1 did not provide a band showing that the region of interest is difficult to reach with the generated primers. However, the two other sites did show bands.

We then performed another set of PCR gels on KI dTAG on DGKα and DGKξ proteins using the sequencing primers we set on the *WT* **(Figure 3.4.19)** and **(Figure 3.4.20)**. We propose establishing dTAG DGKα and DGKξ fusion protein vectors. The colonies for DGKα did not provide the correct band suggesting that a knock-in did not occur **(Figure 3.4.19)**. However, DGKξ did provide one colony with the correct band indicating that a knock-in occurred. Another set of colonies for DGK α did provide the correct band to suggest that a knock-in occurred **(Figure 3.4.20)**.

3.4.8 *Verification of BRD4 and DGKθ KI Protein Expression*

We achieved preliminary results using dTAG technology in live HEK293T cells. Our Western blot results show that we were partially successful in knocking-in the dTAG BRD4 and DGKθ protein of interest (POI) in HEK293T cells **(Figure 3.4.16)**. We tested two degradation ligands dTAG-13 and HaloPROTAC3 to see if we could knock-down our protein of interest, 300nM for 8 hrs **(Figure 3.4.1)**. As shown after expose to anti-HA primary, BRD4 was knocked-down with dTAG-13 but not with the HaloPROTAC3 ligand.

In similar response, DGKθ was knocked-down using dTAG-13, but not with HaloPROTAC3 **(Figure 3.4.2)**. Of interesting note, when using anti-DGKθ, there was no knock-down observed. It suggests that our knock-in is partial and not all

alleles had the dTAG knocked-in. Unfortunately, we did not have the anti-body for BRD4 so we were not able to confirm if BRD4 was completely knocked-in or not. Our preliminary results confirm HEK293T cells expressing DGKθ-FKP12^{F36V} **(Figure 3.4.2)**. It is interesting to note that HEK293T cells are hypotriploid, which made the KI challenging. We attempted to KI in U87MG cell lines, which are diploid, but it was not successful. In addition, we will attempt to transfect COLO205 (hypertriploid) and Jurkat (polyploid) cells but due to it hyperploid alleles, KI of the dTAG was not possible.

3.4.9 *Verification of DGKα and DGKξ KI Protein Expression*

We ran a western blot for our knock-ins of dTAG DGKα and DGKξ fusion protein vectors. Our preliminary results did not show a complete knock-in for both DGKs. Our results show that DGKα was knocked-out **(Figure 3.4.3)** rather than a KI. DGKξ showed no KI of the dTAG.

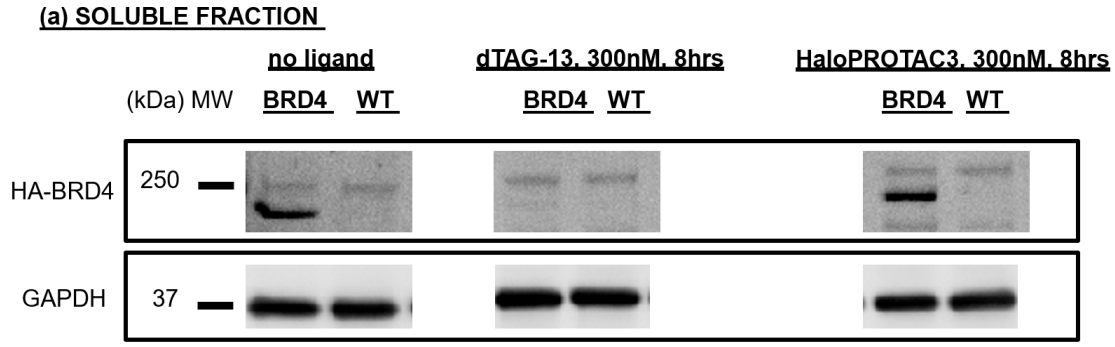

Figure 3.4.1: immunoblot of BRD4. Soluble fraction, analysis of HEK293T cells expressing BRD4-FKBP12^{F36V}. KI, Immunoblot analysis of BRD4 (254 kDa), wild-type, No knock-down observed for DGKθ when using HaloPROTAC3 at 300nM for 8 hrs.

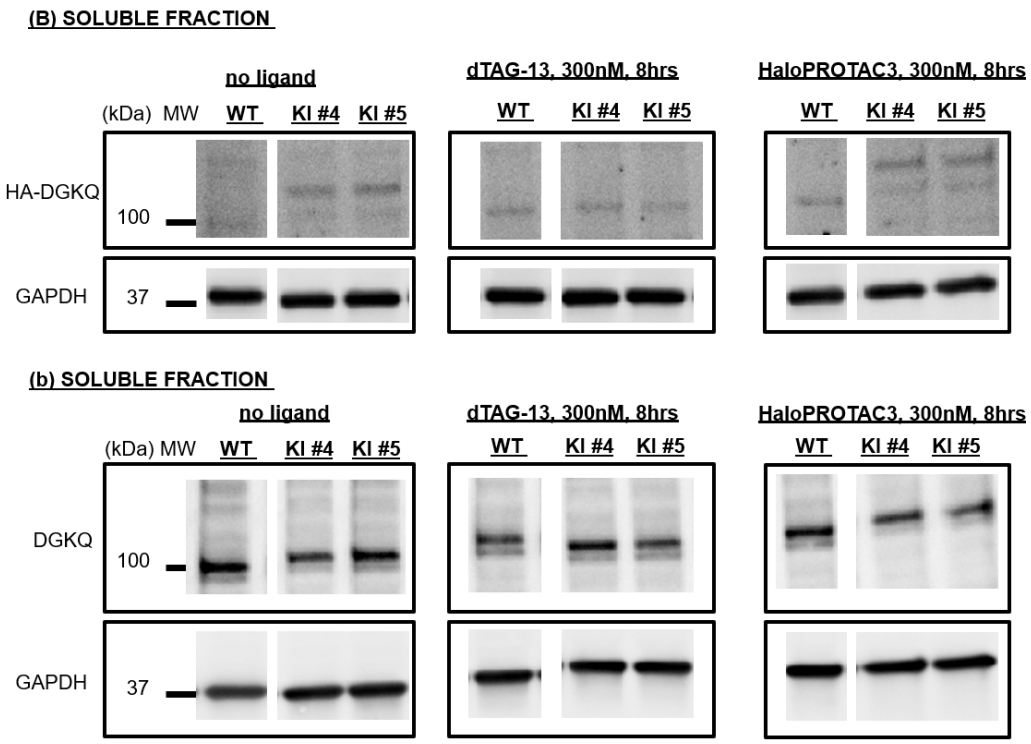

Figure 3.4.2: immunoblot, soluble fraction, analysis of HEK293T cells expressing DGKθ-FKBP12^{F36V}. KI, Immunoblot analysis of BRD4 (154 kDa), DGKθ wild-type (101 kDa), and DGKθ-FKBP12^{F36V} (112 kDa). (a) When using dTAG-13 at 300nM for 8 hrs., HA-tag Knock-down for DRD4 and DGKθ KI#4 and KI#5 observed. When using HaloPROTAC3 at 300nM for 8 hrs., no HA-tag knock-down observed for BRD4 and DGKθ. (b) no correlation to DGKθ band at 112 kDa, suggesting band knock-in of DGKθ-FKBP12^{F36V} was either unsuccessful or partial.

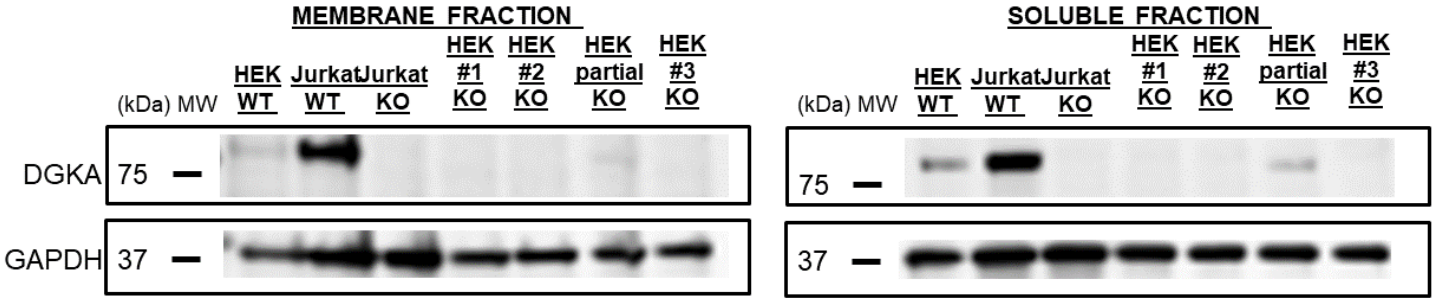

Figure 3.4.3 immunoblot of DGKα. Membrane and soluble partitions, analysis of HEK293T cells expressing DGKα-FKBP12^{F36V}. DGKα cell line expressed KO instead of KI, Immunoblot analysis of DGKα wild-type (82 kDa).

Figure 3.4.4

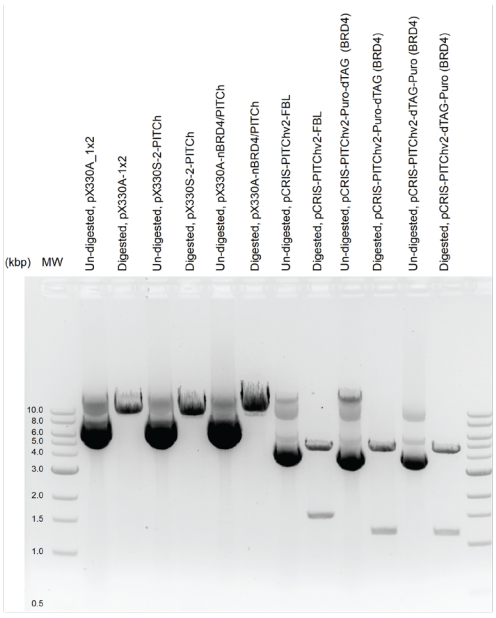

BbsI (BpiI)

Figure 3.4.5

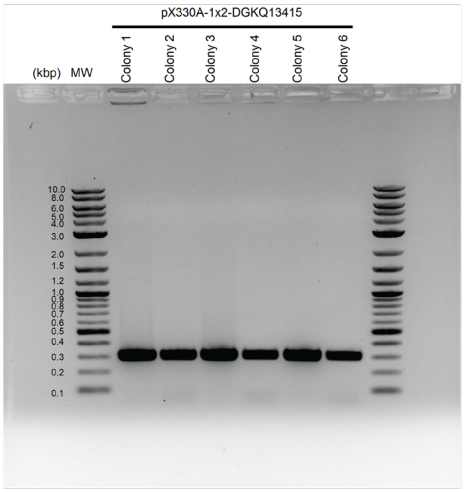

Figure 3.4.6

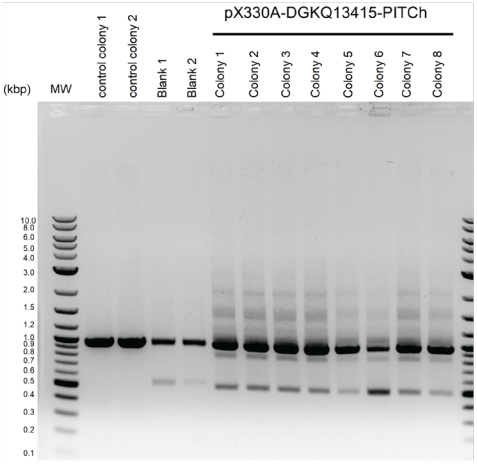

PCR seq

Figure 3.4.7

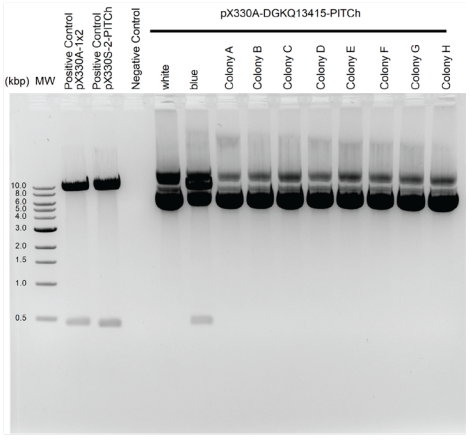

BbsI (BpiI)

Figure 3.4.8

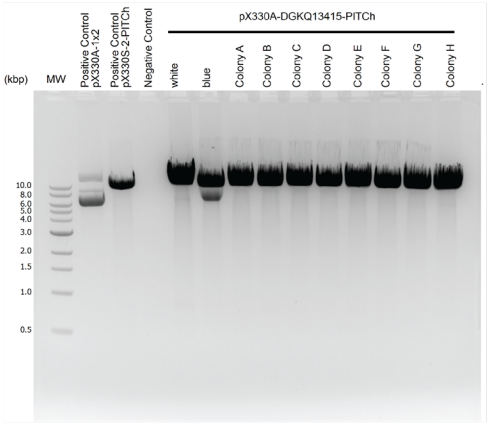

MluI-HF

Figure 3.4.9

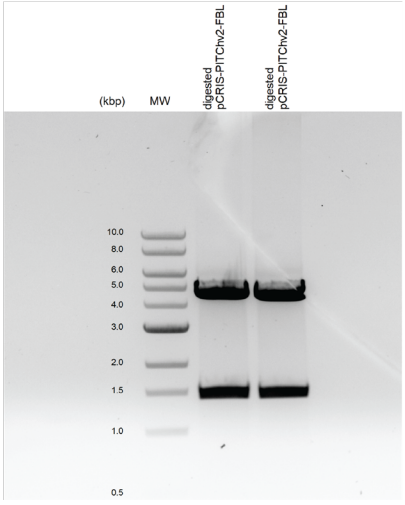

PCR seq

Figure 3.4.10

PCR seq

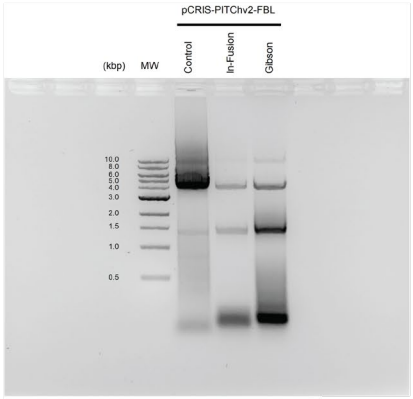

Figure 3.4.11

PCR seq

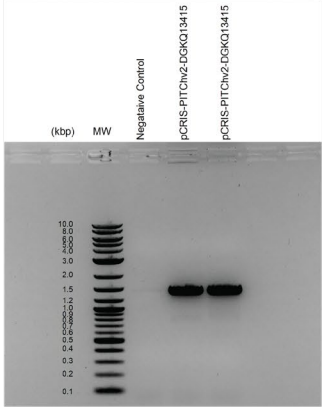

Figure 3.4.12

PCR seq
WT DGKθ

using
θ primers

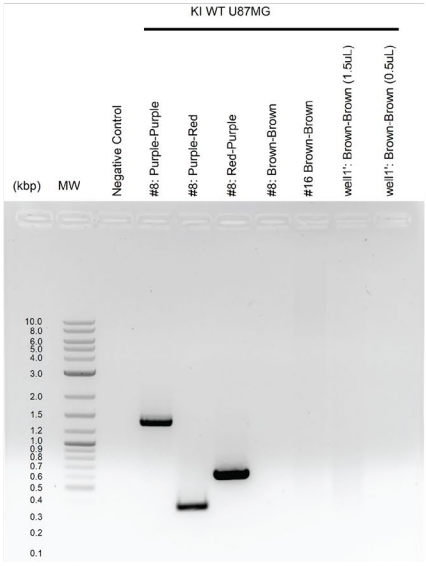

Figure 3.4.13

PCR seq
knock-In
dTAG-DGKθ

using
θ primers

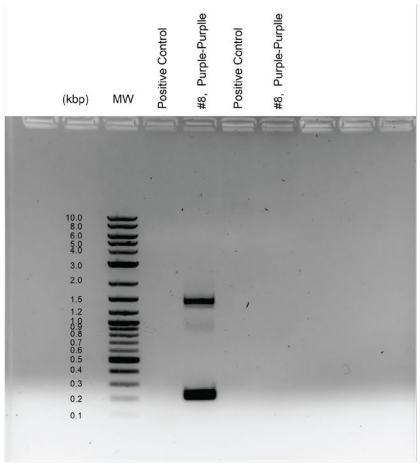

Figure 3.4.14

PCR seq
knock-In
dTAG-BRD4
dTAG-DGKθ

using
BRD4 and
θ primers

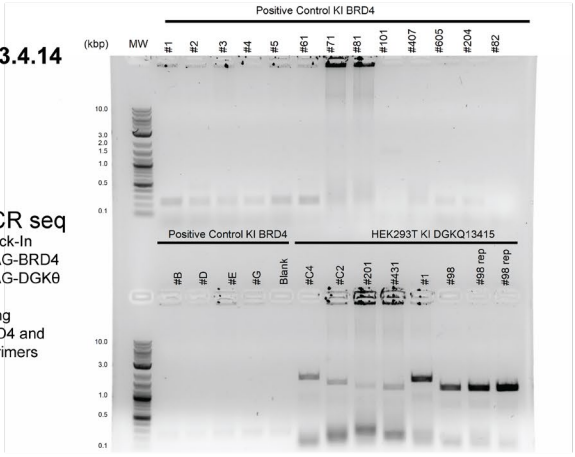

Figure 3.4.15

PCR seq
knock-In
dTAG-BRD4

using
BRD4 primers

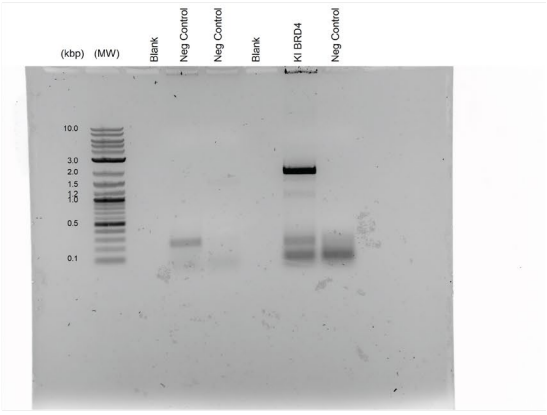

Figure 3.4.16

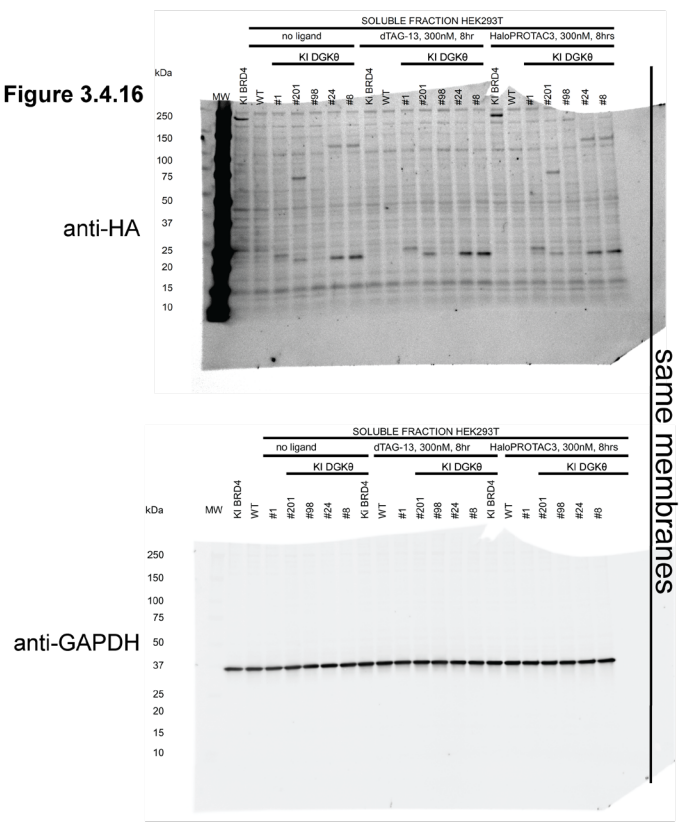

Figure 3.4.17

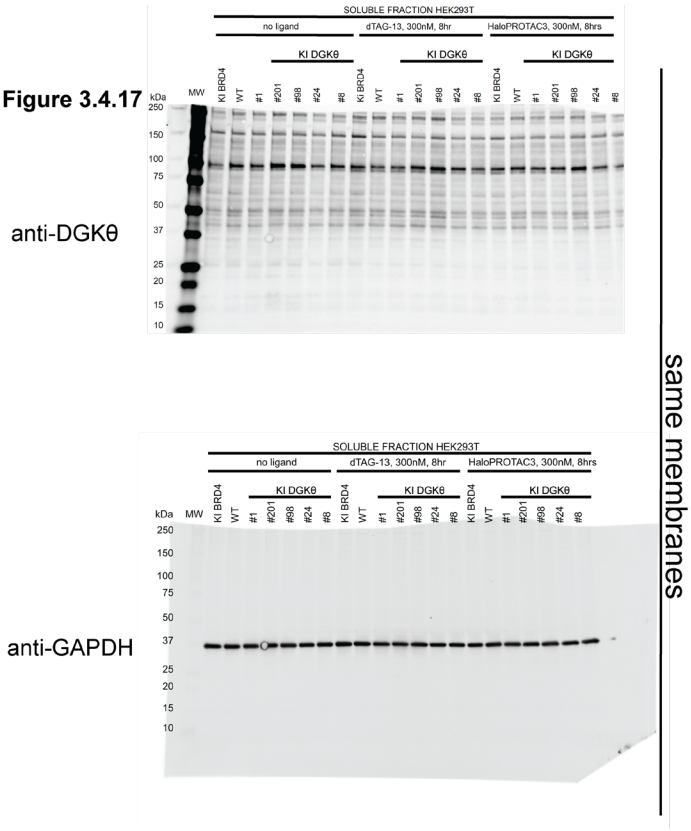

Full panel membranes for **(Figure 3.4.1)** and **(Figure 3.4.2)**

Figure 3.4.18

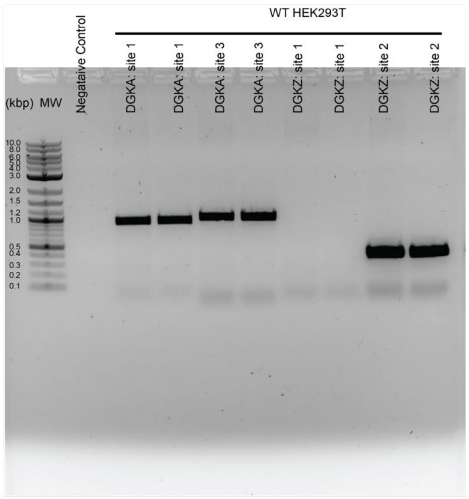

PCR seq
WT DGK

using
α and ζ primers

Figure 3.4.19

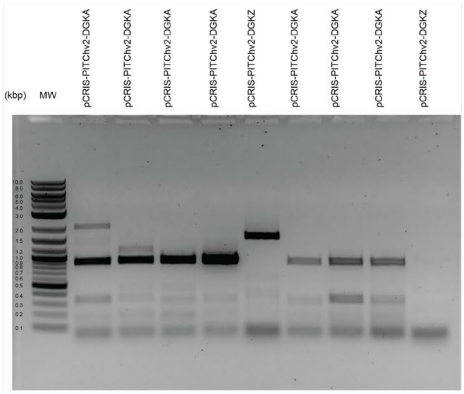

PCR seq
Knock-In
dTAG-DGK α and ζ

using
α and ζ primers

Figure 3.4.20

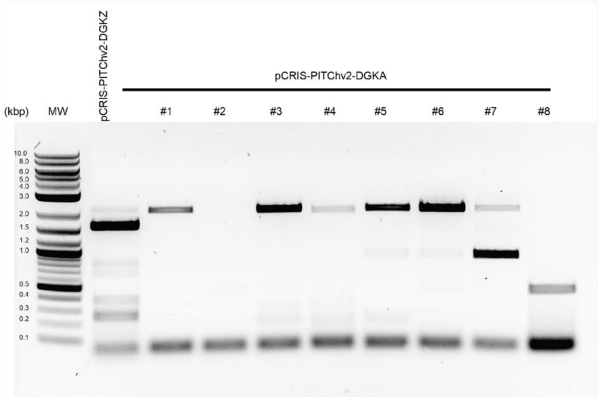

PCR seq
Knock-In
dTAG-DGK α

using
α primers

Figure 3.4.21

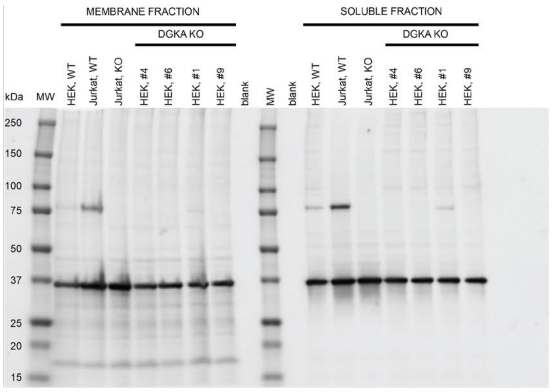

anti-DGKα

anti-GAPDH

(Figure 3.4.21), full panel membrane for **(Figure 3.4.3)**

3.5 *Discussion*

Chemical-genetic model systems capable of precise temporal control of a target protein of interest (at the protein level) can provide important insights into cellular signaling and transcription.[2] Here, we attempted to incorporate dTAG systems into DGK isoforms (θ, α, and ξ) proteins in different cell lines (HEK293T, Col209, U87MG, and Jurkat) to obtain a better understanding of their metabolic mechanisms, which serves as critical regulatory point in cell signaling. We also attempted to place the dTAG either on the N-terminus or the C-terminus on DGK (θ, α, and ξ) proteins to better understand how the dTAG will recruit the CRBN E3 ligase complex to targets fused with $FKBP12^{F36V}$. Here, we deployed dTAG ligand with a dTAG-directed binding element to decrease the abundances of (down regulate) three DGK isozymes in live cells.

There are many workflow approaches when it comes to gene editing a knock-in tag on an endogenous gene target. We presented one approach that we believe is facile enough to engineer a targeted protein degradation using a CRISPR/Cas9 system to achieve locus-specific $FKBP12^{F36V}$ knock-in to exogenously express $FKBP12^{F36V}$ fused to a target of interest with promising results.[2] We showed that the degrader dTAG-13 ligand requires CRBN to induce degradation and is highly selective for $FKBP12^{F36V}$. In other words, to degrade the dTAG protein, it requires nanomolar concentrations of the ligand to achieve high selectivity in the cells.

The dTAG system does not required additional elements to KI the tag on an endogenous protein of interest. The dTAG system relies on the cell's intrinsic

degradation machinery and does not require additional ubiquitin proteasome system machinery, which make the dTAG facile to use and generate. This is unlike other knock-in tags, such as AID tag, which require high doses of auxin and exogenous expression to achieve degradation.[2, 33-35]

Here, we employed the PITCh approach, which uses MMEJ and eliminates the need for creating long homology arms.[18] Instead, we were able to achieve short homology arms. We also generated clonal cell lines with homozygous N-terminal FKBP12^{F36V} knock-in at the DGKθ, DGKα, and DGKξ. We attempted but were not successful in isolating clones with homozygous C-terminal FKBP12^{F36V}.

Our work establishes important foundational work to enable future targeted protein degradation efforts on DGKs. We note that these studies will likely require further verification of the KIs we generated and appropriate cell studies for evaluation of native counterparts. When creating these knock-ins, it is advisable to use lentiviral plasmids to first evaluate exogenous expression of N- or C-terminally tagged targets to ensure protein functionality exists before attempting CRISPR-mediated knock-ins. Despite the issues encountered, our success experiments show that the protocol has potential for further development and may yet be useful in studying the metabolic function of DGKs.

3.6 *Acknowledgments*

We thank all members of the Hsu Lab for helpful discussions about dTAG. We thank Behnam Nabet, Department of Biological Chemistry and Molecular Pharmacology, Harvard Medical School, Boston, MA, USA, for providing insight and guidance with dTAG system. In addition, Xiaolong Wei from the Adli lab for helping us with CRISPR biology techniques. This work was supported by the Pharmacology Science Training Grant, Department of Pharmacology, Charlottesville, VA, USA. In addition, we would like to thank the resource support from Qiagen, Takara, Lucigen, New England BioLabs, Synthesgo, IDT, R&D Systems, and Thermo Scientific.

3.7 *References*

(1) Nabet, B. Charting a New Path Towards Degrading Every Protein. *Chembiochem* **2021**, *22* (3), 483-484. DOI: 10.1002/cbic.202000531.

(2) Nabet, B.; Roberts, J. M.; Buckley, D. L.; Paulk, J.; Dastjerdi, S.; Yang, A.; Leggett, A. L.; Erb, M. A.; Lawlor, M. A.; Souza, A.; et al. The dTAG system for immediate and target-specific protein degradation. *Nature Chemical Biology* **2018**, *14* (5), 431-+. DOI: 10.1038/s41589-018-0021-8.

(3) Moll, J. r.; Colombo, R. *Target identification and validation in drug discovery : methods and protocols*; Humana Press, 2013.

(4) Chopra, R.; Sadok, A.; Collins, I. A critical evaluation of the approaches to targeted protein degradation for drug discovery. *Drug Discovery Today: Technologies* **2019**, *31*, 5-13. DOI: doi.org/10.1016/j.ddtec.2019.02.002.

(5) Collins, I.; Wang, H.; Caldwell, J. J.; Chopra, R. Chemical approaches to targeted protein degradation through modulation of the ubiquitin-proteasome pathway. *Biochem J* **2017**, *474* (7), 1127-1147. DOI: 10.1042/BCJ20160762.

(6) Wang, Y.; Jiang, X.; Feng, F.; Liu, W.; Sun, H. Degradation of proteins by PROTACs and other strategies. *Acta Pharm Sin B* **2020**, *10* (2), 207-238. DOI: 10.1016/j.apsb.2019.08.001.

(7) Lee, J.; Bayarsaikhan, D.; Bayarsaikhan, G.; Kim, J. S.; Schwarzbach, E.; Lee, B. Recent advances in genome editing of stem cells for drug discovery and therapeutic application. *Pharmacol Ther* **2020**, *209*, 107501. DOI: 10.1016/j.pharmthera.2020.107501 From NLM Medline.

(8) Li, H.; Yang, Y.; Hong, W.; Huang, M.; Wu, M.; Zhao, X. Applications of genome editing technology in the targeted therapy of human diseases: mechanisms, advances and prospects. *Signal Transduct Target Ther* **2020**, *5* (1), 1. DOI: 10.1038/s41392-019-0089-y From NLM Medline.

(9) Bensimon, A.; Pizzagalli, M. D.; Kartnig, F.; Dvorak, V.; Essletzbichler, P.; Winter, G. E.; Superti-Furga, G. Targeted Degradation of SLC Transporters Reveals Amenability of Multi-Pass Transmembrane Proteins to Ligand-Induced Proteolysis. *Cell Chemical Biology* **2020**, *27* (6), 728-+. DOI: 10.1016/j.chembiol.2020.04.003.

(10) Buckley, D. L.; Raina, K.; Darricarrere, N.; Hines, J.; Gustafson, J. L.; Smith, I. E.; Miah, A. H.; Harling, J. D.; Crews, C. M. HaloPROTACS: Use of small molecule PROTACs to induce degradation of HaloTag fusion proteins. *ACS Chem Biol* **2015**, *10* (8), 1831-1837. DOI: 10.1021/acschembio.5b00442.

(11) Yesbolatova, A.; Tominari, Y.; Kanemaki, M. T. Ligand-induced genetic degradation as a tool for target validation. *Drug Discov Today Technol* **2019**, *31*, 91-98. DOI: 10.1016/j.ddtec.2018.11.001.

(12) Pettersson, M.; Crews, C. M. PROteolysis TArgeting Chimeras (PROTACs) - past, present and future. *Drug Discov Today Technol* **2019**, *31*, 15-27. DOI: 10.1016/j.ddtec.2019.01.002.

(13) Yesbolatova, A.; Kanemaki, M. T. TAGing for destruction. *Nat Chem Biol* **2018**, *14* (5), 414-415. DOI: 10.1038/s41589-018-0024-5.

(14) Zhong, Y.; Chi, F.; Wu, H.; Liu, Y.; Xie, Z.; Huang, W.; Shi, W.; Qian, H. Emerging targeted protein degradation tools for innovative drug discovery: From classical PROTACs to the novel and beyond. *Eur J Med Chem* **2022**, *231*, 114142. DOI: 10.1016/j.ejmech.2022.114142 From NLM Medline.

(15) Lin, D. W.; Chung, B. P.; Huang, J. W.; Wang, X. R.; Huang, L.; Kaiser, P. Microhomology-based CRISPR tagging tools for protein tracking, purification, and depletion. *Journal of Biological Chemistry* **2019**, *294* (28), 10877-10885. DOI: 10.1074/jbc.RA119.008422.

(16) Winter, G. E.; Buckley, D. L.; Paulk, J.; Roberts, J. M.; Souza, A.; Dhe-Paganon, S.; Bradner, J. E. Phthalimide conjugation as a strategy for in vivo target protein degradation. *Science* **2015**, *348* (6241), 1376-1381. DOI: 10.1126/science.aab1433.

(17) An, S.; Fu, L. Small-molecule PROTACs: An emerging and promising approach for the development of targeted therapy drugs. *EBioMedicine* **2018**, *36*, 553-562. DOI: 10.1016/j.ebiom.2018.09.005.

(18) Sakuma, T.; Nakade, S.; Sakane, Y.; Suzuki, K. T.; Yamamoto, T. MMEJ-assisted gene knock-in using TALENs and CRISPR-Cas9 with the PITCh systems. *Nat Protoc* **2016**, *11* (1), 118-133. DOI: 10.1038/nprot.2015.140.

(19) Sakamoto, K. M.; Kim, K. B.; Kumagai, A.; Mercurio, F.; Crews, C. M.; Deshaies, R. J. Protacs: Chimeric molecules that target proteins to the Skp1-Cullin-F box complex for ubiquitination and degradation. *P Natl Acad Sci USA* **2001**, *98* (15), 8554-8559. DOI: DOI 10.1073/pnas.141230798.

(20) Sakuma, T.; Woltjen, K. Nuclease-mediated genome editing: At the front-line of functional genomics technology. *Dev Growth Differ* **2014**, *56* (1), 2-13. DOI: 10.1111/dgd.12111 From NLM Medline.

(21) Esvelt, K. M.; Mali, P.; Braff, J. L.; Moosburner, M.; Yaung, S. J.; Church, G. M. Orthogonal Cas9 proteins for RNA-guided gene regulation and editing. *Nature Methods* **2013**, *10* (11), 1116-1121. DOI: 10.1038/Nmeth.2681.

(22) Cong, L.; Ran, F. A.; Cox, D.; Lin, S. L.; Barretto, R.; Habib, N.; Hsu, P. D.; Wu, X. B.; Jiang, W. Y.; Marraffini, L. A.; et al. Multiplex Genome Engineering Using CRISPR/Cas Systems. *Science* **2013**, *339* (6121), 819-823. DOI: 10.1126/science.1231143.

(23) Nakade, S.; Tsubota, T.; Sakane, Y.; Kume, S.; Sakamoto, N.; Obara, M.; Daimon, T.; Sezutsu, H.; Yamamoto, T.; Sakuma, T.; et al. Microhomology-mediated end-joining-dependent integration of donor DNA in cells and animals using TALENs and CRISPR/Cas9. *Nature Communications* **2014**, *5*. DOI: ARTN 5560.10.1038/ncomms6560.

(24) Gratz, S. J.; Cummings, A. M.; Nguyen, J. N.; Hamm, D. C.; Donohue, L. K.; Harrison, M. M.; Wildonger, J.; O'Connor-Giles, K. M. Genome engineering of Drosophila with the CRISPR RNA-guided Cas9 nuclease. *Genetics* **2013**, *194* (4), 1029-1035. DOI: 10.1534/genetics.113.152710 From NLM Medline.

(25) Wang, H. Y.; Yang, H.; Shivalila, C. S.; Dawlaty, M. M.; Cheng, A. W.; Zhang, F.; Jaenisch, R. One-Step Generation of Mice Carrying Mutations in Multiple Genes by CRISPR/Cas-Mediated Genome Engineering. *Cell* **2013**, *153* (4), 910-918. DOI: 10.1016/j.cell.2013.04.025.

(26) Yasue, A.; Mitsui, S. N.; Watanabe, T.; Sakuma, T.; Oyadomari, S.; Yamamoto, T.; Noji, S.; Mito, T.; Tanaka, E. Highly efficient targeted mutagenesis in one-cell mouse embryos mediated by the TALEN and CRISPR/Cas systems. *Sci Rep* **2014**, *4*, 5705. DOI: 10.1038/srep05705 From NLM Medline.

(27) Taleei, R.; Nikjoo, H. Biochemical DSB-repair model for mammalian cells in G1 and early S phases of the cell cycle. *Mutat Res-Gen Tox En* **2013**, *756* (1-2), 206-212. DOI: 10.1016/j.mrgentox.2013.06.004.

(28) Sakuma, T.; Nishikawa, A.; Kume, S.; Chayama, K.; Yamamoto, T. Multiplex genome engineering in human cells using all-in-one CRISPR/Cas9 vector system. *Sci Rep* **2014**, *4*, 5400. DOI: 10.1038/srep05400 From NLM Medline.

(29) Erb, M. A.; Scott, T. G.; Li, B. E.; Xie, H. F.; Paulk, J.; Seo, H. S.; Souza, A.; Roberts, J. M.; Dastjerdi, S.; Buckley, D. L.; et al. Transcription control by the ENL YEATS domain in acute leukaemia. *Nature* **2017**, *543* (7644), 270-+. DOI: 10.1038/nature21688.

(30) Julin, D. A. Blue/White Selection. In *Molecular Life Sciences*, Wells, R. D., Bond, J. S., Klinman, J., Masters, B. S. S. Eds.; Springer New York, 2018; pp 72-73.

(31) Fu, Y. F.; Reyon, D.; Joung, J. K. Targeted Genome Editing in Human Cells Using CRISPR/Cas Nucleases and Truncated Guide RNAs. *Use of Crispr/Cas9, Zfns, and Talens in Generating Site-Specific Genome Alterations* **2014**, *546*, 21-45. DOI: 10.1016/B978-0-12-801185-0.00002-7.

(32) Li, L.; Jiang, W. H.; Lu, Y. H. A Modified Gibson Assembly Method for Cloning Large DNA Fragments with High GC Contents. *Synthetic Metabolic Pathways* **2018**, *1671*, 203-209. DOI: 10.1007/978-1-4939-7295-1_13.

(33) Zhou, Q. H.; Derti, A.; Ruddy, D.; Rakiec, D.; Kao, I.; Lira, M.; Gibaja, V.; Chan, H. M.; Yang, Y.; Min, J. X.; et al. A Chemical Genetics Approach for the Functional Assessment of Novel Cancer Genes. *Cancer Research* **2015**, *75* (10), 1949-1958. DOI: 10.1158/0008-5472.Can-14-2930.

(34) Natsume, T.; Kiyomitsu, T.; Saga, Y.; Kanemaki, M. T. Rapid Protein Depletion in Human Cells by Auxin-Inducible Degron Tagging with Short Homology Donors. *Cell Reports* **2016**, *15* (1), 210-218. DOI: 10.1016/j.celrep.2016.03.001.

(35) Sreekanth, V.; Zhou, Q.; Kokkonda, P.; Bermudez-Cabrera, H. C.; Lim, D.; Law, B. K.; Holmes, B. R.; Chaudhary, S. K.; Pergu, R.; Leger, B. S.; et al. Chemogenetic System Demonstrates That Cas9 Longevity Impacts Genome Editing Outcomes. *ACS Cent Sci* **2020**, *6* (12), 2228-2237. DOI: 10.1021/acscentsci.0c00129 From NLM PubMed-not-MEDLINE.

Chapter 4. Identifying Reactive Sites on DGKs for Covalent Binding in Cells

Adapted from: **Mendez, R.**, Shaikh, M., Lemke, M.,Yuan, K., Libby, A., Bai, D., Ross, M., Harris, T., and Hsu, K. Identifying reactive sites on diacylglycerol kinases for covalent binding in cells*. Cell Chemical Biology* (2022) *Under Review*.

Introduction and Relevance to Collective Thesis Work:

There are ten diacylglycerol kinases (DGK) isoforms that share conserved lipid kinase domains, each having two C1 domains (tandem C1A and C1B) with the except of DGKθ having three. The relevance of this work with the rest of the chapters in this dissertation is that this chapter investigates DGK metabolomic functions to bridge gaps in our knowledge by applying novel technologies to explore deeper into DGKs function as seen in Chapter 2 and 3.

My Contribution to this Collaboration:

My contribution to this chapter are gel-based chemical proteomic assay, SILAC sample preparation for MS-based chemical proteomic assay, and run samples on LC-MS/MS chemical proteomics.

4.1 *Abstract*

Diacylglycerol kinases (DGKs) are metabolic kinases involved in regulating cellular levels of diacylglycerol and phosphatidic lipid messengers. The development of selective inhibitors for individual DGKs has been hindered partially by a lack of understanding of ligand binding in cellular environments. Here we utilized a sulfonyl-triazole probe (TH211) to establish a comprehensive map of protein-small molecule interactions for all members of the DGK superfamily in

cells. Treatment of recombinant DGK expressing cells with TH211 facilitated chemoproteomic identification of modified tyrosine and lysine sites found in catalytic and regulatory domains. Notably, we discovered that DGK chimera proteins, containing C1 domains exchanged across subtypes, displayed isoform-specific effects on probe recognition and biochemical activity. Collectively, we provide a family-wide ligand binding map of reactive sites found in functional domains of DGKs to guide inhibitor development efforts.

4.2 *Introduction*

Diacylglycerol kinases (DGKs) are multidomain lipid kinases that catalyze ATP-dependent phosphorylation of diacylglycerol (DAG) to generate phosphatidic acid (PA)[1]. DAG functions as a lipid messenger in signal transduction and can also serve as a structural components of membranes and a building block for lipid metabolism[2]. PA mediates signaling through binding to cognate receptor proteins and can serve as a precursor for lysophospholipids and glycero(phospho)lipids[3]. DGK activity is implicated in regulating the levels and fatty acyl composition of DAG and PA in cells although the molecular basis of this specificity remains poorly understood **(Figure 4.2.1A)**. Recent efforts using chemical proteomics support crosstalk between catalytic and regulatory domains of DGKs as a potential mechanism for substrate selectivity[1, 4].

Mammals express 10 known DGK isoforms that share conserved lipid kinase domains (split into the DAG-kinase catalytic domain (DAGKc and DAGKa) regions) and a minimum of two C1 domains (tandem C1A and C1B). DGKs are differentiated principally by regulatory domains that are implicated in regulation of DGK activation (EF hand motifs), membrane localization (PH domain), and protein-protein interactions (PDZ domain)[5] **(Figure 4.2.1B)**. DGK metabolism and signaling can be regulated through cell type- and tissue-specific expression[5-8]. For example, the expression of DGKα and DGKξ is enriched in T cells compared with other cell and tissue types[9]. Consequently, knockout of these DGK isoforms in mice results in immunological phenotypes including enhanced Ras and mitogen-activated protein kinase (MAPK) activation in response to T cell receptor (TCR)

stimulation[10, 11]. These findings support DGKs as metabolic 'checkpoints' for TCR-MAPK signaling by restricting available DAG messengers for signal transduction. Overactive DGKα and/or DGKξ has been implicated in defective tumor immune responses, and development of selective inhibitors of these T cell-specific DGKs is being actively pursued for immunotherapy[9-23].

Recently, we reported that ATP acyl phosphate activity-based probes can identify DGK sites mediating substrate and inhibitor binding in native lysates[1]. ATP acyl phosphates are used for global, activity-based profiling of ATP-binding pockets of kinases and ATPases. This activity-based probe is directed to kinase active sites by ATP recognition followed by covalent binding of lysines proximal to the acyl phosphate electrophile[24, 25]. Competitive studies with free ATP identified ATP substrate-binding sites in the catalytic domain of representative members of all five DGK subtypes[1]. Furthermore, this study implicated the cysteine rich (C1) domain of rat DGKα (K237), human DGKξ (K323), and human DGKθ (K202) in recognition of the ATP acyl phosphate probe. DGKs – except for DGKβ and DGKγ – express atypical C1 domains of poorly defined function that are distinct from typical counterparts used by protein kinase C (PKC) for DAG-mediated translocation and activation[26, 27]. Functional lipidomics identified C1 domains as important mediators of DAG lipid substrate specificity of DGKs that could be exchanged between type 1 DGK family members[1, 4].

The chemoproteomic studies to date have been performed largely in cell lysates[1]. While informative, the binding profiles obtained in vitro may not reflect protein states that are subject to dynamic regulation in cellular environments. We

developed a first-generation covalent probe, TH211, capable of functional profiling of DGKα in live T cells[28]. The TH211 probe contains a sulfonyl-triazole electrophile (SuTEx[29]) that reacts with tyrosine and lysine sites when directed to DGK active sites with the kinase binding element RF001 derived from the DGK inhibitor ritanserin[30-34]. The prominent TH211 binding to the C1 and catalytic domains of DGKα in living T cells suggests the potential existence of an allosteric site in the C1 domain. Whether probe binding to C1 domains of other DGK members occurs in cellular environments is unknown.

Here we established cellular binding profiles for all members of the DGK superfamily using the covalent SuTEx probe TH211[28]. Treatment of recombinant DGK expressing cells with TH211 facilitated identification of tyrosine and lysines sites, localized to catalytic and regulatory domains, with the propensity for covalent binding in living cells. Notably, we discovered that DGK chimera proteins with exchanged C1 domains could still recognize and bind TH211. Further analysis revealed that swapping of C1 domains between DGKα and DGKξ resulted in differential effects on biochemical activity. Collectively, our findings further expand our understanding of crosstalk between regulatory and catalytic domains in DGK molecular recognition events.

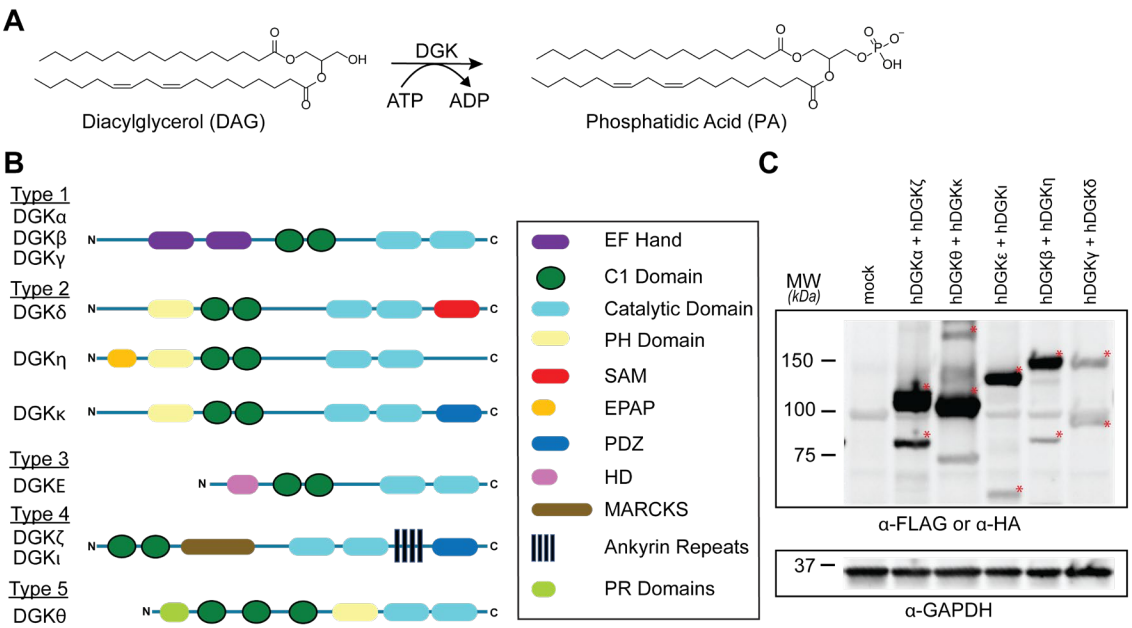

Figure 4.2.1 Diacylglycerol kinases (DGKs) metabolize bioactive lipids in cell metabolism and signaling. (A) DGKs catalyze ATP-dependent phosphorylation of diacylglycerols to biosynthesize phosphatidic acid. DGK-regulated lipid substrates and products regulate downstream protein receptors through changes in localization, activation, and protein-protein interactions. (B) DGKs are multidomain lipid kinases that differ principally in composition of regulatory domains outside of the conserved catalytic domain. (C) Co-expression of recombinant human DGK proteins in HEK293T cells for chemical proteomic evaluation. Expression of recombinant DGKs was detected by western blot with anti-FLAG antibodies except for DGKξ and DGKι, which was detected with anti-HA antibody. Equivalent protein loading was confirmed by anti-GAPDH. All data shown are representative of 3 experiments (n = 3 biologically independent experiments).

4.3 *Materials and Methods*

Reagents. TH211 was synthesized and used for live cell chemoproteomics as previously described[28].

Cell culture. HEK293T cells were cultured with corresponding SILAC media supplemented with 10% dialyzed fetal bovine serum (DFBS, Us. Source, Omega Scientific), 1% L-glutamine (Thermo Fisher Scientific), and either ^{12}C, ^{14}N-lysine and arginine (100 µg/mL) or ^{13}C, ^{15}N-lysine and arginine (100 µg/mL) for light and heavy cells, respectively (Sigma-Aldrich). Cells were maintained at 37 °C with 5% CO_2 and used for experiments at ~90% confluency.

Transient transfection. Recombinant proteins were produced by transient transfection of HEK293T cells with recombinant DNA as previously described[33]. The following constructs were generated by recombination of Addgene plasmids using the Gateway cloning system (Invitrogen): pGCFlag-DGKG-FLAG (human), pGCFlag-DGKK-FLAG (human) and pGCFlag-PRKCH-FLAG (human). The following plasmids were purchased commercially from GenScript: pcDNA3.1-DGKA-FLAG (human), pcDNA3.1-DGKB-FLAG (human), pcDNA3.1-DGKE-FLAG (human), pcDNA3.1-DGKH-FLAG (human), pcDNA3.1-DGKQ-FLAG (human), pcDNA3.1-FLAG-DGKzC1a (human) and pcDNA3.1-FLAG-DGKaC1z (human). The following plasmids were purchased commercially from Gene Universal: pcDNA3.1-FLAG-DGKaC1a (rat), pcDNA3.1-FLAG-DGKaC1 (rat), pcDNA3.1-FLAG-DGKbC1a (rat) and pcDNA3.1-FLAG-DGKgC1a (rat). All other vectors were gifted to Dr. Thurl Harris (University of Virginia, School of Medicine) by Dr. Kaoru Goto (Yamagata University, School of Medicine) and Dr. Fumio Sakane (Chiba

University) and were kindly shared with us: pcDNA3-HA-DGKZ (human), pcDNA3-HA-DGKI (human) and pCMV-7.13xFLAG-DGKD (human).

Western blot analysis. Western blot analysis of recombinant protein expression was performed as previously described[35].

TH211 covalent binding to DGKs *in situ*. Media was aspirated from recombinant DGK-HEK293T cells when cells reached ~90% confluency (~48 h after transient transfection). Cells were washed gently with PBS and treated with serum-free media containing DMSO vehicle or TH211 probe (50 μM final; 50X stock in DMSO). Cells were returned to the incubator for 2 h at 37 °C. After removal of media, cells were washed with cold PBS 2X and then harvested into 15 mL conical tubes. Samples were pelleted by centrifugation (500 x *g*, 5 min, 4 °C) to remove PBS. Samples were resuspended in 500 μL of PBS containing protease and phosphatase inhibitor (EDTA-free) and transferred to 1.5 mL Eppendorf tubes. Samples were sonicated (1 sec, 20% amp, 3x). Protein concentrations were determined by Bio-Rad DC protein assay and sample concentrations adjusted to 2 mg/mL. Samples were snap frozen in liquid N_2 and stored at -80 °C until analyzed.

Gel-based chemical proteomic assay. Samples were taken thawed from -80 °C. Conjugation of alkyne-modified proteomes with fluorophore was accomplished by copper-catalyzed azide-alkyne cycloaddition (CuAAC) with rhodamine-azide (TAMRA-azide, 1.25 mM, 1 μL, final concentration of 25 μM) in the presence of tris(2-carboxyethyl)phosphine (TCEP, 50 mM fresh in water, 1 μL, final concentration of 1 mM), tris[(1-benzyl-1H-1,2,3-triazol-4-yl)methyl]amine (TBTA,

1.7 mM in 4:1 *t*-butanol/DMSO, 3 µL, final concentration of 100 µM) and $CuSO_4$ (50 mM, 1 µL, final concentration of 1 mM) for 1 h at room temperature followed by SDS-PAGE and in-gel fluorescence scanning as previously described[28].

SILAC sample preparation for MS-based chemical proteomic assay. Light and heavy proteomes from TH211-treated cells were prepared for LC-MS chemical proteomic assay as previously described[28].

LC-MS/MS chemical proteomics. The enriched probe-modified peptide samples were analyzed by LC-MS/MS using an Easy-nLC 1200 (Thermo Scientific) coupled with Q Exactive Plus Orbitrap mass spectrometer (Thermo Scientific) as previously described[28]. Identification of peptides and target proteins from the LC-MS/MS raw data was accomplished as previously described[28]. Data were searched using Byonic and then analyzed using Skyline. Byonic search parameters were as follows: up to 3 missed cleavages, 10 ppm precursor mass tolerance, 50 ppm fragment mass tolerance, too high (narrow) 'precursor isotope off by x', precursor and charge assignment computed from MS1, maximum of one precursor per MS2, 0.01 smoothing width, and 1% protein false discovery rate. Variable common modifications included methionine oxidation (+15.9949 Da), SILAC labels on arginine and lysine (+10.008269 Da and +8.014199 Da respectively), and our sulfonyl probe modification on tyrosine and lysine (+635.27374 Da). A fixed common modification of carbamidomethylation on cysteine (+57.021464 Da) was also included. Isoform data were searched using a modified human protein database (UniProt human database 06/2019, angiotensin I and vasoactive intestinal peptides standards). For the chimeric data sets, the plasmid DNA

sequences were converted to proteins sequences using Benchling (Benchling [Biology Software]. (2022). Retrieved from https://benchling.com) and added to the modified database. Results from Byonic and Skyline were combined and filtered in R to retain high confidence peptides as determined by the following criteria: Byonic score ≥ 500, a precursor mass error within 5 ppm; normalized SR ≥ 5, with both isotope dot-product (iDOTP) and ratio dot-product (rDOTP) ≥ 0.8. These results were used for all analyses. All other data analyses generated was based on Byonic analysis only and the results were filtered using these criteria: Score ≥ 300, precursor mass error within 5 ppm, Delta Score ≥ 25, DeltaMod Score ≥ 20 and Log Prob ≥ 3.0.

Biochemical substrate assay of DGK chimeras. A liposomal substrate assay for measuring DAG kinase activity was performed as previously described[4, 30, 36]. In brief, each reaction, performed in triplicate, comprised of buffer B, 1 mM DTT, 0.1 mM $CaCl_2$, 2 mM lipids as well as each respective lysate overexpressing either DGK or GFP as a control. Due to relative expression differences between separate preparations, the amount of lysate protein used in each reaction was confirmed to fall within the linear range of detection (4, 8 and 16 µg for each DGK and GFP control) to account for the variability in enzyme activity due to transfection efficiency. Each reaction received 10 µL of 10 mM ATP spiked with [γ^{32}P]-ATP (100 µL final volume) and incubated at 30 °C for 20 min. 0.5 mL of methanol with 0.1 N HCl was used to quench each reaction, followed by 1 mL of ethyl acetate and 1 mL of 1 M $MgCl_2$ for organic phase separation. Each reaction was vortexed, and 0.5 mL of the organic phase was removed. The incorporation of [^{32}P] into DAG

was measured from these organic phase samples via scintillation counter. Each construct's specific activity was calculated as average nmol of product per minute per μg of total lysate protein.

4.4 *Results*

4.4.1 *Chemoproteomic Profiling of the DGK Superfamily In Situ*

Recombinant DGK-expressing cells were treated with TH211 to identify tyrosines and lysines covalently bound by SuTEx probes *in situ*. We reasoned that a recombinant overexpression system will minimize differences in expression of native DGKs to enable chemical proteomic profiling of all 10 isoforms. The use of SuTEx probes such as TH211 can provide important information on dynamic regulation of DGK activity states in cells.

SILAC light (L) and heavy (H) HEK293T cells were transiently transfected with plasmids encoding recombinant DGKs of the entire mammalian superfamily. We performed chemical proteomic studies on cells co-expressing DGK pairs to (i) understand covalent probe binding to multiple DGKs in a cellular environment, and (ii) streamline our workflow to minimize sample-to-sample variations. DGK isoform pairs were chosen based on distinct subtype classification and gel-resolvable molecular weights to permit facile verification of expression by Western blots. A comparison between co-expression (β and η) and single-expression (β) was performed **(Figure 4.4.17)** showing identical expression levels and number of peptides identified. Based on these criteria, the selected pairs for chemoproteomic evaluation included a mixture of type 1 (DGKα):4 (DGKξ), type 2 (DGKκ):5 (DGKθ), type 4 (DGKι):3 (DGKε), type 1 (DGKβ):2 (DGKη), and type 1 (DGKγ):2 (DGKδ; **(Figure 4.2.1C)**).

First, we overexpressed DGK pairs in HEK293T cells and verified protein expression of recombinant DGKs in L and H cells by Western blot (α-FLAG

antibodies, **(Figure 4.2.1C)**. Next, DGK-expressing SILAC HEK293T cells were treated with either DMSO vehicle or TH211 (50 μM, 2 h, 37 °C). Following probe labeling, cells were lysed, proteomes conjugated to desthiobiotin-azide by copper-catalyzed azide-alkyne cycloaddition (CuAAC). Proteomes were subjected to trypsin protease cleavage followed by avidin chromatography enrichment of probe-modified peptides. Liquid chromatography-tandem mass spectrometry (LC-MS/MS) analysis facilitated identification of TH211 covalently modified tyrosines and lysines on DGKs in live cells **(Figure 4.4.1)**. Our mixing conditions accounted for specific enrichment of probe-modified sites on DGKs (L-TH211/H-DMSO) as well as a 1:1 condition (L-TH211/H-TH211) to serve as a 1:1 mixing control as previously described[28].

Probe-modified sites specifically enriched in our studies were identified by a SILAC ratio (SR) >5 for TH211 probe (L)- compared with DMSO (H)-treated samples. These peptides were further evaluated with quality control confidence criteria that include a Byonic search algorithm score of $\geq$500, 1% protein false discovery rate (FDR), and mass accuracy ($\leq$5 ppm) as previously described[28, 37, 38].

4.4.2 *Location of Covalent Binding Sites Detected on Human DGKs*

Our chemical proteomic studies revealed TH211 binding to tyrosine and lysine residues across all 10 DGK isoforms. In total, we detected 3760 and 2519 distinct probe-modified tyrosine (Y) and lysine (K) sites, respectively, in our aggregate chemical proteomic studies (Y/K ratio ~1.5) **(Figure 4.4.2)**. The covalent

labeling profiles agree with our previous finding that 1,2,3-sulfonyl-triazoles, including TH211, show increased lysine binding activity[28, 29]. The lower natural abundance of tyrosine compared with that of lysine[39] is reflected in the frequency of modified residues that is dependent, to some degree, on amino acid composition of DGKs (average tyrosine and lysine composition of 2 and 6%, respectively).

As expected, we identified prominent probe binding in the catalytic domains of all DGKs evaluated (**(Figure 4.4.3)** and **(Figure 4.4.4)**). We identified at least a single modified tyrosine or lysine in the catalytic domain and in some instances, multiple binding events to the DAGKc and DAGKa regions of DGKs (e.g. DGKξ, DGKδ, DGKι; **(Figure 4.4.3)** and **(Figure 4.4.4)**). We also identified trends in TH211 binding at regulatory domains that support potential differences in molecular recognition between DGK members. For example, probe-modified sites, and tyrosine specifically, were identified only on EF hands of DGKα among the type 1 DGKs (Y169, **(Figure 4.4.3)**). The pattern of tyrosine modifications in C1 domains across the DGKs also matched our previous finding that probe binding is prominent in C1A and C1A/C1B of DGKα and DGKγ, respectively, and absent in DGKβ[4]. In contrast, probe-modified lysines were frequent in C1 domains of non-type 1 DGKs members except for DGKκ, DGKε and DGKη that were devoid of probe binding at these regions (**(Figure 4.4.3)** and **(Figure 4.4.4)**).

In contrast to previous ATP acyl phosphate studies[32], we detected covalent binding in regulatory domains orthogonal to C1 and catalytic domains that can serve as potential sites for pharmacological investigation of DGKs. For example, several probe-modified sites were detected in the ankyrin repeats of type 4 DGKs

and the Ras-association domain of DGKQ. Additional probe-modified sites of interest include covalent binding to the PH domain of DGKκ (K286) and the SAM domain of DGKδ (K1191, **(Figure 4.4.3)** and **(Figure 4.4.4)**). The presence of probe-modified tyrosines and lysines in the peptide region between the DAGKc and DAGKa of DGKδ, κ and η should enable future investigations of these poorly annotated regions that differentiate type 2 DGKs from the rest of the superfamily (**(Figure 4.4.3)** and **(Figure 4.4.4)**).

4.4.3 *Covalent Binding Profiles of DGK Chimeras*

Next, we tested TH211 binding activity against recombinant DGK C1 chimera proteins **(Figure 4.4.5A)**. We previously developed these mutant proteins to exchange tandem C1 domains between type 1 DGKs for evaluating corresponding effects on DGK metabolism in live cells[4]. These findings support the C1 domains of type 1 DGKs as important regulators of fatty acid chain specificity[4]. Here we investigated whether probe recognition and binding specificity is inherently encoded by C1 domains within (α, β, γ) and across DGK subtypes (α,ξ). These studies would also test whether other domains of the DGK protein affect C1 domain site probe binding.

We expressed recombinant rat type 1 DGK C1 chimeras that are a composite of regulatory and catalytic domains of one isoform (DGKα, β or γ) and C1 domains from a separate isoform (C1α, β or γ)[4]. First, we confirmed that DGK C1 chimeras were expressed to detectable levels in HEK293T cells using western blots as previously reported[4] **(Figure 4.4.5B)**. Then, we confirmed and validated

manually all chimeras **(Figure 4.4.6)** and **(Figure 4.4.7)**. We also generated chimera proteins that have exchanged C1 domains between DGK subtypes. Specifically, we produced chimeras that evaluated DGKξ C1 domains engrafted into DGKα (DGKαC1ξ) and the complementary counterpart (DGKξC1α). See Supporting Information for sequences and functional validation of DGKαC1ξ and DGKξC1α plasmids **(Figure 4.4.8)**.

Next, we treated DGK chimera-expressing HEK293T cells with TH211 (50 μM, 2 h, 37 °C) followed by quantitative chemoproteomics. Our studies identified TH211 binding profiles that provided evidence of interchangeability of C1 domains between DGK members. Prominent TH211 binding was observed in C1A and C1B of DGKαC1γ that was distinct from reduced binding activity in C1s of DGKβC1α **(Figure 4.4.9)**. These data agree with previous findings that activity-based probe binding is enriched for DGKγ compared with DGKβ C1 domains[4]. These observations of C1 intrinsic behavior are in contrast with examples of probe binding to C1 that was influenced by the flanking DGK backbone. For example, the C1 domains of DGKα showed clear differences in TH211 binding that was dependent on whether these domains were contained in the backbone domains of DGKγ compared with DGKβ **(Figure 4.4.9)**.

C1 domain swaps across DGK subtypes also revealed TH211 binding profiles in support of C1 effects on molecular recognition. The lack of TH211 probe modifications on tyrosine residues in C1 domains of DGKξ was retained when swapped into the DGKα backbone (DGKαC1ξ, **(Figure 4.4.10)**). Interestingly,

covalent binding of TH211 to lysines on DGKξ C1A (K123, K134, K147) and C1B (K189, K194) was largely retained when these domains were engrafted into the DGKα backbone (C1A: K231, K242, K255; C1B: K297, K302; DGKαC1ξ, **(Figure 4.4.3)** and 5). In contrast, TH211 binding to transplanted C1 domains from DGKα appeared to be influenced by the surrounding DGKξ backbone. The specific labeling of C1A (Y240) on wild-type DGKA was exchanged with prominent TH211 binding to tyrosine and lysine sites of C1A and C1B on DGKξC1α ((**Figure 4.4.3)** and 5).

Collectively, our findings support inherent features of C1 domains as well as the influence of the surrounding DGK backbone topology in mediating functional probe binding.

4.4.4 *DGK C1 Chimeras show Isoform-specific Perturbation to Catalytic Activity*

Next, we tested whether C1 domains swaps between DGKα and DGKξ affected biochemical activity of resulting chimeras. We compared catalytic activity of recombinant DGK chimera-expressing proteomes using a radiolabeled ATP substrate assay in DAG liposomes as previously described[30, 36]. Recombinant overexpression of recombinant wild-type DGKα or DGKξ resulted in a protein concentration dependent increase in DAG phosphorylation activity compared with a GFP-expressing control sample **(Figure 4.4.11A)**. Exchange of DGKα C1 domains into the DGKξ backbone construct did not impact catalytic activity of the resulting DGKξC1α chimera protein. In contrast, DGKα was less tolerant of a C1

domain exchange between subtypes. Inserting DGKξ C1 domains into the DGKα backbone produced a chimera protein that displayed significantly reduced catalytic activity compared with wild-type counterpart (0.002 vs 0.006 nmol min^{-1} μg^{-1} for DGKαC1ξ compared with DGKα, respectively; **Figure 4.4.11B)**.

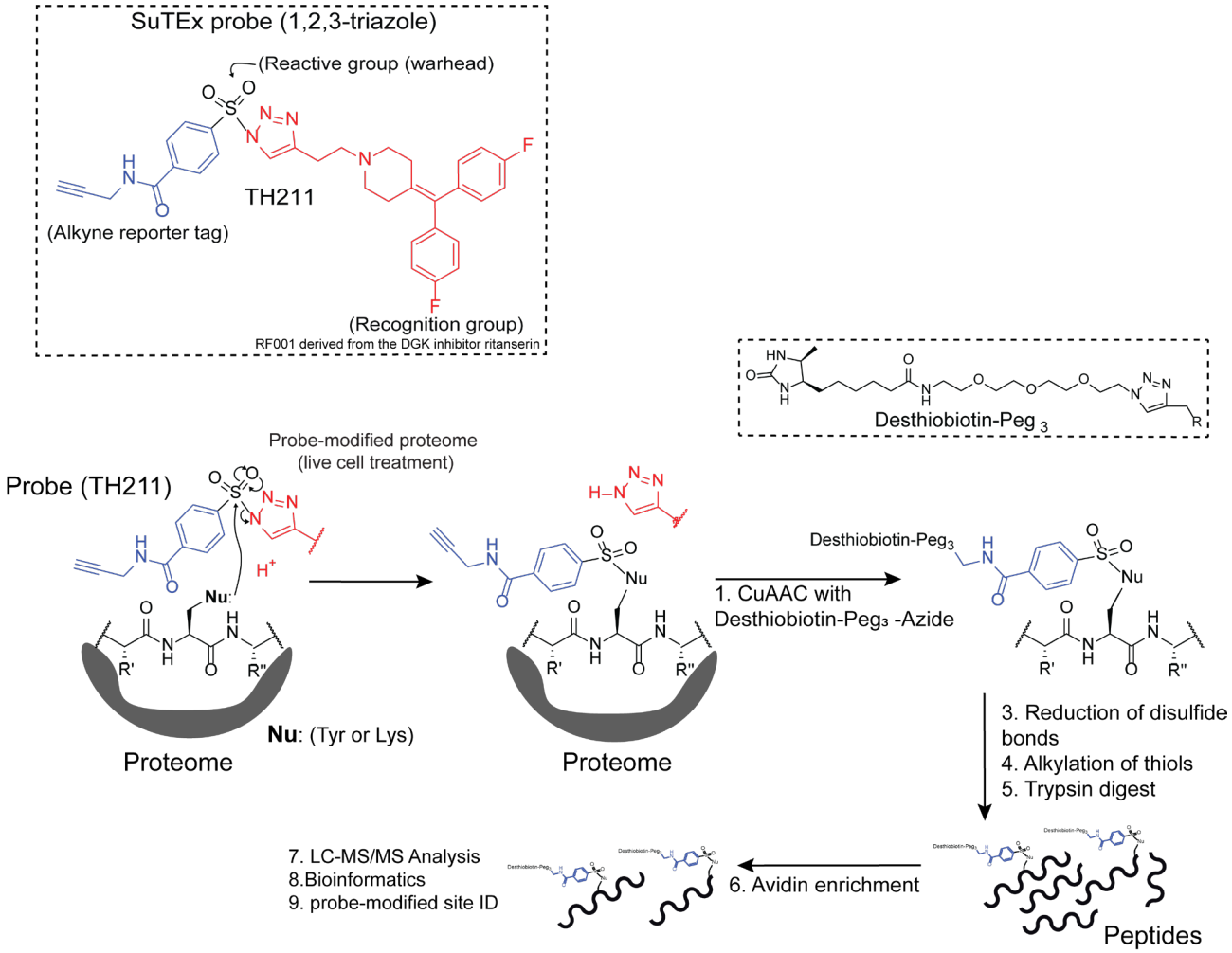

Figure 4.4.1 Chemoproteomic profiling of the DGK superfamily in live cells.[28] 1,2,3-Sulfonyl-triazoles modify tyrosine and lysine sites, with a preference for the former residue, on proteins through sulfur-triazole exchange chemistry (SuTEx) chemistry. Proteins modified with SuTEx probes such as TH211 contain an alkyne reporter tag that facilitates copper-catalyzed azide-alkyne cycloaddition (CuAAC) conjugation of a desthiobiotin-azide enrichment handle. Desthiobiotinylated proteins are digested with trypsin protease to produce probe-modified peptides that are enriched by avidin chromatography followed by LC-MS/MS analysis. Bioinformatics can identify probe-modified peptide sequences and site of probe modification that can be used to infer covalent binding of SuTEx probes to intact

proteins from lysate and live cell studies. Reprinted with permission Huang, T.; Hosseinibarkooie, S.; Borne, A. L.; Granade, M. E.; Brulet, J. W.; Harris, T. E.; Ferris, H. A.; Hsu, K.-L. Chemoproteomic profiling of kinases in live cells using electrophilic sulfonyl triazole probes. *Chemical Science* **2021**, *12* (9), 3295-3307. Copyright 2019 American Chemical Society.

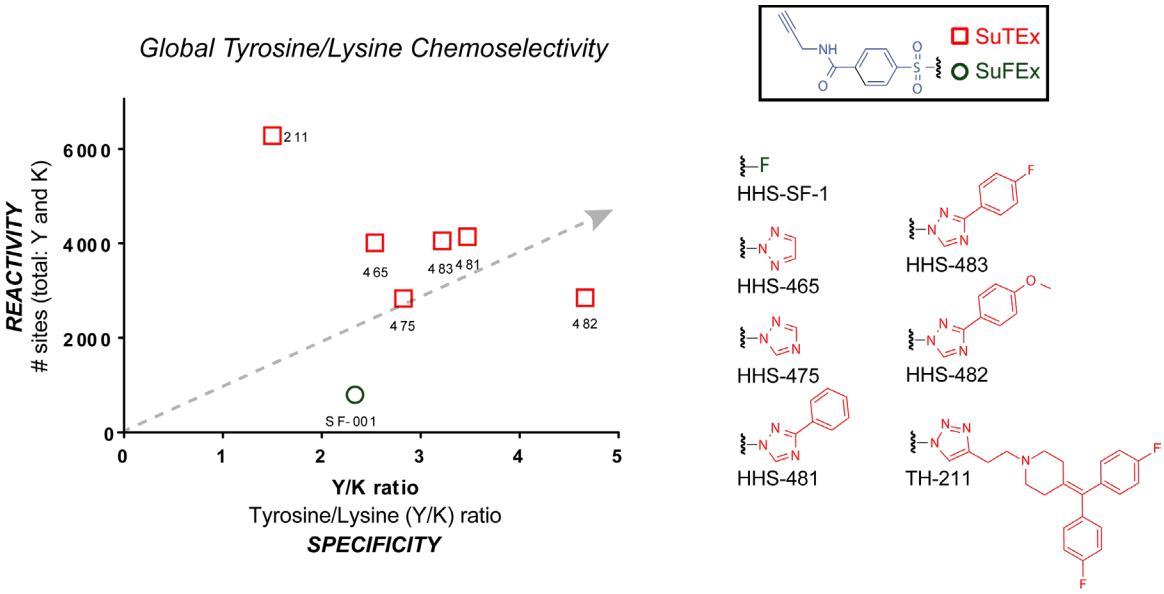

Figure 4.4.2 Chemoproteomic profiling of the DGK superfamily in live cells.[40, 41] 1,2,3-Sulfonyl-triazoles modify tyrosine and lysine sites, with a preference for the former residue, on proteins through SuTEx chemistry. Proteome-wide structure activity relationship (SAR) of sulfonyl probes. Reprinted with permission from Hahm HS, et al. *Nature, Chem Biol*. 2020 Feb;16(2):150-159. Copyright 2019 American Chemical Society.

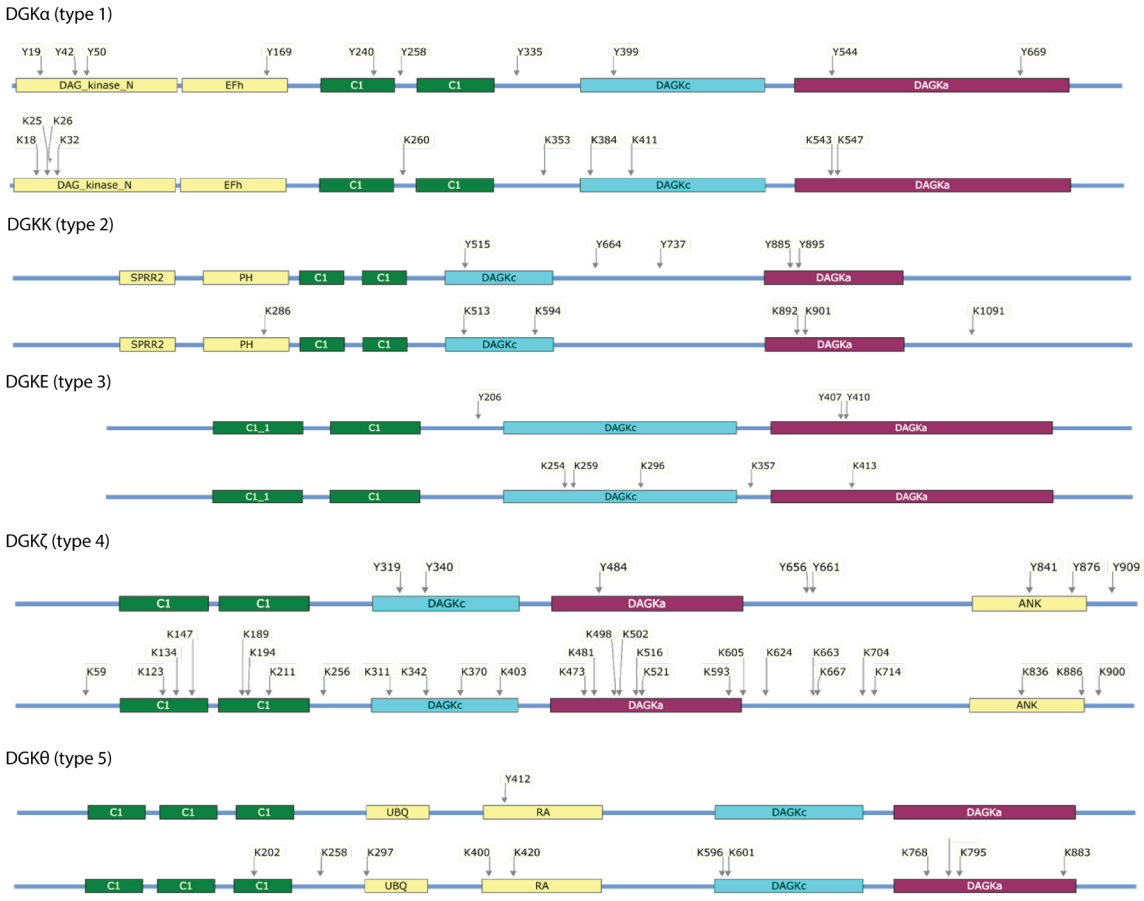

Figure 4.4.3 Covalent binding profiles of DGK members in living cells. Ten mammalian DGK isoforms are divided into five subtypes based on conserved structural motifs. All DGK isoforms share at least two cysteine rich C1 domains and a catalytic domain. The TH211 binding sites detected from live cell treatments of recombinant DGK overexpressed-HEK293T cells and quantitative chemical proteomics are depicted. Cells were treated with TH211 (50 μM) for 2 h at 37 °C. Representative DGK members from each subtype are shown here. The covalent binding profiles of remaining DGK proteins can be found in **(Figure 4.4.4)**. All data shown are representative of 3 experiments (n = 3 biologically independent experiments). Figures were generated using SnapGene software (snapgene.com).

The DGK domain plots are depicted to show modified tyrosine (top) and lysine sites (bottom).

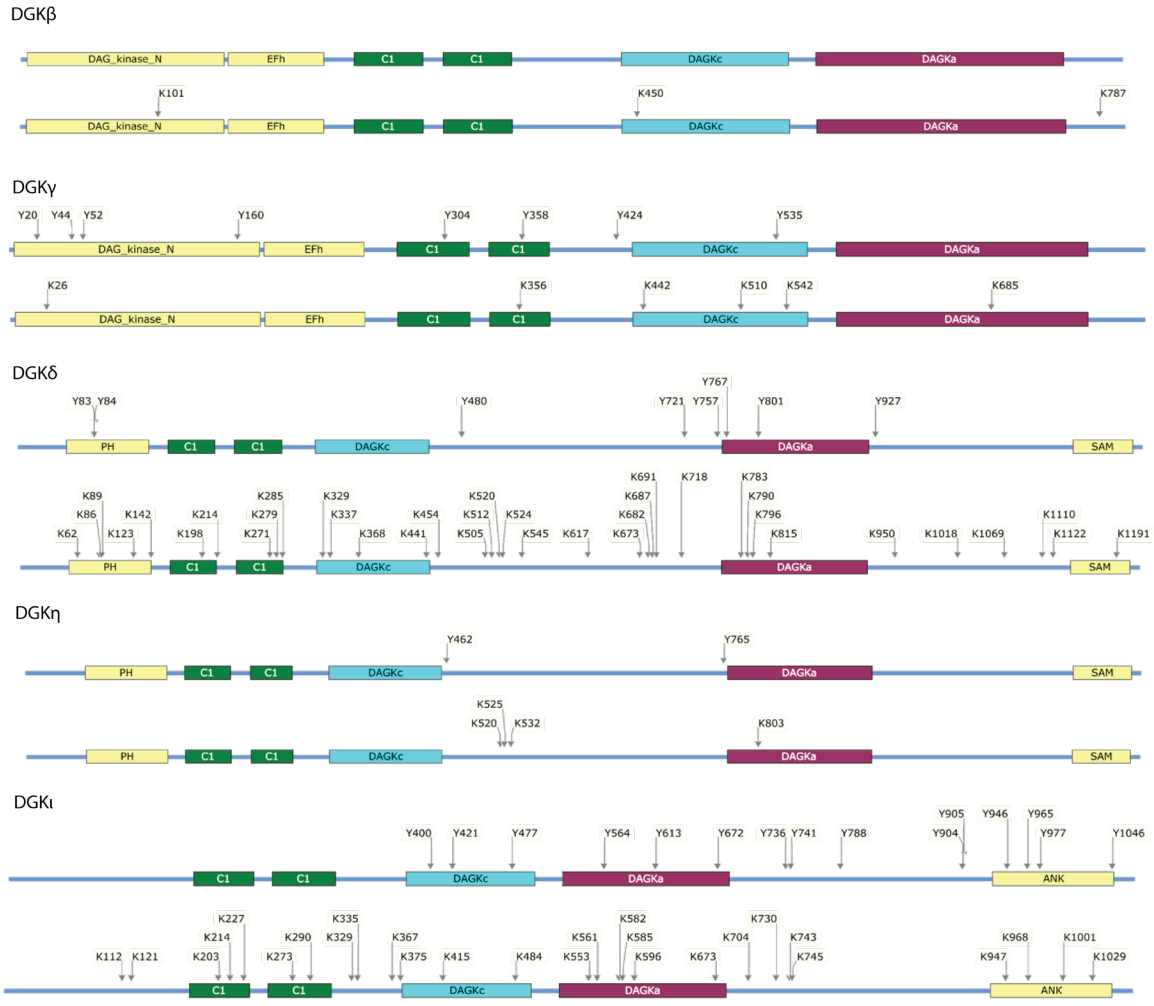

Figure 4.4.4 Covalent binding profiles of remaining DGK members in living cells. The TH211 binding sites were detected by live cell treatments of recombinant DGK overexpressed-HEK293T cells with TH211 (50 μM, 2 h, 37 °C) followed by quantitative chemical proteomics. All data shown are representative of 3 experiments (n = 3 biologically independent experiments). Figures were generated using SnapGene software (snapgene.com). The DGK domain plots are depicted to show modified tyrosine (top) and lysine sites (bottom).

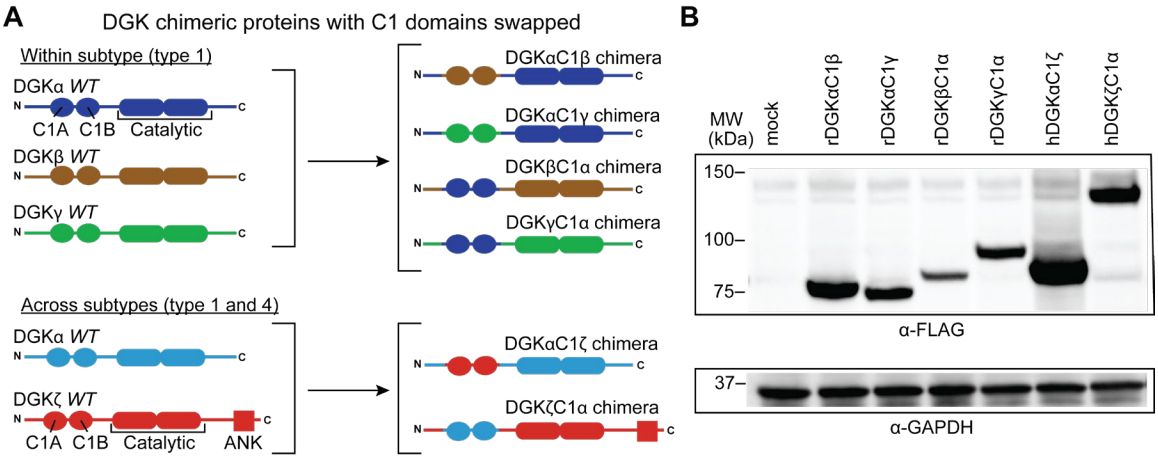

Figure 4.4.5 Generation of DGK C1 domain chimera proteins. (A) Schematic of the DGK C1 chimera proteins tested in this study. DGK chimeras of C1 domains exchanged within and between subtypes are expressed as determined by western blot using anti-FLAG antibodies. Equivalent protein loading was confirmed by anti-GAPDH. All data shown are representative of 3 experiments (n = 3 biologically independent experiments).

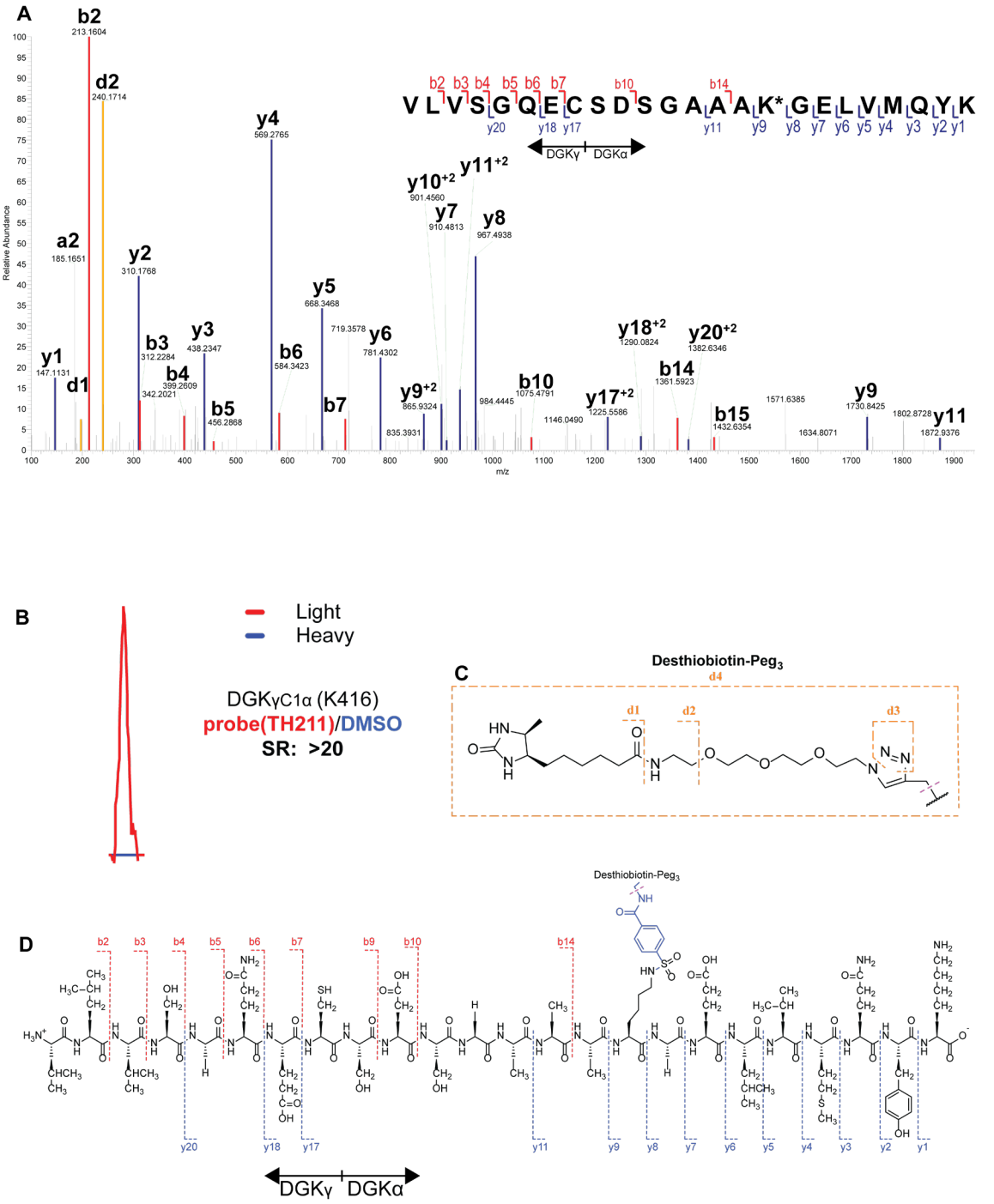

Figure 4.4.6 Identification and verification of DGKγC1α domain chimera proteins. (A) MS/MS spectrum annotation of a TH211-modified lysine site (Lys416) found in chimeric DGKγC1α, a representative example and supports the proposed SuTEx reaction mechanism. (B) SILAC ratios, SR>20. (C) Yellow dash

box represents desthiobiotin azide moiety for probe-modified location. (D) Represents region of chimera between γ and α.

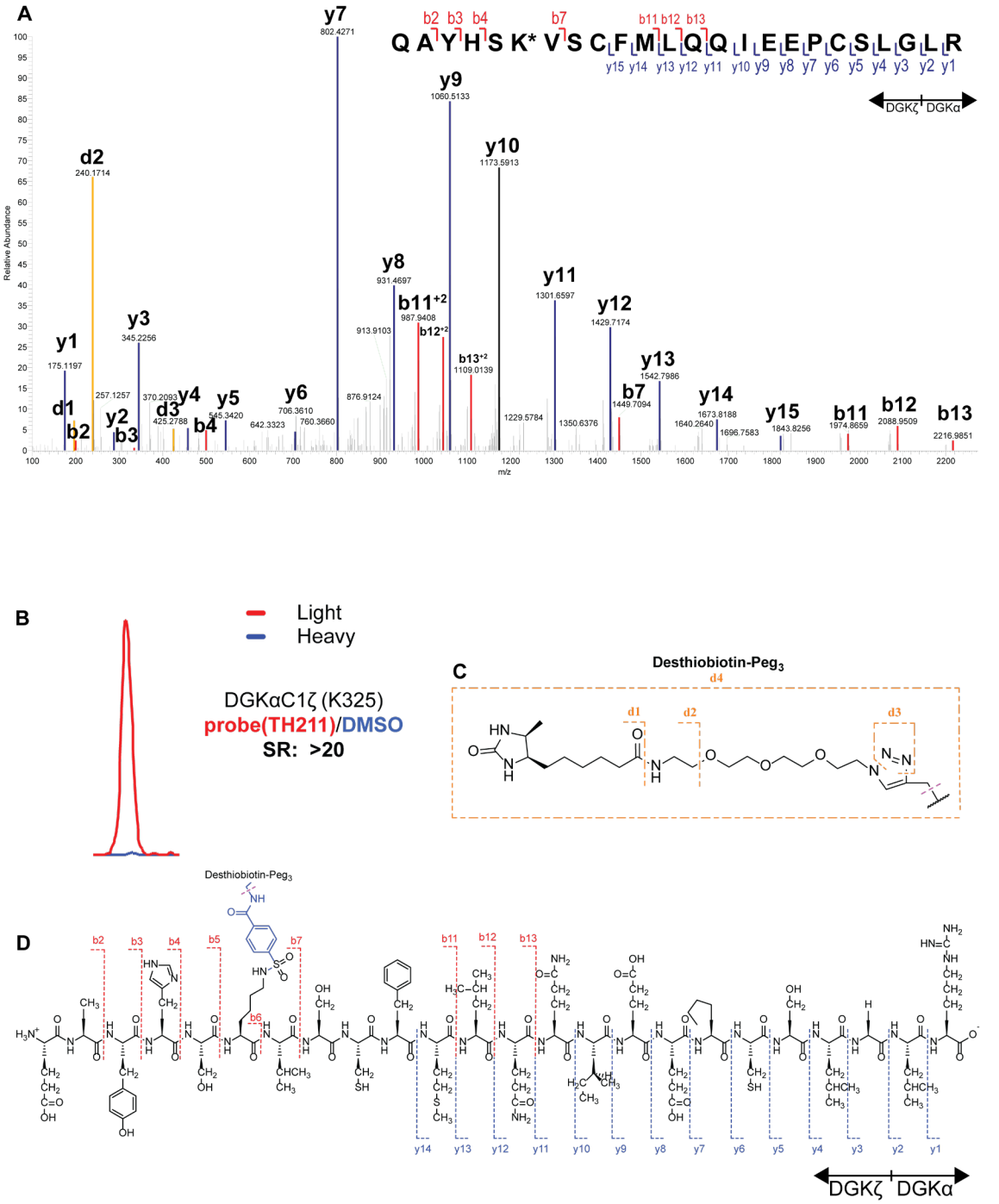

Figure 4.4.7 Identification and verification of DGKαC1ξ domain chimera proteins. (A) MS/MS spectrum annotation of a TH211-modified lysine site (Lys325) found in chimeric DGKαC1ξ, a representative example and supports the proposed SuTEx reaction mechanism. (B) SILAC ratios, SR>20. (C)Yellow dash

box represents desthiobiotin azide moiety for probe-modified location. (D) Represents region of chimera between ξ and α.

Human_DGKαC1ξ_FLAG_pcDNA3.1(+)

MDYKDDDDKEFTMAKERGLISPSDFAQLQKYMEYSTKKVSDVLKLFEDGEMAK
YVQGDAIGYEGFQQFLKIYLEVDNVPRHLSLALFQSFETGHCLNETNVTKDVVC
LNDVSCYFSLLEGGRPEDKLEFTFKLYDTDRNGILDSSEVDKIILQMMRVAEYLD
WDVSELRPILQEMMKEIDYDGSGSVSQAEWVRAGATTVPLLVLLGLEMTLKDD
GEHIWFETNVSGDFCYVGEQYCVARMLKSVSRRKCAACKIVVHTPCIEQLEKIN
FRCKPSFRESGSRNVREPTFVRHHWVHRRRQDGKCRHCGKGFQQKFTFHSK
EIVAISCSWCKQAYHSKVSCFMLQQIEEPCSLGLRDHILPPSSIYPSVLASGPDR
KNSKTSQKTMDDLNLSTSEALRIDPVPNTHPLLVFVNPKSGGKQGQRVLWKFQ
YILNPRQVFNLLKDGPEIGLRLFKDVPDSRILVCGGDGTVGWILETIDKANLPVLP
PVAVLPLGTGNDLARCLRWGGGYEGQNLAKILKDLEMSKVVHMDRWSVEVIP
QQTEEKSDPVPFQIINNYFSIGVDASIAHRFHIMREKYPEKFNSRMKNKLWYFEF
ATSESIFSTCKKLEESLTVEICGKPLDLSNLSLEGIAVLNIPSMHGGSNLWGDTR
RPHGDIYGINQALGATAKVITDPDILKTCVPDLSDKRLEVVGLEGAIEMGQIYTKL
KNAGRRLAKCSEITFHTTKTLPMQIDGEPWMQTPCTIKITHKNQMPMLMGPPP
RSTNFFGFLS

Human_DGKξC1α_FLAG_pcDNA3.1(+)

MDYKDDDDKEFTMETFFRRHFRGKVPGPGEGQQRPSSVGLPTGKARRRSPA
GQASSSLAQRRRSSAQLQGCLLSCGVRAQGSSRRRSSTVPPSCNPRFIVDKV
LTPQPTTVGAQLLGAPLLLTGLVGMNEEEGVQEDVVAEASSAIQPGTKTPGPP
PPRGAQPLLPLPRYLRRASSHLLPADAVYDHALWGLHGYYRRLSQRRPSGQH
PGPGGRRASGTTAGTMLPTRVRPLSRRRQVALRRKAAGPQAWSALLAKAITKS
GLQHLAPPPPTPGAPCSESERQIRSTVDWSESATYGQHMWRPKRFPRPVYCN
LCESSIGLGKQGLSCNLCKYTVHDQCAMKALPCEVSTYAKSRKDIGVQSHVWV
RGGCESGRCDRCQKKIRIYHSLTGLHCVWCHLEIHDDCLQAVGHECDCGLHAA
VVIPPTWILRARRPQNTLKASKKKKRASFKRKSSKKGPEEGRWRPFIIRPTPSPL
MKPLLVFVNPKSGGNQGAKIIQSFLWYLNPRQVFDLSQGGPKEALEMYRKVHN
LRILACGGDGTVGWILSTLDQLRLKPPPPVAILPLGTGNDLARTLNWGGGYTDE
PVSKILSHVEEGNVVQLDRWDLHAEPNPEAGPEDRDEGATDRLPLDVFNNYFS
LGFDAHVTLEFHESREANPEKFNSRFRNKMFYAGTAFSDFLMGSSKDLAKHIR
VVCDGMDLTPKIQDLKPQCVVFLNIPRYCAGTMPWGHPGEHHDFEPQRHDDG
YLEVIGFTMTSLAALQVGGHGERLTQCREVVLTTSKAIPVQVDGEPCKLAASRI
RIALRNQATMVQKAKRRSAAPLHSDQQPVPEQLRIQVSRVSMHDYEALHYDKE
QLKEASVPLGTVVVPGDSDLELCRAHIERLQQEPDGAGAKSPTCQKLSPKWCF
LDATTASRFYRIDRAQEHLNYVTEIAQDEIYILDPELLGASARPDLPTPTSPLPTS
PCSPTPRSLQGDAAPPQGEELIEAAKRNDFCKLQELHRAGGDLMHRDEQSRTL
LHHAVSTGSKDVVRYLLDHAPPEILDAVEENGETCLHQAAALGQRTICHYIVEA
GASLMKTDQQGDTPRQRAEKAQDTELAAYLENRQHYQMIQREDQETAV

Figure 4.4.8 Type 1 rat DGK C1 chimera construct plasmids were custom synthesized by Gene Universal and used for chemoproteomic studies are previously described.[4] Human DGKα and DGKξ chimera construct plasmids

were custom synthesized by GenScript. The sequences are shown below - DGKα (isoform 1) sequence, DGKξ (isoform 2) sequence, FLAG-tag insert:

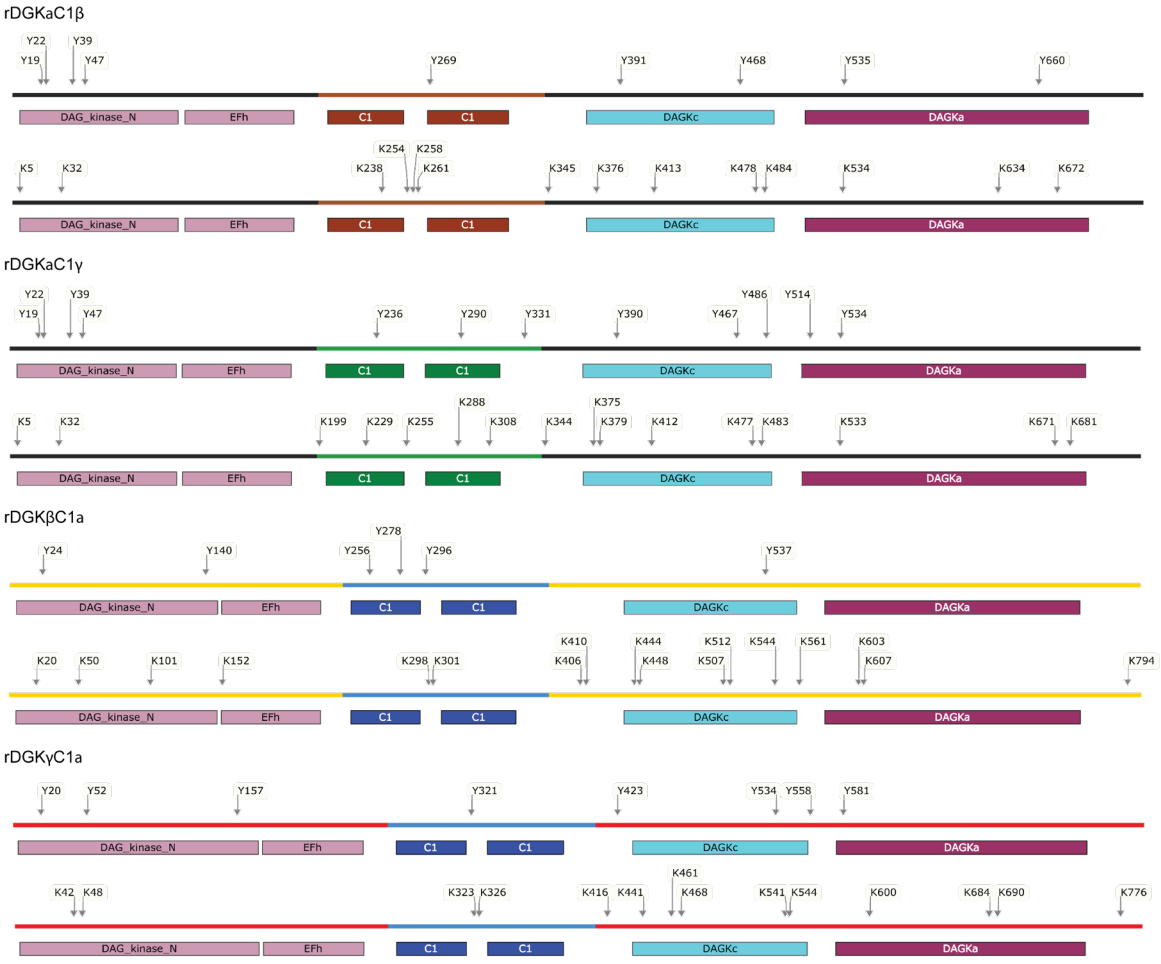

Figure 4.4.9 Covalent binding profiles of DGK type 1 chimeras. TH211 binding to rat DGK chimeras was detected by treatment of recombinant expressing HEK293T cells with TH211 (50 μM) for 2 h at 37 °C followed by quantitative chemoproteomics. DGK chimera proteins are composed of catalytic and regulatory backbone of a type 1 DGK (DGKα, DGKβ, or DGKγ) that contains tandem C1 domains from another type 1 DGK protein (C1α, C1β, or C1γ). All data shown are representative of 3 experiments (n = 3 biologically independent experiments). Figures were generated using SnapGene software (snapgene.com). The DGK

chimera domains are depicted to show modified tyrosine (top) and lysine sites (bottom).

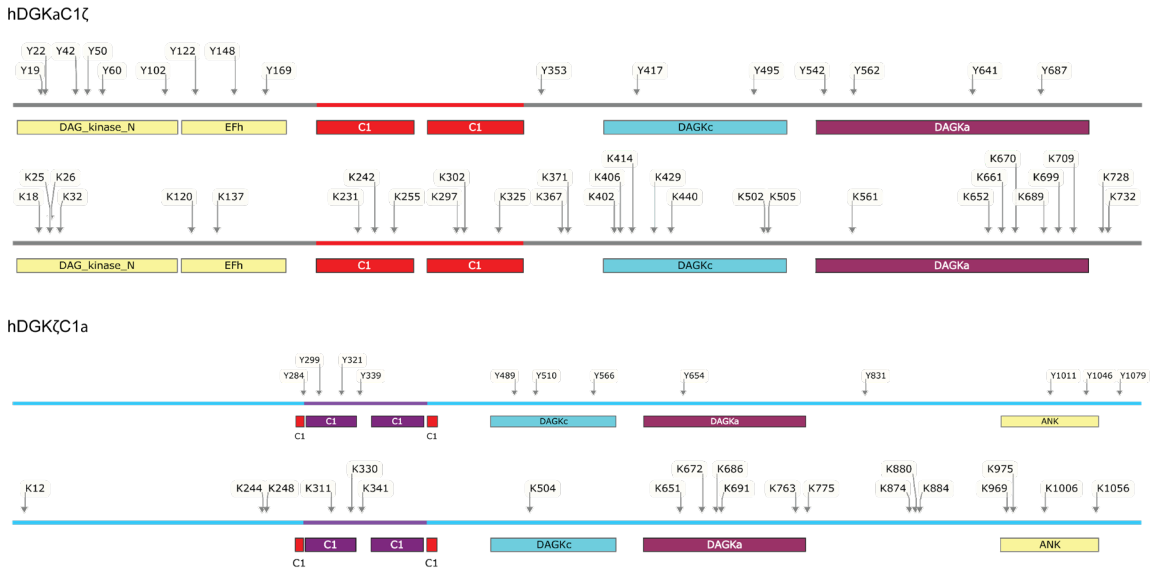

Figure 4.4.10 Covalent binding profiles of DGK type 1 and 4 C1 domain chimeras. DGK chimera proteins are composed of catalytic and regulatory backbone of a DGK protein (DGKα or DGKξ) that contains tandem C1 domains from a different DGK protein (C1α or C1ξ). TH211 binding to human DGKαC1ξ or DGKξC1α was detected by treatment of recombinant expressing HEK293T cells with TH211 (50 μM) for 2 h at 37 °C followed by quantitative chemoproteomics. All data shown are representative of 3 experiments (n = 3 biologically independent experiments). The DGK chimera domains are depicted to show modified tyrosine (top) and lysine sites (bottom). Figures were generated using SnapGene software (snapgene.com).

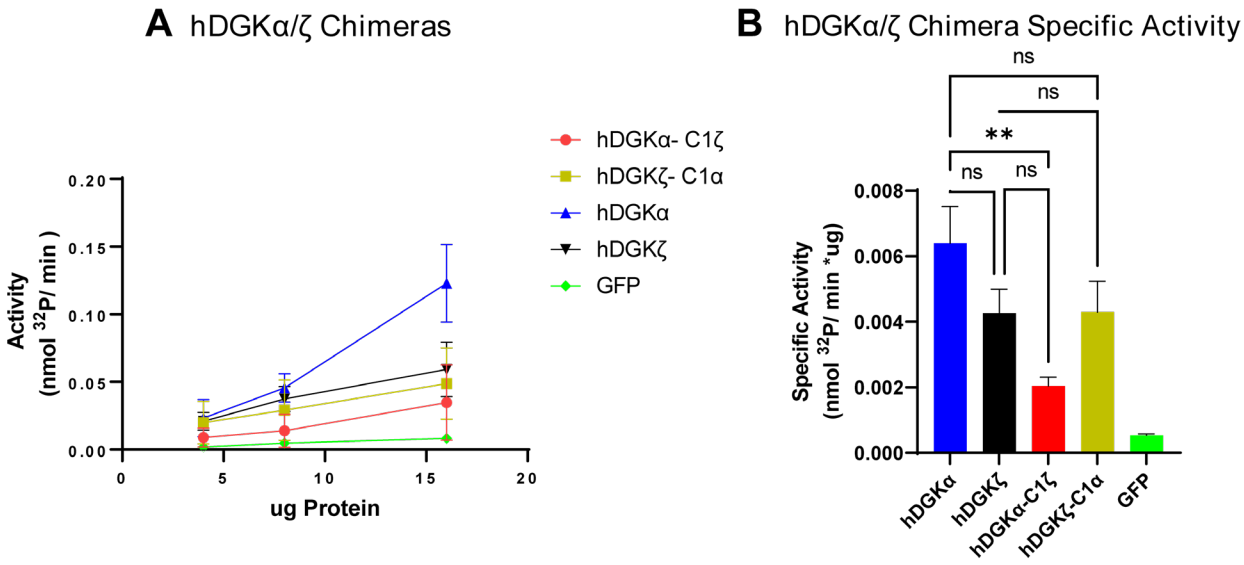

Figure 4.4.11 Biochemical evaluation of type 1 and 4 DGK chimeras. (A) DGKα/ζ wild-type, chimera, and GFP lysates enzyme activity dose response (4, 8, 16 µg of respective lysates) measured by ATP incorporation into product per minute (nmol ^{32}P/min). (B) Average specific activity of each respective lysate calculated from (A) normalized to the protein amount used in each assay. **p < 0.01, Two-way ANOVA with Tukey's MC correction (n = 3 biologically independent experiments).

Figure 4.4.12

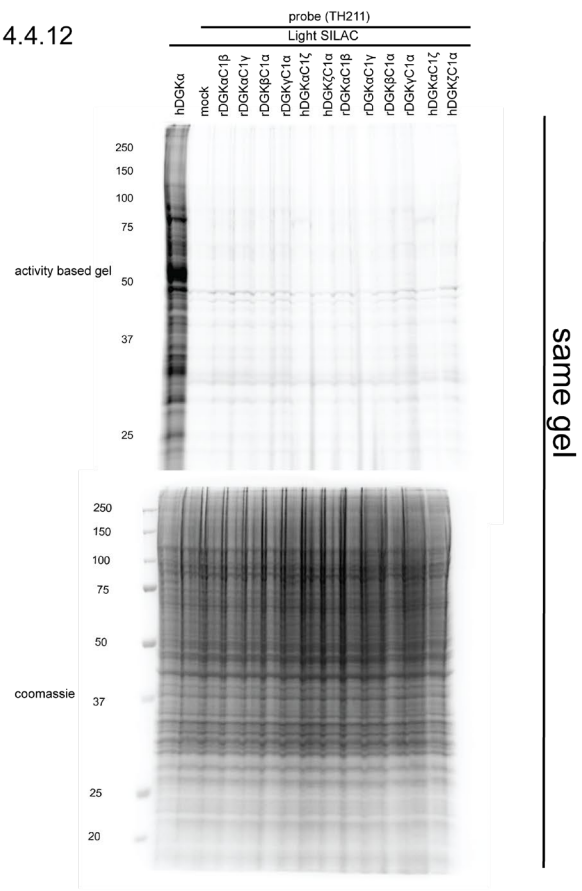

Figure 4.4.13

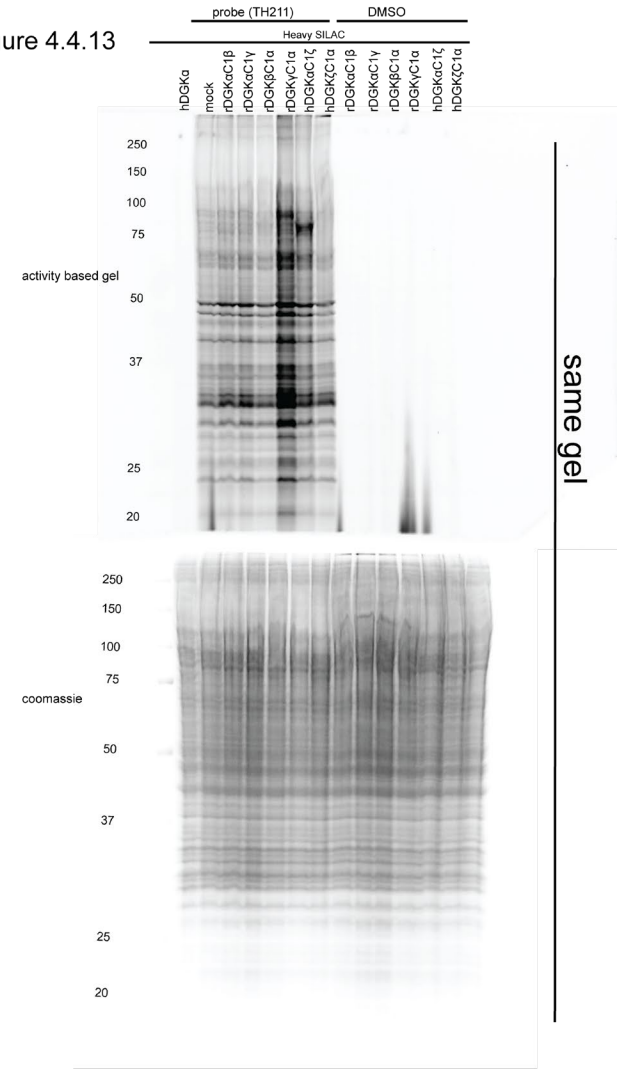

Figure 4.4.14

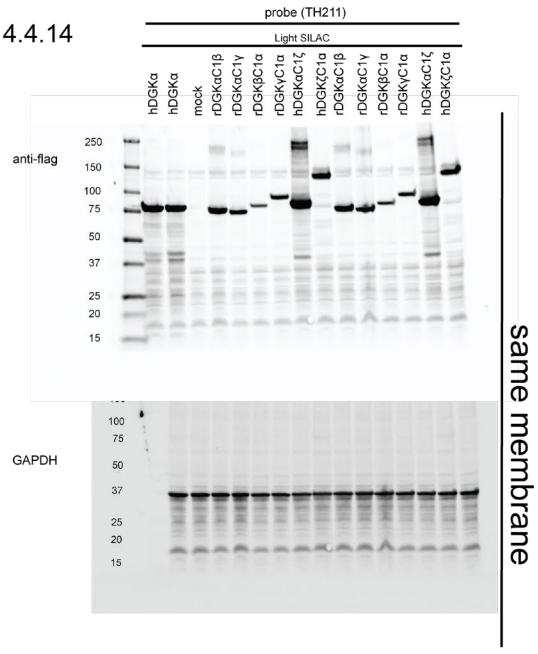

Figure 4.4.15

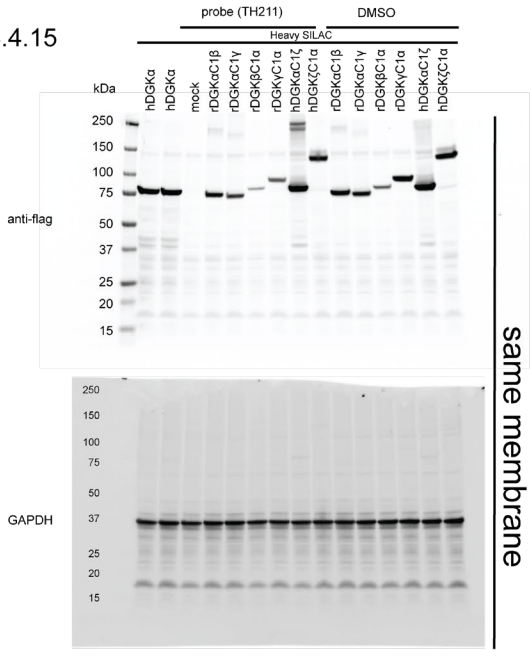

Figure 4.4.14 and Figure 4.4.15 are full panel membranes for Figure 4.2.1

Figure 4.4.16

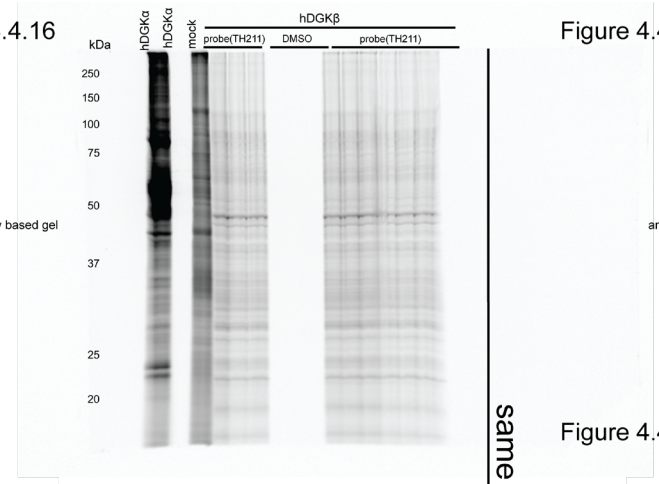

Figure 4.4.17

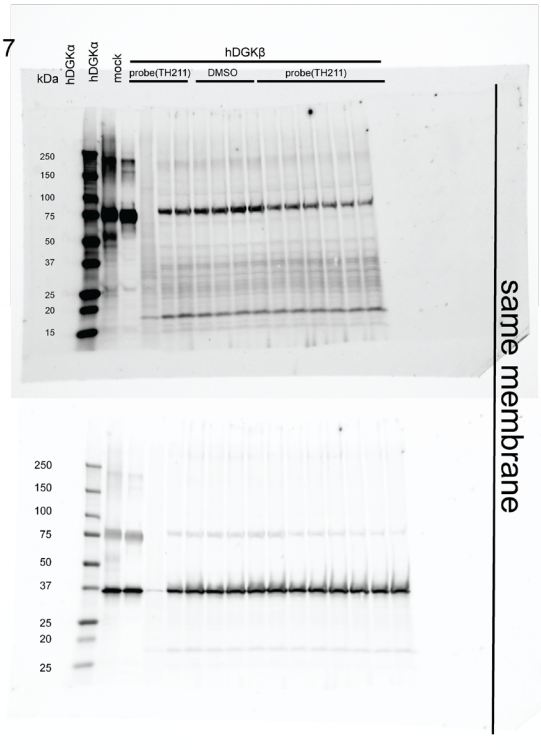

Figure 4.4.18

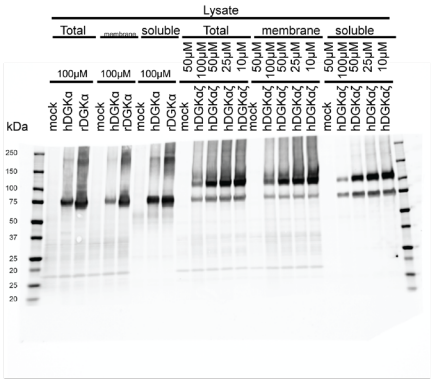

Figure 4.4.19

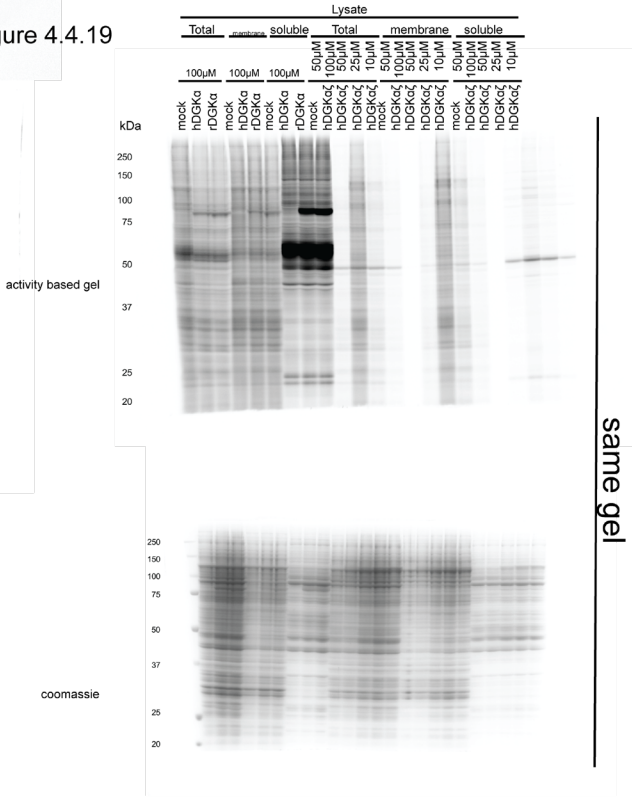

Figure 4.4.20

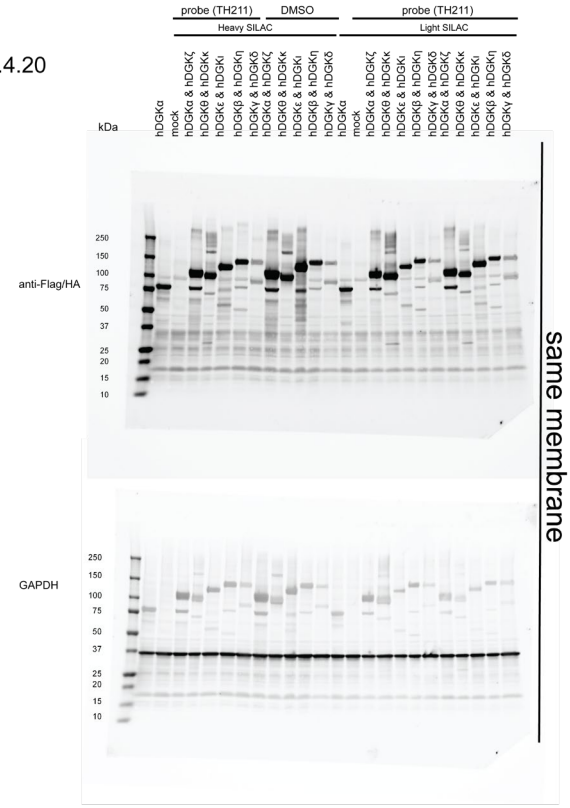

Figure 4.4.20 is the full panel membrane for Figure 4.2.1

4.5 *Discussion*

DGKs are metabolic enzymes implicated in regulation of cellular DAG and PA biology[5-7, 42]. The structural, bioenergetic and signaling roles of these lipids position these enzymes as key hubs for supplying general and bespoke metabolites in diverse cellular biology. The existence of ten mammalian DGKs support the potential for functional diversification to tailor lipid metabolism to specific cellular programs. The molecular basis of this substrate specificity remains ill-defined though chemical proteomic studies are unraveling the principles of active site recognition through covalent probe binding[1]. Here, we deployed sulfonyl-triazole probes containing a DGK-directed binding element to define covalent binding profiles of the DGK superfamily in live cells.

Our experimental workflow adopted a robust recombinant DGK overexpression system previously established for lipidomics[4] and applied here for chemoproteomic evaluations of the DGK superfamily. Importantly, the ability to standardize expression of all DGK isoforms provides confidence that TH211 binding profiles reflect recognition and not detection limit-based effects. The resulting TH211 binding profiles identified modified sites in the catalytic domain of all DGK members. These results are not surprising given the high primary sequence conservation and the high propensity of this domain to interact with diverse covalent probes[1]. The restricted probe binding profiles of EF hands and C1 domains within the type 1 DGKs further support these regulatory regions of DGKs as a differentiator of molecular recognition. By expanding TH211 chemical proteomics beyond DGKα to additional isoforms, we were able to identify reactive

tyrosine and lysine residues in protein-protein interaction motifs including ankyrin repeats (Y841, Y876, K836, K886) and the Ras-association domain of DGKs (Y412, K400, K420; DGKθ, **(Figure 4.4.3)**). We note the lower frequency of identified tyrosine compared with lysine sites on DGKs that can be potentially exploited in future studies for targeted covalent inhibitors bearing a 1,2,4-sulfonyl triazole electrophile with enhanced tyrosine chemoselectivity[29].

We generated DGK chimera proteins that exchanged C1 domains between DGK subtypes to compare with our previous study of type 1 DGK chimeras[4]. Specifically, we exchanged C1 domains between DGKα and DGKξ given their key role in T cell activation and the interest in developing isoform-selective inhibitors for cancer (immuno)therapy[9, 23, 30, 31, 43]. While type 1 DGK C1 domains were moderately interchangeable, the tolerability of C1 domain swaps between subtypes appeared to be isoform specific. The substantial loss of catalytic activity of DGKαC1ξ compared with DGKα wild-type counterpart suggested the importance of C1 domains for biochemical function of this isoform. In contrast, DGKξ biochemical activity appeared to be insensitive to the identity of C1 domains **(Figure 4.4.11)**. Whether this difference in C1 domain exchangeability between DGKα and DGKξ can be leveraged for developing active site and/or allosteric inhibitors is an important subject of future studies.

We recognize that the covalent binding profiles reported here were detected on recombinant but not native DGKs. While important, we note that these studies will likely require SuTEx probes tailored for individual DGKs to screen and identify appropriate cell and tissue types for chemoproteomic evaluation of native

counterparts. Covalent probe binding, while important as a first step towards establishing functional relevance requires complementary biochemical and cell biological assays. Future studies can evaluate the cell biological effects of mutating these residues on lipid metabolism and signaling in recombinant gain of function or native mutants introduced by CRISPR-Cas9[44]. We envision that the strategy reported here will serve as a guide to prioritize binding sites for mutagenesis, biochemical and eventually cell biological verification of DGK function.

In summary, we present a comprehensive ligand binding map of reactive tyrosine and lysine residues that are readily accessible in live cell probe labeling studies. This resource should guide future efforts to explore regulatory and catalytic DGK domains for basic biochemistry and inhibitor discovery efforts.

4.6 *Acknowledgements*

We thank all members of the Hsu Lab for helpful discussions. We thank Tim Ware and Anthony Ciancone for help with molecular biology. This work was supported by the National Institutes of Health grant nos. DA043571 (K.-L.H.), GM007055 (R.M.), University of Virginia Cancer Center (NCI Cancer Center Support Grant No. 5P30CA044579-27 to K.-L.H.), U.S. Department of Defense (Grant W81XWH-17-1-0487 to K.-L.H.), the Robbins Family MRA Young Investigator Award from the Melanoma Research Alliance (http://doi.org/10.48050/pc.gr.80540 to K.-L.H.) and the Mark Foundation for Cancer Research (Emerging Leader Award to K.-L.H).

4.7 *References*

(1) Ware, T. B.; Hsu, K. L. Advances in chemical proteomic evaluation of lipid kinases-DAG kinases as a case study. *Curr Opin Chem Biol* **2021**, *65*, 101-108. DOI: 10.1016/j.cbpa.2021.06.007.

(2) Carrasco, S.; Merida, I. Diacylglycerol, when simplicity becomes complex. *Trends Biochem Sci* **2007**, *32* (1), 27-36. DOI: S0968-0004(06)00321-5 [pii].10.1016/j.tibs.2006.11.004.

(3) Fang, Y.; Vilella-Bach, M.; Bachmann, R.; Flanigan, A.; Chen, J. Phosphatidic acid-mediated mitogenic activation of mTOR signaling. *Science* **2001**, *294* (5548), 1942-1945. DOI: 10.1126/science.1066015.

(4) Ware, T. B.; Franks, C. E.; Granade, M. E.; Zhang, M.; Kim, K. B.; Park, K. S.; Gahlmann, A.; Harris, T. E.; Hsu, K. L. Reprogramming fatty acyl specificity of lipid kinases via C1 domain engineering. *Nat Chem Biol* **2020**, *16* (2), 170-178. DOI: 10.1038/s41589-019-0445-9 From NLM Medline.

(5) Shulga, Y. V.; Topham, M. K.; Epand, R. M. Regulation and Functions of Diacylglycerol Kinases. *Chemical Reviews* **2011**, *111* (10), 6186-6208. DOI: 10.1021/cr1004106 (acccessed 2012/08/27).

(6) Merida, I.; Avila-Flores, A.; Merino, E. Diacylglycerol kinases: at the hub of cell signalling. *Biochem J* **2008**, *409* (1), 1-18. DOI: 10.1042/BJ20071040.

(7) Sakane, F.; Imai, S.; Kai, M.; Yasuda, S.; Kanoh, H. Diacylglycerol kinases: why so many of them? *Biochim Biophys Acta* **2007**, *1771* (7), 793-806. DOI: 10.1016/j.bbalip.2007.04.006.

(8) Tu-Sekine, B.; Raben, D. M. Regulation and roles of neuronal diacylglycerol kinases: a lipid perspective. *Crit Rev Biochem Mol Biol* **2011**, *46* (5), 353-364. DOI: 10.3109/10409238.2011.577761.

(9) Merida, I.; Andrada, E.; Gharbi, S. I.; Avila-Flores, A. Redundant and specialized roles for diacylglycerol kinases alpha and zeta in the control of T cell functions. *Sci Signal* **2015**, *8* (374), re6. DOI: 10.1126/scisignal.aaa0974.

(10) Olenchock, B. A.; Guo, R.; Carpenter, J. H.; Jordan, M.; Topham, M. K.; Koretzky, G. A.; Zhong, X. P. Disruption of diacylglycerol metabolism impairs the induction of T cell anergy. *Nat Immunol* **2006**, *7* (11), 1174-1181. DOI: 10.1038/ni1400.

(11) Zha, Y.; Marks, R.; Ho, A. W.; Peterson, A. C.; Janardhan, S.; Brown, I.; Praveen, K.; Stang, S.; Stone, J. C.; Gajewski, T. F. T cell anergy is reversed by

active Ras and is regulated by diacylglycerol kinase-alpha. *Nat Immunol* **2006**, *7* (11), 1166-1173. DOI: 10.1038/ni1394.

(12) Jing, W.; Gershan, J. A.; Holzhauer, S.; Weber, J.; Palen, K.; McOlash, L.; Pulakanti, K.; Wesley, E.; Rao, S.; Johnson, B. D.; et al. T cells deficient in diacylglycerol kinase zeta are resistant to PD-1 inhibition and help create persistent host immunity to leukemia. *Cancer Res* **2017**, *77* (20), 5676-5686. DOI: 10.1158/0008-5472.CAN-17-1309.

(13) Merida, I.; Torres-Ayuso, P.; Avila-Flores, A.; Arranz-Nicolas, J.; Andrada, E.; Tello-Lafoz, M.; Liebana, R.; Arcos, R. Diacylglycerol kinases in cancer. *Adv Biol Regul* **2017**, *63*, 22-31. DOI: 10.1016/j.jbior.2016.09.005.

(14) Sakane, F.; Mizuno, S.; Komenoi, S. Diacylglycerol Kinases as Emerging Potential Drug Targets for a Variety of Diseases: An Update. *Front Cell Dev Biol* **2016**, *4*, 82. DOI: 10.3389/fcell.2016.00082.

(15) Prinz, P. U.; Mendler, A. N.; Masouris, I.; Durner, L.; Oberneder, R.; Noessner, E. High DGK-alpha and disabled MAPK pathways cause dysfunction of human tumor-infiltrating CD8+ T cells that is reversible by pharmacologic intervention. *J Immunol* **2012**, *188* (12), 5990-6000. DOI: 10.4049/jimmunol.1103028.

(16) Riese, M. J.; Wang, L. C.; Moon, E. K.; Joshi, R. P.; Ranganathan, A.; June, C. H.; Koretzky, G. A.; Albelda, S. M. Enhanced effector responses in activated CD8+ T cells deficient in diacylglycerol kinases. *Cancer Res* **2013**, *73* (12), 3566-3577. DOI: 10.1158/0008-5472.CAN-12-3874.

(17) Chen, S. S.; Hu, Z.; Zhong, X. P. Diacylglycerol Kinases in T Cell Tolerance and Effector Function. *Front Cell Dev Biol* **2016**, *4*, 130. DOI: 10.3389/fcell.2016.00130.

(18) Riese, M. J.; Moon, E. K.; Johnson, B. D.; Albelda, S. M. Diacylglycerol Kinases (DGKs): Novel Targets for Improving T Cell Activity in Cancer. *Front Cell Dev Biol* **2016**, *4*, 108. DOI: 10.3389/fcell.2016.00108 From NLM PubMed-not-MEDLINE.

(19) Guo, R.; Wan, C. K.; Carpenter, J. H.; Mousallem, T.; Boustany, R. M.; Kuan, C. T.; Burks, A. W.; Zhong, X. P. Synergistic control of T cell development and tumor suppression by diacylglycerol kinase alpha and zeta. *Proc Natl Acad Sci U S A* **2008**, *105* (33), 11909-11914. DOI: 10.1073/pnas.0711856105.

(20) Jung, I. Y.; Kim, Y. Y.; Yu, H. S.; Lee, M.; Kim, S.; Lee, J. CRISPR/Cas9-Mediated Knockout of DGK Improves Antitumor Activities of Human T Cells. *Cancer Res* **2018**, *78* (16), 4692-4703. DOI: 10.1158/0008-5472.CAN-18-0030.

(21) Yang, J.; Wang, H. X.; Xie, J.; Li, L.; Wang, J.; Wan, E. C. K.; Zhong, X. P. DGK alpha and zeta Activities Control TH1 and TH17 Cell Differentiation. *Front Immunol* **2019**, *10*, 3048. DOI: 10.3389/fimmu.2019.03048.

(22) Fu, L.; Li, S.; Xiao, W.; Yu, K.; Li, S.; Yuan, S.; Shen, J.; Dong, X.; Fang, Z.; Zhang, J.; et al. DGKA Mediates Resistance to PD-1 Blockade. *Cancer Immunol Res* **2021**, *9* (4), 371-385. DOI: 10.1158/2326-6066.CIR-20-0216.

(23) Dominguez, C. L.; Floyd, D. H.; Xiao, A.; Mullins, G. R.; Kefas, B. A.; Xin, W.; Yacur, M. N.; Abounader, R.; Lee, J. K.; Wilson, G. M.; et al. Diacylglycerol kinase alpha is a critical signaling node and novel therapeutic target in glioblastoma and other cancers. *Cancer Discov* **2013**, *3* (7), 782-797. DOI: 10.1158/2159-8290.CD-12-0215.

(24) Patricelli, Matthew P.; Nomanbhoy, Tyzoon K.; Wu, J.; Brown, H.; Zhou, D.; Zhang, J.; Jagannathan, S.; Aban, A.; Okerberg, E.; Herring, C.; et al. In Situ Kinase Profiling Reveals Functionally Relevant Properties of Native Kinases. *Chemistry & Biology* **2011**, *18* (6), 699-710. DOI: dx.doi.org/10.1016/j.chembiol.2011.04.011.

(25) Patricelli, M. P.; Szardenings, A. K.; Liyanage, M.; Nomanbhoy, T. K.; Wu, M.; Weissig, H.; Aban, A.; Chun, D.; Tanner, S.; Kozarich, J. W. Functional interrogation of the kinome using nucleotide acyl phosphates. *Biochemistry* **2007**, *46* (2), 350-358. DOI: 10.1021/bi062142x.

(26) Colon-Gonzalez, F.; Kazanietz, M. G. C1 domains exposed: from diacylglycerol binding to protein-protein interactions. *Biochim Biophys Acta* **2006**, *1761* (8), 827-837. DOI: 10.1016/j.bbalip.2006.05.001.

(27) Das, J.; Rahman, G. M. C1 domains: structure and ligand-binding properties. *Chem Rev* **2014**, *114* (24), 12108-12131. DOI: 10.1021/cr300481j.

(28) Huang, T.; Hosseinibarkooie, S.; Borne, A. L.; Granade, M. E.; Brulet, J. W.; Harris, T. E.; Ferris, H. A.; Hsu, K.-L. Chemoproteomic profiling of kinases in live cells using electrophilic sulfonyl triazole probes. *Chemical Science* **2021**, *12* (9), 3295-3307, 10.1039/D0SC06623K. DOI: 10.1039/d0sc06623k.

(29) Borne, A. L.; Brulet, J. W.; Yuan, K.; Hsu, K. L. Development and biological applications of sulfur-triazole exchange (SuTEx) chemistry. *Rsc Chem Biol* **2021**, *2* (2), 322-337, 10.1039/D0CB00180E. DOI: 10.1039/d0cb00180e.

(30) Boroda, S.; Niccum, M.; Raje, V.; Purow, B. W.; Harris, T. E. Dual activities of ritanserin and R59022 as DGKalpha inhibitors and serotonin receptor antagonists. *Biochem Pharmacol* **2017**, *123*, 29-39. DOI: 10.1016/j.bcp.2016.10.011.

(31) Olmez, I.; Love, S.; Xiao, A.; Manigat, L.; Randolph, P.; McKenna, B. D.; Neal, B. P.; Boroda, S.; Li, M.; Brenneman, B.; et al. Targeting the mesenchymal

subtype in glioblastoma and other cancers via inhibition of diacylglycerol kinase alpha. *Neuro Oncol* **2018**, *20* (2), 192-202. DOI: 10.1093/neuonc/nox119.

(32) Franks, C. E.; Campbell, S. T.; Purow, B. W.; Harris, T. E.; Hsu, K. L. The Ligand binding landscape of diacylglycerol kinases. *Cell Chem Biol* **2017**, *24* (7), 870-880 e875. DOI: 10.1016/j.chembiol.2017.06.007.

(33) McCloud, R. L.; Franks, C. E.; Campbell, S. T.; Purow, B. W.; Harris, T. E.; Hsu, K. L. Deconstructing Lipid Kinase Inhibitors by Chemical Proteomics. *Biochemistry* **2018**, *57* (2), 231-236. DOI: 10.1021/acs.biochem.7b00962.

(34) Granade, M. E.; Manigat, L. C.; Lemke, M. C.; Purow, B. W.; Harris, T. E. Identification of ritanserin analogs that display DGK isoform specificity. *Biochem Pharmacol* **2022**, *197*, 114908. DOI: 10.1016/j.bcp.2022.114908.

(35) Toroitich, E. K.; Ciancone, A. M.; Hahm, H. S.; Brodowski, S. M.; Libby, A. H.; Hsu, K. L. Discovery of a Cell-Active SuTEx Ligand of Prostaglandin Reductase 2. *Chembiochem* **2021**, *22* (12), 2134-2139. DOI: 10.1002/cbic.202000879.

(36) Granade, M. E.; Harris, T. E. Purification of Lipin and Measurement of Phosphatidic Acid Phosphatase Activity from Liposomes. *Methods Enzymol* **2018**, *607*, 373-388. DOI: 10.1016/bs.mie.2018.04.028.

(37) Bern, M.; Kil, Y. J.; Becker, C. Byonic: advanced peptide and protein identification software. *Curr Protoc Bioinformatics* **2012**, *Chapter 13*, Unit13 20. DOI: 10.1002/0471250953.bi1320s40.

(38) MacLean, B.; Tomazela, D. M.; Shulman, N.; Chambers, M.; Finney, G. L.; Frewen, B.; Kern, R.; Tabb, D. L.; Liebler, D. C.; MacCoss, M. J. Skyline: an open source document editor for creating and analyzing targeted proteomics experiments. *Bioinformatics* **2010**, *26* (7), 966-968. DOI: 10.1093/bioinformatics/btq054.

(39) Echols, N.; Harrison, P.; Balasubramanian, S.; Luscombe, N. M.; Bertone, P.; Zhang, Z.; Gerstein, M. Comprehensive analysis of amino acid and nucleotide composition in eukaryotic genomes, comparing genes and pseudogenes. *Nucleic Acids Res* **2002**, *30* (11), 2515-2523. DOI: 10.1093/nar/30.11.2515.

(40) Hahm, H. S.; Toroitich, E. K.; Borne, A. L.; Brulet, J. W.; Libby, A. H.; Yuan, K.; Ware, T. B.; McCloud, R. L.; Ciancone, A. M.; Hsu, K. L. Global targeting of functional tyrosines using sulfur-triazole exchange chemistry. *Nat Chem Biol* **2020**, *16* (2), 150-159. DOI: 10.1038/s41589-019-0404-5 From NLM Medline.

(41) Hsu, K. L.; Borne, A. L.; Brulet, J. W.; Hahm, H. S.; Toroitich, E. K.; Libby, A. H.; Yuan, K.; Ware, T. B.; McCloud, R. L.; Ciancone, A. M. Global targeting of functional (phospho)tyrosines using sulfur-triazole exchange chemistry. *Journal of Immunology* **2020**, *204* (1).

(42) Tu-Sekine, B.; Goldschmidt, H. L.; Raben, D. M. DGK-theta: Structure, enzymology, and physiological roles. *Front Cell Dev Biol* **2016**, *4*, 101. DOI: 10.3389/fcell.2016.00101.

(43) Purow, B. Molecular Pathways: Targeting Diacylglycerol Kinase Alpha in Cancer. *Clinical Cancer Research* **2015**, *21* (22), 5008-5012. DOI: 10.1158/1078-0432.ccr-15-0413.

(44) Knott, G. J.; Doudna, J. A. CRISPR-Cas guides the future of genetic engineering. *Science* **2018**, *361* (6405), 866-869. DOI: 10.1126/science.aat5011.

Chapter 5. Automated Spatially Targeted Optical Microproteomics (autoSTOMP) to Determine Protein Complexity of Subcellular Structure

Adapted with permission from: Yin, B., **Mendez, R.**, YuZhao, R., Rakhit, R., Hsu, K., Ewald, S., Automated spatially targeted optical microproteomics (autoSTOMP) to determine protein complexity of subcellular structure. *Anal. Chem.* 2020, 92, 2, 2005–2010

Introduction and Relevance to Collective Thesis Work:

There are ten diacylglycerol kinases (DGK) isoforms that share conserved lipid kinase domains. The relevance of this work with the rest of the chapters in this dissertation is that this chapter investigates spatially targeted optical microproteomics (STOMP) as a method which we may apply novel technologies to explore deeper into DGKs function as seen in Chapter 2 and 3.

My Contribution to this Collaboration:

My contribution to this chapter includes the peptide identifications by LC-MS/MS chemical proteomics.

5.1 *Abstract*

Spatially targeted optical microproteomics (STOMP) is a method to study region-specific protein complexity in primary cells and tissue samples. STOMP uses a confocal microscope to visualize structures of interest and to tag the proteins within those structures by a photo driven cross-linking reaction so that they can be affinity purified and identified by mass spectrometry (*eLife***2015***, 4, e09579*). However, the use of a custom photo-cross-linker and the requirement for

extensive user intervention during sample tagging have posed barriers to the utilization of STOMP. To address these limitations, we developed automated STOMP (autoSTOMP) which uses a customizable code in SikuliX to coordinate image capture and cross-linking functions in Zeiss Zen Black with image processing in FIJI. To increase protocol accessibility, we implemented a commercially available biotin-benzophenone photo-cross-linking and purification protocol. Here we demonstrate that with autoSTOMP we can efficiently label, purify, and identify proteins belonging to 1–2 μm structures in primary human foreskin fibroblasts or mouse bone marrow-derived dendritic cells infected with the protozoan parasite Toxoplasma gondii (*Tg*). AutoSTOMP can easily be adapted to address a range of research questions using Zeiss Zen Black microscopy systems and LC-MS protocols that are standard in many research cores facilities.

5.2 *Introduction*

Currently, there is a tremendous demand for biochemical and microscopy techniques to assess regional protein complexity and function in tissues, cells, and organelles. Spatially targeted optical microproteomics (STOMP) was designed to identify the proteome of regional structures including amyloid plaques in mouse and human brain sections.[1] In STOMP, structures of interest (SOIs) are stained by labeling reagents (e.g., antibodies, stains) and identified by fluorescence microscopy **(Figure 5.2.1A−B)**. Images are used to generate "MAP" files identifying the SOI **(Figure 5.2.1C)**. Using a custom macro, each "MAP" file guides the 2-photon laser to revisit each SOI pixel and conjugate bifunctional, UV-activated affinity purification tags to proteins within the SOI **(Figure 5.2.1D)**. The tagged proteins are affinity-purified for identification by liquid chromatography−mass spectrometry (LC-MS) **(Figure 5.2.1E)**.

STOMP can be performed on custom SOIs of a wide range of primary cell culture and biopsy tissue sections.[1, 2] This is an advantage compared to proximity biotinylation methods (BioID, APEX) that are largely limited to cell lines amenable to genetical modifications.[2, 3] Moreover, these antibody mediated proximity biotinylation methods (SPPLAT, BAR)[2, 4] will tag many structures if the label-targeting protein exists in more than one location (e.g., ER and plasma membrane). In comparison, STOMP uses a microscope image to guide tagging so the user can customize the photo-crosslinking coordinates. For example, colocalization stains can be used to selectively target subpopulations of the SOI, by dilating, eroding, or finding the edges of an SOI; protein belonging to the core

structure or near-neighbor structures can be identified. The resolution of STOMP approaches 1 μm (BioID, APEX, and BAR approach 10 nm), which is sufficient to study many subcellular structures. The resolution of laser capture microdissection, by comparison, is approximately 10 μm or the level of single cells.[1, 5]

The original STOMP protocol used a bifunctional 6-HISbenzophenone UV-cross-linker which was synthesized cost effectively and easily eluted from nickel agarose columns (the benzophenone covalently attacks local carbon or nitrogen upon UV-excitation). However, diethyl pyrocarbonate (DEPC) treatment was necessary to block binding of endogenous histidine to the nickel agarose matrix which could negatively impact peptide identification by LC-MS.[6,7] Moreover, researchers without a peptide synthesizer did not have access to STOMP. A second limitation of the original STOMP protocol was that the user manually processed images in Zeiss Zen black and FIJI at each field of view. Approximately 48 h of laser time were necessary to tag sufficient protein (0.4− 1 μg) for MS analysis, requiring user intervention at 20−90 min intervals.[1]

Our goal was to develop a fully automated protocol for STOMP (autoSTOMP) using commercially available reagents, an intuitive user interface, and hardware standard in many laboratories and research cores facilities. To do this we implemented a new biochemistry protocol to selectively tag and enrich proteins with biotin-benzophenone **(Figure 5.2.1E−F)**. AutoSTOMP integrates an autofocus and tile array platform that eliminates the need for time-consuming user intervention **(Figure 5.2.1G)**. To communicate between Zeiss Zen Black and FIJI software, SikuliX (http://sikulix.com), a Jython language based open-source icon

recognition software is used **(Figure 5.2.1H)**. To validate the specificity of autoSTOMP, we infected primary human or murine cells with the protozoan parasite Toxoplasma gondii (Tg). Tg has a diverse proteome (~6,000 protein-coding genes expressed across three life stages) and diverged from the common mammalian ancestor 2 billion years ago, so this sample provides an organelle-scale target within the host cell with a distinct proteome to validate autoSTOMP.[8, 9, 10] These proof-of-principle experiments establish autoSTOMP as a robust and reproducible tool to identify regional proteomes at a micron-scale in biological samples.

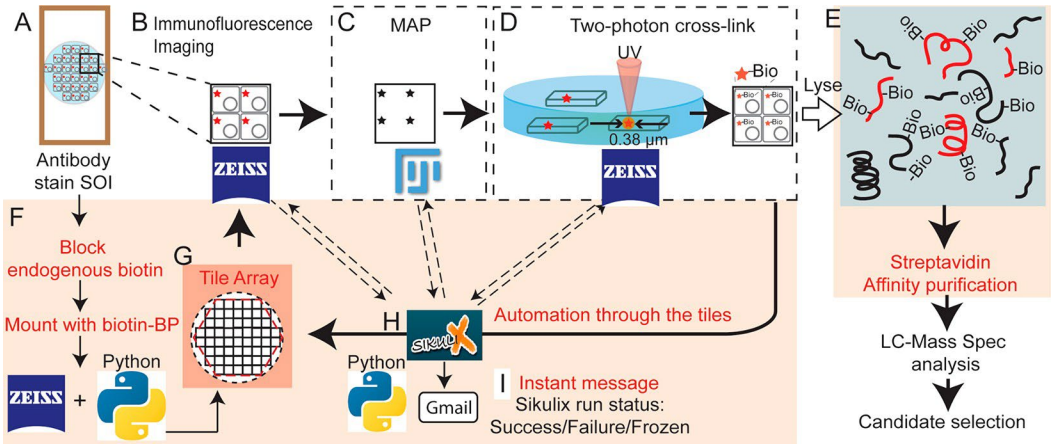

Figure 5.2.1 Overview of automated spatially targeted optical microproteomics (autoSTOMP). (A−B) Structures of interest (SOIs) are stained and identified by fluorescence imaging in visible wavelengths using Zeiss Zen Black software. (C) Images are exported to FIJI software to generate a binary "MAP" file. (D) In Zen Black a custom STOMP macro imports the MAP file, guiding UV excitation by the 2-photon laser to conjugate a bifunctional photoreactive affinity tag to SOI proteins. (E−H) AutoSTOMP modifications include: endogenous biotin blocking and a biotin- benzophenone (biotin-BP) photoreactive affinity tag and streptavidin precipitation (E−F); (G) a custom Python script to tile array fields of view across the sample; (H) the SikuliX icon recognition software to automate the basic STOMP protocol (B−D) and loop through the tile array (G). (I) the run status of omation by SikuliX updated to the user instantly via email. Reprinted with permission from Yin, B., **Mendez, R.**, YuZhao, R., Rakhit, R., Hsu, K., Ewald, S., Automated spatially targeted optical microproteomics (autoSTOMP) to determine protein complexity of subcellular structure. *Anal. Chem.* 2020, 92, 2, 2005–2010. Copyright 2019 American Chemical Society.

5.3 *Materials and Methods*

Material. Unless otherwise noted chemical reagents and consumables were purchased from Thermo Fisher Scientific, USA and used according to manufacturer instructions.

***Tg* infections and immunofluorescence staining.** *Tg* is cultured and stored under BSL2 conditions in accordance with the University of Virginia Environmental Health and Safety approved Biosafety Protocol. The Type II *Tg* parasite strain ME49 was used in all experiments. *Tg* was passaged in confluent human foreskin fibroblasts (HFFs) grown in 25 cm^2 tissue culture flasks. Parasites and HFFs were cultured in complete DMEM media containing DMEM (11965118), 10% heat-shocked FBS (12303C-500ML, Sigma Aldrich), 1% Penicillin/Streptomycin solution (15140163, Fisher Scientific), 1% L-glutamine solution (25030164, Fisher Scientific), and 1% 100 mM sodium pyruvate solution (11360070, Life Technologies), 1% 1 M HEPES solution (15630080, Life Technologies). Media was stored at 4 °C and warmed to 37 °C before use. C57BL/6 mice were bred in the University of Virginia vivarium in accordance with ABSL-1 standards and AALAC approved protocol. Mouse bone marrow-derived dendritic cells (mBMDCs) were differentiated for 6-8 days in complete RPMI media supplemented with 10% mouse GMCSF supernatant derived from B16 cells stably expressing mouse GMCSF as previously described9. THP-1 cells were cultured in suspension in complete RPMI media containing RPMI (10-040-CV, Corning), 10% heat-shocked FBS, 1% Penicillin/Streptomycin solution, 1% L-glutamine solution, and 1% 100 mM sodium pyruvate solution, 1% 1 M HEPES.

For experimental infections, $0.5x10^6$ THP-1 cells were differentiated with complete RPMI media containing 100 ng/mL PMA (AAJ63916MCR, Fisher Scientific) for 2 days on 12 mm cover glass (64-0712, Harvard Apparatus, USA) coated with poly-D-lysine (ICN15017550). $0.5x10^6$ immortalized bone marrow derived macrophages (iBMDM, mouse) were grown in complete RPMI media for 1 day on 12 mm cover glass coated with poly-D-lysine. mBMDCs were plated $1.35x10^6$ per well of a 12 well plate containing a single 18 mm round cover glass (64-0714, Harvard Apparatus, USA) coated with poly-D-lysine. HFFs were grown to confluency on 18mm round cover glass. *Tg* was grown in HFFs until large intracellular parasite vacuoles were observed. Intracellular *Tg* was harvested by scraping infected HFF monolayers with a rubber policeman and syringe lysing the HFFs through a 25G blunt-ended syringe needle. *Tg* was counted on a hemocytometer and added to host cells at a multiplicity of infection (MOI) of 10, or for HFF infections, $8.8x10^4$ parasites per mm^2. The *Tg*-infected HFFs on coverslips were harvested after 2 hrs.

Slide preparation for STOMP. *Tg*-infected HFFs on coverslips were fixed with 100% methanol at -20 to -30 °C (prechilled) for 15 min. Methanol was decanted, and samples were washed three times with room temperature PBS. If staining did not take place immediately, PBS was aspirated, and coverslips were stored at -30 °C. To stain *Tg*, the slides were blocked with 2% BSA in TBS at room temperature for 1 hr, a rabbit polyclonal antibody specific to soluble tachyzoite antigen (STAG) directly conjugated to FITC (PA1-7253, Invitrogen) was diluted 1:300 in TBS-T (0.1% Tween20) and coverslips were stained at room temperature for 1 hr. Slides

were washed three times with TBST. Endogenous biotin was blocked with Avidin/Biotin Blocking Kit (SP-2001, Vector Laboratories) following the manufacturer's protocol. The stock solution of 0.5 M biotin-dPEG®3-benzophenone (biotin-BP, 10267, Quanta BioDesign) in anhydrous DMSO (89139-666, VWR) is stable for 12 months when stored with desiccant in the dark at -30°C. The biotin-BP mounting media must be prepared fresh (used within 4 hrs) by diluting the biotin-BP stock solution in 50/50 (v/v) DMSO/water to a working concentration of 1 mM biotin-BP. Coverslips were mounted in 12 µL biotin-BP mounting media in a cold room (4 °C) with weak light and sealed with nail polish (Insta-DriFast Dry Nail and Double Duty Base and Topcoat, Sally Hansen). If multiple slides were necessary, coverslips were mounted the day of crosslinking and stored in the dark at room temperature before microscopy.

Validation of biotin-benzophenone cross-linking by microscopy. Following biotin-BP cross-linking, each coverslip was soaked in DI water (RT, dark) for 30 minutes, and the nail polish seal was gently pulled away. Excess mounting media was removed by three washes with 50/50 (v/v) DMSO/water followed by three washes with Mili-Q water. Slides were blocked in 2% BSA in TBST for 30 min, and then incubated in TBST (0.1% Tween20) containing 1: 500 dilution Alexa Fluor® 594 Streptavidin (#016-580-084, Jackson ImmunoResearch Laboratiories) for 45 min. Coverslips were washed three times in TBST (0.1% Tween20) and mounted with mounting media containing DAPI (H-1000, Vector Laboratories) for imaging.

Image acquisition, **mask generation and UV-biotinylation using autoSTOMP.** All microscopy and cross-linking were performed on an LSM880 confocal

microscope (Carl Zeiss, Inc., Germany) and a Chameleon multiphoton light source (Coherent Inc., USA) in the Ewald Lab at the University of Virginia. Images were acquired using Zen Black (Carl Zeiss). Image modification and MAP file generation were performed in FIJI (FIJI Is Just ImageJ)12. Structures of Interest (SOI, *Tg* here) were visualized using the 25x oil emersion lens (LD LCI Plan-Apochromat 25x/0.81 mm KorrDIC M27) with immersion oil (518 F for 30 °C, refractive index = 1.518, 444970-9000-000, Carl Zeiss) and the argon ion laser source (488 nm) with 500-530 nm bandwidth. A 512 x 512 pixel2image was acquired for each field of view. Sikulix version 1.1.4 (http://sikulix.com/) was used to automate tasks between software platforms. Python (version 3.6, www.python.org) and Spyder (version 3.2.8, www.spyder-ide.org) were used to generate a tile array across the slide surface (~ 500 tiles). Using the SikuliX automation platform, each field of view was processed as follows. First, the SOI in each field of view were imaged. The.czifile was exported into FIJI where a binary image was created, thresholded and/or “erode”, “dilate” or “ROI manager” functions were used to create a “MAP file” of the regions to be photo crosslinked. The MAP file is converted to a .txt file, which is imported by the STOMP macro in Zen Black. In Zen Black, the STOMP macro directs the Chameleon to deliver two-photon 720 nm light to each pixel defined in the MAP file. Crosslinking four to five million pixels typically labeled sufficient protein (approximately 1 µg) for mass spectrometry analysis. A step-by-step tutorial of the autoSTOMP protocol, and all the source codes are deposited at GitHub (GitHub Inc.).

https://github.com/boris2008/Sikulix-automates-a-workflow-performed-in-multiple-software-platforms-in-Windows.git

Streptavidin precipitation. Once the UV-cross-linking is complete for each slide, the coverslip was soaked in DI water (RT, dark) for 30 min, and the nail polish seal was gently pulled away. Excess mounting media was eliminated by three washes with 50/50 (v/v) DMSO/water followed by three washes with Mili-Q water. Excess water was aspirated and the coverslip was stored at -30 °C while photo-cross-linking was performed on additional slides.

Our purification protocol for MS analysis is modified from *Hadley et al*.[1] Samples are dissociated from the coverslip in 8 M urea lysis buffer containing 100 mM NaCl, 25 mM Tris, 2% SDS, 0.1% tween 20, 2 mM EDTA, 0.2 mM PMSF, and 1x Roche cOmpleteProtease inhibitor (11873580001). Coverslips were placed on a parafilm (Bemis) membrane with cells facing up and incubated with 50 µL urea lysis buffer at room temperature for 30 min. The coverslip was then rinsed with 100 µL Mili-Q water and followed by another incubation with 50 µL urea lysis buffer at room temperature for 30 min. All of the solutions after lysis were collected and combined as lysate in low protein binding 1.5 mL microcentrifuge tubes. To reduce the nucleic acid-protein complex formation and associated lysate viscosity, Benzonase (E1014-25KU) and RNase A from bovine pancreas (10109142001) were used. Benzonase (0.1 µL per 5 x 10^6cells) was added and incubated at 37 °C for 30 min followed by RNase (0.5 µL per 5 x 10^6cells) treatment at 65 °C for 15 min. The lysate was cooled to room temperature and ready for affinity purification.

Four different buffers were used for the affinity purification: TU (50 mM Tris-Cl, 2 M urea, and 150 mM NaCl at pH = 7.4), TUST (TU buffer spiked with 0.1% SDS and 0.1% Tween 20 at pH = 7.4), TUB (0.5 mM biotin in TU buffer) and 100 mM NH4HCO3buffer. The volume of lysate of each sample was filled up to 1 mL with TUST. 10 µL Pierce™ Streptavidin (SA) Magnetic Beads (88817) 50% slurry was washing with 1 mL TUST once and then added to the lysate and mixed by vortexing. The mixture was incubated on a rotator at room temperature for 1 hr to bind the biotinylated proteins (longer incubation time is not recommended as it will increase unspecific binding). The magnet (DynaMagTM-2, Invitrogen) was used to pellet the SA beads. To remove nonspecific-bound proteins, samples were washed three times with 1 mL TUST, five times with 1 mL TU, 1 time with 1 mL TUB, and three times with 1 mL 100 mM NH_4HCO_3 buffer. After each wash, SA beads were pelleted on the magnet for 3 min, and the buffer was removed by pipetting while on the magnet. For each wash, the SA beads were mixed by vortexing and incubated for 5 min before the SA beads were applied to the magnet again. After all washing, the SA beads were resuspended in 100 µL 100 mM NH_4HCO_3 buffer.

AutoSTOMP workflow. Endogenous biotin was blocked with an Avidin/Biotin Blocking Kit (SP-2001, Vector Laboratories). *Tg* was identified with an antibody specific to *Tg* soluble tachyzoite antigen (STAG) conjugated to FITC (PA1-7253, Invitrogen). The coverslips were mounted with biotin-$dPEG_3$ benzophenone (biotin-BP, Quanta BioDesign) in 50/50 (v/v) DMSO/water. Images were acquired on a LSM880 microscope (Carl Zeiss, Inc., Germany) with a Chameleon multiphoton light source (Coherent Inc., USA) using Zen Black and a 25× oil

immersion lens (LD LCI Plan- Apochromat 25×/0.81 mm Korr DIC M27). Image processing and MAP files were made in FIJI.[11] A Python script to tile array fields of view, and a SikuliX (version 1.1.4, http://sikulix.com) script were used to coordinate the images-acquisition in Zen Black, MAP file generation in FIJI, and MAP-guided UV excitation in Zen Black macro. Typically, 4−5 million pixels yields 1 µg of protein for LC-MS analysis. A step-by-step tutorial of the autoSTOMP protocol and source codes are available at https://github.com/boris2008/Sikulix-automates-a-workflow-performed-inmultiple-software-platforms-in-Windows.git.

After photo-cross-linking, coverslips were detached and washed, and samples were dissociated in urea buffer. Benzonase (E1014-25KU) and RNase A (10109142001) treatment degraded nucleic acids, and biotinylated proteins were isolated by streptavidin precipitation (SA-P) (Pierce 88817). Samples were on-bead digested with trypsin/LysC for LC-MS analysis using a Thermo Scientific LTQ mass spectrometer coupled with a Shimadzu LC-20AD system **(Figure 5.3.1)**. The peptide and proteins were each identified with a false discovery rate (FDR) smaller than 1%. Alternatively, a Thermo Scientific Q Exactive HF-X mass spectrometer system was used **(Figure 5.3.2)** with FDR < 0.2% for peptide identification and FDR < 2% for protein identification. Custom R scripts for protein assignment and statistical analysis are available at https://github.com/boris2008/codes-forvalidating-STOMP-with-MS.git.

Western blot. To validate *Tg* protein enrichment by Western blot, total protein content for each sample was normalized using PierceTMMicro BCA kit (#23235, Pierce). Proteins were separated by SDS-PAGE using Mini Gel Tank tool kit

(25977, Thermo Fisher) and were transferred to PVDF membrane (1704274, Bio-Rad) using Trans-Blot Turbo Transfer System (Bio-Rad). The PVDF membrane was blocked in 2% milk TBST (0.1% Tween 20) solution for 1 hr at room temperature followed by sequential incubation with antibody diluted in TBST (0.1% Tween 20) and alternating washing with TBST (0.1% Tween 20). Streptavidin-HRP (016-030-084, Jackson ImmunoResearch) was used to probe biotin. Proteins were visualized on ChemiDocTM Touchimaging system (Bio-Rad) with HRP substrate (WBLUF0100, Millipore).

Sample preparation for LC-MS. After affinity purification, on-bead reduction and alkylation of SA beads were performed in 1 mL 25 mM NH_4HCO_3 by adding 25 µL 10 mM DTT at room temperature for 30 min and 25 µL 15 mM iodoacetamide in dark at room temperature for 1 hr in sequence. To quench excess iodoacetamide, 25 µL 5 mM DDT solution was added and incubated for 10 min. Trypsin/Lys-C (V5072 Promega) was directly spiked into the protein lysate at a ratio of Trypsin/Protein = 1:25. Digestion was continued overnight (~12 h) at 37 °C. Formic acid was added to a final concentration of 1% (v/v) to stop the trypsinization. SA beads were removed by the magnet, and the supernatant was saved. 7.5 nmol Angiotensin/Vasoactive Standard (A9650-1MG/V0131-.1MG, Sigma) was spiked into the peptide digest. The peptide digest was desalted using Pierce™ C18 Tips with binding, washing (with 0.1% formic acid in water), and eluting (with 60% acetonitrile in water) steps by following the manufacturer's instructions. The sample was dried completely on the SpeedVac concentrator (Model: SPD131DDA-115). The peptide digest was dissolved in 21 µL of LC-MS grade

water containing 0.1% formic acid (F0507-100ML, Sigma). The digest was filtered with a 0.65 µm pore-size micro-centrifuge filter before it was loaded to an HPLC auto-injection sample.

Peptide mass identification by LC-MS. For the initial validation of autoSTOMP, LC-MS was performed on a linear ion trap MS (Thermo Scientific LTQ, Thermo Fisher, USA) coupled with LC (LC-20AD, Shimadzu, USA) in the Hsu lab at the University of Virginia. 1 µL (5%) of the peptide digest was injected to a C18 capillary column (20 cm of 5 µmC18 (YMC*GEL) packed in 360 µmo.d.x 75 µmi.d. fused silica) and desalted with 0.05% acetic acid at a 185 nL/min for 30 min at room temperature. After desalting, a gradient of acetonitrile/0.1 M formic acid was applied for 200 min: solvent A (water + 0.05% acetic acid) and solvent B (80% acetonitrile + 0.05% acetic acid) were applied in the order of 0% B for 5 min, 0-25% B for 111 min, 25-45% B for 35 min, 45-95% B for 1 min, 95% B for 7 min, 95-0% B for 6 min, 0% B for 34 min, and re-equilibration with 0% B for 10 min. The separation column ran at room temperature. The eluted peptides were electrosprayed into the LTQ MS, which was operated in the positive ion mode with a “top 3” data-dependent acquisition method that consisted of one MS scan (m/z: 350-1800) followed by three MS/MS scans of the most abundant ions recorded in the preceding MS scan. For mass assignment IP2 (the Integrated Proteomics Applications, Inc., USA) using the ProLuCID algorithm was used to search against human protein database (https://www.uniprot.org) and *Tg*-protein database (released 41, https://toxodb.org/toxo/) with reversed sequence decoys. The peptide and proteins were identified with false discovery rate (FDR) smaller than

1%, separately. Differences in protein and peptide abundances between the samples were based on MS/MS spectral counting using the COMPARE function in the IP2-Integrated Proteomics Pipeline. The resulting MS2 spectra matches were assembled into protein identifications.

To compare protein enrichment in *Tg* with protein enrichment at the parasite vacuole membrane using the “donut” MAP file function, a Thermo Electron Q Exactive HF-X mass spectrometer system with an Easy Spray ion source connected to a Thermo 75 µm x 15 cm C18 Easy Spray column was used at the University of Virginia Biomolecular Analysis Facility Core Laboratory. 7 µL (33.3%) of the extract was injected and the peptides eluted from the column by a gradient at a flow rate of 0.3 µL/min at 40 °C for more than 1 hr. Solvent A (water + 0.1% formic acid) and solvent B (80% acetonitrile + 0.1% formic acid) were applied in the order of 2% B for 1.5 min, 2-23% B for 51 min, 23-35% B for 10 min, 35-95% B for 1 min, and 95% B for 5 min. The nanospray ion source was operated at 1.9 kV. The digest was analyzed using a Top10 method with the MS scan set to 120K resolution and HCD scans set to 30K resolution. This mode of analysis produces approximately 25000 MS/MS spectra of ions ranging in abundance over several orders of magnitude. The data were analyzed by database searching using the Sequest search algorithm deployed in Proteome Discoverer™ (Thermo Fisher Scientific Inc. USA) against Uniprot mouse and *Tg* database from ToxoDB with reversed sequence decoys separately. Protein (FDR < 2%) and peptide identification (FDR < 0.2%) were organized and summarized by Scaffold (Proteome Software, Inc).

Data analysis. Common contaminants listed on the MaxQuant website http://www.coxdocs.org/doku.php?id=maxquant:start_downloads.htmhave been identified and excluded from our protein data. The proteins possess high similarly (> 90% proteins identification and >80% peptide sequence coverage) between human and *Tg* protein were excluded from downstream analysis using a custom python script “myBlast.py” running on the Rivanna computing server (https://arcs.virginia.edu/rivanna) at the University of Virginia. A Student’s t-test was used to perform pairwise comparison across the three replicates of each sample with R scripts in Rstudio (version 1.1.456, www.rstudio.com/) with R packages (for examples, readr, xlsx, dplyr, tidyverse) and p-values for each protein were reported. Gene Ontology (GO) and KEGG pathway annotation were added using David Bioinformatics Resources 6.813. The enriched proteins and the statistical summarization were made in R scripts with the table organization and statistical tool packages mentioned above. These custom scripts are deposited at GitHub (GitHub Inc.) https://github.com/boris2008/codes-for-validating-STOMP-with-MS.git. Plots were created with R package “ggplot2 and ”ggrepel” in R or GraphPad Prism (version 8.2.1).

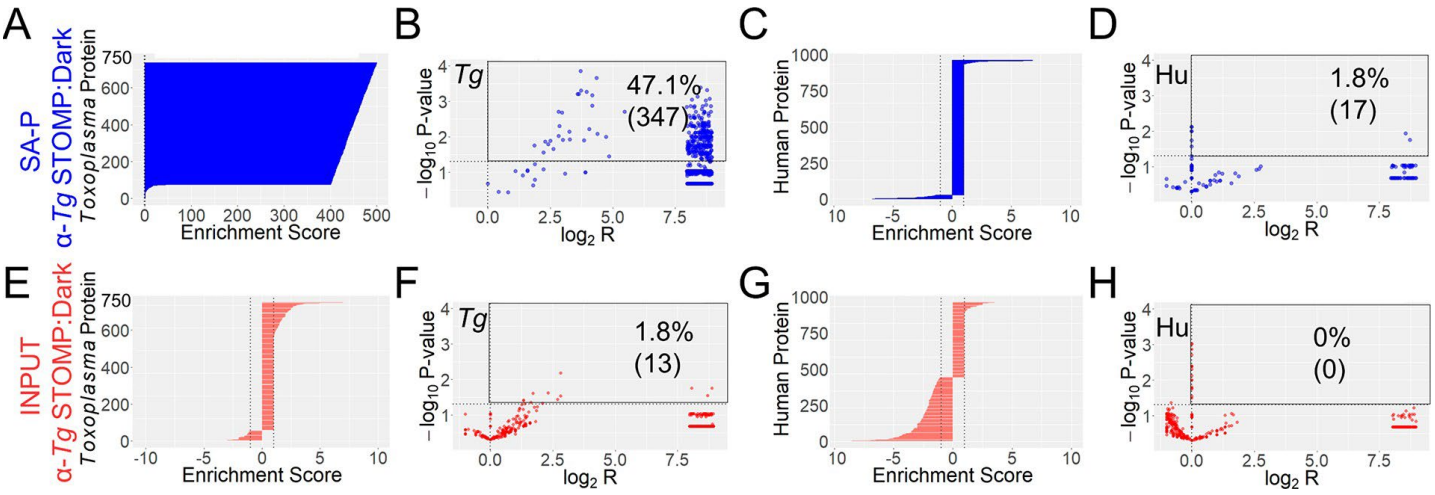

Figure 5.3.1 *Tg* proteins enriched by auto-STOMP are detected by LC-MS. *Tg* infected HFFs or Dark controls were streptavidin precipitated (SA-P) as described in **(Figure 5.5.2)**. (A−B) *Tg* proteins were enriched in *α-Tg* STOMP SA-P samples relative to the Dark SA-P controls; few human proteins were similarly enriched (C−D), (E−H) *Tg* proteins (E−F) and human proteins (G−H) are similar in INPUT samples (*α-Tg* STOMP vs Dark). Enrichment score (ES) = spectral count ratio (SCR) of "*α-Tg* STOMP SA-P" over "Dark SA-P"; a negative ES = (−1/SCR). Volcano plots represent the significant enrichment of identified *Tg* or human proteins (*y* axis: $-\log_{10}$ of p-value, Student's *t* test) versus fold enrichment (*x* axis: $\log_2$ of SCR). *N* = 3 independent experiments. Reprinted with permission from Yin, B., **Mendez, R.**, YuZhao, R., Rakhit, R., Hsu, K., Ewald, S., Automated spatially targeted optical microproteomics (autoSTOMP) to determine protein complexity of subcellular structure. *Anal. Chem.* 2020, 92, 2, 2005–2010. Copyright 2019 American Chemical Society.

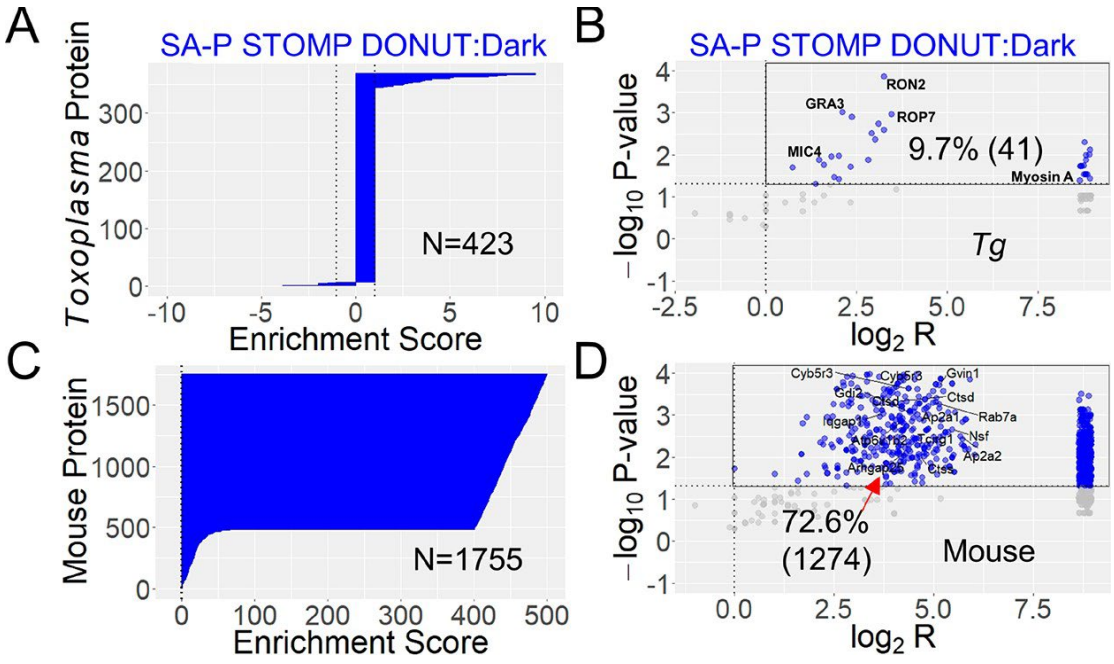

Figure 5.3.2 AutoSTOMP selectively identifies host (mouse) and parasite proteins in custom SOIs surrounding *Tg*. The regions surrounding but excluding *Tg* (STOMP DONUT) in mBMDCs or Dark controls were streptavidin precipitated (SA-P) and identified by LC-MS. (A−B) Enrichment scores of 423 *Tg* proteins detected (A) and significance of enrichment as described in **(Figure 5.3.1)** (B). (C−D) Enrichment scores of the 1755 mouse proteins detected (C), and significance of enrichment (D). Confirmed PVM-associated proteins are annotated. *N* = 3 independent experiments. Reprinted with permission from Yin, B., **Mendez, R.**, YuZhao, R., Rakhit, R., Hsu, K., Ewald, S., Automated spatially targeted optical microproteomics (autoSTOMP) to determine protein complexity of subcellular structure. *Anal. Chem.* 2020, 92, 2, 2005–2010. Copyright 2019 American Chemical Society.

5.4 *Results*

5.4.1 *AutoSTOMP Selectively Biotinylates SOIs*

The photoexcitation conditions for autoSTOMP were determined experimentally by modifying the laser power (P), the number of iterations (I), and pixel dwell time (D). P/I/ D = 3/1/1 was chosen to minimize the total time necessary to photo-cross-link the sample (optimal photobleaching) without overheating. The concentration of biotin-BP in the mounting media was also titrated to identify the minimum concentration necessary to achieve a robust SA-594 signal.

To determine if autoSTOMP can effectively enrich proteins from subcellular SOIs, we infected human foreskin fibroblasts (HFFs) with the Me49 strain of Type II Toxoplasma gondii (*Tg*) **(Figure 5.5.1A)**. After 2 h of infection, the coverslips were fixed and stained with *Tg*-specific antibody (α-Tg-488) to identify *Tg* as the SOIs **(Figure 5.5.1B)**. A MAP file was generated and used to guide UV-excitation and biotinylation of *Tg* SOIs using the autoSTOMP platform **(Figure 5.5.1C)**. After UV-crosslinking, coverslips were lifted and stained with streptavidin-Alexa Fluor594 (SA-594) and reimaged **(Figure 5.5.1D−F)**. Colocalization of the α-*Tg* signal and SA-594 signal confirmed the accuracy of UV targeting and the efficiency of biotinylation. As expected, the α-*Tg*-488 signal was slightly photobleached upon reimaging **(Figure 5.5.1E vs 2B)**. Tile imaging confirmed that autoSTOMP selectively biotinylated SOIs in the MAP without increasing the background SA-594 signal in the targeted or nontargeted fields of view **(Figure 5.5.1G−H)**. These data indicate that autoSTOMP efficiently tags biotin-BP to regions defined as SOIs by immunofluorescence imaging.

5.4.2 *AutoSTOMP Biotinylation and Precipitation Procedures Enrich SOI Protein*

To validate the efficiency of SOI biotinylation and streptavidin purification, *Tg* infected HFFs were stained and biotinylated as described in **(Figure 5.5.1) (Figure 5.5.2, α-*Tg* STOMP)**. Negative control samples were prepared identically but not exposed to UV-light **(Figure 5.5.2, Dark)**. Samples were then washed of excess biotin and dissociated in urea lysis buffer. Half of each sample was reserved as an "INPUT" control; biotinylated proteins were enriched from the other half on streptavidin magnetic beads **(Figure 5.5.2A, SAP)**. *Tg* proteins were enriched in α-*Tg* STOMP SA-P samples, not the Dark SA-P sample (**(Figure 5.5.2B)**, note that the α-*Tg* STAG antibody recognizes multiple parasite proteins). Both INPUT controls had similar amounts of *Tg* proteins and human GAPDH **(Figure 5.5.2C)**. Unlike *Tg* proteins, human GAPDH was not enriched in the α-*Tg* STOMP SA-P sample **(Figure 5.5.2C)**. Probing the blots with streptavidin horseradish peroxidase (HRP) confirmed that biotinylated proteins were only present in the α-*Tg* STOMP samples **(Figure 5.5.2D)**. These data indicate that autoSTOMP effectively conjugates biotin-BP to SOI proteins and that biotinylated SOI proteins are enriched by the SA-P procedure.

5.4.3 *AutoSTOMP Enriches SOI Proteins by LC-MS*

We next asked if *Tg* SOI proteins could be enriched and identified by LC-MS using autoSTOMP. Samples were prepared as described in **(Figure 5.5.2)**, and then, peptides were digested and eluted from the SA-beads with trypsin/lys-C

(Figure 5.3.1). Peptide masses were determined by ion trap mass spectrometry coupled with liquid chromatography. Peptides that aligned uniquely to the *Tg* protein database or the human protein database were quantified by the number of spectral counts and ranked in order of abundance **(Figure 5.3.1)**.

In total, 736 parasite proteins and 960 human proteins were detected with a false discovery rate (FDR) < 1% for peptide and for protein identification. Of the *Tg* proteins identified in the α-*Tg* STOMP SA-P samples relative to Dark SA-P samples **(Figure 5.3.1A)**, 47.1% of the 736 *Tg* proteins were significantly enriched **(Figure 5.3.1B, black box)**. As expected, few human proteins **(Figure 5.3.1C)** were significantly enriched **(Figure 5.3.1D)** in α-*Tg* STOMP SA-P samples. In the INPUT controls, the spectral counts ratios for most *Tg* **(Figure 5.3.1E−F)** and human proteins **(Figure 5.3.1G−H)** were close to 1, and few, if any proteins were significantly enriched confirming similar representation of proteins in both samples.

Using the spectral count distribution model,[12] we found that 90.2% (46 of 51) of the “high abundance” *Tg* proteins (spectral counts ≥5) and 43.9% (301 of 685) of the “low abundance proteins” (spectral counts < 5) were significantly enriched in α-*Tg* STOMP SA-P relative to Dark SA-P. Both analyses indicate that STOMP reliably reports the high abundance proteins and a major portion of low abundance proteins in the sample.

5.4.4 *AutoSTOMP Selectively Enriches Proteins from Custom SOIs Adjacent to the Stained Targets*

The region surrounding the parasite is a biologically relevant organelle called the parasite vacuole membrane (PVM). The PVM is composed of secreted parasite effector proteins as well as host-derived lipids, regulators of vesicle trafficking, immunity, and organelle recruitment.[13] We reasoned that generating a MAP file from the 1 μm region surrounding but excluding the parasite would allow us to identify candidate host and parasite proteins belonging to the PVM. To do this, a MAP file was generated by identifying the perimeter of the α- Tg-488 signal **(Figure 5.5.3A−B)** and dilating the perimeter by two pixels (~1 μm) using the "donut macro" in FIJI **(Figure 5.5.3C)**. Spatial selectivity of the biotinylation reaction to the Tg "DONUT" SOI **(Figure 5.5.3D−F)** was confirmed by reimaging the slides with SA-Alexa Fluor594 staining and comparing SA-594 intensity to Tg signal in adjacent, nontargeted fields of view and comparing the SOI pattern to Tg SOI.

Next, the DONUT SOI or Dark controls were streptavidin precipitated and submitted for mass spectrometry using a high performance Q Exactive HF-X LC-MS **(Figure 5.3.2)**. 423 Tg proteins were identified in the STOMP DONUT SA-P sample **(Figure 5.3.2A)** of which 9.7% (41 proteins) were significantly enriched **(Figure 5.3.2B)**. Several of these were secreted Tg proteins with known localization to the PVM or the adjacent intravacuolar network including rhoptry neck protein RON2, rhoptry protein ROP7, dense granule protein GRA3, and microneme proteins MIC4.[14-16] Although differences in the MS protocol limited direct comparison of the α-Tg STOMP SA-P **(Figure 5.3.1B)** and STOMP DONUT

SA-P **(Figure 5.3.2B)**, most Tg proteins identified in the Tg SOI are not enriched in the DONUT SOI, consistent with spatial selection of parasite proteins trafficked to the PVM. In contrast to the α-Tg STOMP SA-P sample, where fewer host proteins than Tg proteins were significantly enriched, 1755 mouse proteins were identified **(Figure 5.3.2C)**, 72.6% of these were significantly enriched in the STOMP DONUT SA-P relative to Dark SA-P **(Figure 5.3.2D)**. Fourteen of these host proteins are known to localize at the PVM or the intravacuolar network during Tg infection **(Figure 5.3.2D)**. These include Rab-7, AP-2, and cathepsin D, which are associated with endolysosomal vesicles at the PVM and Tg clearance by the autophago-lysosome.[13, 17-20]

Searching the significantly enriched mouse proteins against gene ontology (GO) and Kyoto Encyclopedia of Genes and Genomes (KEGG) annotation libraries indicated proteins belonging to the annotation groups “transport”, “metabolic processes”, “protein binding”, “ATP binding”, and “membrane” were enriched. These are consistent with the biology of parasite scavenging host metabolic substrates,[21, 22] regulated membrane fusion,[23] and organelle recruitment to the PVM including endolysosomal vesicles and endoplasmic reticulum.[13, 23-25] Based on these data, we conclude that autoSTOMP selectively enriches proteins belonging to subcellular regions with a spatial resolution of approximately 1 μm.

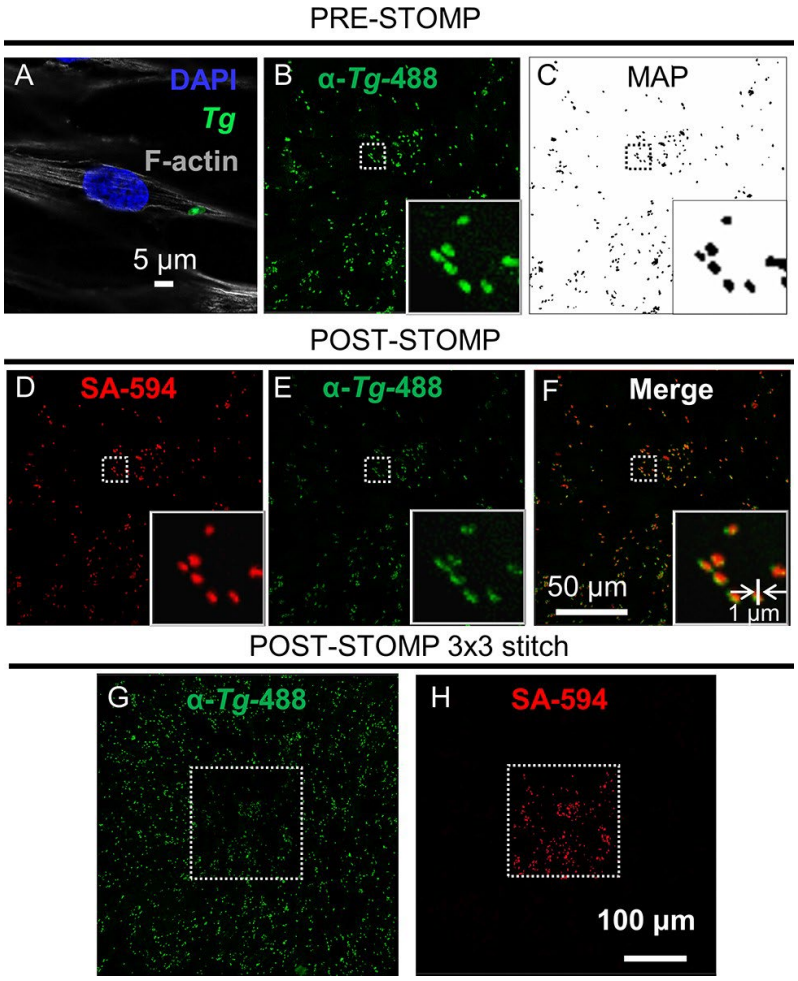

Figure 5.5.1 *Tg* proteins are selectively biotinylated by autoSTOMP UV-cross-linking. (A) Representative image of GFP-expressing *Tg* in human foreskin fibroblasts (HFF) stained for nuclei (DAPI) and F- actin (phalloidin-660). (B) *Tg*-specific antibody staining identifies *Tg* as the SOI (*α-Tg*-488, green). (C) MAP file generated from (B). (D− F) After UV-mediated biotin-BP tagging, samples are reimaged for biotin (D, SA-594, red) and *Tg* signal (E, *α-Tg*-488, green) merged in (F). The inset is an enlarged view of the dashed box. (G−H) 3 × 3 tile array centered on autoSTOMP field of view stained for *Tg* (G, green) or SA-594, (H, red). Reprinted with permission from Yin, B., **Mendez, R.**, YuZhao, R., Rakhit, R., Hsu, K., Ewald, S., Automated spatially targeted optical microproteomics (autoSTOMP) to

determine protein complexity of subcellular structure. *Anal. Chem.* 2020, 92, 2, 2005–2010.

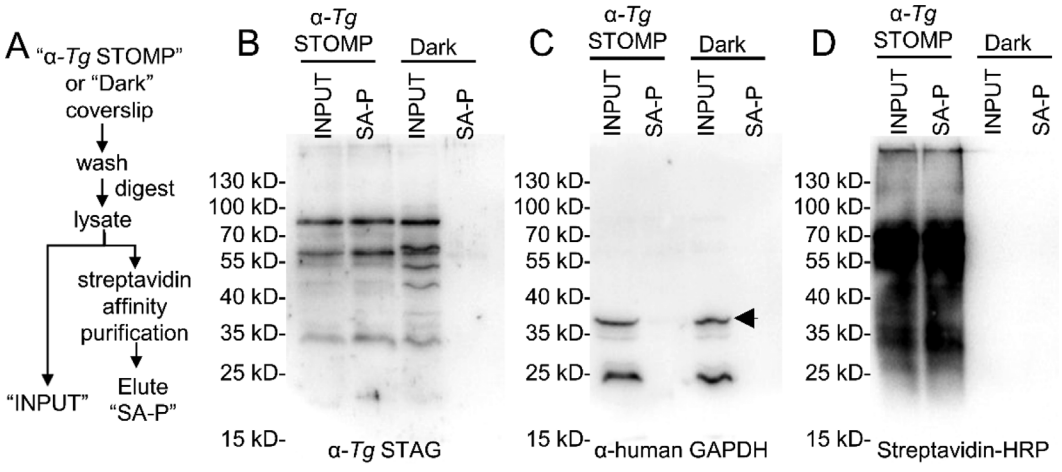

Figure 5.5.2 *Tg* proteins are enriched by autoSTOMP mediated-biotinylation and streptavidin precipitation. (A) *Tg* SOIs inside HFFs (*α-Tg* STOMP) were photo-cross-linked as described in **(Figure 5.5.1)** or not exposed to UV light (Dark). Half of each lysate was reserved for the loading control (INPUT); the other half was streptavidin precipitated (SA-P) and then immunoblotted with *α-Tg* STAG antibody (B, note: *α-Tg* STAG detects multiple *Tg* proteins) and *α*-human GAPDH antibody (C, arrow) and then reprobed with SA-HRP (D). Representative of three independent experiments. Reprinted with permission from Yin, B., **Mendez, R.**, YuZhao, R., Rakhit, R., Hsu, K., Ewald, S., Automated spatially targeted optical microproteomics (autoSTOMP) to determine protein complexity of subcellular structure. *Anal. Chem.* 2020, 92, 2, 2005–2010. Copyright 2019 American Chemical Society.

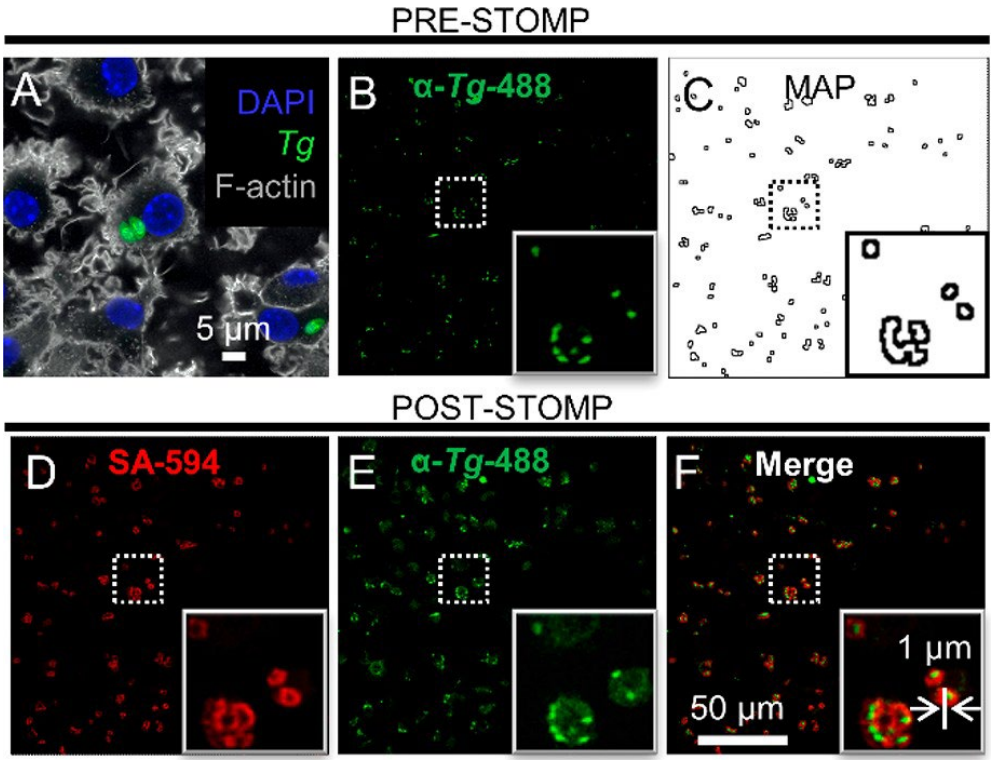

Figure 5.5.3 AutoSTOMP selectively biotinylates custom SOI proteins. (A) Representative image of mouse bone marrow derived dendritic cells (mBMDCs) infected with GFP-expressing *Tg* and stained for nuclei (DAPI) and F-actin (phalloidin-660). (B−C) *Tg* infected mBMDCs stained with a *Tg*-specific antibody (*α-Tg*-488, green) (B) and used to generate MAP files identifying the region surrounding but excluding *Tg* as the SOI (C, DONUT). (D−F) After UV-mediated biotin-BP tagging, biotinylated proteins were visualized using streptavidin Alexa Fluor594 staining (D, SA-594, red), and compared to the *Tg* signal (E, *α Tg*-488, green; F, merge). Reprinted with permission from Yin, B., **Mendez, R.**, YuZhao, R., Rakhit, R., Hsu, K., Ewald, S., Automated spatially targeted optical microproteomics (autoSTOMP) to determine protein complexity of subcellular structure. *Anal. Chem.* 2020, 92, 2, 2005–2010. Copyright 2019 American Chemical Society.

5.5 *Discussion*

Here we show that autoSTOMP is a fully automated platform to visualize, tag, affinity-purify, and identify proteins by mass spectrometry. AutoSTOMP represents a significant technological advance because it liberates the user from field-by-field task management previously required to perform STOMP. In automating the STOMP protocol, we retained and refined the ability to define regions of interest based on structure size, shape, or localization using FIJI image analysis software. This flexibility is a major advantage of STOMP compared to other proximity-based tagging tools.[2, 4]

Our choice of biotin-BP was based on the low background reactivity of the BP group and the high affinity of the biotin−streptavidin interaction.[1] However, the cost of this tagging strategy is that most BP modified peptides will remain attached to the SA beads. Any eluted peptides bearing biotin-BP will not be recognized by MS, due to the uncertain mass shift imparted by the tag. The ideal labeling condition to maximize sensitivity and yield would lead to one biotin-BP attachment per protein such that each protein is precipitated, and only one peptide fragment is rendered undetectable by the biotinylation modification. However, the optimal labeling ratio for any protein will be a function of the protein's size, accessibility, and the percent sequencing coverage by mass spectrometry. We can optimize biotin-BP labeling conditions for low abundance proteins of interest for their best recovery rate accordingly. We anticipate that autoSTOMP can be used to identify proteins belonging to 1 μm scale subcellular structures in a range of biological specimens.

5.6 *Acknowledgments*

We thank N. E. Sherman and J.-J. Park for LC-MS services at the W.M. Keck Biomedical Mass Spectrometry Laboratory. We thank Anson Parker for the introduction to SikuliX and Dr. Hardik for assistance building the Python script to assign Tg and mammalian proteins. We thank J. Elias at The Chan Zuckerberg Institute for guidance in LC-MS experimental design. We are extremely grateful to A. Chakraborty and K. Hadley at the University of Toronto for extensive discussion and assistance with the STOMP Macro. This work was supported by NIH K22 AI116727 (SEE) and AHA/Allen Institute 31315 (SEE).

5.7 *References*

(1) Hadley, K. C.; Rakhit, R.; Guo, H.; Sun, Y.; Jonkman, J. E.; McLaurin, J.; Hazrati, L. N.; Emili, A.; Chakrabartty, A. Determining composition of micron-scale protein deposits in neurodegenerative disease by spatially targeted optical microproteomics. *Elife* **2015**, *4*. DOI: 10.7554/eLife.09579 From NLM Medline.

(2) Chen, C. L.; Perrimon, N. Proximity-dependent labeling methods for proteomic profiling in living cells. *Wiley Interdiscip Rev Dev Biol* **2017**, *6* (4). DOI: 10.1002/wdev.272 From NLM Medline.

(3) Nadipuram, S. M.; Kim, E. W.; Vashisht, A. A.; Lin, A. H.; Bell, H. N.; Coppens, I.; Wohlschlegel, J. A.; Bradley, P. J. In Vivo Biotinylation of the Toxoplasma Parasitophorous Vacuole Reveals Novel Dense Granule Proteins Important for Parasite Growth and Pathogenesis. *Mbio* **2016**, *7* (4). DOI: 10.1128/mBio.00808-16 From NLM Medline.

(4) Bar, D. Z.; Atkatsh, K.; Tavarez, U.; Erdos, M. R.; Gruenbaum, Y.; Collins, F. S. Biotinylation by antibody recognition - a method for proximity labeling (vol 15, pg 127, 2018). *Nature Methods* **2018**, *15* (9), 749-749. DOI: 10.1038/s41592-018-0073-4.

(5) Espina, V.; Wulfkuhle, J. D.; Calvert, V. S.; VanMeter, A.; Zhou, W. D.; Coukos, G.; Geho, D. H.; Petricoin, E. F.; Liotta, L. A. Laser-capture microdissection. *Nat Protoc* **2006**, *1* (2), 586-603. DOI: 10.1038/nprot.2006.85.

(6) Wallis, R. B.; Holbrook, J. J. Reaction of a Histidine Residue in Glutamate Dehydrogenase with Diethyl Pyrocarbonate. *Biochemical Journal* **1973**, *133* (1), 183-187. DOI: DOI 10.1042/bj1330183.

(7) Kim, M. S.; Zhong, J.; Pandey, A. Common errors in mass spectrometry-based analysis of post-translational modifications. *Proteomics* **2016**, *16* (5), 700-714. DOI: 10.1002/pmic.201500355.

(8) Ewald, S. E.; Chavarria-Smith, J.; Boothroyd, J. C. NLRP1 Is an Inflammasome Sensor for Toxoplasma gondii. *Infect Immun* **2014**, *82* (1), 460-468. DOI: 10.1128/Iai.01170-13.

(9) Hatter, J. A.; Kouche, Y. M.; Melchor, S. J.; Ng, K.; Bouley, D. M.; Boothroyd, J. C.; Ewald, S. E. Toxoplasma gondii infection triggers chronic cachexia and sustained commensal dysbiosis in mice. *PLoS One* **2018**, *13* (10), e0204895. DOI: 10.1371/journal.pone.0204895 From NLM Medline.

(10) Coppens, I. Exploitation of auxotrophies and metabolic defects in Toxoplasma as therapeutic approaches. *Int J Parasitol* **2014**, *44* (2), 109-120. DOI: 10.1016/j.ijpara.2013.09.003.

(11) Schindelin, J.; Arganda-Carreras, I.; Frise, E.; Kaynig, V.; Longair, M.; Pietzsch, T.; Preibisch, S.; Rueden, C.; Saalfeld, S.; Schmid, B.; et al. Fiji: an open-source platform for biological-image analysis. *Nature Methods* **2012**, *9* (7), 676-682. DOI: 10.1038/Nmeth.2019.

(12) Choi, H.; Larsen, B.; Lin, Z. Y.; Breitkreutz, A.; Mellacheruvu, D.; Fermin, D.; Qin, Z. S.; Tyers, M.; Gingras, A. C.; Nesvizhskii, A. I. SAINT: probabilistic scoring of affinity purification-mass spectrometry data. *Nat Methods* **2011**, *8* (1), 70-73. DOI: 10.1038/nmeth.1541 From NLM Medline.

(13) Clough, B.; Frickel, E. M. The Toxoplasma Parasitophorous Vacuole: An Evolving Host-Parasite Frontier. *Trends Parasitol* **2017**, *33* (6), 473-488. DOI: 10.1016/j.pt.2017.02.007.

(14) Besteiro, S.; Michelin, A.; Poncet, J.; Dubremetz, J. F.; Lebrun, M. Export of a Toxoplasma gondii rhoptry neck protein complex at the host cell membrane to form the moving junction during invasion. *Plos Pathog* **2009**, *5* (2), e1000309. DOI: 10.1371/journal.ppat.1000309 From NLM Medline.

(15) Dunn, J. D.; Ravindran, S.; Kim, S. K.; Boothroyd, J. C. The Toxoplasma gondii Dense Granule Protein GRA7 Is Phosphorylated upon Invasion and Forms an Unexpected Association with the Rhoptry Proteins ROP2 and ROP4. *Infect Immun* **2008**, *76* (12), 5853-5861. DOI: 10.1128/Iai.01667-07.

(16) Camejo, A.; Gold, D. A.; Lu, D.; McFetridge, K.; Julien, L.; Yang, N. H.; Jensen, K. D. C.; Saeij, J. P. J. Identification of three novel Toxoplasma gondii rhoptry proteins. *Int J Parasitol* **2014**, *44* (2), 147-160. DOI: 10.1016/j.ijpara.2013.08.002.

(17) Stoka, V.; Turk, V.; Turk, B. Lysosomal cathepsins and their regulation in aging and neurodegeneration. *Ageing Res Rev* **2016**, *32*, 22-37. DOI: 10.1016/j.arr.2016.04.010.

(18) Luzio, J. P.; Hackmann, Y.; Dieckmann, N. M.; Griffiths, G. M. The biogenesis of lysosomes and lysosome-related organelles. *Cold Spring Harb Perspect Biol* **2014**, *6* (9), a016840. DOI: 10.1101/cshperspect.a016840 From NLM Medline.

(19) Nakano, R.; Ohira, M.; Yano, T.; Imaoka, Y.; Tanaka, Y.; Ohdan, H. Hepatic irradiation persistently eliminates liver resident NK cells. *PLoS One* **2018**, *13* (6), e0198904. DOI: 10.1371/journal.pone.0198904 From NLM Medline.

(20) Kelly, F. D.; Wei, B. M.; Cygan, A. M.; Parker, M. L.; Boulanger, M. J.; Boothroyd, J. C. Toxoplasma gondii MAF1b Binds the Host Cell MIB Complex To

Mediate Mitochondrial Association. *Msphere* **2017**, *2* (3). DOI: ARTN e00183-17.10.1128/mSphere.00183-17.

(21) Huang, D. W.; Sherman, B. T.; Lempicki, R. A. Systematic and integrative analysis of large gene lists using DAVID bioinformatics resources. *Nat Protoc* **2009**, *4* (1), 44-57. DOI: 10.1038/nprot.2008.211.

(22) Blume, M.; Seeber, F. Metabolic interactions between Toxoplasma gondii and its host. *F1000Res* **2018**, *7*. DOI: 10.12688/f1000research.16021.1 From NLM Medline.

(23) Hakansson, S.; Charron, A. J.; Sibley, L. D. Toxoplasma evacuoles: a two-step process of secretion and fusion forms the parasitophorous vacuole. *Embo J* **2001**, *20* (12), 3132-3144. DOI: DOI 10.1093/emboj/20.12.3132.

(24) Sinai, A. P.; Webster, P.; Joiner, K. A. Association of host cell endoplasmic reticulum and mitochondria with the Toxoplasma gondii parasitophorous vacuole membrane: a high affinity interaction. *J Cell Sci* **1997**, *110 (Pt 17)*, 2117-2128. DOI: 10.1242/jcs.110.17.2117 From NLM Medline.

(25) Pernas, L.; Adomako-Ankomah, Y.; Shastri, A. J.; Ewald, S. E.; Treeck, M.; Boyle, J. P.; Boothroyd, J. C. Toxoplasma effector MAF1 mediates recruitment of host mitochondria and impacts the host response. *Plos Biol* **2014**, *12* (4), e1001845. DOI: 10.1371/journal.pbio.1001845 From NLM Medline.

Chapter 6. Conclusions and Future Directions

6.1 *Conclusions and Future Directions*

The aim of this thesis is to develop a rational approach for the application of lipidomics and chemoproteomics to understand DGK metabolism. Through a methodical and quantitative analysis of global DGK metabolism, several key discoveries were made that impact the wider lipid biochemistry field: (i) identified lipid species when perturbating DGKθ and DGKη lipid composition using LC-MS/MS analysis, (ii) identified possible knock-in dTAG sites for N-terminus of DGKθ, α, and ξ, (iii) identified possible ligandable sites for developing DGK small-molecule inhibitors with selectivity.

A theme throughout the thesis work was the emphasis on studying enzyme function in dynamic biological environments, such as lysates, as presented in Chapter 2 and Chapter 4. Such data can be used to gain a wide range of insights; for instance, characterizing the functions of specific proteins, the relationships among these isozymes, their regulation and coordination and the therapeutic potential of DGKs. It is apparent that the information obtained from mass spectrometry analysis, as exemplified by the gain of function (overexpression) and live-cell treatment (Chapters 2 and 4, respectively) studies, provides interesting insight into molecular lipid composition at the level of fatty acyl chain length and unsaturation, using tandem LC-MS/MS techniques. This has allowed us to explore into substrate specificity and its critical role in the Lands cycle. Future studies will be required to elucidate if the Lands cycle does ultimately play a role in DGKθ's

metabolism. Tuning of small molecules may afford the opportunity to target specific sites on DGKθ and other DGK isoforms.

Additionally, the method development studies in Chapter 3 highlight the potential for new modalities that operate using alternative mode of actions, via temporal inhibition. In Chapter 3, we propose a chemical knockdown on DGKθ, DGKα, and DGKξ target protein, which would allow novel knockdown strategies for basic and therapeutic discoveries. In chapter 3, we turned our attention to novel degradation technology (dTAG) that uses small molecule degraders on targeted proteins of interest, which has the added advantage that introduces hybrid chemical biology system combining the benefits of small molecule perturbations with precision genetic editing (CRISPR-Cas9) allowing for temporal studies. As exciting as the possibilities dTAG may offer, further studies are needed to determine dTAG efficiency *in vivo*. Future studies examining the knockdown of dTAG therapeutic targets will be critical in expanding our understanding of DGK. One possible future study may be to create a novel PROTAC molecule that binds irreversibility to a DGK active site causing a polyubiquitination. In other words, the insights that we gained in Chapter 2 and 3 may be used to create SuTEx/PROTAC molecule. Another future study may require the use of FACS to sort KI dTAG cells to provide a higher yield of KI dTAG cell line. As we shown in Chapter 3, there is plenty of room for improvement before reaching any conclusions in understanding specific regulatory metabolic mechanisms.

In Chapter 4, we present a comprehensive ligand binding map of reactive tyrosine and lysine residues that are readily accessible in live cell probe labeling

studies. This resource should guide future efforts to explore regulatory and catalytic DGK domains for basic biochemistry and inhibitor discovery efforts. And efforts to identified possible ligandable sites for developing DGK small-molecule inhibitors with selectivity.

Future studies include the following: (i) perform untargeted and targeted mass spectrometry analysis of specific lipid species of interest. Currently, the work we performed in Chapter 2 provides a small window of the untargeted lipid species, which may miss broader lipid species in the collection of data. A targeted approach would provide focused data collection which can aid in making better deductions in metabolic pathways for DGK and in general. (ii) target different regions when knocking-in a dTAG of interest. Currently our N-terminus seems to be functional rather than attempted C-terminus knock-ins. In addition, attempt to KI other DGKs beside DGKθ, α, and ξ. In addition to performing an immunoprecipitated blot, perform an RT-PCR analysis would expand our scope in verifying dTAG KIs.. In addition, attempt to KI other sites on the locus of interest other than the N- or C-terminus regions. (iii) Although C1 domains have provided valuable information on the metabolic function of DGKs, performing a chimeric switch of other domains besides C1 domains could provide insight into DGK metabolic function. And, (iv) use autoSTOMP as an automated platform to visualize and identify small molecules for possible tag in creating PROTAC molecules or even inhibitors for SuTEx inhibitors, which then can be used to identify active sites in DGK proteins. We are anticipating that autoSTOMP can be used to possibility identify proteins

belonging in the range of 1 μm scale subcellular structures in a range of biological specimens as described in Chapter 5.

The broader impact of my thesis work in the lipid biology and DGK field are (i) understand DGKs metabolic activities by way of finding creative methods with already established approaches in lipid analysis. This will assist in resolving issues in our current understanding of DGKs. (ii) create better probes and inhibitors that will target specific sites to either inhibit or promote a catalytic function of a protein.

In conclusion, we apply modern technologies for perturbing protein function, such as CRISPR/Cas9, PROTAC, and autoSTOMP to probe DGK metabolic function. We have demonstrated that targeted protein degradation (dTAG) can be used to probe lipid substrate specificity of DGK isoforms. This allows us to then focus our chemoproteomic efforts to identify important/critical sites on all ten DGK enzymes with importance for metabolic function. Collectively, the ligandable sites identified represent the first step towards developing potent and selective inhibitors for individual DGK isoforms. Based on my collective work, we are confident that the knowledge gained here can provide insight into our understanding DGK metabolism and expand the application of our methods described here.

6.2 *Publications Resulting from This Work*

Mendez, R., Shaikh, M., Lemke, M.,Yuan, K., Libby, A., Bai, D., Ross, M., Harris, T., and Hsu, K. Identifying reactive sites on diacylglycerol kinases for covalent binding in cells. *Cell Chemical Biology* (2022) *Under Review*.

Yin, B., **Mendez, R.**, YuZhao, R., Rakhit, R., Hsu, K., Ewald, S., Automated spatially targeted optical microproteomics (autoSTOMP) to determine protein complexity of subcellular structure. *Anal. Chem.* 2020, 92, 2, 2005–2010